Ultrasonic study of the elastic properties of calcium tungstate and other scheelites

Farley, John Michael

ULTRASONIC STUDY OF THE ELASTIC PROPERTIES OF CALCIUM TUNGSTATE AND OTHER SCHEELITES

by

JOHN MICHAEL FARLEY B.Sc.

A thesis submitted to the University of Durham

for the degree of

Doctor of Philosophy

October 1973

Department of Applied Physics
and Electronics
Science Laboratories
Durham City

ABSTRACT

A study of the elastic properties of the scheelite structure crystals $CaWO_4$, $CaMoO_4$, $SrMoO_4$ and $PbMoO_4$ is presented. The seven independent components of the elastic stiffness constant tensor of $CaWO_4$ have been determined between 1.5 K and 300 K by pulse superposition measurements of ultrasound velocities. A computer fitting procedure has been used to obtain the elastic constants from the velocity data; this has allowed the elastic constants to be determined even though large energy flux deviations prevented the measurement of the velocities of the quasi-shear modes propagated in the [100] and [110] directions. Experiments on $SrMoO_4$ single crystals have shown that similar difficulties were the cause of inconsistencies in recently published velocity data; a new, correct set of elastic constants for $SrMoO_4$ has been determined.

Scheelites belong to the TII Laue group. The signs of C_{16} and S_{16} depend on the definition of the sense of the +Z axis with respect to the atomic arrangement. A convention previously used for $CaMoO_4$ has been adopted, the Z axis sense has been found in $CaWO_4$ and $PbMoO_4$ by a novel spin resonance technique and in $SrMoO_4$ by an x-ray method: in each material C_{16} has been shown to be negative. Elastic behaviour and wave propagation characteristics, and their orientation dependence in the four materials, have been compared and contrasted. The work has provided a new insight into the acoustic properties of TI and TII Laue group materials; in the latter the "axes of acoustic symmetry" in the (001) plane do not coincide with the <100> and <110>

crystallographic directions (as in TI's) but deviate from them by angles which are between 15^{o} and 23^{o} in the scheelites studied. Knowledge of the positions of these axes should facilitate further ultrasonic studies.

ACKNOWLEDGEMENT

I am most grateful to my supervisors Dr. G A Saunders and Dr J S Thorp for their enthuastic guidance and support for this research project. I have benefited enormously from many discussions with members of Dr. Saunders' ultrasonics research group.

My thanks are due to Professor D A Wright for allowing me to use the facilities of the Department, and to the workshop staff for their assistance. In particular I am grateful to Mr. R T Harcourt for his patient, painstaking efforts in cutting and polishing ultrasonics specimens.

Finally I must thank my wife, Kay, for her enoouragement, support and practical help with the preparation of this thesis.

gM Farley

30.10.73

CONTENTS

CHAPTER 8: CONCLUSIONS

CHAPTER ONE

INTRODUCTION

Scheelite structure tungstate and molybdate crystals occur naturally and are sources of the elements tungsten and molybdenum. Scheelite is the mineral name for Calcium tungstate ($CaWO_4$); other mineral names and other scheelite structure materials are listed in Table 1.1.

Calcium tungstate was used until about 1940 as a phosphor in fluorescent lamps, and assumed further technological importance in the 1960's with the discovery that single crystals could be grown doped with neodymium (Nd^{3+}) in concentrations suitable for laser action. A Nd^{3+}:$CaWO_4$ laser was the first crystalline laser to give continuous operation at room temperature (Johnson et al 1962), and such devices became available commercially. More recently there has been interest in scheelite structure tungstates and molybdates for acousto-optic device applications. Calcium molybdate ($CaMoO_4$) and lead molybdate ($PbMoO_4$) have attracted most attention. The operation of a $CaMoO_4$ tunable acousto-optic filter has been demonstrated (Harris et al 1970) and $PbMoO_4$ has been the subject of several studies (Pinnow et al 1969, Coquin et al 1971). Lead molybdate beam steering and light modulating devices have been produced and marketed (Hobden 1972). For these devices the acousto-optic figure-of-merit† is proportional

† The figure of merit of a beam deflector may be defined by the expression

$$M = n^6 p^2 / \rho v^3$$

where n is the refractive index, p the appropriate photoelastic constant, ρ the density and v the sound velocity (Flinchbaugh 1971).

to the sixth power of the refractive index and the inverse of the cube of ultrasound velocity; $PbMoO_4$ is particularly attractive because it has a large refractive index and sound velocities in the material are comparatively low.

These applications of scheelite structure crystals have stimulated studies of crystal growth, doping, defect, thermal and optical vibrational properties (reviewed in Chapter 2). Until the present work was begun investigations of elastic properties were rather limited (see Section 2.4.4), probably because of experimental difficulties. However there is a need to understand the mechanical properties of technologically interesting materials, and the intention of this study has been to provide further knowledge of elastic behaviour and wave propagation characteristics — properties directly relevant to acoustic device applications. Knowledge of elastic properties can provide information about interatomic binding in a material. In the scheelites such information was expected to be interesting in view of the unusual structure and the presence of well defined sub-units (WO_4 or MoO_4 groups. Another important aspect of the work has arisen because the scheelites are the only well known materials belonging to the TII group — the less symmetrical of the two tetragonal Laue groups (TI and TII). Particular attention has been devoted to the need in TII solids to specify uniquely the axial set to which the elastic constants are referred, and to the origin of the experimental difficulties which arise in studying solids of this Laue symmetry. The elastic properties of a TII solid are

characterised by a stiffness tensor with seven independent components. The first objective has been the determination of the components of the stiffness tensor of $CaWO_4$ single crystals in the temperature range 1.5 K to 300 K by pulse superposition measurements of ultrasound velocity. Subsequently experimental work has been extended to $SrMoO_4$ and $PbMoO_4$ to permit comparison between the elastic properties of a series of scheelites.

In Chapter 2 the properties of scheelite structure crystals are reviewed, with particular emphasis on properties relevant to the present study. The convention for defining the axial set is established. In Chapter 3, the formal theory of anisotropic elasticity is applied to tetragonal crystals and the relationships and differences between the elastic properties and wave propagation characteristics of the TI and TII groups are emphasised. The principles of the ultrasonics methods used in the work are outlined in Chapter 4, and in Chapter 5 details of the measuring system are given. The characterisation and preparation of ultrasonics specimens is described; novel methods of determining the sense of Z axis in a boule are given. The results of ultrasound experiments on $CaWO_4$ are presented in Chapter 6 and the elastic behaviour is described. Related experimental studies on $SrMoO_4$ and $PbMoO_4$ single crystals are described in Chapter 7, and in Chapter 8 the elastic properties of $CaWO_4$, $CaMoO_4$, $SrMoO_4$ and $PbMoO_4$ are compared and contrasted. Certain deductions are made about the interatomic binding. The phenomena of "acoustic symmetry" is discussed. It is

shown how in TII Laue group crystals the origin of the experimental difficulties in determining elastic constants, the need to define a sense as well as a direction of the Z axis, and the relationships between the elastic properties of TII and TI crystals can each be explained in terms of the deviation of "axes of acoustic symmetry" from the conventional crystallographic axes.

Computer programmes used in the work are given in Appendix I, and publications which embody the results of the work are listed in Appendix II.

TABLE 1.1

Scheelite structure materials

Mineral names of tungstates and molybdates

$CaWO_4$	Scheelite
$CaMoO_4$	Powellite
$SrWO_4$	
$SrMoO_4$	
$BaWO_4$	
$BaMoO_4$	
$PbWO_4$	Stolzite
$PbMoO_4$	Wulfenite
$CdMoO_4$	

Other scheelite structure crystals

$NaIO_4$	$ZrGeO_4$
KIO_4	$HfGeO_4$
	$CeGeO_4$
	$ThGeO_4$

CHAPTER TWO

SCHEELITE STRUCTURE CRYSTALS

In this chapter those properties of scheelite structure crystals which are relevant to the present work are reviewed. Most attention is paid to the properties of $CaWO_4$, but details of work on other scheelite structure tungstates and molybdates are given when available.

2.1 CRYSTAL STRUCTURE

The scheelite structure is tetragonal with a point group 4/m (see the stereogram in Figure 2.1a) and a space group $I4_1/a$. The symmetry elements of the space group are a fourfold screw axis and a glide plane which is normal to this axis. The equivalent points for this space group are

$$\begin{aligned}(0\ 0\ 0;\ \ 1/2\ 1/2\ 1/2) + {} & x,y,z;\ \ \bar{x},\bar{y},z;\ \ \bar{y},x,\bar{z};\\ & y,\bar{x},\bar{z};\ \ \bar{x},1/2-y,1/4-z;\\ & y,1/2-x,1/4+z;\ \ \bar{y},1/2+x,1/4+z\end{aligned} \qquad (2.1)$$

if an origin is taken at a $\bar{4}$ point (International Tables for X-ray Crystallography 1952).

In the tungstates and molybdates with the scheelite structure the metal atoms are in "special positions"; they are sited at the equivalent points generated by expression 2.1 on setting x,y,z equal to 0,0,0 (for the tungsten or molybdenum atoms) and equal to 0,0,1/2 (for the calcium, strontium, barium, cadmium or lead atoms). A body-centred tetragonal unit cell is defined by reference to the metal atom positions (see Figure 2.2). Crystallographic X, Y and Z axes are conventionally defined parallel to the basis vectors $\underline{a}$, $\underline{b}$ and $\underline{c}$ of the tetragonal cell, the Z direction being taken parallel to the fourfold symmetry axis. Thus all the metal atoms lie on planes normal to the X, Y and Z axes with interplanar spacings of a/2, a/2 and c/4 measured along these axes. Taken on their own the metal atoms lie on a lattice which has mirror planes of symmetry parallel to the fourfold axis and a point group 4/mmm (see the stereogram, Figure 2.1b).

The oxygen atoms are sited in "general positions" in the unit cell. These are given by the expression 2.1 in terms of coordinates x_O, y_O, z_O. Determination of these oxygen atom positions is difficult because x-ray scattering is dominated by the much heavier metal atoms. However accurate measurements of the oxygen coordinates in $CaWO_4$ have been made by neutron diffraction (Kay et al 1964) and x-ray methods (Zalkin and Templeton 1964). The results are compared in Table 2.1 and show good agreement. The positions of the four nearest neighbour oxygen atoms with respect to a tungsten atom are shown in Figure 2.3a. The four oxygen atoms are located at the corners of a tetrahedron which is slightly squashed in the direction of the Z axis, to give a tungstate anion with a W—O distance of 1.783Å and O—W—O angles of $113^{\circ}27'$ (twice) and $107^{\circ}56'$ (four times). With respect to each of the calcium atoms in $CaWO_4$ the eight neighbouring oxygen atoms form two interpenetrating bisphenoids with Ca—O distances of 2.44Å and 2.48Å respectively as shown in Figure 2.4.

A projection of the tungstate tetrahedron on to the XY plane is shown in Figure 2.3b. The tungsten-oxygen bonds do not lie within the planes of the metal atoms, nor in the planes which bisect them. The diagonal plane of the tetrahedron makes angles of 31° and 14° with the [100] and [110] directions respectively. Similarly the axes of the oxygen framework surrounding the calcium atoms (shown in projection form in Figure 2.5) are rotated about the Z axis with respect to the bisector of the X and Y axes. A description of the sense of these rotations depends on the

choice of the sense of the +Z direction with respect to the atomic arrangement. The +Z and -Z axes are therefore distinguishable even though the mirror operation of the point group brings one into coincidence with the other. The sense of the Z axis must be referred to the positions of the oxygen atoms in the unit cell as it is these atoms alone which render the opposite senses non-equivalent. Zalkin and Templeton (1964) recognised this; the oxygen coordinates given by these workers for $CaWO_4$ define a sense of +Z axis in the unit cell such that the projections of the oxygen sites on to the XY plane have the form shown in Figure 2.3b and 2.5. The necessity for the definition of a sense of the Z axis has important consequences affecting the study of some of the physical properties of scheelite materials: the signs of some tensor properties depend on the sense of Z axis chosen (Farabaugh et al 1966), and the crystals to be studied must be uniquely oriented. Some novel methods devised in the course of the present work for finding the sense of Z axis in scheelite crystals will be described in later chapters of this thesis.

Neutron diffraction refinements of the crystal structures of the scheelite materials $SrMoO_4$, $SrWO_4$, $CaMoO_4$, $BaWO_4$ (Gürmen et al 1971) and $PbMoO_4$ (Leciejewicz 1965) have given the oxygen coordinates in these materials to an accuracy one order of magnitude better than that of earlier work by Sillén and Nylander (1943). The crystallographic data for each of these materials is compared with that for $CaWO_4$ in Table 2.1. Unit cell parameters, deduced from x-ray powder photograph data (National Bureau of Standards 1962) are

included. The table also gives the setting angle of the tungstate or molybdate anion in the XY plane. This is the angle between the X direction and the projection of a W—O or Mo—O bond, as illustrated in Figure 2.3b . The oxygen coordinates and the signs of the setting angles have been tabulated using the sense of +Z axis taken by Zalkin and Templeton (1964) and subsequently followed by Farabaugh et al (1966) and Gürmen et al (1971). Throughout this work this definition of the sense of Z axis will be taken as the established convention.

The scheelite structure can be considered to be a complex layer structure; it has been described as such by Arbel and Stokes (1965). Each unit cell may be divided into four horizontal (001) layers of equal packing density (numbered 1 to 5 in Figure 2.2). Cleavage and slip occur parallel to these layers in $CaWO_4$. The layers are the closest packed planes in the structure: each tungsten and its four associated oxygen atoms is surrounded by four calcium atoms (labelled A, B, C and D in Figure 2.2) in the same layer. These calcium atoms lie at the corners of a square with side equal to the lattice parameter (a).

2.2 GROWTH AND DOPING OF SINGLE CRYSTALS

Large single crystals of scheelites, suitable for laser or acousto-optic applications, can be grown by the Czochralski technique of pulling from the melt. Czochralski growth of $CaWO_4$ was first reported by Nassau and Van Uitert (1960). This method can yield boules of high optical perfection, several inches in length and up to one inch in diameter. By using different seed crystals, boules can

be produced (Nassau and Broyer 1962) with growth axes parallel to the <001>, <100> and <110> crystallographic directions. Boules grown with diameters less than half that of the crucible containing the melt have characteristic cross-sections indicating different growth rates ($r_{hk\ell}$) in the order:

$$r_{100} > r_{h0\ell} > r_{001} \quad \text{and} \quad r_{100} > r_{hk0} > r_{110}.$$

The technique has subsequently been used by many different workers to grow single crystals of most other scheelite structure tungstates and molybdates (Preziosi et al (1962),, Bonner and Zydzik (1970)) with particular attention being given recently to the growth of $PbMoO_4$. Despite having a comparatively low melting point (1070°C), $PbMoO_4$ is not particularly easy to grow in good optical quality. There is a tendency for the melt to lose PbO and O_2 causing variations in stoichiometry, and it is necessary to anneal the crystals in air or oxygen for considerable periods (Hobden 1972). Optical perfection is much improved if very high purity starting materials are used (Esashi and Namikata 1972).

Crystals of the tungstates and molybdates can be grown doped with trivalent paramagnetic rare earth ions in concentrations suitable for laser action. Charge neutrality is maintained either by vacancy compensation or by the deliberate addition of monovalent sodium (Na^+) in atomic concentration equal to that of the dopant. The rare earth ions Nd^{3+}, Gd^{3+}, Sm^{3+}, Eu^{3+} etc. have radii (0.85 to 1.14Å) comparable to that of Ca^{2+} (0.99Å) and have been shown to substitute for the divalent cation in $CaWO_4$ (Nassau and

Loiacono (1963), Nassau (1963)). No evidence for interstitial substitution was found, presumably because of the compact nature of the structure.

The sites of the dopant rare earth ions are thus of the type shown in Figure 2.5; each is surrounded by eight oxygen atoms which dominate the crystal field at the impurity site. Consequently the principle axes of the crystal field in the XY plane (the "magnetic axes") do not coincide with the crystallographic axes but with the diagonals of the framework of the oxygen atoms which are situated closest to the plane of the impurity ion. This was demonstrated by Hemstead and Bowers (1959) who, by observation of the extremes in the positions of particular lines of the Mn^{2+} and Gd^{3+} spectra, found the deviation of the magnetic axes in the XY plane from the <110> axes to be $9^{o} \pm 2^{o}$.

A determination of the positions of the magnetic axes relative to the crystallographic axes in a boule can therefore be used to indicate the positions of the oxygen atoms. It has been stated earlier (section 2.1) that it is these oxygen positions which render the +Z and -Z directions non-equivalent; the Figure 2.5 shows the projection of the oxygen sites on to the XY plane for the definition of the sense of the +Z axis used here, and a right handed XYZ axial set. The magnitude of the angular deviation of the magnetic axes from these crystallographic axes (see Figure 2.6) can be estimated from the coordinates of the oxygen atoms; values are $8.5^{o}(CaWO_4)$, $9^{o}(CaMoO_4)$, $9.2^{o}(SrMoO_4)$, $9^{o}(PbMoO_4)$.

Location of the magnetic axes in a boule of a doped scheelite structure tungstate or molybdate therefore provides a means of identifying the sense of the +Z axis in the boule. This method was used in the present work to orient uniquely boules of Gd^{3+} doped $CaWO_4$ and $PbMoO_4$, and allowed the relationship between certain direction-dependent properties and the atomic arrangements to be determined uniquely for the first time.

2.3 DEFECT PROPERTIES

For use in laser or acousto-optic devices a material must be available in high optical quality. Since scheelite structure crystals are uniaxial they are optically anisotropic, and a high degree of optical perfection can only be achieved by a correspondingly high degree of crystal perfection. There have been several studies of the defect properties of as-grown $CaWO_4$ crystals. Nassau and Broyer (1962) observed scattering centres which were considered to be inclusions of solid or gaseous material, but which could be avoided by careful control of growth parameters. As-grown crystals were found to be very susceptible to cleavage parallel to the (001) plane, but this tendency was reduced if the crystals were annealed at temperatures close to the melting point. Many workers have observed the presence of grown-in dislocations by using etch-pit techniques (Chadhuri and Phaneuf (1963), Levinstein et al (1963), Cockayne et al (1964), Arbel and Stokes (1965), Buchanan and Casselton (1966)). After chemical polishing, typically by boiling for 5 minutes in orthophosphoric acid

(Cockayne and Robertson 1964) to remove surface damage, the points of emergence of dislocation lines on the {001}, {100} and {110} planes were revealed by various etches. On the {001} planes the etch-pits were found to be square with sides parallel to the [100] and [010] directions (Levinstein et al 1963), and on the {100} and {110} planes they were "lozenge shaped" and had mirror symmetry about a long axis parallel to the (001) plane. In the present work (see Chapter 5) the orientation of these pits has been related to the sense of the Z axis in the material, and now provides a useful means of identifying the sense of this axis in a boule.

Complementary work on the plastic deformation of $CaWO_4$ by Cockayne and Hollox (1964) and Arbel and Stokes (1965) has yielded information which is relevant to understanding the interatomic binding in scheelite structure tungstates and molybdates. At low temperatures $CaWO_4$ was found to be brittle, and plastic deformation did not occur below 400°C. From this temperature up to 900°C slip on the (001) <100> system was the only deformation mode that was observed. The slip plane (001) is parallel to the layers of the structure, and Arbel and Stokes point out that the slip direction, <100>, is in fact the direction in which slip can occur with the least overlap of oxygen atoms and the least distortion of the WO_4 tetrahedra.

The defect properties of $PbMoO_4$ have been the subject of two recent studies (Namikata and Esashi (1972), Esashi and Namikata (1972)). Etch-pits were observed on the Z and X faces by etching for three to four minutes in

a 5% caustic soda solution at room temperature. On the Z face the pits were square while on the X faces they had a "lozenge" shape. Pit densities were found to be larger in crystals grown from low purity starting materials. On the Z faces the etch-pits were found to have edges which were inclined at about 30° to the <100> axes. In the course of the present work the sense of this inclination has been determined with respect to the conventional definition of Z axis, and now provides a means of determining the sense of Z axis in a boule of pure or doped $PbMoO_4$. Details are given in Chapter 7.

2.4 THERMAL PROPERTIES

Study of the thermal properties of the scheelites was stimulated by the need to develop the technology of the materials for device applications. The melting points, densities and Moh's hardness numbers of several scheelites are listed in Table 2.2 and the results of specific heat, thermal expansion, and thermal conductivity measurements are detailed below. Vibrational properties are also discussed.

2.4.1 Specific heat

The room temperature specific heat of mineral scheelite was first measured over a century ago (Kopp 1865). Somewhat more recently the temperature dependence of the constant pressure specific heat (C_P) of pure $CaWO_4$ and $CaMoO_4$ single crystals has been measured (King and Weller (1961), Weller and King (1963) and Lyon and Westrum (1968)) from 5 K to 350 K. At higher temperatures the specific heat of $CaWO_4$ has been measured by Yakoleva and Rezukhina (1960).

The measurements are compared in Figure 2.7. Data obtained by Klein (1968) from simultaneous thermal conductivity and thermal diffusivity measurements on a Nd doped (0.5 mol%Nd) $CaWO_4$ crystal are also shown. A striking feature of the results is the close similarity of the specific heats of $CaWO_4$ and $CaMoO_4$ over a wide temperature range; only at low temperatures (< 75 K) do the measured specific heats differ significantly. In both cases the specific heat curves deviate from the normal sigmate shape predicted by simple Debye theory. This will be discussed further in Section 6.2.2.

2.4.2 Thermal expansion

Scheelite structure materials have an anisotropic thermal expansion. The coefficients $\alpha_{\parallel}$ ($=\alpha_c$) and $\alpha_{\perp}$ ($=\alpha_a$) which describe the expansion parallel and perpendicular to the fourfold axis respectively have been measured over a wide temperature range for $CaWO_4$. Nassau and Broyer (1962) quote average values over four regions of temperature between $-196^{o}C$ and $1025^{o}C$. Yates and Bailey (1971) have reported values at temperature intervals of approximately 10 K between 30 K and 270 K. Above room temperature and up to $350^{o}C$, α_c and α_a have been found to obey the relationships

$$\alpha_a = 5.96\times10^{-6} + 12.23\times10^{-9}T + 24.85\times10^{-12}T^2 \qquad (2.2)$$

$$\alpha_c = 11.69\times10^{-6} + 22.07\times10^{-9}T + 21.43\times10^{-12}T^2 \qquad (2.3)$$

where T denotes the temperature in ^{o}C (Deshpande and Suryanarayana 1972). In Figure 2.8 the different measurements for temperatures up to 300 K are compared. Considerable

disagreement is apparent even though it is difficult to compare measurements which represent mean values over different ranges.

Comparison of the room temperature thermal expansions of different scheelites (see Table 2.3) shows that all the materials exhibit the same type of anisotropy; $\alpha_{\parallel}(=\alpha_c)$ is substantially greater than $\alpha_{\perp}(=\alpha_a)$. Deshpande and Suryanarayana (1969) suggest that the anisotropy of thermal expansion is indicative of weaker binding in the direction parallel to the Z axis than in directions normal to it. This is discussed in Chapter 8.

2.4.3 Thermal conductivity

Thermal conductivity measurements in $CaWO_4$ and other scheelite materials are somewhat limited. A room temperature measurement was made on $CaWO_4$ by Nassau and Broyer (1962). Measurements on a c-axis grown, doped $CaWO_4$ sample were made between 77 K and 300 K by Klein (1968) while Holland (1962) reported the thermal conductivity of doped c- and a-axis specimens at about 4.2 K, about 40 K and room temperature. The results, reproduced in Figure 2.9, show reasonably good agreement, and between 80 K and 200 K lie on the straight line $K_T = 8.22/T$ fitted by Klein to his measurements. The curves drawn by Holland (also reproduced in Figure 2.9) illustrate how the measurements may fit the usual pattern of temperature variation of thermal conductivity for a doped insulator. The height of the maximum is determined by impurity scattering of phonons and is reduced for increasing dopant concentration. Above the maximum the most significant contribution to the thermal

resistivity would be expected to be Umklapp scattering, which depends only on the phonon spectrum and not on the doping. Umklapp process thermal resistivity is generally found to be proportional totemperature (Klemens 1958); the straight line fitted by Klein between 80 K and 200 K agrees with this. Above these temperatures Klein's measurements show a deviation from the linear dependence, but this may be the result of experimental error since in this temperature range the specific heat derived from these and simultaneous thermal diffusivity measurements deviates markedly from the specific heat determinations of other workers (see Figure 2.7). The results indicate that the thermal conductivity does not have significant anisotropy in $CaWO_4$. Similarly, almost isotropic thermal conductivities have been measured for $CaMoO_4$ (K_a = 0.0395, K_c = 0.0382 watt cm^{-1} K^{-1}), and $SrMoO_4$ (K_a = 0.0404, K_c = 0.0416 watt cm^{-1} K^{-1}) by Flournoy and Brixner (1965) and for $PbMoO_4$ ($K_a \simeq K_c$ = 0.015 watt cm^{-1} K^{-1}) by Pinnow et al (1969).

2.4.4 Vibrational properties

Studies of the optical vibrational spectra of the scheelite structure tungstates and molybdates have been extensive. There have been infra-red investigations of $CaWO_4$ and $CaMoO_4$ (Barker (1964), Khanna and Lippincott (1968)), Raman spectroscopy studies of $CaWO_4$, $CaMoO_4$, $SrWO_4$, $SrMoO_4$, $PbWO_4$ and $PbMoO_4$ (Russell and Laudon (1965), Russell (1966), Porto and Scott (1967), Khanna et al (1968)). It has been established through the above work that the vibrational modes of the different materials are somewhat

similar, and that in each case the optical modes can be separated into two sets. The first set comprises 18 vibrational modes whose frequencies closely match those of the free tungstate (or molybdate) ion in aqueous solution (Scott 1968), and which are therefore considered to be "internal" modes (vibrational modes in which the centre of gravity of the WO_4 or MoO_4 group is not displaced). The second set is made up of lower frequency "external" modes (in which the WO_4 or MoO_4 groups vibrate as rigid units).

Compared with the optical lattice modes, the acoustical lattice modes of scheelites had received little attention when the present work was begun. Reported work on $CaWO_4$ was limited to the measurements of several ultrasound velocities at room temperature (Gerlich 1964). The measurements obtained were not sufficient to allow calculation of the components of the elasticity tensor and further measurements were prevented by difficulties in exciting certain modes. For $CaMoO_4$ there were two separate determinations of the elastic constants, both at room temperature (Alton and Barlow 1967, Wachtmann et al 1968). The present work thus includes the first determination of the complete elastic constant tensor of $CaWO_4$ and the first investigation of the temperature dependence of the elastic constants of any scheelite structure material. During the progress of the present work the room temperature elastic constants of $SrMoO_4$ (Chung and Li 1971b) and $PbMoO_4$ (Coquin et al 1971) were reported. Experiments have been carried out to complement these investigations and to permit the first comparison of the orientation dependence of elastic properties in $CaWO_4$, $CaMoO_4$, $SrMoO_4$ and $PbMoO_4$.

Table 2.1

Crystallographic data

Material	Lattice parameters			Oxygen coordinates				Anion setting angle†
	c(Å)	a(Å)	ref.	x_O	y_O	z_O	ref.	
$CaWO_4$	11.376	5.243	[1]	0.2415	0.1504	0.0861	[1]	$+31^\circ55'$
$CaWO_4$				0.2413	0.1511	0.0861	[2]	$+32^\circ3'$
$CaMoO_4$	11.43	5.226	[6]	0.2428	0.1465	0.0826	[3]	$+31^\circ6'$
$SrWO_4$	11.951	5.417	[6]	0.2362	0.1395	0.0818	[3]	$+30^\circ34'$
$SrMoO_4$	12.02	5.394	[6]	0.2374	0.1357	0.0809	[3]	$+29^\circ45'$
$BaWO_4$	12.72	5.613	[6]	0.2332	0.1227	0.0781	[3]	$+27^\circ45'$
$BaMoO_4$	12.76	5.56	[5]	0.25	0.11	0.075	[5]	$+23^\circ45'$
$PbMoO_4$	12.08	5.41	[5]	0.2352	0.1366	0.0811	[4]	$+30^\circ9'$
$CdMoO_4$	11.17	5.14	[5]	-	-	-		-

† measured from +X axis towards +Y axis

[1] Zalkin and Templeton (1964)

[2] Kay et al (1964)

[3] Gürmen et al (1971)

[4] Leciejewicz (1965)

[5] Wyckoff (1960)

[6] National Bureau of Standards (1962)

Table 2.2

Material	Melting Point ^{o}C	Hardness Moh's No.	Density g cm^{-3}	Reference
$CaWO_4$	1580	4.5	6.120	1,2,3
$CaMoO_4$	1480	4.3	4.255	4,5,6
$SrWO_4$	1535	-	6.187	1,5
$SrMoO_4$	1490	-	4.54	4,5
$BaWO_4$	1475	-	6.428	1,3
$BaMoO_4$	1480	-	4.65	5
$PbMoO_4$	1070	3	6.95	7
$CdMoO_4$	1175	-	-	8

1. Chang, Scroger and Philips (1966)
2. Thornton, Fountain, Flint and Crow (1969)
3. Shapolalova, Mikhailova, Gerasimov (1960)
4. Flournoy and Brixner (1965)
5. Handbook of Chemistry and Physics (1966-7)
6. Swanson, Gilfrich and Cook (1956)
7. Bonner and Zydzik (1970)
8. Brixner (1968)

Table 2.3

Thermal expansion coefficients of scheelite structure tungstates and molybdates at 30°C

Material	$\alpha_a \times 10^6$ K^{-1}	$\alpha_c \times 10^6$ K^{-1}	Reference
$CaWO_4$	6.35	12.38	[1]
$CaMoO_4$	7.67	11.88	[1]
$SrWO_4$	5.86	13.21	[1]
$BaWO_4$	4.43	18.35	[1]
$PbMoO_4$	10.00	25.00	[2]
$CdMoO_4$	6.85	15.13	[1]

[1] Deshpande and Suryanarayana (1969)

[2] Coquin et al (1971)

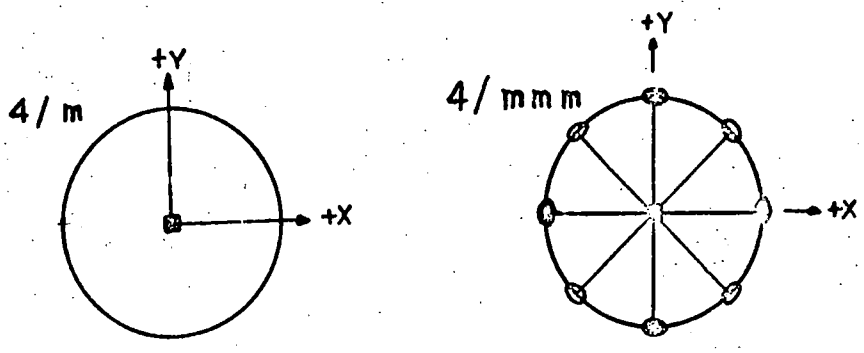

FIGURE 2.1: Stereograms of 4/m and 4/mmm point groups

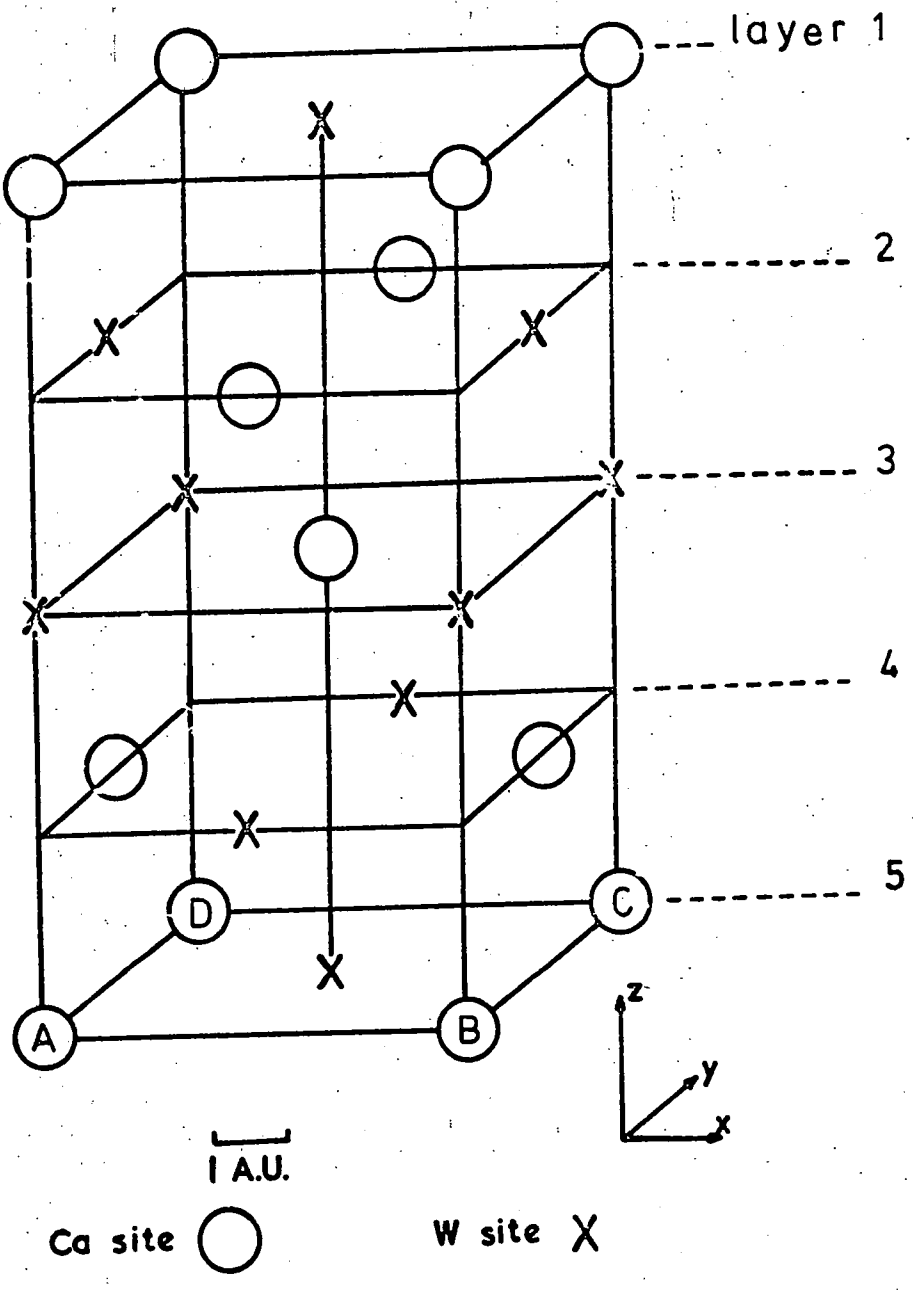

FIGURE 2.2: Metal atom sites in the scheelite structure

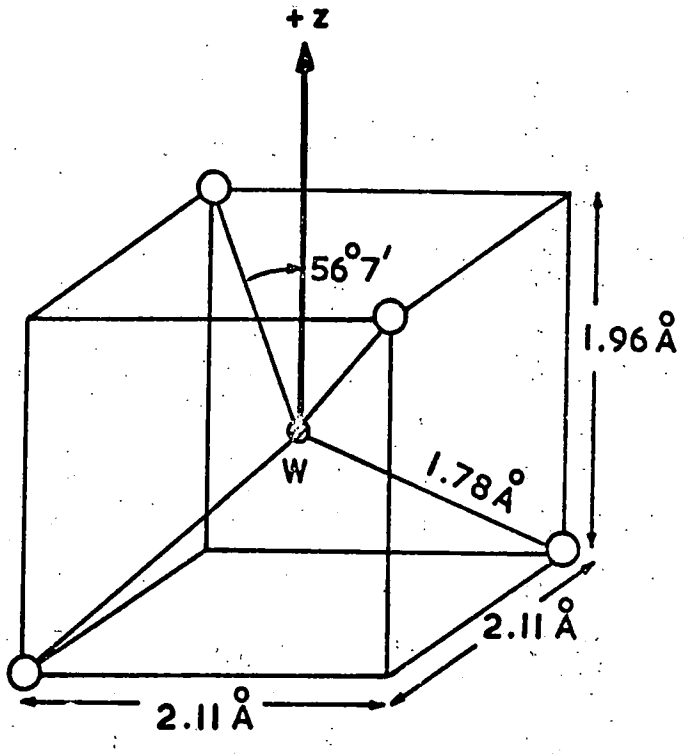

○ oxygen atom

(a)

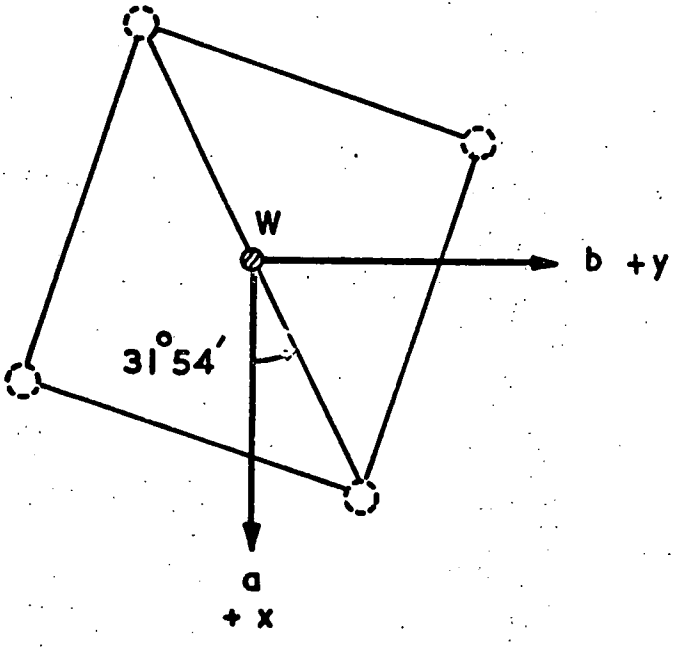

◌ Projection of oxygen atom onto xy plane.

(b)

FIGURE 2.3

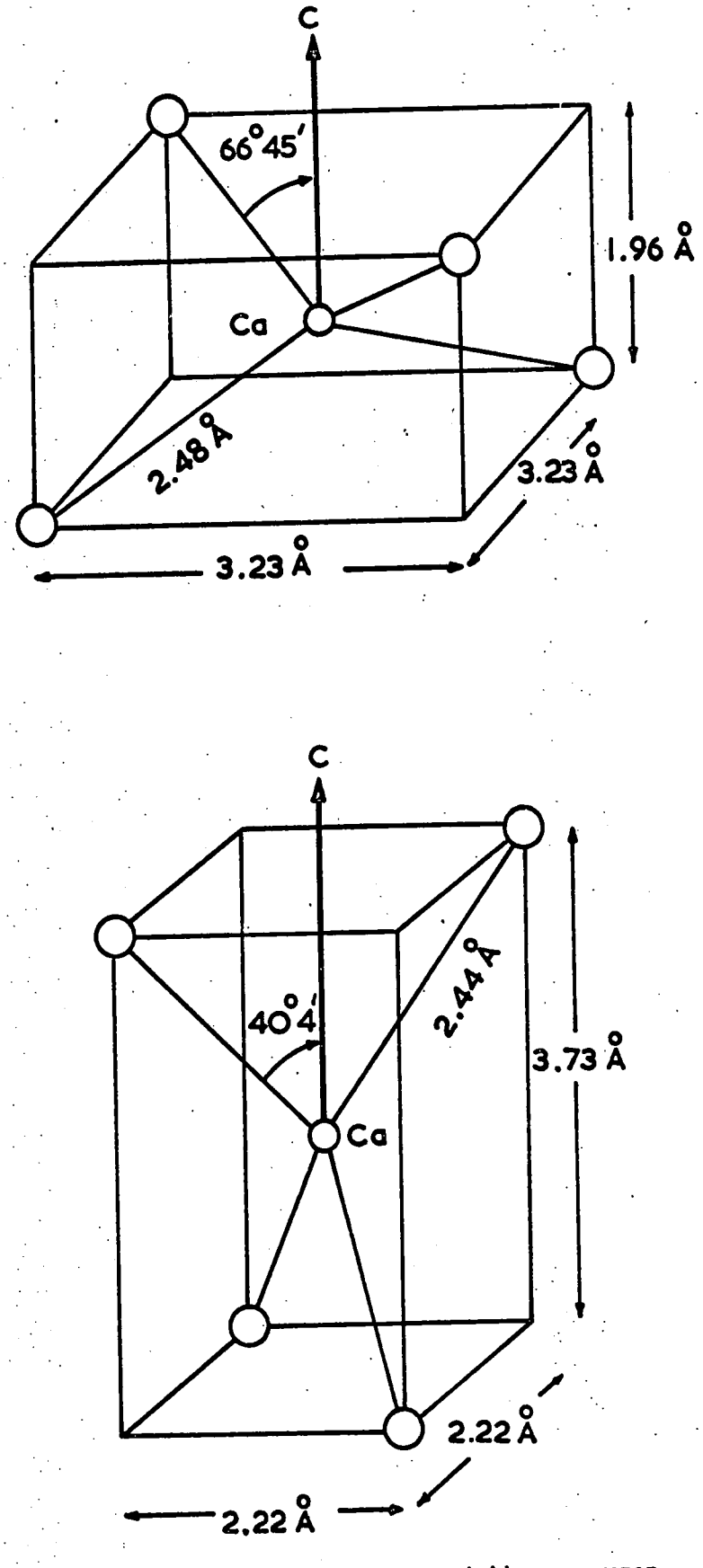

FIGURE 2.4: Positions of nearest neighbour oxygen atoms (O) with respect to a Ca site in $CaWO_4$

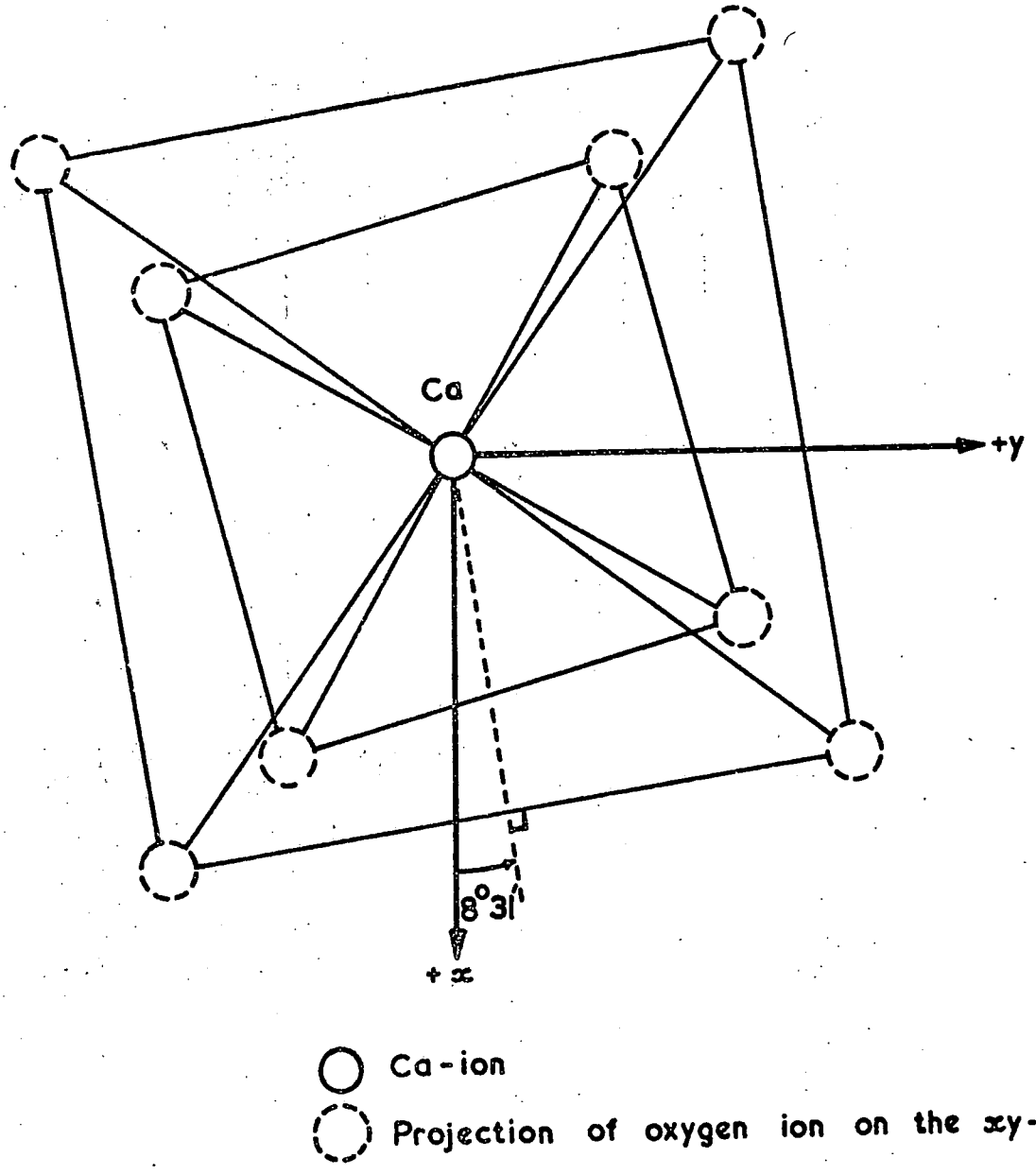

FIGURE 2.5: Projection on to the (001) through a Calcium atom of the eight nearest neighbour oxygen atom sites. The conventional +Z axis emerges from the plane of the paper.

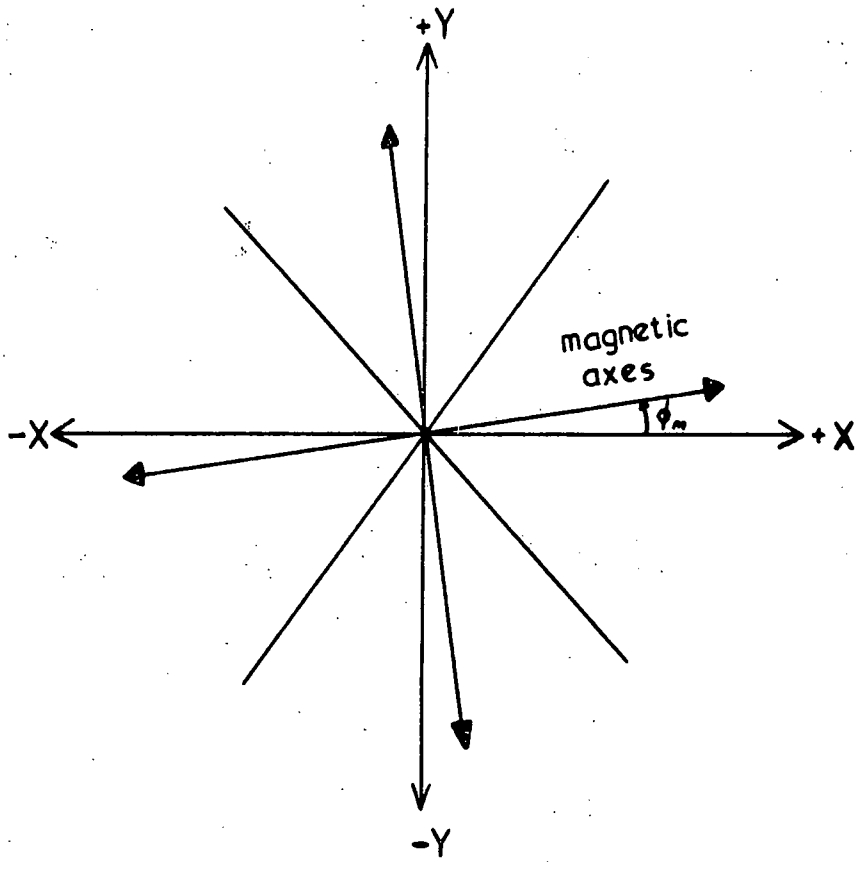

FIGURE 2.6: The positions of the magnetic axes relative to the crystallographic axes in scheelite structure tungstates and molybdates. The conventional +Z axis emerges from the plane of the paper.

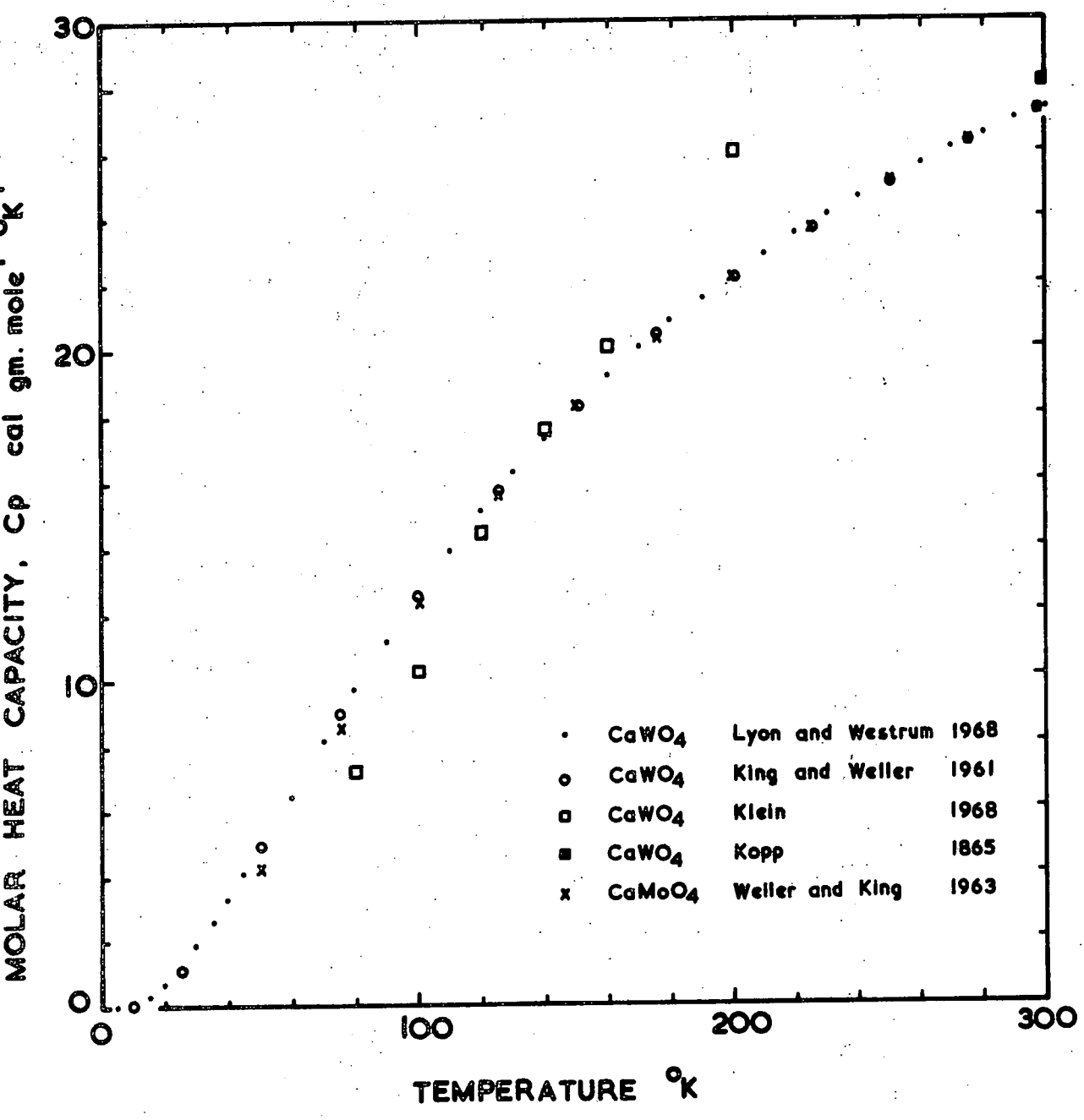

FIGURE 2.7: Specific heat capacity per gm.mole versus temperature for $CaWO_4$ and $CaMoO_4$

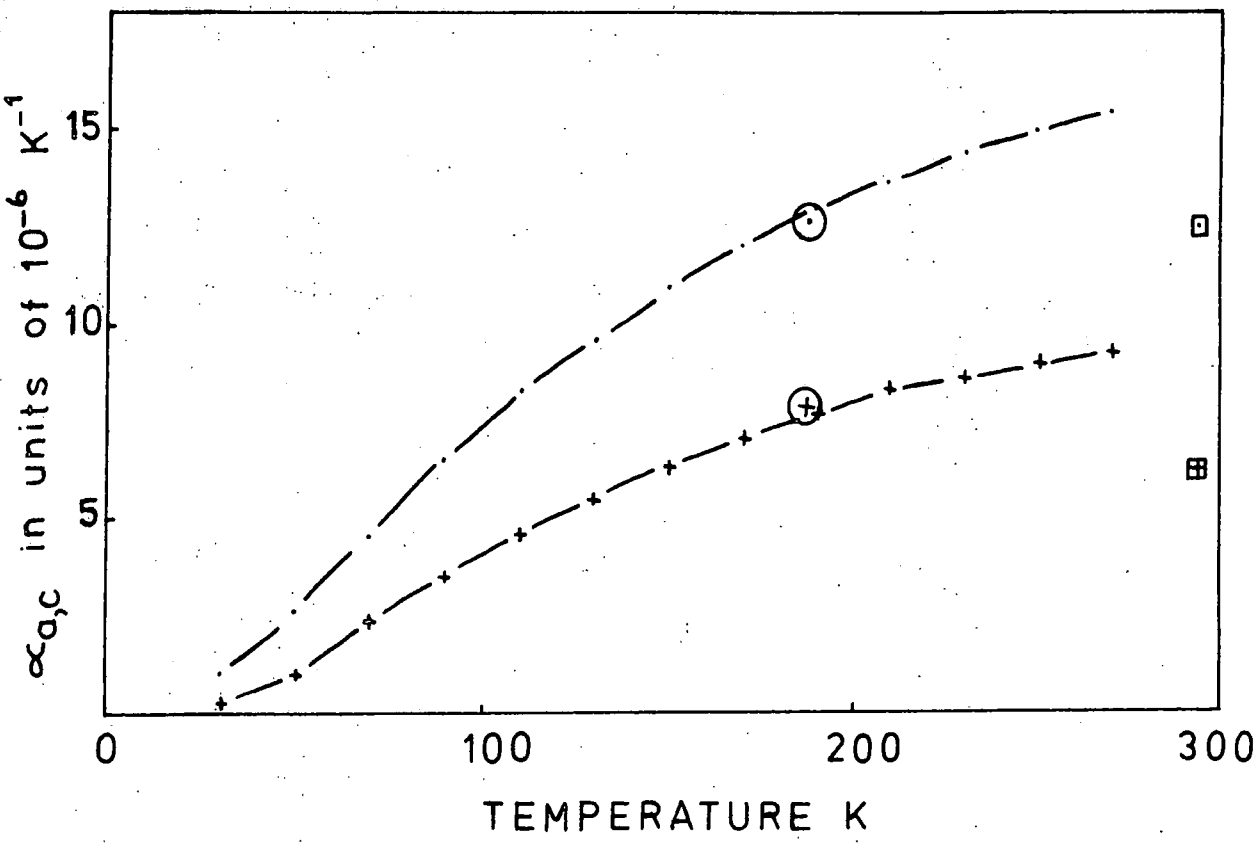

α_a, α_c — Nassau and Broyer (1962) mean value over the temperature range 77 K to 295 K

α_a, α_c — Deshpande and Suryanarayana (1972)

α_a, α_c — Yates and Bailey (1971)

FIGURE 2.8: Thermal expansion of $CaWO_4$

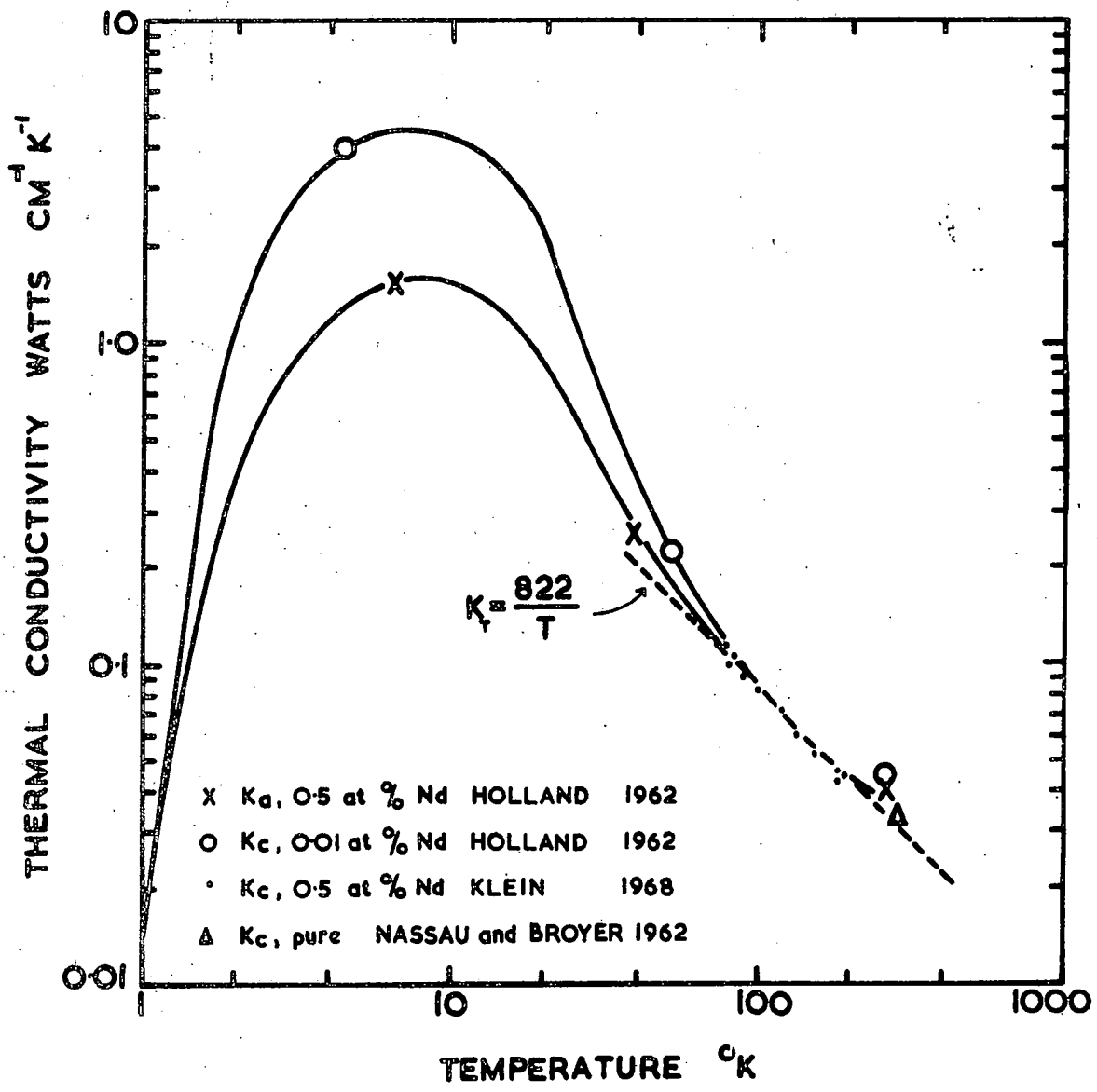

FIGURE 2.9: Thermal conductivity of $CaWO_4$

CHAPTER 3

ELASTIC PROPERTIES OF TETRAGONAL CRYSTALS

Robert Hooke's publication in 1676 of the law which now bears his name, marked the beginning of the classical theory of elasticity in solids that was later to be extended to anisotropic media by Christoffel (1877) and Lord Kelvin (1904). With the development of experimental techniques capable of generating clearly defined ultrasound beams — high frequency elastic waves — more extensive study of the characteristics of elastic wave propagation in solids became essential. Musgrave (1954), Borgnis (1955) and Waterman (1959) were among the first modern authors to extend the theory of elastic wave propagation in anisotropic crystals. Ultrasonics has now become an important tool for the investigation of physical properties of solids and for the non-destructive testing of materials. Ultrasonic wave propagation in solids is used in many applications including bulk and surface wave filters and delay lines, and acousto-optic devices. Continuing study of the propagation characteristics of elastic waves is of fundamental importance in ensuring the validity and accuracy of experimental investigations and in developing devices.

In this chapter the classical theory of elasticity is introduced and the propagation of elastic waves in anisotropic solids described. Particular reference is made to solids of tetragonal symmetry; the relationships and differences between the elastic properties of the two tetragonal Laue groups are emphasised. This chapter forms the basis for the

determination of the elastic constants of such crystals by ultrasound wave velocity measurements, and for the description of the details of the anisotropy of elastic wave propagation and elastic behaviour in $CaWO_4$ and other scheelite structure materials.

3.1 ELASTIC PROPERTIES OF ANISOTROPIC MEDIA

3.1.1 The Stress tensor

A body which is acted on by external forces, or more generally a body in which one part exerts a force on neighbouring parts is said to be in a state of stress. Two types of forces may act on an element of volume within a body. Firstly there may be forces such as gravity which act throughout the body on all its elements, and secondly forces which are exerted on the surface of the elementary volume by the material surrounding it. These latter forces are proportional to area and the force per unit area is called the stress. The six possible independent components of stress σ_{ij} form a symmetric second rank tensor. A component σ_{ij} represents the force in the i direction on unit area perpendicular to the j direction, so that the σ_{ij} (i=j) represent tensile stresses whilst the σ_{ij} ($i \neq j$) represent shear stresses. It is conventional to represent a normal component of stress acting outwards from the bounding surface by a positive sign. In the case of shear stresses the signs are determined with respect to the conventional axial set in the material as shown in Figure 3.1.

3.1.2 The Strain tensor

If a body located in a Cartesian reference frame of three dimensions undergoes a translation, change in orientation and deformation, a point with coordinates x_1, x_2, x_3 will be displaced according to the linear transformation

$$
\begin{aligned}
x_1' &= \chi_{10} + (1+\chi_{11})x_1 + \chi_{12}\,x_2 + \chi_{13}\,x_3 \\
x_2' &= \chi_{20} + \chi_{21}\,x_1 + (1+\chi_{22})x_2 + \chi_{23}\,x_3 \\
x_3' &= \chi_{30} + \chi_{31}\,x_1 + \chi_{32}\,x_2 + (1+\chi_{33})x_3
\end{aligned} \tag{3.1}
$$

to the new position x_i'. Here the χ_{io} represent the translational displacement of the body, and the χ_{ij} are elements defining a linear transformation. The change in length of each component of a line due to such a transformation (see Figure 3.2) is given by

$$\Delta x_i' - \Delta x_i = \chi_{ij}\,\Delta x_j \tag{3.2}$$

This expression may be written in terms of the symmetric and anti-symmetric parts of χ_{ij}

$$\Delta x_i' - \Delta x_i = \tfrac{1}{2}\,[(\chi_{ij} + \chi_{ji}) + (\chi_{ij} - \chi_{ji})]\,\Delta x_j \tag{3.3}$$

When χ_{ij} equals $-\chi_{ji}$, the linear transformation (3.1) would represent just a translation and rotation of the element. Therefore the rotation is identified with the anti-symmetric part of (3.3) and denoted by

$$\omega_{ij} = \tfrac{1}{2}\,(\chi_{ij} - \chi_{ji}) \tag{3.4}$$

while the symmetric quantity

$$\varepsilon_{ij} = \tfrac{1}{2}\,(\chi_{ij} + \chi_{ji}) \tag{3.5}$$

is directly related to the change in length of the element and its deformation.

Transformations involving zero dilation are often termed simple shears when accompanied by non-zero rotation (Figure 3.3a) and pure shears when the rotation is zero (Figure 3.3b).

The ε_{ij} form six independent components of the symmetric second rank strain tensor, the diagonal components representing tensile strains, and the off-diagonal components shear strains. Twice ε_{ji} $(j \neq i)$ equals the change in angle between two elements drawn parallel to the Ox_i and Ox_j axes before the deformation, and is positive if the angle decreases (Figure 3.3).

The components of strain may be related to small displacements, such as those induced by a small amplitude elastic wave, by consideration of infinitesimal forms of relations such as (3.3). A displacement $u_i(x_j)$ will change an element dx_i with length ds and

$$ds^2 = dx_i \, dx_i \tag{3.6}$$

to an element with a new length ds' and

$$(ds')^2 = (dx_i + u_{i,j} \, dx_j) \quad (dx_j + u_{i,k} \, dx_k) \tag{3.7}$$

Then

$$(ds')^2 - ds^2 = dx_i \, dx_j \, (u_{i,j} + u_{j,i} + u_{k,i} \, u_{k,j}) \tag{3.8}$$

In the limit of small displacements and small displacement derivatives, the product $u_{k,i} \, u_{k,j}$ in the above expression may be neglected and the Lagrangian components of strain specified by this relation may be identified with the linear strains defined above (3.5) so that

$$\varepsilon_{ij} = \frac{1}{2} (u_{i,j} + u_{j,i}) \tag{3.9}$$

By means of this expression the components of the strain tensor can readily be related to the derivatives of the small displacements which occur when an elastic wave is propagated through a medium.

3.1.3 Relationship between stress and strain in a linear elastic medium

The application of stress to a deformable body must result in the body passing into a state of strain. If, on removal of the external stress system, the body returns to its original shape, it is said to be elastic. For most solids it is observed that for sufficiently small stresses the amount of strain is linearly proportional to the applied stress. In an anisotropic medium a general linear constitutive relation between stress and strain is adopted, and usually written as

$$\varepsilon_{ij} = S_{ijkl}\,\sigma_{kl} \tag{3.10}$$

or in its reciprocal form

$$\sigma_{ij} = C_{ijkl}\,\varepsilon_{kl} \tag{3.11}$$

where the S_{ijkl} are the elastic compliance constants, and the C_{ijkl} are the elastic stiffness constants. These relations are generalised forms of Hooke's law and form the basis of the classical theory of the elasticity of solids. Generally in an anisotropic solid a single component of stress will give rise to six independent components of strain described by (3.10).

Since they relate second rank tensors, each with nine elements, the elastic constants S_{ijkl} and C_{ijkl} themselves form fourth-rank tensors with 81 elements each. The symmetry of both the stress and the strain tensors demands that the elastic constant tensors also must be symmetrical with respect to indices ij and kl so that

$$S_{ijkl} = S_{jikl} = S_{ijlk} = S_{jilk} \tag{3.12}$$

$$C_{ijkl} = C_{jikl} = C_{ijlk} = C_{jilk} \tag{3.13}$$

and only 36 of the 81 elements are independent.

3.1.4 Matrix Notation

The symmetry of the S_{ijkl} and C_{ijkl} in the first two and last two indices ((3.12) and (3.13)) allows the use of a matrix notation in which the pairs of suffices are abbreviated and each replaced by a single suffix according to the scheme:

tensor notation	11	22	33	23,32	31,13	12,21
matrix notation	1	2	3	4	5	6

It is then conventional (Nye 1957) to write the stress and strain tensor components as

$$\begin{pmatrix} \sigma_1 & \sigma_6 & \sigma_5 \\ \sigma_6 & \sigma_2 & \sigma_4 \\ \sigma_5 & \sigma_4 & \sigma_3 \end{pmatrix} \quad \text{and} \quad \begin{pmatrix} \varepsilon_1 & \tfrac{1}{2}\varepsilon_6 & \tfrac{1}{2}\varepsilon_5 \\ \tfrac{1}{2}\varepsilon_6 & \varepsilon_2 & \tfrac{1}{2}\varepsilon_4 \\ \tfrac{1}{2}\varepsilon_5 & \tfrac{1}{2}\varepsilon_4 & \varepsilon_3 \end{pmatrix} \tag{3.14}$$

and the stiffness constants

$$C_{ijkl} = C_{mn} \quad (i,j,k,l = 1,2,3; \quad m,n = 1,\ldots 6) \tag{3.15}$$

For the compliances, factors of two and four must be introduced as follows

$$\begin{aligned} S_{ijkl} &= S_{mn} && \text{when m and n are 1,2, or 3} \\ 2S_{ijkl} &= S_{mn} && \text{when either m or n are 4,5, or 6} \\ 4S_{ijkl} &= S_{mn} && \text{when both m and n are 4,5, or 6} \end{aligned} \tag{3.16}$$

These factors, and those in the strain components (3.14) are

included so that Hooke's law can also be written in the contracted notation as

$$\varepsilon_i = S_{ij}\,\sigma_j \tag{3.17}$$

or

$$\sigma_i = C_{ij}\,\varepsilon_j \tag{3.18}$$

The matrices of S_{ij} and C_{ij} are written in squares

$$\begin{bmatrix} S_{11} & S_{12} & S_{13} & S_{14} & S_{15} & S_{16} \\ S_{21} & S_{22} & S_{23} & S_{24} & S_{25} & S_{26} \\ S_{31} & S_{32} & S_{33} & S_{34} & S_{35} & S_{36} \\ S_{41} & S_{42} & S_{43} & S_{44} & S_{45} & S_{46} \\ S_{51} & S_{52} & S_{53} & S_{54} & S_{55} & S_{56} \\ S_{61} & S_{62} & S_{63} & S_{64} & S_{65} & S_{66} \end{bmatrix} \quad \text{and} \quad \begin{bmatrix} C_{11} & C_{12} & C_{13} & C_{14} & C_{15} & C_{16} \\ C_{21} & C_{22} & C_{23} & C_{24} & C_{25} & C_{26} \\ C_{31} & C_{32} & C_{33} & C_{34} & C_{35} & C_{36} \\ C_{41} & C_{42} & C_{43} & C_{44} & C_{45} & C_{46} \\ C_{51} & C_{52} & C_{53} & C_{54} & C_{55} & C_{56} \\ C_{61} & C_{62} & C_{63} & C_{64} & C_{65} & C_{66} \end{bmatrix} \tag{3.19}$$

Musgrave (1970) has pointed out that although the relations (3.14), (3.15) and (3.16) listed here are the conventional identifications of the matrix notation they do not give a symmetrical self-consistent scheme. Such a symmetrical scheme could be obtained using a definition of the σ_j which would include factors of a half in the identification of the off-diagonal components of the stress tensor, but would not conform to the established practice which will be followed here.

3.1.5 Elastic strain energy density

The internal energy per unit volume of a strained elastic body may generally be written in the form

$$\Phi = \Phi(0) + \frac{1}{2!}\,C_{ijkl}\,\varepsilon_{ij}\,\varepsilon_{kl} + \frac{1}{3!}\,C_{ijklmn}\,\varepsilon_{ij}\,\varepsilon_{kl}\,\varepsilon_{mn} + \ldots \tag{3.20}$$

with each primed term summed over its repeated indices and the C_{ijklmn} denoting the third order elastic constants. $\Phi(O)$ is the internal energy in the state from which the strain is measured. A requirement of the existence of an elastic potential is that the internal energy Φ must be independent of the path by which the state of strain is reached. This leads to the expression

$$C_{ijkl} = \left(\frac{\partial^2 \Phi}{\partial \varepsilon_{ij} \partial \varepsilon_{kl}} \right)_o = C_{klij} \tag{3.21}$$

and results in the further conditions

$$S_{ijkl} = S_{klij}$$

$$\text{and} \qquad C_{ijkl} = C_{klij} \tag{3.22}$$

being imposed on the second order elastic constant tensors—reducing the number of independent components of these from 36 to 21, a reduction which applies to all elastic media, linear or non-linear.

In a linear elastic medium the third and higher order constants are neglected, the generalised Hooke's law applies and the strain energy density is given by

$$\frac{1}{2} C_{ijkl} \varepsilon_{ij} \varepsilon_{kl} \tag{3.23}$$

An elastic body is only stable when work has to be done to create a state of strain from the equilibrium state; in the linear elasticity approximation the strain energy density (3.23) must be positive definite. This requirement is met if the principal minors of the elastic constant matrix (3.19) are all positive (Born and Huang 1954).

3.1.6 Elastic constants of a crystalline medium

Although their appearance in the matrix notation (3.19) can be misleading the S_{ij} and C_{ij} are not components of second rank tensors. They, in fact, are just matrices representing the S_{ijkl} and C_{ijkl} which are fourth rank tensors. As such their components transform on change of axes according to the law:

$$S'_{ijkl} = A_{im} A_{jn} A_{ko} A_{lp} S_{mnop} \qquad (3.24)$$

where A_{im} denotes the direction cosine of the new i axis with respect to the old m axis etc. It follows that each elastic constant has a definite meaning and numerical value only with respect to a particular reference frame within a medium. If in a crystalline medium, the reference frame is chosen to coincide with the three conventionally adopted orthogonal crystallographic axes as specified by the Standards on Piezoelectric crystals (1949) then the elastic constants are known as the "fundamental" elastic constants.

The elastic constant tensors are "matter" tensors; unlike the stress and strain tensors which just describe an applied stress system and the resulting strains, and are known as "field" tensors, the stiffness C_{ijkl} and compliance S_{ijkl} tensors are physical properties of the material. Accordingly they must obey Neumann's principle and have at least the symmetry of the crystal point group. In crystals of symmetry higher than triclinic this leads to relationships among the components of the elastic constant tensors, and a reduction in the number of independent components.

In fact the elastic properties of a crystal have a symmetry greater than that of the point group. Under a

transformation of the type

$$S'_{ijkl} = \delta_{im}\,\delta_{jn}\,\delta_{ko}\,\delta_{lp}\,S_{mnop} \qquad (3.25)$$

which corresponds to the operation of a centre of symmetry, the values of the elastic constants are unchanged, indicating that whatever the crystal symmetry the elastic properties will be centrosymmetrical. The elastic behaviour of a crystal is therefore classified according to its Laue group rather than its point group. The eleven possible Laue groups to which a crystal may belong and their constituitive point groups are listed in Table 3.1

The conditions imposed on the elastic constant tensor by the Laue symmetry of the material can be deduced by inspection. Tables are available (Nye 1957) which illustrate the elastic constant schemes for materials of the different symmetries. The numbers of independent components of the elastic constant tensor for the different Laue groups are given here in Table 3.1. This illustrates how the number of independent constants is drastically reduced from 21 in a medium of triclinic symmetry to three in a cubic, and only two in an isotropic material.

3.1.7 Elastic constants of solids with tetragonal symmetry

The scheelite structure materials have a point group $4/m$. Along with point groups 4 and $\bar{4}$ they belong to the TII Laue group. Solids (e.g. tin, indium, InBi) with a point group $4/mmm$, which includes planes of symmetry parallel to the fourfold axis and those with point groups 422, $4mm$ and $\bar{4}2m$, belong to the higher symmetry ditetragonals, and to the TI Laue group.

It is conventional (Standards on Piezoelectric Crystals 1949) for TII Laue symmetry to define the Z axis of the right handed axial set to which physical properties are to be referred as parallel to the fourfold symmetry axis. X and Y axes are then taken in the plane normal to Z parallel to the equal lattice translation vectors ($\underline{a}$ and $\underline{b}$) of the tetragonal unit cell. The sense of the Z axis must also be defined in these solids (see Section 3.1.11) but no convention was specified by the Standards on Piezoelectric crystals. The definition used in this work and described in Chapter 2 is consistent with that of Zalkin and Templeton (1964) and Farabaugh et al (1966).

The +X, +Y, +Z axial set so defined will be transformed in the manner

$$1 \longrightarrow 2 \qquad 2 \longrightarrow -1 \qquad 3 \longrightarrow -3$$

by the operations of the TII Laue group, which comprise a fourfold axis and a mirror plane perpendicular to it. In the four-suffix notation this will change the indices in the fashion $11 \longrightarrow 22$ $22 \longrightarrow 11$ $33 \longrightarrow 33$ $23 \longrightarrow 13$ $31 \longrightarrow -32$ $12 \longrightarrow -21$ and give a new array of suffices in the elastic constant matrix:

$$\begin{bmatrix} 22 & 21 & 23 & 25 & -24 & -26 \\ 21 & 11 & 13 & 15 & -14 & -16 \\ 23 & 13 & 33 & 35 & -35 & -36 \\ 25 & 15 & 35 & 55 & -54 & -56 \\ -24 & -14 & -35 & -54 & 44 & 46 \\ -26 & -16 & -36 & -56 & 46 & 66 \end{bmatrix} \tag{3.26}$$

Equating this array, component by component with the original one (3.19), inspection shows that the conditions imposed by the TII Laue symmetry are sufficient to reduce the number of independent components to seven and the array to

$$\begin{bmatrix} 11 & 12 & 13 & 0 & 0 & 16 \\ 12 & 11 & 13 & 0 & 0 & -16 \\ 13 & 13 & 33 & 0 & 0 & 0 \\ 0 & 0 & 0 & 44 & 0 & 0 \\ 0 & 0 & 0 & 0 & 44 & 0 \\ 16 & -16 & 0 & 0 & 0 & 66 \end{bmatrix} \tag{3.27}$$

For TI Laue symmetry crystals the same convention in defining the +X, +Y, +Z axial set is used, but +Z and -Z axes do not need to be distinguished. The presence of the vertical planes of symmetry in the Laue group imposes the further condition that C_{16} (and S_{16}) should be zero, so that in these materials the number of independent coefficients is six, and the form of the elastic constant array is:

$$\begin{bmatrix} 11 & 12 & 13 & 0 & 0 & 0 \\ 12 & 11 & 13 & 0 & 0 & 0 \\ 13 & 13 & 33 & 0 & 0 & 0 \\ 0 & 0 & 0 & 44 & 0 & 0 \\ 0 & 0 & 0 & 0 & 44 & 0 \\ 0 & 0 & 0 & 0 & 0 & 66 \end{bmatrix} \tag{3.28}$$

The non-zero value of C_{16} (and S_{16}) in the TII symmetry solids leads to elastic behaviour which may be significantly different from that in the corresponding crystallographic directions in a TI symmetry solid.

3.1.8 Relationship between the elastic constant tensors of TII and TI Laue symmetry solids

Despite the differences discussed above, the same symmetry properties are exhibited by the elastic behaviour of both groups of tetragonals. This interesting observation, first made by Khatkevich (1962) before any experimental investigations of TII symmetry materials had been carried out, has some important consequences for solids of this Laue group; it affects the response of such a solid to certain applied stresses and determines the mode of propagation of certain acoustic waves. In fact Khatkevich pointed out that the separation of tetragonal solids into two groups is not strictly necessary because the difference between the two groups amounts simply to a specific rotation of the topology of the elastic properties with respect to the crystallographic axes.

For a rotation about the fourfold axis through an angle ϕ the non-zero C'_{ij} are given by the transformation expressions:

$$
\begin{aligned}
C'_{11} &= C_{22} = \tilde{C}_{11} + C\cos 4\phi + C_{16}\sin 4\phi \\
C'_{66} &= \tilde{C}_{66} - C\cos 4\phi - C_{16}\sin 4\phi \\
C'_{12} &= \tilde{C}_{12} - C\cos 4\phi - C_{16}\sin 4\phi \\
C'_{16} &= -C'_{26} = -C\sin 4\phi + C_{16}\cos 4\phi \\
C'_{33} &= C_{33} \qquad C'_{44} = C_{55} = C_{44} \qquad C'_{13} = C'_{23} = C_{13}
\end{aligned}
\tag{3.29}
$$

where

$$
C = \tfrac{1}{4}(C_{11} - C_{12} - 2C_{66})
$$

$$
\tilde{C}_{11} = C_{11} - C \qquad \tilde{C}_{66} = C_{66} + C \qquad \tilde{C}_{12} = C_{12} + C
$$

In the particular case of a rotation by an angle

$$\phi = \left[\tfrac{1}{4} \tan^{-1} (C_{16}/C)\right] \tag{3.30}$$

the transformed constant C'_{16} will become equal to zero. The number of independent elastic constants of the TII symmetry solid with respect to the new axial set will be reduced to six, and the matrix (3.27) will be reduced to the form of (3.28):

$$\begin{bmatrix} 11' & 12' & 13' & 0 & 0 & 0 \\ 12' & 11' & 13' & 0 & 0 & 0 \\ 13' & 13' & 33' & 0 & 0 & 0 \\ 0 & 0 & 0 & 44' & 0 & 0 \\ 0 & 0 & 0 & 0 & 44' & 0 \\ 0 & 0 & 0 & 0 & 0 & 66' \end{bmatrix} \tag{3.31}$$

Equation (3.30) has two roots, separated by $\pi/4$, in each quadrant. In a TI Laue material C'_{16} is zero only when ϕ equals zero or $\pi/4$ (and for the other directions related by the fourfold symmetry); the reference axes then coincide with either the <100> or the <110> directions of the conventional axial set. Therefore, with respect to a set of axes rotated by a particular angle ϕ — given by (3.30) — about the fourfold axis, the elastic stiffness constant tensor of a TII symmetry tetragonal has the same number of independent components and the same structure as that which a ditetragonal TI solid has with respect to its conventional crystal axes.

Thus with regard to the elastic properties, separation of tetragonal solids into the two Laue groups is not strictly required; in each case the elastic modulus tensor

may be described in terms of six parameters which are invariant on rotation about the fourfold axis. If however the elastic properties are to be related to the conventional orientation of the crystal — and this of course is usually desired — then separation into the TI and TII groups is necessary. The close relationship of the two Laue groups has some interesting repercussions for scheelite structure solids; these will be discussed in the light of the experimental results given in later chapters of this thesis.

3.1.9 Interconversion between elastic stiffnesses and compliances

The general relationship between the components of the elastic stiffness and the elastic compliance tensors is the usual one for the inversion of a symmetric matrix:

$$S_{ij} = (-1)^{i+j} \Delta^C_{ij} / \Delta^C \qquad (3.32)$$

where Δ^C is the determinant of the C_{ij} terms and Δ^C_{ij} is the minor of the element C_{ij}. Explicit expressions for materials of the TII tetragonal system have not previously been given, and are presented below:

$$\begin{aligned}
S_{11} &= \left[C_{11}C_{33}C_{66} - C_{13}^2C_{66} - C_{16}^2C_{33}\right] C_{44}^2/\Delta^C \\
S_{12} &= -\left[C_{12}C_{33}C_{66} - C_{13}^2C_{66} + C_{16}^2C_{33}\right] C_{44}^2/\Delta^C \\
S_{13} &= \left[C_{13}(C_{12}C_{66} - C_{11}C_{66} + 2C_{16}^2)\right] C_{44}^2/\Delta^C \\
S_{16} &= -\left[C_{16}(C_{12}C_{33} + C_{11}C_{33} - 2C_{13}^2)\right] C_{44}^2/\Delta^C \\
S_{33} &= \left[C_{66}(C_{11}^2 - C_{12}^2) - 2(C_{11}+C_{12})C_{16}^2\right] C_{44}^2/\Delta^C \\
S_{44} &= 1/C_{44} \\
S_{66} &= \left[(C_{33}(C_{11} + C_{12}) - 2C_{13}^2)(C_{11} - C_{12})\right] C_{44}^2/\Delta^C
\end{aligned} \qquad (3.33)$$

where

$$\Delta^C = [((C_{11} - C_{12})C_{66} - 2C_{16}^2)(C_{11}C_{33} + C_{12}C_{33} - 2C_{13}^2)]C_{44}^2$$

These expressions are symmetrical in S_{ij} and C_{ij} and can be used to convert compliances to stiffnesses just by writing S for C and C for S. It is significant that the only fundamental compliance to depend on the sign of C_{16} is S_{16}. C_{16} and S_{16} always have opposite signs. By making $C_{16} = 0$ the expressions for TI symmetry solids can be obtained.

3.1.10 Physical meaning of the elastic constants

The elastic constants of a material describe its resistance to deformation, large values of the stiffness constants indicating that a material is not readily deformable. It is thus the stiffness of a medium which is described by the elastic constants, and not the hardness or the strength of the material.

In an anisotropic medium a single stress gives rise to many different strains which have magnitudes dependent on the relative values of the different elastic constants. If a general stress system, arbitrarily oriented with respect to the symmetry axes, is applied to a crystalline body, then all the possible strains allowed by the generalised Hooke's law (3.10) will arise. The relative values of the strains will depend on the elastic constants S'_{ijkl} defined with respect to the arbitrary stress axes (and obtained from the fundamental elastic constant set by the tensor transformation rule (3.24)). The resultant strains and their relation to the applied stress system will be somewhat complex, but knowledge of the complete set of elastic moduli

C_{ijkl} or S_{ijkl} allows the material's response to be calculated.

To understand the meaning of individual elastic constants, it is useful to consider the effect of simple stresses applied along or perpendicular to the symmetry axes. For example, if a longitudinal stress is applied parallel to the X direction of a crystal with TII Laue symmetry, and all other stresses are zero then the generalised Hooke's law (3.17) reduces to

$$\begin{aligned} \varepsilon_1 &= S_{11}\ \sigma_1 \\ \varepsilon_2 &= S_{12}\ \sigma_1 \\ \varepsilon_3 &= S_{13}\ \sigma_1 \\ \varepsilon_4 &= 0 \\ \varepsilon_5 &= 0 \\ \varepsilon_6 &= S_{16}\ \sigma_1 \end{aligned} \qquad (3.34)$$

A single stress σ_1 thus gives rise to four different non-zero strains. The ratio of the longitudinal strain parallel to the applied longitudinal stress to that stress is given by S_{11}, while the tensile strains perpendicular to the X direction and parallel to the Y and Z directions respectively are given by S_{12} and S_{13}. In a cubic material the Y and Z directions are equivalent, S_{12} is equal to S_{13} and the strains (ε_2 and ε_3) would be equal. The value of S_{16} is a measure of the shear strain ε_6 ($2\varepsilon_{12}$ in tensor notation) and describes how the angle between the X and Y axes is changed from $\pi/2$ (See Fig. 3.3).

The constant S_{33} is a measure of the longitudinal strain (ε_3) in the Z direction resulting from the application of a single tensile stress (σ_3) in that direction.

The meaning of the shear constants S_{44} and S_{66} is seen by considering the application of particular shear stresses. When the shear stress σ_4 is applied to the faces of a cube normal to the Z axis only one strain results, a shear strain ε_4 which is a measure of the change of the angle between the Y and Z axes. The ratio ε_4/σ_4 equals S_{44}. The constant S_{66} is given by the ratio ε_6/σ_6 when σ_6, a shear stress in the X direction on a plane perpendicular to the Y direction, is the only applied stress. Through the constant S_{16} this particular shear also gives rise to tensile strains in the X and Y directions — strains which would not occur in a ditetragonal solid.

3.1.11 The signs of S_{16} and C_{16}

The physical meaning of the elastic constant S_{16} (= S_{61}) was explained in Section 3.1.10; S_{61} (equal to $4S_{1211}$ in tensor notation) gives the shear strain ε_{12} which results from an applied stress σ_{11} and so describes the change in angle between the X and Y axes due to such a stress. The sign of S_{16}, and thus of S_{61}, determines whether this angle is increased (as in Fig. 3.4b) or decreased (Fig. 3.4c) on application of a compressional stress.

For a right handed axial set defined with respect to the body as shown in Figure 3.4b, the sign of S_{16} (=S_{61}) would be positive (because a compressional stress is conventionally given a negative sign, and a strain ε_{ij} is taken as positive if the angle between the Ox_i and Ox_j axes is decreased).

For an alternative definition of axial set with the sense of the +Z axis reversed, the X axis parallel to the

applied stress and the +Y axis chosen to complete a right-handed set, then the result of the same applied stress $-\sigma_{11}$ now gives a decrease in the angle between these +X and +Y axes, so that for this definition of axial set S_{16} must have a negative sign. Consequently, the signs of S_{16} and C_{16} depend on the sense chosen for the +Z axis with respect to the internal crystal structure. This was overlooked in the Standards on Piezoelectric Crystals (1949). The definition of the sense of +Z axis with respect to the crystal structure, used in this work, was described in Chapter 2 of this thesis; it is the definition of Zalkin and Templeton (1964), and the one used by Farabaush et al (1966), the only previous workers to have emphasised the distinction between +Z and -Z axial directions in TII symmetry materials.

3.1.12 The response of an elastic body to hydrostatic pressure

The elastic moduli particularly useful in the study and assessment of interatomic binding in solids are the compressibilities, volume and linear. These moduli describe the response of a material to uniform hydrostatic pressure. Such an external pressure P leads to tensile stresses

$$\sigma_{kl} = - P\delta_{kl} \tag{3.35}$$

and a volume dilation

$$\Delta = \varepsilon_{ii} = - P\, S_{iikk} \tag{3.36}$$

so that the volume compressibility β_v is S_{iikk} and thus is the sum of the nine components in the upper left-hand corner of the compliance matrix:

$$\beta_v = S_{11} + S_{12} + S_{33} + 2(S_{12} + S_{23} + S_{31}) \tag{3.37}$$

The linear compressibility (β_ℓ) of a solid is the relative decrease in length of a line when the solid is subjected to unit hydrostatic pressure. In all solids of symmetry lower than cubic β_ℓ varies with direction and in general is given by

$$\beta_\ell = S_{ijkk}\, m_i\, m_j \tag{3.38}$$

in the direction of a unit vector $\underline{m}$. In uniaxial crystals which include all the tetragonal, trigonal and hexagonal point groups, the linear compressibility depends only on the angle between the Z axis and the unit vector, and can be represented by just two principal linear compressibilities

$$\beta_Z = S_{33} + 2S_{13} \tag{3.39}$$

$$\beta_{XY} = S_{11} + S_{13} + S_{12} \tag{3.40}$$

which represent the relative length changes in the Z direction and in directions in the XY plane respectively. In terms of the stiffness constants (C_{ij}) the volume and linear compressibilities in media of TII symmetry are given by

$$\beta_V = \frac{C_{11} + C_{12} + 2C_{33} - 4C_{13}}{C_{11}C_{33} + C_{12}C_{33} - 2C_{13}^2} \tag{3.41}$$

$$\beta_Z = \left[C_{66}(C_{11}^2 - C_{12}^2) - 2(C_{11} + C_{12})C_{16}^2 + 2(C_{13}(C_{12}C_{66} - C_{11}C_{66}) + 2C_{16}^2)\right] \frac{C_{44}^2}{\Delta^c} \tag{3.42}$$

$$\beta_{XY} = \left[C_{66}(C_{11}C_{33} - C_{13}^2) - C_{16}^2 C_{33} - C_{66}(C_{12}C_{33} - C_{13}^2) - C_{16}^2 C_{33} + C_{13}(C_{66}(C_{12} - C_{11}) + 2C_{16}^2)\right] \frac{C_{44}^2}{\Delta^c} \tag{3.43}$$

where Δ^C has the value given in 3.33 . The bulk modulus (K) is defined as the reciprocal of the volume compressibility.

In a uniaxial solid, although a net volume contraction must occur, the application of a uniform hydrostatic pressure can lead to contraction in some directions but expansion in others. This has been observed in arsenic (Pace et al 1970) and tellurium (Malgrange et al 1964) whilst in some crystals very large anisotropies of linear compressibility have been found (Akgöz, Farley and Saunders 1973).

3.1.13 Anisotropy of the technical elastic moduli

Generally in the technical literature elastic behaviour is not discussed in terms of C_{ij} or S_{ij}, but the familiar technical moduli — Young's modulus, rigidity modulus bulk modulus, torsional modulus, and also Poisson's ratio — are used. In isotropic materials these parameters have single values but in anisotropic solids they (with the exception of the bulk modulus) vary with orientation and show at least the Laue symmetry of the material. As described in Section (3.1.10), in an anisotropic medium a single applied stress will give rise to many resulting strains. Therefore definitions of the technical moduli for anisotropic media must specify the directions of the stresses and strains uniquely.

Young's modulus describes the ratio of the resulting longitudinal strain parallel to the direction of a single applied longitudinal stress. In the X direction this modulus will be equal to $(S_{11})^{-1}$ and in any other direction will be $(S'_{11})^{-1}$. By the tensor transformation law it can be shown that in TII tetragonal crystals the

anisotropy of the Young's modulus is described by

$$YM = (S'_{11})^{-1} = (m_1^4 + m_2^4)S_{11} + m_3^4 S_{33} + m_1^2 m_2^2 (2S_{12} + S_{66}) + m_3^2(1 - m_3^2)\ (2S_{13} + S_{44}) + 2m_1 m_2 (m_1^2 - m_2^2) S_{16} \quad (3.44)$$

where m_1, m_2, m_3 are the direction cosines of the applied stress. Young's modulus is a single valued function of the direction cosines and elastic moduli, and can be represented by a surface which provides a useful visual illustration of the anisotropy of elastic behaviour of the material, although it does not describe the whole of the elastic behaviour. Models of the Young's modulus surface of crystalline mercury (Crocker and Singleton 1971) and cross-sections of the Young's modulus surfaces of the semimetals arsenic, antimony and bismuth (Gunton and Saunders 1972) have provided vivid illustrations of the extreme elastic anisotropy in some of these solids.

Cady (1964) following Voigt, defines the torsional compliance as

$$T_h = \frac{1}{2}(S'_{44} + S'_{55}) \quad (3.45)$$

for a torsion about an arbitrary Z' axis. This formula is used in the determination of elastic constants by a static method in which torsion about the axis of a cylindrical specimen is measured. Elastic constants may also be determined from the fundamental frequencies of torsional and longitudinal vibrations in thin cylindrical specimens. Such a method was used by Wachtmann et al (1968) to find the elastic tensor set of single crystal $CaMoO_4$.

The torsional compliance must be distinguished from the modulus of rigidity which is defined as the reciprocal of S'_{44} with respect to axes Y' and Z' (Cady 1962), and has an orientation dependence given by the tensor transformation law (3.24). The rigidity modulus, and also Poisson's ratio in an anisotropic solid, are functions of more than one direction and cannot be represented by surfaces.

3.1.14 Thermodynamic basis of elastic moduli

The elastic constants were introduced, and their physical meaning has been described, through the empirical formulation of Hooke's law (3.10). A more fundamental significance to the elastic constants arises through their thermodynamic basis.

It follows from the first law of thermodynamics that the total energy of a solid is the sum of different types of energy and may include among others magnetic, electrical, mechanical and thermal terms. In a situation where other contributions may be considered to be independent of strain, the increase in internal energy ($d\Phi$) with strain will arise due to the strain energy contribution alone. Then by (3.21) the second order elastic constants can be seen to be related to the second differential of the internal energy with respect to strain:

$$C_{ijkl} = \left(\frac{\partial^2 \Phi}{\partial \varepsilon_{ij} \partial \varepsilon_{kl}} \right)_o \qquad (3.46)$$

From equation (3.20) it can be seen that, in general, constants of the n^{th} order may be defined by

$$C_{ijkl\cdots} = \left(\frac{\partial^n \Phi}{\partial \varepsilon_{ij} \partial \varepsilon_{kl} \cdots} \right)_o \qquad (3.47)$$

The elastic constants thus have basic thermodynamic as well as mechanical significance. In particular the volume compressibility (3.37), given by

$$\frac{1}{\beta_V} = \left(\frac{\partial^2 \phi}{\partial V^2} \right)_{V=V_o} V \tag{3.48}$$

is of great importance in assessing the interatomic binding in crystals.

3.1.15 Relation between adiabatic and isothermal elastic moduli

In the usual experimental range of frequency and temperature the propagation of small amplitude ultrasonic waves in solids can be assumed to be isentropic; the elastic constants so determined are the adiabatic moduli. These are related to the isothermal elastic moduli by the expression

$$(S_{ij})_{\text{adiabatic}} - (S_{ij})_{\text{isothermal}} = - \frac{\alpha_i \alpha_j T}{\rho C_P}$$

where α_i and α_j are thermal expansion coefficients, T is the temperature, ρ the density and C_P the specific heat capacity per unit mass at constant pressure.

3.2 ELASTIC WAVES IN ANISOTROPIC MEDIA

3.2.1 Elastic waves in tetragonal solids

If the stresses in a body are inhomogeneous then each element of volume of the body will be subject to forces equal to the stress gradients in different directions. These components of force will be related to the appropriate

accelerations by Newton's second law:

$$\sigma_{ij,j} = \rho\ddot{u}_i \qquad (i = 1,2,3) \tag{3.49}$$

for a medium of density ρ. Here the indices after the comma denote differentiation with respect to position (x) and the dots denote differentiation with respect to time. Using Hooke's law (3.10) gives

$$C_{ijkl}\ \varepsilon_{kl,j} = \rho\ddot{u}_i \qquad (i = 1,2,3)$$

and from the definition of strain this becomes

$$C_{ijkl}\ (u_{k,jl} + u_{l,kj})/2 = \rho\ddot{u}_i \qquad (i = 1,2,3)$$

Since the stiffness tensor (C_{ijkl}) is symmetrical with respect to ij and kl this reduces to

$$C_{ijkl}\ u_{k,jl} = \rho\ddot{u}_i \qquad (i = 1,2,3) \tag{3.50}$$

Plane bulk wave solutions to this equation of motion are of interest here. For a plane harmonic wave of angular frequency ω the components of the particle displacement ($\underline{u}$) of the wave can be written as

$$\begin{aligned} u_i &= u_{o_i} \exp\left[i(\omega t - \underline{k}.\underline{r})\right] \\ &= u_{o_i} \exp\left[i(\omega t - k_m x_m)\right] \end{aligned} \tag{3.51}$$

where u_{o_i} represents the maximum amplitude of the displacement in the direction i; $\underline{k}$ (k_1, k_2, k_3) is the wave vector, equal to $(\omega/v)\underline{n}$ where v is the phase velocity and $\underline{n}$ (n_1, n_2, n_3) is a unit vector — known as the wave normal or propagation vector — normal to the planes of constant phase. The components n_1, n_2 and n_3 of the propagation vector are the direction cosines of the direction of propagation. Differentiating (3.51) and

substituting in the equation of motion gives

$$\rho v^2 u_{o_i} = C_{ijkl} n_j n_l u_{o_k} \qquad (i = 1,2,3) \qquad (3.52)$$

This may be written in the form due to Christoffel (1877) as

$$(C_{ijkl} n_j n_l - \rho v^2 \delta_{ik}) u_{o_k} = 0$$

or

$$(L_{ik} - \rho v^2 \delta_{ik}) u_{o_k} = 0 \qquad (i = 1,2,3) \qquad (3.53)$$

where L_{ik} are the Christoffel coefficients.

The Christoffel equations (3.53) are three linear homogeneous simultaneous equations in u_{o_1}, u_{o_2}, u_{o_3} which have solutions only when the determinant of the coefficients is zero; the solutions correspond to the plane waves which can be propagated in a particular direction defined by the wave normal ($\underline{n}$). The method of solution is given here for solids of tetragonal symmetry.

In a medium of TII Laue symmetry the Christoffel coefficients are given by the expressions:

$$\begin{aligned}
L_{11} &= n_1^2 C_{11} + n_2^2 C_{66} + n_3^2 C_{44} + 2n_1n_2 C_{16} \\
L_{22} &= n_1^2 C_{66} + n_2^2 C_{11} + n_3^2 C_{44} - 2n_1n_2 C_{16} \\
L_{33} &= n_1^2 C_{44} + n_2^2 C_{44} + n_3^2 C_{33} \\
L_{12} &= n_1^2 C_{16} - n_2^2 C_{16} + n_1n_2 (C_{12} + C_{66}) \\
L_{13} &= n_1n_3 (C_{13} + C_{44}) \\
L_{23} &= n_2n_3 (C_{13} + C_{44})
\end{aligned} \qquad (3.54)$$

For the higher symmetry TI Laue group these coefficients are simplified since C_{16} is zero.

Equation (3.53) written out in full gives three linear homogeneous equations in the three unknowns, u_{o_1}, u_{o_2} and u_{o_3}, the components of the particle displacement. These secular equations

$$\begin{aligned}
(L_{11}-\rho v^2)\, u_{o_1} + L_{12}\, u_{o_2} + L_{13}\, u_{o_3} &= 0 \\
L_{12}\, u_{o_1} + (L_{22}-\rho v^2)\, u_{o_2} + L_{23}\, u_{o_3} &= 0 \\
L_{13}\, u_{o_1} + L_{23}\, u_{o_2} + (L_{33}-\rho v^2)\, u_{o_3} &= 0
\end{aligned} \tag{3.55}$$

must be obeyed for a bulk wave solution to exist. They can have a non-trivial solution only when the determinant of their coefficients is zero, that is when

$$\begin{vmatrix}
L_{11} - \rho v^2 & L_{12} & L_{13} \\
L_{12} & L_{22} - \rho v^2 & L_{23} \\
L_{13} & L_{23} & L_{33} - \rho v^2
\end{vmatrix} = 0 \tag{3.56}$$

The determinantal equation is cubic in ρv^2; for each direction of propagation there are three possible modes with velocities given by the roots of this equation. The roots represent the eigenvalues of the Christoffel equations, and the corresponding eigenvectors, $\underline{u}_o$, specify the particle displacements or polarisations of the modes which can be propagated. As a result of the symmetry of the coefficients in (3.55) the polarisations of these modes are mutually orthogonal.

Thus in any particular specified direction in a crystal, three distinct mutually orthogonal modes can be propagated, each with its own velocity. These modes are generally neither pure longitudinal (for which $\underline{u}_o \times \underline{n} = 0$) nor pure transverse (for which $\underline{u}_o \cdot \underline{n} = 0$) as in the general case the particle displacement direction need not be either

parallel or perpendicular to the propagation vector. The mode for which the polarisation is closest to the propagation direction (and which will often have the greatest velocity) is known as quasi-longitudinal, and the other two modes as quasi-shear (or quasi-transverse). Directions in which the shear waves (pure or quasi) propagate with equal velocities are known as acoustic axes.

3.2.2 Pure modes in anisotropic media

The special directions in which pure modes can propagate may be divided into two types. "Pure mode directions of the first kind" are those directions in which a pure longitudinal and hence also two pure shear modes can be propagated. Brugger (1965), using the method of Borgnis (1955), has given expressions by which these directions, more often known just as "pure mode axes" can be located in crystals of the orthorhombic, tetragonal, cubic, rhombohedral and hexagonal systems. "Pure mode directions of the second kind" or "semi-pure mode directions" are those directions in which a single pure shear mode can be propagated, along with two other impure modes. The existence of these directions in crystals of various symmetries has been studied by Chang (1968).

Pure mode directions of both the first and second kinds occur for certain specific symmetry directions in crystals. Both kinds of pure mode direction can also occur for propagation axes in which the accidental combination of direction cosines n_1, n_2, n_3 and numerical values of the elastic constants renders either a longitudinal or transverse mode pure. Those directions, determined by the values of the elastic constants and not the symmetry alone, in which pure

longitudinal waves can be propagated are known as "accidental pure mode axes ".

3.2.3 Pure modes in solids of tetragonal symmetry

In a TII tetragonal material the only pure mode direction whose position does not depend on the values of the elastic moduli is that along the fourfold symmetry axis. For propagation in this direction the Christoffel equations (3.55) reduce to

$$\begin{aligned} (C_{44} - \rho v^2)\, u_{o_1} &= 0 \\ (C_{44} - \rho v^2)\, u_{o_2} &= 0 \\ (C_{33} - \rho v^2)\, u_{o_3} &= 0 \end{aligned} \qquad (3.57)$$

and the determinantal equation has roots C_{44}, C_{44} and C_{33}. For ρv^2 equal to C_{33}, then as in general $C_{33} \neq C_{44}$, u_{o_1} and u_{o_2} must be zero and u_{o_3} equal to one; the mode has particle displacement in the [001] direction and is pure longitudinal, and the [001] direction is a pure mode axis of the first kind. The corresponding pure shear modes are degenerate, each with velocities equal to $(C_{44}/\rho)^{\frac{1}{2}}$

Directions of propagation in the (001) plane, the Laue symmetry mirror plane of a TII tetragonal material, are in general semi-pure mode directions. With the direction cosine n_3 equal to 0 for these propagation directions, the determinant of the Christoffel coefficients reduces to

$$\begin{vmatrix} L_{11} - \rho v^2 & L_{12} & 0 \\ L_{12} & L_{22} - \rho v^2 & 0 \\ 0 & 0 & L_{33} - \rho v^2 \end{vmatrix} = 0 \qquad (3.58)$$

where for propagation at an angle ϕ measured from [100] towards [010]

$$\begin{aligned} L_{11} &= C_{11}\cos^2\phi + C_{66}\sin^2\phi + 2C_{16}\sin\phi\cos\phi \\ L_{22} &= C_{66}\cos^2\phi + C_{11}\sin^2\phi - 2C_{16}\sin\phi\cos\phi \\ L_{33} &= C_{44} \\ L_{13} &= L_{23} = 0 \\ L_{12} &= C_{16}(\cos^2\phi - \sin^2\phi) + (C_{12} + C_{66})\sin\phi\cos\phi \end{aligned} \tag{3.59}$$

For all directions in this plane the root $\rho v^2 = C_{44}$ corresponds to a pure shear mode with particle motion in the [001] direction. The other two modes with velocities given by

$$\rho v^2 = (L_{11} + L_{22}) \pm \left[(L_{11} - L_{22}) + 4\,L_{12}^2\right]^{\frac{1}{2}} \tag{3.60}$$

are quasi-longitudinal and quasi-shear respectively. It follows that the sum of the squares of the velocities of these modes is constant for all directions in the (001) plane and equal to

$$(C_{11} + C_{66})/\rho \tag{3.61}$$

This rule forms a useful cross-check on practical velocity measurements.

The directions [100] and [110] are not axes of symmetry in the TII solids, and the longitudinal modes propagated in these directions are not pure. The only pure modes of the first kind which occur in the (001) plane are accidental pure modes whose positions depend on the numerical values of the elastic constants and therefore may be different

for different scheelite structure materials. Brugger (1965) has designated these accidental pure mode directions at angles ϕ_κ and ϕ_γ measured from [100] towards [010], κ and γ respectively and given expressions by which their positions can be calculated when the values of the elastic moduli are known. The two directions are $\pi/4$ apart, and a similar pair of directions occur in each quadrant. Accidental pure modes, designated π and β by Brugger (1965) also occur outside the (001) plane — in planes which contain the fourfold and the κ or γ axes respectively — as shown in Figure (3.5). All propagation directions in these planes are semi-pure mode axes (Chang 1968).

In the higher symmetry TI Laue group of tetragonal solids which have mirror planes perpendicular to the <100> and <110> directions the Christoffel coefficients are simplified because C_{16} is zero and modes propagated in the <100> and <110> directions are pure. There are no accidental pure modes in the (001) plane so effectively by virtue of the TI symmetry the angles ϕ_κ and ϕ_γ are equal to 0^o and 45^o respectively (see Figure 3.5b). The π and β accidental pure mode axes then lie in the {100} and {110} planes, but are not symmetry axes themselves. The existence of the π accidental pure mode axis has been demonstrated for the TI symmetry material InBi. It was shown (Akgöz, Farley and Saunders 1973) that for propagation in the semi-pure mode directions in the (100) plane, the deviation of the particle displacement vector of the quasi-longitudinal wave from the propagation vector becomes zero for $\phi = 53.5^o$ (measured from [001] towards [100]) in InBi.

3.2.4 Direction of energy flux associated with elastic waves

In an anisotropic medium the direction in which energy is propagated by a plane wave is not necessarily parallel to the propagation vector. This deviation of the energy flux vector — the acoustic Poynting vector — from the normal to the plane wavefronts is both interesting theoretically and of importance in experimental work and in practical devices.

According to Huygen's principle a plane wave can be considered to be formed as the envelope of secondary fronts emanating from a planar array of point sources. In an isotropic medium the secondary fronts are spherical but in an elastically anisotropic medium the orientation dependence of the phase velocities leads to non-spherical secondary wavefronts, whose shape is determined by the shape of the wave surface. This is one of the three characteristic surfaces — the others being the velocity and the slowness (index) surfaces — used to represent elastic wave propagation in three dimensions. The inter-relationships between the three surfaces are discussed by Musgrave (1970). Each surface has three sheets which correspond to the quasi-longitudinal and the two quasi-transverse modes for all possible directions of propagation vector.

The phase velocity surface is obtained as the locus of three vectors drawn parallel to the propagation vector and proportional in length to the phase velocities of the three modes. Cross-sections of the phase velocity surface of $CaWO_4$ and other scheelites are given in later chapters. The

relationship between the velocity surface and the slowness surface is a simple one; the three vectors are drawn with lengths inversely proportional to the velocity to obtain the slowness surface. Geometrically the wave surface is the 'envelope' of the velocity surface, the 'polar reciprocal' of the slowness surface. Its shape may be constructed from the slowness surface by the following procedure:

(i) for a point on the slowness surface find the corresponding pedal point — the point on the tangential plane where the normal passes through the origin.

(ii) the reciprocal of the slowness at the pedal point gives the point on the wave surface corresponding to the original chosen point.

(iii) the procedure is repeated for all other points on the slowness surface. The method is illustrated in Figure 3.6.

This construction gives only the shape of the wave surface for an arbitrary radial scale; the radial scale for the true wave surface (defined as the locus of points of equal phase after unit time following a disturbance which emanates from a point source at t=0) is found by use of the appropriate multiplier (Musgrave 1970).

The direction of energy flux of a plane wave can be obtained either by construction from the slowness or the wave surfaces, or by calculation. The normal to the slowness surface for a propagation vector ($\underline{n}$) coincides with the energy flux direction for a mode with this propagation vector (see Fig. 3.7a). From the wave surface the energy flux direction is readily obtained; the particular element of a wave surface which is normal to the propagation vector

of a plane wave forms the advancing front of that wave after unit time (see Fig. 3.7b). The constructions show that the energy flux must always deviate from the propagation vector of a mode except when the propagation vector is a radius vector of the three characteristic surfaces.

The direction of the energy flux may be calculated using the expression given by Love (1944); the i^{th} component (P_i^g) of the energy flux of a mode (g) is given by the negative scalar product of the components of the stress tensor (σ_{ij}) with the particle displacement velocity of the mode ($\dot{u}^g_{o_j}$):

$$P_i^g = -\sigma_{ij} \cdot \dot{u}^g_{o_j} \tag{3.62}$$

For a plane wave, with propagation vector $\underline{n}$, using relations (3.9), (3.10) and (3.51) and taking the time average gives components

$$P_i^g = \left[\frac{(p^g\omega)^2}{2v^g}\right] C_{ijkl}\, d_j^g\, d_k^g\, n_\ell^g \qquad (i=1,2,3) \tag{3.63}$$

where p^g is the scalar amplitude of the mode, ω is the angular frequency, d_j^g, d_k^g are the direction cosines of the particle displacement, and u^g is the phase velocity. The direction of the energy flux is thus independent of the wave frequency and amplitude.

By means of this equation (3.63) the direction of energy flow can be found for any mode in any propagation direction. Only for cases when the propagation vector coincides with the radius vector of the wave surface is the deviation of the energy flux zero. Waterman (1959) has

shown that this must always be true for a pure longitudinal mode. For a pure transverse wave he showed that the energy flux must be parallel to the propagation direction if this direction is a twofold, fourfold or sixfold axis of rotational symmetry or is normal to a plane of reflection symmetry. Other conditions sufficient for the deviation of the energy flux to be zero ("normal propagation") have been found by Levelut (1969).

3.2.5 Energy flux direction in tetragonal solids

In a medium of TII tetragonal symmetry the expressions for the components of the energy flux may be written out in full as

$$\begin{aligned} P_1 = A \{ & (C_{11}d_1^2 + 2C_{16}d_1d_2 + C_{66}d_2^2 + C_{44}d_3^2)\, n_1 \\ & + (C_{16}d_1^2 + C_{66}d_1d_2 + C_{12}d_1d_2 - C_{16}d_2^2)\, n_2 \\ & + (C_{44}d_1d_3 + C_{13}d_1d_3)\, n_3 \} \end{aligned} \qquad (3.64$$

$$\begin{aligned} P_2 = A \{ & (C_{16}d_1 + C_{12}d_1d_2 + C_{66}d_1d_2 - C_{16}d_2^2)\, n_1 \\ & + (C_{66}d_1^2 - 2C_{16}d_1d_2 + C_{11}d_2^2 - C_{44}d_3^2)\, n_2 \\ & + (C_{44}d_2d_3 + C_{13}d_2d_3)\, n_3 \} \end{aligned} \qquad (3.65$$

$$\begin{aligned} P_3 = A \{ & (C_{13}d_1d_3 + C_{44}d_1d_3)\, n_1 \\ & + (C_{13}d_2d_3 + C_{44}d_2d_3)\, n_2 \\ & + (C_{44}d_1^2 + C_{44}d_2^2 + C_{33}d_3^2)\, n_3 \} \end{aligned} \qquad (3.66$$

where $A = (p^g\omega)^2/2v^g$.

From these expressions it can be seen that there is no deviation of energy flux for propagation in the [001] pure mode direction. For directions in the (001) plane, the component P_3 is always zero and the energy flux is confined to the mirror plane, though for the quasi-longitudinal and quasi-shear modes — including those in the <100> and <110> directions — it deviates from the propagation vector. For the pure shear mode which can be excited for all propagation directions in the mirror plane (as described in Section 3.2.3) the energy flux path is parallel to the propagation direction.

3.2.6 Internal conical refraction

One of the most interesting and theoretically important consequences of the deviation of energy flux from a wave normal is the phenomenon of internal conical refraction. This arises for propagation along an acoustic axis, if the energy flux of one or both of the transverse waves deviates from the axis. For such a propagation direction (which has equal transverse wave velocities) there is an infinite set of transverse polarisation directions for the single wave normal, and each has a corresponding energy flux direction. When the transverse wave polarisation is rotated about that of the longitudinal wave through an angle of 180° the direction of maximum energy flux sweeps around 360° to form a cone of internal refraction, whose section denotes all the points at which the wave surface is tangential to the front of the wave. A circular cone of internal refraction has been predicted and demonstrated

for pure transverse waves with wave vectors along the [111] directions in cubic crystals (de Klerk and Musgrave 1955) and along the [001] direction in trigonal crystals (Waterman 1959).

In tetragonal crystals the phenomenon arises in those directions for which the velocities of the two quasi-transverse modes are equal, and in general the resulting cone of internal refraction will be elliptical in section (Khatkevich 1963). This was first predicted by Musgrave (1957) for the acoustic axis in the (110) plane of a TI symmetry tetragonal crystal. For such an acoustic axis in a plane of symmetry, or for one perpendicular to an axis of twofold symmetry Khatkevich (1963) showed that one of the axes of the ellipse must also lie in the symmetry plane, or in the plane formed by the acoustic and the twofold axes. In the case of an acoustic axis perpendicular to the fourfold axis of a tetragonal, one of the transverse modes is pure and has zero deviation of energy flux (see Section 3.2.5). As a result the cone of refraction must include the acoustic axis; it has an elliptical section with principal axes parallel to the [001] direction, and in the (001) plane respectively. For this particular acoustic axis the senses of rotation of quasi-transverse wave polarisation and the corresponding energy flux vector are the same (Khatkevich 1963); for the acoustic axes previously discussed the rotations have opposite senses.

3.2.7 Reflection of elastic waves from a solid-vacuum boundary

Pulsed ultrasound experiments involve the reflection

of a plane elastic wave normally incident on a stress-free, solid-vacuum boundary. For polished specimens, the specimen surface features will be of much smaller dimensions than the elastic wavelength and the surface may be regarded as a plane boundary.

In the case of an isotropic medium it has been shown that longitudinal and shear waves normally incident on such a boundary are wholly reflected with no loss or mode conversion (Arenberg 1948). This is also true for any arbitrary infinite plane wave normally incident on the plane boundary of an anisotropic solid (Waterman 1959). In such a solid the reflection law for the energy flux is important: the energy flux is reflected back on itself from a boundary which is normal to the propagation vector of the wave. This law of reflection means that in a pulsed ultrasound experiment the signal is reflected back to the source without loss, and single-ended pulse echo operation is possible.

3.3 DETERMINATION OF ELASTIC CONSTANTS OF CRYSTALLINE SOLIDS BY WAVE VELOCITY MEASUREMENTS

3.3.1 Introduction

The elastic constants of a crystalline solid can be determined by measuring the wave velocities of a number of different modes. Equations relating the wave velocities to the elastic constants are obtained by finding the eigenvalues of the Christoffel equations (3.53) for the appropriate propagation directions. The determinantal

equation (3.56) is cubic in ρv^2. For certain specific directions (parallel or normal to axes of symmetry, parallel or normal to planes of mirror symmetry) the cubic equation decomposes to give simple analytical expressions for the velocities of the three modes that can propagate. In other, arbitrary directions expressions for the sum of roots and the sum of the squares of the roots can be obtained by the theory of equations, or if the elastic constants are known (or guessed) the cubic equation can be solved numerically.

To determine the elastic constants, the number of velocities to be measured and the choice of directions depends upon the symmetry of the material. For a cubic crystal the three elastic constants can be found directly from the velocities of the three pure modes which can be propagated in the [110] direction. These velocities are related to the elastic constants by the expressions

$$\begin{aligned} v_{\ell_{[110]}} &= ((C_{11} + C_{12} + 2C_{44})/\rho)^{\frac{1}{2}} \\ v_{s_{[001]}} &= (C_{44}/\rho)^{\frac{1}{2}} \\ v_{s_{[\bar{1}10]}} &= ((C_{11} - C_{12})/2\rho)^{\frac{1}{2}} \end{aligned} \tag{3.67}$$

For lower symmetry solids the elastic constants cannot wholly be determined by measuring in pure mode directions alone. Hexagonal, rhombohedral and tetragonal (TI) solids each have one elastic constant which can only be found by measuring the velocity of at least one impure mode. In TII tetragonals only two of the seven elastic constants can be found by measuring pure mode velocities.

Usually the propagation directions for which measurements are made are chosen because they have simple direction cosines (e.g. 1, 0, 0; $2^{-\frac{1}{2}}$, $2^{-\frac{1}{2}}$, 0; $3^{\frac{1}{2}}/2$, 1/2, 0 and are directions for which the Christoffel determinant decomposes. Comparatively simple relationships between the elastic constants and velocities then hold. Such a choice is necessary if an analytical solution for the elastic constants is required. From a practical point of view however, the directions preferred are those which make economical use of small single crystals or for which modes are nearly pure and the energy flux deviation a minimum.

In the next two sections the different choices of measurement directions and methods of solution which have been applied to TII tetragonal crystals are described. A novel method by which the elastic constants of a material of any symmetry can be found from velocity measurements in a number of known, but completely arbitrary directions is discussed.

3.3.2 Elastic constants of tetragonal (TII) crystals

The expressions relating the velocities of several different modes to the elastic constants for a TII crystal are given in Table 3.2. Only the elastic constants C_{33} and C_{44} can be obtained from single velocity measurements in pure mode directions. For directions parallel and normal to the fourfold axis there are analytical expressions for each velocity (see Table 3.2) but for the propagation direction with cosines 0, $2^{-\frac{1}{2}}$, $2^{-\frac{1}{2}}$ only expressions for the

sums of the roots and squares of the roots can be written down. Alton and Barlow (1967) used such expressions for six different propagation directions to obtain by cross-substitution a quartic equation in the elastic constant C_{11}. Numerical solution yielded four possible values for this constant and substitution then gave the corresponding values of the other elastic constants. The choice of the correct set from the four is discussed in Section 7.1. Chung and Li (1971b) have given details of an analytical solution method for the seven elastic constants. They have found expressions for each constant in terms of seventeen elastic wave velocities — those of modes propagated in the directions (cosines) 0,0,1; 1,0,0; $2^{-\frac{1}{2}}$,$2^{-\frac{1}{2}}$,0; 0,$2^{-\frac{1}{2}}$,$2^{-\frac{1}{2}}$; 1/2,$3^{\frac{1}{2}}$/2,0 (as listed in Table 3.2) plus the direction $3^{\frac{1}{2}}$/2, 1/2,0. Both these methods require the measurement of a particular set of velocities.

An alternative method employing computing techniques has been used in the present work. The method depends upon choosing a set of values for the elastic constants and adjusting these values until the magnitudes of the parameters Z_i calculated from them (by the equations of Table 3.2) most nearly agree with the values obtained from the measurements. This is accomplished by computer minimisation of a parameter SUMSQ which is defined by the expression

$$\text{SUMSQ} = \sum_{i=1}^{N} \left[\frac{\text{calculated } Z_i}{\text{measured } Z_i} - 1.0 \right]^2 \qquad (3.68)$$

The basis of this minimisation procedure was discussed by Jeavons and Saunders (1969). The computer programme used here is listed in Appendix 1, and its mode of operation

is outlined below.

An arbitrary set of elastic constants (INITIAL SOLN) is guessed (the use of realistic values increases the speed of operation) and read into the computer. Each constant in turn is adjusted by increments, referred to in the programme as STEP, until SUMSQ is a minimum. The size of STEP is then reduced and the procedure repeated. This is continued either for a predetermined number of cycles (usually 501 here), or until SUMSQ becomes equal to a prefixed value (SMALL). The procedure is completed by printing out the final values of the elastic constants (FINAL SOLN), the corresponding values of Z_i for comparison with the measured values and the final value of SUMSQ. In the absence of experimental error the final value of SUMSQ would be zero, each calculated Z_i would then equal each measured Z_i and a perfect solution for the C_{ij} would be obtained. In the presence of experimental error SUMSQ/N is a measure of the quality of the overall fit. Local minima are avoided by starting with a large value of STEP ($\simeq 0.1\ C_{ij}$), and repeating the search using different starting values of the elastic constants.

3.3.3 Novel method for determination of elastic constants from measurements in arbitrary directions

In many cases, usually because of the limitations of single crystal size it may not be possible to measure the velocities of some of the modes required for solutions of the types employed by Alton and Barlow (1967) or Chung and Li (1971b). Indeed in the case of $CaWO_4$ the least

squares fitting procedure described above was developed because the velocities of certain modes could not at first be measured. By an extension of the least squares procedure, a powerful method is available for calculation of elastic constants from wave velocity data obtained from a set of known propagation directions which are chosen for their experimental convenience.

The method uses an IBM Scientific Subroutine EIGEN which calculates the eigenvalues and eigenvectors of a matrix. The subroutine can be used to calculate, from the Christoffel coefficients, the velocities of the three elastic waves which can be propagated in a particular direction. In the first place the Christoffel coefficients would be obtained from a guessed set of elastic constants by the equations

$$L_{ik} = C_{ijk\ell}\, n_j\, n_\ell \quad (i,k = 1,2,3) \qquad (3.69)$$

for the directions ($\underline{n}$) in which velocities had been measured. The guesses would then be adjusted to give agreement between the velocities calculated by EIGEN and those measured. Either the SUMSQ fitting procedure or a more powerful minimisation technique could be used.

This method should be applicable to solids of any symmetry. Always the number of velocities measured in arbitrary directions would have at least to equal, but preferably exceed, the number of independent elastic constants of the material. The method may prove invaluable when the size of single crystal specimens governs the choice of propagation directions. When ample material is available, it provides a means of reducing the errors which arise owing

to misorientation of specimens. In cases where the computer search procedure reveals more than one solution set which predicts the measured velocities correctly, then the choice between the sets may be made by reference to the Born stability criteria or by comparison of the calculated eigenvectors with the transducer polarisations required to excite particular modes (see for example Section 6.1.2).

TABLE 3.1

Laue groups and constituitive point groups			
	Laue Groups	Point Groups	No.of elastic constants
Triclinic	N	1, $\bar{1}$	21
Monoclinic	M	2, m, 2/m	13
Orthorhombic	O	mm, 222, mmm	9
Tetragonal	TII	4, $\bar{4}$, 4/m	7
	TI	4mm, $\bar{4}$2m, 42, 4/mmm	6
Trigonal	RII	3, $\bar{3}$	7
	RI	3m, $\bar{3}$m, 32	6
Hexagonal	HII	6, $\bar{6}$, 6/m	5
	HI	622, 6mm, $\bar{6}$m2, 6/m 2/m 2/m	5
Cubic	CII	23, 2/m$\bar{3}$	3
	CI	432, $\bar{4}$3m, 4/m $\bar{3}$ 2/m	3
Isotropic	I		2

TABLE 3.2: Relationships between ultrasound velocity and elastic constants for several different propagation directions in TII symmetry crystals

Direction cosines of propagation vector	Mode	Polarisation	Velocity	Relationships between velocity and elastic constants
0, 0, 1	pure long	[001] direction	v_1	$z_1 = \rho v_1^2 = C_{33}$
0, 0, 1	pure shear	[100] direction	v_2	$z_2 = \rho v_2^2 = C_{44}$
1, 0, 0	pure shear	[001] direction	v_3	$z_3 = \rho v_3^2 = C_{44}$
1, 0, 0	quasi-long	in (001) plane	v_4	$z_4 = \rho v_4^2 = 1/2\ \{(C_{11}+C_{66})+[(C_{11}-C_{66})^2+4C_{16}^2]^{\frac{1}{2}}\}$
1, 0, 0	quasi-shear	in (001) plane	v_5	$z_5 = \rho v_5^2 = 1/2\ \{(C_{11}+C_{66})-[(C_{11}-C_{66})^2+4C_{16}^2]^{\frac{1}{2}}\}$
$2^{-\frac{1}{2}}$, $2^{-\frac{1}{2}}$, 0	pure shear	[001] direction	v_6	$z_6 = \rho v_6^2 = C_{44}$
$2^{-\frac{1}{2}}$, $2^{-\frac{1}{2}}$, 0	quasi-long	in (001) plane	v_7	$z_7 = \rho v_7^2 = 1/2\ \{(C_{11}+C_{66})+[(C_{12}+C_{66})^2+4C_{16}^2]^{\frac{1}{2}}\}$
$2^{-\frac{1}{2}}$, $2^{-\frac{1}{2}}$, 0	quasi-shear	in (001) plane	v_8	$z_8 = \rho v_8^2 = 1/2\ \{(C_{11}+C_{66})-[(C_{12}+C_{66})^2+4C_{16}^2]^{\frac{1}{2}}\}$
0, $2^{-\frac{1}{2}}$, $2^{-\frac{1}{2}}$	quasi-long		v_9	$z_9 = \rho(v_9^2+v_{10}^2+v_{11}^2) = 1/2\{C_{11}+C_{66}+C_{33}+3C_{44}\}$
0, $2^{-\frac{1}{2}}$, $2^{-\frac{1}{2}}$	quasi-shear		v_{10}	$z_{10} = \rho^2(v_9^4+v_{10}^4+v_{11}^4) = \{5C_{44}^2/4+C_{33}^2/4+C_{13}^2/2+C_{44}(C_{11}+C_{33}+C_{66}+2C_{13})/2+C_{11}^2+C_{66}^2+2C_{16}^2)/4\}$
0, $2^{-\frac{1}{2}}$, $2^{-\frac{1}{2}}$	quasi-shear		v_{11}	
1/2, $3^{\frac{1}{2}}/2$, 0	pure shear	[001] direction	v_{12}	$z_{11} = \rho v_{12}^2 = C_{44}$
1/2, $3^{\frac{1}{2}}/2$, 0	quasi-long	in (001) plane	v_{13}	$z_{12} = \rho v_{13}^2 = 1/2\{(C_{11}+C_{66})+[((C_{11}-C_{66})/2+3^{\frac{1}{2}}C_{16})^2+4(3^{\frac{1}{2}}(C_{12}+C_{66})/4-C_{16}/2)^2]^{\frac{1}{2}}\}$
1/2, $3^{\frac{1}{2}}/2$, 0	quasi-shear	in (001) plane	v_{14}	$z_{13} = \rho v_{14}^2 = 1/2\{(C_{11}+C_{66})-[((C_{11}-C_{66})/2+3^{\frac{1}{2}}C_{16})^2+4(3^{\frac{1}{2}}(C_{12}+C_{66})/4-C_{16}/2)^2]^{\frac{1}{2}}\}$
cos21.5°, sin21.5°, 0	pure shear	[001] direction	v_{15}	$z_{14} = \rho v_{15}^2 = C_{44}$
cos21.5°, sin21.5°, 0	quasi-long	in (001) plane	v_{16}	$z_{15} = \rho v_{16}^2 = 1/2\{(C_{11}+C_{66})+[(C_{11}+C_{66})^2-4(L_{11}L_{22}-L_{12}^2)]^{\frac{1}{2}}\}$
cos21.5°, sin21.5°, 0	quasi-shear	in (001) plane	v_{17}	$z_{16} = \rho v_{17}^2 = 1/2\{(C_{11}+C_{66})-[(C_{11}+C_{66})^2-4(L_{11}L_{22}-L_{12}^2)]^{\frac{1}{2}}\}$
				where $L_{11} = C_{11}\cos^2(21.5°) + C_{66}\sin^2(21.5°) + 2C_{16}\sin(21.5°)\cos(21.5°)$
				$L_{22} = C_{66}\cos^2(21.5°) + C_{11}\sin^2(21.5°) - 2C_{16}\sin(21.5°)\cos(21.5°)$
				$L_{12} = C_{16}\cos^2(21.5°) - C_{16}\sin^2(21.5°) + \sin(21.5°)\cos(21.5°)(C_{12}+C_{66})$

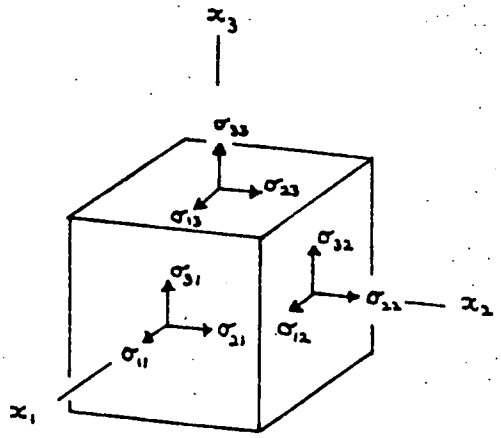

FIGURE 3.1: The forces on the faces of a unit cube in an homogenously strained body

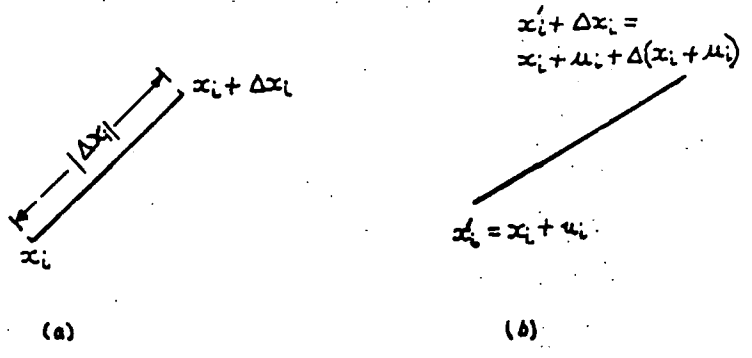

FIGURE 3.2: (a) Initial position of a line element Δx_i

(b) Line element after translation rotation and deformation

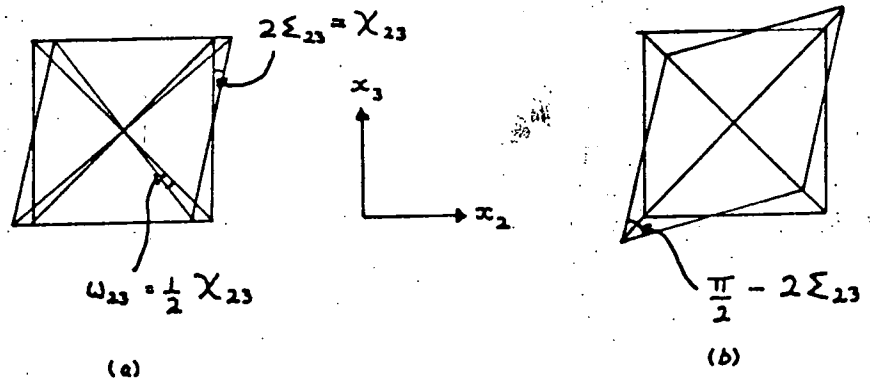

FIGURE 3.3: (a) Simple shear deformation of cube face to rhombus by χ_{23} involving strain e_{23} and rotation ω_{23}

(b) Pure shear deformation of cube face to rhombus by e_{23}

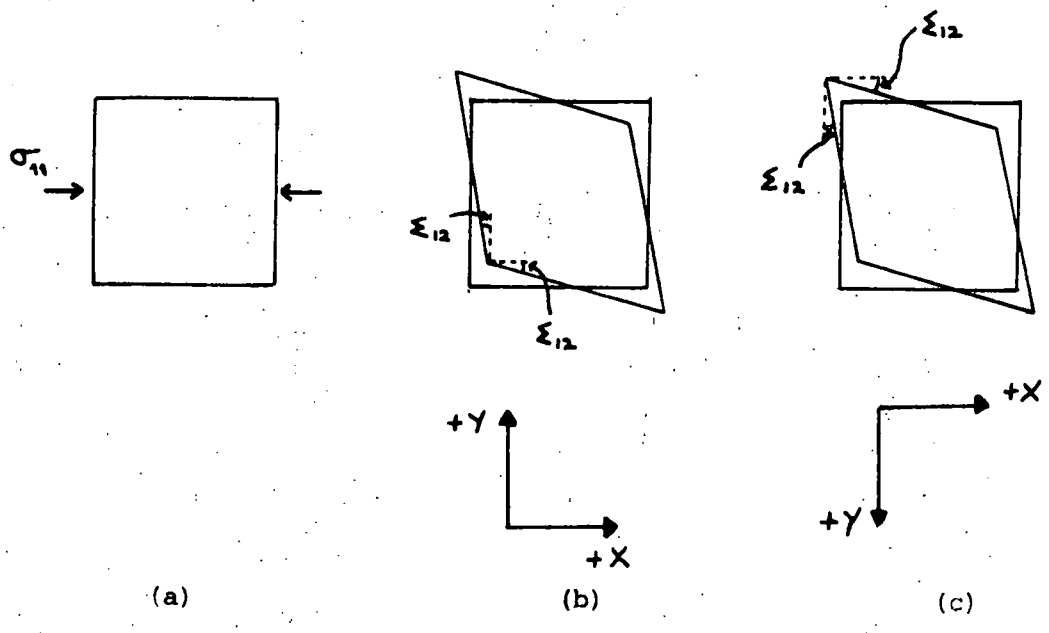

FIGURE 3.4: Shear strain resulting from a compressive stress σ_{11} if s_{16} is positive (b) or negative (c)

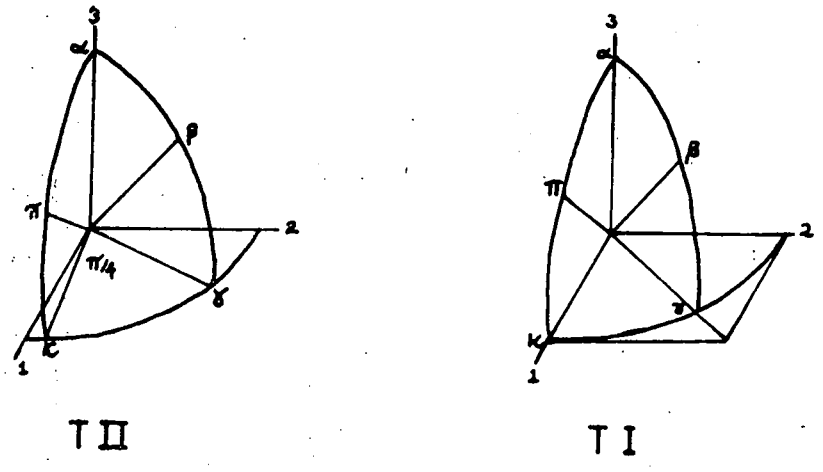

FIGURE 3.5: Positions of pure mode axes in tetragonal crystals of Laue groups TII and TI (after Brugger 1965)

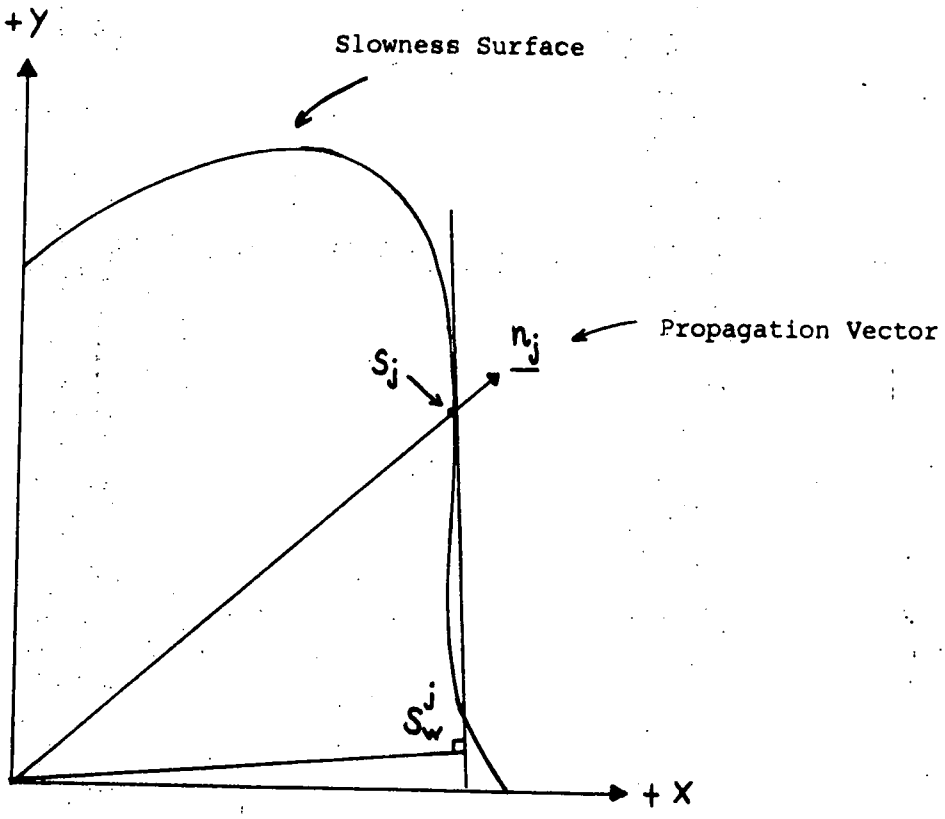

S_w^j is the pedal point corresponding to the point S_j on the slowness surface. W_j is then the point on the wave surface corresponding to the propagation vector $\underline{n}_j$.

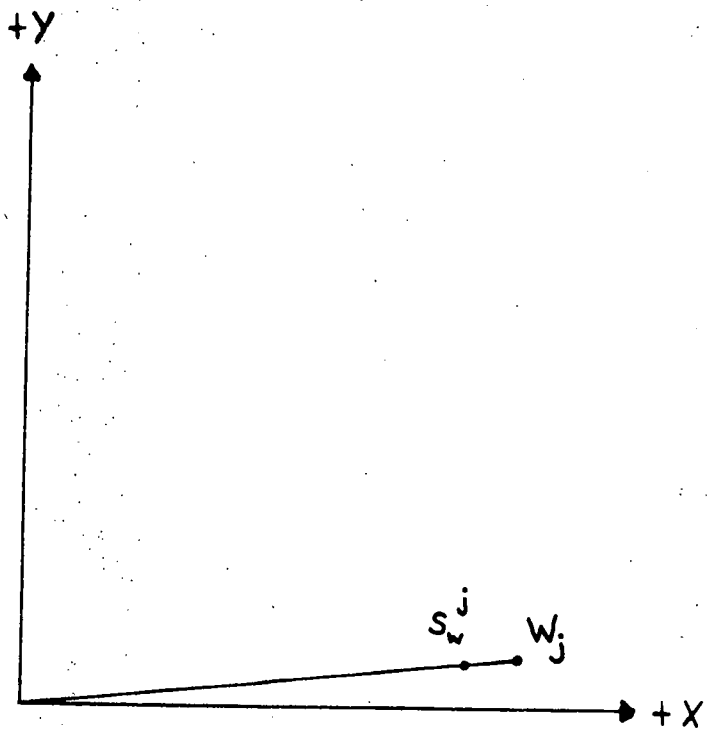

FIGURE 3.6: Construction of the wave surface from the slowness surface.

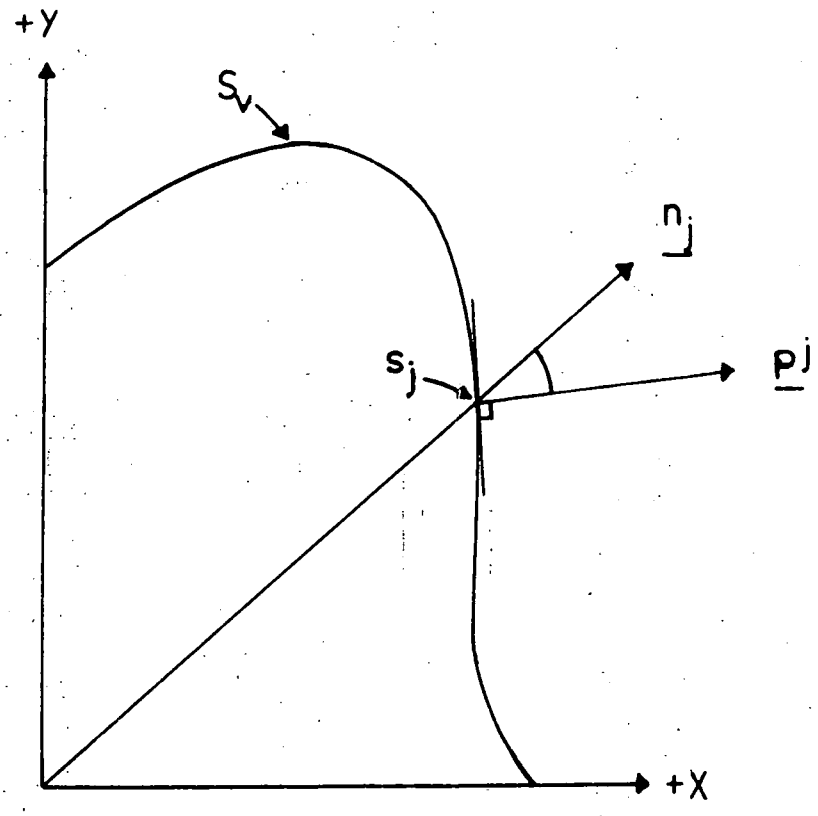

FIGURE 3.7a: P^j is the energy flux direction for the mode with propagation vector n_j. (The slowness surface S_v is that of $SrMoO_4$.)

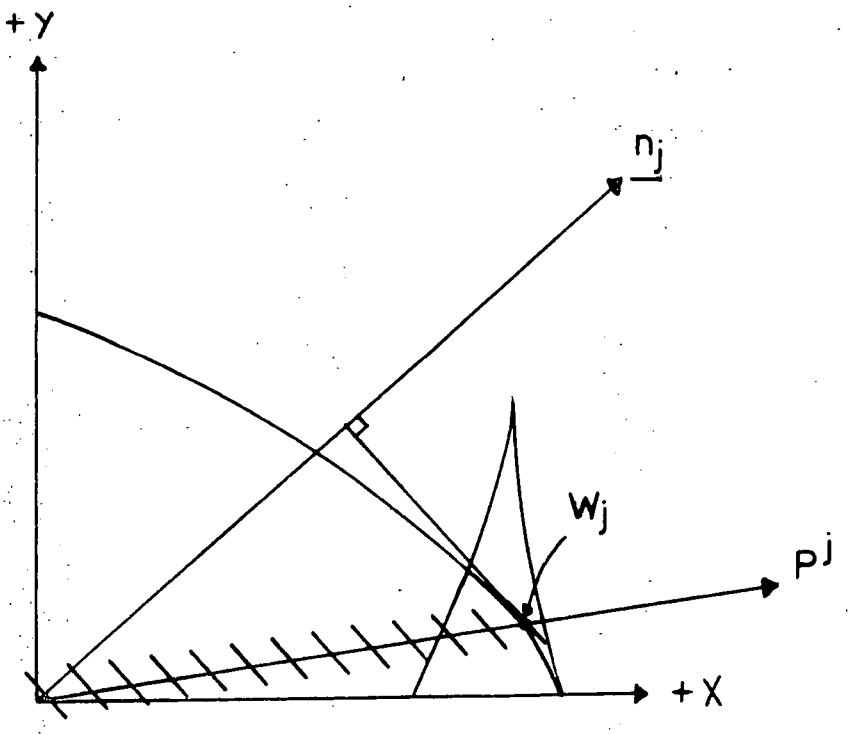

FIGURE 3.7b: The plane normal to the propagation direction n_j is tangential to the wave surface at the point W_j. P^j is the energy flux direction of the ^{j}mode with direction n_j. (The wave surface is that of $SrMoO_4$).

CHAPTER FOUR

ULTRASONIC STUDY OF SOLIDS

Ultrasonic methods are in widespread use for the study of the elastic and anelastic properties of solids, liquid and gases. For solids pulse echo methods are particularly important, and are employed both in the study of fundamental physical properties of materials and in non-destructive testing. Pulse techniques are particularly valuable for measurements at frequencies in the range 5 MHz to 50 GHz. At such frequencies plane bulk waves may be generated in samples of centimetre dimensions. In a typical solid (with longitudinal sound velocity equal to say 5×10^5 cm s^{-1}) these frequencies correspond to wavelengths of 10^{-1} to 10^{-5} cm and are many times greater than interatomic distances ($<10^{-7}$ cm). The solid can be considered to behave as an elastic continuum and the classical description (Chapter 3) of the propagation of plane waves in an elastically anisotropic medium is appropriate. In this chapter the principles of the pulsed ultrasonic methods used in the present work are described, beginning in Section 4.1 with the simple pulse echo method and continuing in Section 4.2 with pulse superposition, a modification of the pulse echo method used for more precise velocity measurements. The interpretation of results and the factors which can cause errors in the measurement of velocity and attenuation are discussed in Section 4.3. Details of equipment and its operation are given in Chapter 5.

4.1 PULSE ECHO TECHNIQUES

4.1.1 Basis of the pulse echo method

In essence the pulse echo method is simple; it involves exciting a pulse of ultrasound in a sample with parallel end-faces and observing the multiple reflections which occur. In practice the precise measurement of ultrasound velocity and attenuation is not so simple and can involve many subtleties of technique and interpretation.

A packet of high frequency stress waves of chosen polarisation may be introduced into the sample by use of a suitable transducer (see Section 5.3.3) which is closely coupled to one of the end-faces of the specimen. A single transducer can be used as both the transmitter and receiver of ultrasound pulses (single-ended pulse echo method) or separate transmitting and receiving transducers can be used (double-ended method). A circular plate transducer greater than about 0.5 cm in diameter behaves as a near-ideal piston source at megahertz frequencies (>10MHz) and generates waves which are very nearly plane and have a wave-normal perpendicular to the end-faces of the specimen (and the plane of the transducer disc). The transducer may be activated by a burst of rf (rf pulse), or by a sharp rectangular pulse. Either piezoelectric (e.g. quartz crystal slices attached to the specimen with a suitable acoustic bond, or evaporated thin films of CdS or ZnO) or magnetostrictive (e.g. Ni film) transducers can be employed. In the case of a resonant transducer an rf pulse is tuned to either the resonant frequency or an odd harmonic of this.

The echo train resulting from a pulse of ultrasound may be observed by exciting the transducer with rf pulses short in duration compared to the transit time in the sample. The repetition rate of the rf pulses is kept low enough to ensure that the echoes arising from each pulse die away completely (due to losses in the sample) before the next is excited. Typically for a sample 1 cm in length, a pulse length of ∿1 μsec and a repetition rate of 1kHz are allowed. Each pulse is reflected back on its own path almost without loss when it is incident on the sample-vacuum (or sample-air) interface at the end of the sample (see Section 3.2). When the first echo arrives back at the transducer, a small amount of the ultrasound energy is converted back into an electrical signal, the rest is reflected at the acoustic impedance mismatch and traverses the sample again. The process repeats many times to give a train of echoes which are amplified and displayed (often in a rectified and detected form) on an oscilloscope triggered at the same time as the pulsed rf generator. A block diagram of a typical system is given in Figure 5.16 and details of the equipment used here are given in Chapter 5.

4.1.2 Velocity and attenuation

An advantage of pulsed ultrasonic techniques is that the velocity and attenuation of a mode can be measured simultaneously. The mode velocity is found from the sample length (ℓ) and the ultrasound transit time (t), the time for one complete round trip, which can be obtained by using a calibrated delay to move a time marker into

coincidence with successive echoes. Corrections, which may need to be applied to the measurement, are discussed in Section 4.3.

The decay of the amplitude of successive echoes of a train is a measure of the ultrasound losses due to absorption and scattering in the material — so long as these losses are substantially greater than those due to reflection at the transducer end of the sample and other extraneous effects (Section 4.3). Absorption and scattering processes each give an intensity loss (dI) per unit length (dx) which is proportional to the intensity (I(x)) of the beam, and thus

$$dI(x) \propto I(x)\, dx$$

so that

$$I(x) = I_o\, e^{-\alpha' x} \tag{4.1}$$

where α' is a constant. The "attenuation" is generally defined by the relations

$$\alpha_{np/cm} = \frac{\alpha'}{2} = \frac{1}{(x_p - x_q)} \ln\left(\frac{u_p}{u_q}\right) \text{ nepers cm}^{-1} \tag{4.2}$$

$$\alpha_{dB/cm} = \frac{20}{(x_p - x_q)} \log_{10}\left(\frac{u_p}{u_q}\right) \text{ dB cm}^{-1} \tag{4.3}$$

in units which measure respectively the decay of ultrasound amplitude (u) and of intensity (I) with distance (x). In units of dB μs^{-1} the attenuation is given by

$$\alpha_{dB/\mu s} = \frac{20v}{(t_p - t_q)} \log_{10}\left(\frac{u_p}{u_q}\right) \text{ dB } \mu s^{-1} \tag{4.4}$$

If the receiver is accurately linear, then the echo heights will be proportional to the ultrasound wave amplitude. The attenuation can be measured directly by fitting a calibrated exponential curve to the echo train.

4.1.3 Precision methods for measuring ultrasound velocity

Although in many cases, useful, valid measurements of velocity can be made directly from the echo train in the way described above, more sensitive techniques are needed if small changes in velocity are to be observed. Many such techniques have been reported. Pulse methods for precision velocity measurement include phase comparison (McSkimin (1957), Williams and Lamb (1958)), sing-around (Forgacs (1960), Drabble and Brammer (1967)), pulse superposition (McSkimin 1961), pulse echo overlap (May (1958), Papadakis (1967)) and a digital averaging technique (Lacy and Daniel (1972)). Highly sensitive continuous wave methods including the sampled-CW technique, are also used. These CW techniques have recently been reviewed by Bolef and Miller (1971).

When the ultrasound velocities to be studied include those of impure modes with unknown polarisation and energy flux directions, pulse methods are advantageous. They allow a continuous and direct observation of the quality of the echo train, and it is possible to check that only the required mode is being excited and that spurious reflections are being avoided. In the present work on $CaWO_4$, the pulse superposition method has been used.

4.2 PULSE SUPERPOSITION

4.2.1 Superposition method

The pulse superposition method was introduced by McSkimin in 1961 and since then has found widespread use in ultrasonic studies of solids, particularly in the measurement of the changes of ultrasound velocities which accompany

changes of environment (temperature, pressure, magnetic field etc.). The method is a modification of the simple pulse echo technique described above (Section (4.1.1)). In the basic form (used here) sensitivities of 1 part in 10^5 are possible on low attenuation materials, and with modifications (McSkimin and Andreatch (1967), Holder (1970)) sensitivities of 1 part in 10^{10} are claimed.

In pulse superposition, transit times are measured by increasing the repetition rate of the rf pulses applied to the ultrasonic transducer until the repetition period T (equal to the reciprocal of pulse repetition frequency) is comparable to a multiple (p=1,2,3...) of the transit time of ultrasound in the sample. Echoes of increasing order from successive rf pulses will then tend to interfere, and, when the pulse repetition frequency is critically adjusted so that echoes of successive orders arrive at the transducer in phase, a maximum will occur in the detected signal. The echoes from many pulses are simultaneously superposed — the pulse superposition is actually a superposition of elastic waves in the specimen — and the reciprocal of the pulse repetition frequency gives the wave transit time and the phase velocity. The situation is illustrated in Figure 4.1a for a case with repetition period equal to the transit time and in Figure 4.1b for the repetition period equal to three times the transit time. In practice (see Section 5.3.2) the superposition is found by omitting several pulses from the input train and observing the summation of echoes (in detected form) from previous input pulses. The pulse repetition frequency

is critically adjusted to make the amplitude of the train of superposed echoes a maximum.

4.2.2 Cycle-to-cycle matching

At superposition the pulse repetition period (T) is equal to the round trip phase delay (the apparent travel time) and can be represented by an equation:

$$T = p\delta - p\gamma/360f + n/f \qquad (4.5)$$

where f is the ultrasound frequency, $p\delta$ represents the time delay in the specimen for p round trips, $p\gamma/360f$ is a delay arising from the phase change on reflection at the transducer coupling interface and n/f is a term which takes account of the fact that a series of superposition maxima can be obtained. The maxima are separated by integer multiples of the rf ultrasound period, and the parameter n represents the number of cycles of mismatch. To obtain an accurate measurement of phase velocity, correct in-phase cycle-to-cycle matching is required, and a correction for the phase change due to the transducer coupling is needed.

(a) McSkimin ΔT criterion

A method for determining the correct cycle-to-cycle matching (n=0 condition) in pulse superposition experiments has been described by McSkimin (1961) and McSkimin and Andreatch (1962), and is used also in pulse echo overlap measurements (Papadakis 1967, 1969b). The method is applicable when resonant transducers are used to generate the ultrasound.

Transmission line analysis of the specimen-bond-transducer system (see Williams and Lamb (1958), McSkimin (1961))

in terms of the respective specific acoustic impedances (Z_s, Z_1, Z_2 in mechanical ohms cm^{-2}) yields an expression for the phase change (ϕ) introduced on reflection of a wave at the specimen-bond-transducer interface:

$$\phi = \pi - 2 \tan^{-1} (Z_d/jZ_s) \tag{4.6}$$

On reflection at the unbounded end of the specimen in a single-ended pulse echo experiment the phase change is π, so that the net phase shift (γ) between successive echoes is

$$\gamma = - 2 \tan^{-1} (Z_d/j\, Z_s) \tag{4.7}$$

The impedance Z_d terminates the acoustic transmission line (see Figure 4.2) and is given by the expression

$$Z_d = j\, Z_1 \frac{Z_1/Z_2 \tan B_1\ell_1 + \tan B_2\ell_2}{Z_1/Z_2 - \tan B_2\ell_2 \tan B_1\ell_1} \tag{4.8}$$

in terms of the bond and transducer thicknesses ℓ_1 and ℓ_2, and the phase shift constants B_1 (= 2πf/(sound velocity in bond)) and B_2 (= 2πf/(sound velocity in transducer)). Dissipation is neglected and Z_s, Z_1 and Z_2 are taken as being real and equal to $\rho_s v_s$, $\rho_1 v_1$ and $\rho_2 v_2$ respectively. For a bonding material for which the impedance is known, Z_d and γ can be calculated. The variation of γ with bond thickness and ultrasound frequency is plotted for specimens of various acoustic impedances in Figures 4.3a and 4.3b (after McSkimin and Andreatch (1962)). These curves were drawn for x-cut and y-cut quartz transducers with Dow resin 276-V9 bonds (for mechanical impedances see Table 5.4). From these figures it is clear that γ is only zero at the transducer resonant frequency if the bond is negligibly thin.

If the bond has a finite thickness, then γ will be zero at a frequency away from resonance.

It is then possible to calculate, using equation 4.5, how the apparent travel time will change with a change of ultrasound frequency, for different values of the mismatch parameter n. The McSkimin criterion depends on a comparison between the calculated and observed changes (ΔT) in the apparent travel time (T) with frequency for each of the different superposition maxima. In this way the n=0 condition should be identifiable.

Usually the change in apparent travel time is measured for a decrease of 10% in the ultrasound frequency from the transducer resonant frequency. Then

$$\Delta T = T_{0.9f_R} - T_{f_R} = \frac{1}{0.9f_R}\left(n - \frac{p\gamma_{0.9f_R}}{360}\right) - \frac{1}{f_R}\left(n - \frac{p\gamma_{f_R}}{360}\right) \quad (4.9)$$

If the bond is very thin ($B_1\ell_1 < 5^o$), at the resonant frequency of the transducer (when $B_2\ell_2 = \pi$) the expression (4.8) for Z_d reduces to

$$Z_d = jZ_1 \tan B_1\ell_1 \simeq j\, Z_1 B_1 \ell_1 \quad (4.10)$$

and (see equation 4.7) $\gamma_{f_R} \simeq 0$. Under such conditions ΔT is given by

$$\Delta T = \left[\frac{1}{f_R}\left(0.112\, n - \frac{p\gamma_{0.9f_R}}{360}\right)\right] \quad (4.11)$$

From this expression (4.11) lower bounds on ΔT may be calculated (a finite thickness of bond adds a small positive increment to ΔT) for the maxima corresponding to different values of n, and the correct maximum (n=0) identified.

Alternatively by using the full expression (4.9) values of ΔT can be calculated as a function of bond thickness. Comparison with the measured values of ΔT will then yield the correct cycle-to-cycle matching, and may give an estimate of the bond thickness. In Figures 4.4a and 4.4b (after McSkimin 1961) the variation of ΔT with bond thickness is shown for correct cycle-to-cycle matching (n=0) of alternate echoes (p=2), and different values of specimen impedance. Since (see equation (4.9)) ΔT is just a linear function of n and p, similar curves can easily be drawn for other superposition conditions.

When proper cyclic matching has been obtained (n=0), the measured transit time can be corrected for the effect of the phase change on reflection at the transducer end of the specimen. Either the estimate of bond thickness (obtained as discussed above) is used to calculate the correction ($p\gamma/360f$), or the effect is estimated directly by observing the change in measured transit time which results from bonding a "dummy" transducer to the end-face of the specimen opposite the transmit/receive transducer.

Although the McSkimin ΔT method detailed here is accepted as the primary method for determining the correct in-phase matching in both pulse superposition and pulse echo overlap experiments, it is not without difficulties and may fail if the bond is insufficiently thin or excessively lossy. Excessive bond loss is particularly a problem with Nonaq stopcock grease bonds (H.J. McSkimin, private communication). The method also breaks down if multimode guided wave propagation occurs (Papadakis 1969),

and similar interference effects caused by beam spreading, non-parallelism or energy flux deviation would be expected to render the method invalid.

(b) Alternative methods

Papadakis (1969) has suggested a modification of the pulse echo overlap technique which can supplement or replace the ΔT method for establishing proper cyclic matching in situations where multimode guided wave propagation occurs. Instead of using an rf burst to excite the ultrasound in a specimen, the transducer is activated by a short rectangular video pulse and an acoustic pulse is produced in the medium as the transducer rings. By adjusting the repetition rate of the video pulses, visual overlap of the first and second echoes is obtained. The repetition rate for proper cyclic matching of echoes from an rf burst is then the one found closest to that giving the video pulse overlap. This method will also be applicable to pulse superposition and to finding the correct (n=0) maximum in the presence of other interference effects besides multimode guided wave propagation, but has not been used in the work reported here.

A third method of choosing the correct matching condition depends upon the assumption that the medium is not dispersive (group velocity equals phase velocity), and is applicable in samples with transit times between 2 and 10 μs only at low megahertz frequencies (10 to 20 MHz). At these frequencies a mismatch of one cycle of rf at superposition will change the apparent transit time by between 0.1 to 0.05 μs. By using an accurate time-marker

method the transit time of the echo train to be used in pulse superposition can be measured to within ± 0.05 μs by measuring the time delay between the peaks of the detected envelopes of successive echoes. The pulse repetition frequency is then increased to give superposition and the correct maximum (n=0) is that for which the repetition period is closest to the measured transit time. This method is essentially that used for cyclic matching in a new pulse echo technique using real time digital averaging, reported by Lacy and Daniel (1972). These workers use a computing counter to measure the delay time between chosen rf cycles of two selected echoes. The correct cycles are chosen by comparison of the transit time obtained with that measured between the detected envelopes of the same echoes.

4.2.3 Measurement of temperature variation of transit times

Pulse superposition is particularly suited to measuring the variation of transit times with changes of temperature; at all temperatures the effects of the coupling between the transducer and specimen can be minimised. This is possible because the pseudo-resonance at a maximum is obtained by varying the pulse repetition rate, and the ultrasound frequency can be tuned as required (cf. resonance methods where the sample resonance is found by tuning the ultrasound frequency). This feature of pulse superposition is important because bond properties often vary considerably with temperature. Estimation of the phase change at the transducer-bond-specimen interface would be tedious if repeated at many temperatures.

In pulse superposition the effect of changes in bond properties on ratios of transit time at different temperatures is minimised by maintaining the ultrasound frequency at the transducer resonant frequency as this changes with temperature. When the transducer is operated at its resonant frequency, according to equation 4.10 the impedance Z_d is given by

$$Z_d = j\, Z_1 \tan B_1 \ell_1$$

which for a thin bond reduces to

$$Z_d = j\, Z_1 B_1 \ell_1 \qquad (4.12)$$

If B_1 is written as ω/v_1 and Z_1 as $\rho_1 v_1$ where v_1 is the sound velocity in the bond, this becomes

$$Z_d = j\, \omega \rho_1 \ell_1 \qquad (4.13)$$

The terminating impedance thus takes the form of a mass loading and will be effectively independent of temperature. Hence as long as the bond is thin and the transducer maintained at resonance, the phase angle for reflected waves (γ) will remain essentially constant as temperature is changed.

The ratio of ultrasound phase velocities v/v_o at two temperatures is inversely proportional to the ratio of transit times (δ_o/δ), which from (4.5) is given by

$$\frac{\delta_o}{\delta} = \frac{T_o/p + \gamma_o/360f_o - n/pf_o}{T/p + \gamma/360f - n/pf} \qquad (4.14)$$

Since $\gamma/360f$ and n/f are usually small compared to T/p this expression (4.6) may be written as

$$\frac{\delta_o}{\delta} = \frac{T_o}{T}\left[1 + \frac{p\gamma_o}{360 f_o T_o} - \frac{p\gamma}{360 f T} + \frac{n_o}{f_o T_o} - \frac{n}{fT}\right] \qquad (4.15)$$

In the conditions described above,

$$\frac{p\gamma_o}{360 f_o T_o} \approx \frac{p\gamma}{360 f T} \qquad (4.16)$$

and so long as the same cycle-to-cycle matching is maintained throughout a temperature run (i.e. $n_o = n$),

$$\frac{n_o}{f_o T_o} \approx \frac{n}{fT} \qquad (4.17)$$

Then δ_o/δ is equal to T_o/T to within a few parts in 10^4 (if n is a small integer) or to within a few parts in 10^5 if the correct cycle-to-cycle maximum (n=0) has been chosen.

4.3 EXTRANEOUS FACTORS AFFECTING VELOCITY AND ATTENUATION

4.3.1 The diffraction field of the transducer

A finite area transducer does not behave as a perfect piston pressure source but has an associated diffraction field. Such a transducer does not generate a perfectly parallel beam of plane waves but excites a slightly divergent beam whose pressure profile varies in a complex way across the face of the transducer and into the specimen. The beam divergence can cause gross errors, or even prevent valid velocity and attenuation measurements if it causes the ultrasound beam to impinge on the sidewalls (the effect is additional to any energy flux deviation which may occur). In an isotropic medium the beam divergence angle (β) is given by

$$\beta = \sin^{-1}(1.22\,\lambda/D) \qquad (4.18)$$

for a circular disc transducer of diameter D and a sound wavelength λ in the specimen. In the case of a small transducer with a diameter of say 2 mm, generating 15 MHz ultrasound waves in an isotropic medium with longitudinal velocity equal to 5×10^5 cm s^{-1}, the divergence is about 5^o (see Figure 4.5).

For anisotropic media the beam is not conical and the full solution for arbitrary propagation directions is complex (Kharusi and Farnell 1970). However a comparatively simple method for estimating the angular beam width due to diffraction spreading in anisotropic media has been suggested by Liu and Green (1972). A finite acoustic source is considered to have associated with it a finite bundle of wave vectors, each with its own energy flux direction parallel to the appropriate gradient vector of the slowness surface. Acoustic modes associated with large curvatures of the slowness surface are expected to experience larger beam spreading effects than those which occur in isotropic materials (which have spherical slowness surfaces), while modes associated with small curvatures will have a smaller beam width. Indeed Liu and Green (1972) have found an approximately linear relationship between measured angular beam width and slowness surface curvature for arbitrary propagation directions in NaCl, quartz crystal and fused quartz. Beam spreading will be largest for directions of propagation near the minima on the slowness surface, and least for directions of propagation near maxima.

Even when the beam divergence is not sufficient to cause the ultrasound beam to impinge on the sample walls, diffraction can have a significant effect on measurements. Phase velocity is increased slightly, some dispersion is introduced and the measured attenuation may be increased appreciably (Papadakis 1966).

(a) Velocity measurements

The effect of diffraction on measured velocity has been discussed empirically by McSkimin (1960, 1964) and analysed for anisotropic materials by Papadakis (1966). Papadakis' analysis was limited to longitudinal waves propagating along pure mode axes but is useful for assessment of the effect of diffraction on pulse superposition measurements. The phase advance (ϕ) for a pure longitudinal wave from a circular piston source of radius a, computed by Papadakis (1966) as a function of the distance from the source into an elastic half-space is shown in Figure 4.6 for a sound wavelength λ. For directions within a few degrees of a pure mode axis the velocity surface is approximated in terms of an anisotropy parameter (b) by the expression

$$v(\theta) = v_o (1-b\theta^2) \qquad (4.19)$$

where $v(\theta)$ is the velocity in a direction which makes an angle θ with the pure mode direction for which the velocity is v_o. For all values of b (see Figure 4.6) the change in relative phase shift from the source (S=0) to infinity ($S=\infty$) is $\pi/2$ radians. With increasing anisotropy ϕ tends to approach $\pi/2$ more rapidly.

To estimate the magnitude of the effect of this phase advance on measurements of phase velocity, an isotropic medium can be considered. For a typical sample, say 0.7 cm thick, with a longitudinal velocity of 5×10^5 cm s^{-1}, the diffraction effect due to two sizes of transducer can be estimated:

(i) transducer radius = 0.5 cm, frequency = 18 MHz.

The echoes will occur at very small values of S ($=z\lambda/a^2$); the twentieth echo corresponding to $S \simeq 3$. Successive echoes are thus separated by different times which depend on the respective phase shifts. The true travel time t between two echoes n and m is given by the measured time t' plus an increment (Δt) to correct for phase advance, given by

$$\Delta t = \left[\phi(S_n) - \phi(S_m) \right] / 2\pi f \qquad (4.20)$$

The pulse superposition method sums echoes of all different orders and many different phase advances. The superposition measurement of transit time thus gives a weighted average of the diffraction effects, the weighting being dependent on the ultrasound attenuation. In a situation where the superposition of echoes from say twenty rf pulses is observed, then the error in the measured transit time due to diffraction can be taken as the average error per transit over twenty transits — giving in this case an error of about 0.01% in the measured transit time.

(ii) transducer radius = 1 mm, frequency = 15 MHz

The values of S corresponding to the 1st, 2nd, 3rd ... echoes will be 4.66, 9.33, 13.99 ... etc. Thus,

from Figure 4.6 , after the first echo, successive echoes will all have nearly the same relative phase, and will be separated by the actual transit time in the sample. Measurement by pulse superposition will thus give the correct value of the transit time.

For a material such as $CaWO_4$ where the isotropy assumption does not hold the error in case (ii) will be unchanged, while in case (i) it could increase to a maximum of approximately 0.03% with increasing anisotropy. Papadakis' analysis is limited to pure longitudinal waves. If no significant dependence of velocities on frequency or transducer size is observed for shear and impure modes, then the errors in velocity may be assumed to be of the same order as those for longitudinal modes.

(b) Attenuation measurements

Diffraction field effects are evident in the characteristic way in which the echo decay departs from a true exponential. Usually two or three loss maxima can be seen in the early part of the echo train, and the decay tends gradually to a near-exponential form with increasing delay (see Figure 4.7).

The diffraction loss has been computed for isotropic specimens by Seki et al (1956) and for anisotropic solids by Papadakis (1966). The latter work shows that, associated with the phase shift due to diffraction, there is a diffraction loss which can be plotted as a function of normalised distance $S(= z\lambda/a^2)$ from the source (see Figures 4.8a and 4.8b). The loss per unit travel time due to diffraction (to be subtracted from the attenuation

measured by reference to echoes m and n) is readily calculated using these Figures by means of the expression

$$\alpha = \frac{v[dB(S_n) - dB(S_m)]}{2\ell\ (n - m)} \quad dB\ \mu s^{-1} \qquad (4.21)$$

for a sample of length ℓ (cm) and phase velocity v (cm μs^{-1}).

4.3.2 Non-parallelism of specimen faces

In a pulse echo experiment a burst of ultrasound generated by a suitable ultrasonic transducer is reflected back and forth between opposite parallel faces of a specimen, and detected by the same or another transducer. The transducer is a phase sensitive device ; any phase variations which occur over its area lead to interference and are a source of error. Such phase variations can arise if the opposite faces of a sample are not perfectly parallel. Then the reflected ultrasound wave meets the transducer at a small angle and different surface elements of the transducer detect different phases of the wave. Errors in attenuation and velocity measurement can result, and to prevent these specimens must be prepared to high degrees of parallelism, especially for studies at higher megahertz frequencies.

For a wedged sample with wedge angle θ, it has been shown (Truell et al 1969) that the echo pattern will be modulated by a factor

$$\left| \frac{2\ J_1(2kna\theta)}{2kna\theta} \right| \qquad (4.22)$$

where J_1 is a Bessel function, a is the transducer radius,

n the echo number and $k = 2\pi f/v$. The form of this function is illustrated in Figure 4.9. Thus the echo train has nodes (known as the 1st, 2nd, ... zero points) at z (= 2kanθ) equal to 3.83, 7.01 ... and maxima at z equal to 5.1, 8.45... Each echo is reduced in amplitude compared with that it would have had if the sample had been parallel: the attenuation usually appears to be increased. In such a situation the measured attenuation—most conveniently obtained by fitting a calibrated exponential curve to the first echo and the maximum at z = 5.1—can be corrected by use of Figure 4.9, using either the known wedge angle of a sample or an "effective" wedge angle determined by finding how the position of the first minimum depends upon the ultrasound frequency. As the ultrasound frequency is increased, this first zero moves nearer the source (because the values of z for each echo are proportional to frequency) and the correction required (usually in dB cm^{-1} or dB μs^{-1}) increases. However at high frequencies it is possible for the echoes to be so widely spaced in z-value that the apparent attenuation may be less than the real value and correction is then difficult. When measurements are made on samples with high intrinsic attenuation, echoes beyond the zero point at z = 3.83 may not be visible. In this case ($z < 1$) the modulating factor (4.22) can be simplified to $e^{-z^2/8}$ and the measured attenuation between the first and the n^{th} echo can be suitably corrected.

Although in principle the effects of non-parallelism on measured attenuation can be corrected, in practice there are several difficulties due to the limitations of the

theory which (i) deals only with one-dimensional wedging in isotropic materials and (ii) cannot take account of interference which may occur if, after multiple reflections between the misoriented faces, the ultrasound beam is sufficiently deflected sideways to hit the specimen walls. Similar difficulties prevent the correction of the non-parallelism errors in measured velocities. The effects of non-parallelism, while not apparent when the simple pulse echo method is used, show up when more precise measuring techniques are employed. In the sampled-continuous wave technique, non-parallelism leads to spurious maxima which are often as large as the true resonance maxima (Miller and Bolef 1970). In pulse superposition experiments on non-parallel specimens it is sometimes impossible to distinguish the true maxima from their spurious neighbours (see Section 5.3.2). Thus a prime requirement for accurate measurement of velocity as well as attenuation is an echo train with an exponential decay. Parallelism of the opposite sample faces to better than 10^{-4} radians is required for studies at 10 MHz — or better than 10^{-7} radians at 1 GHz — and a similar parallelism of the transducer-sample bond is necessary. Limits on parallelism are most severe in low attenuation dielectric materials (e.g. quartz, YAG, Al_2O_3, scheelites).

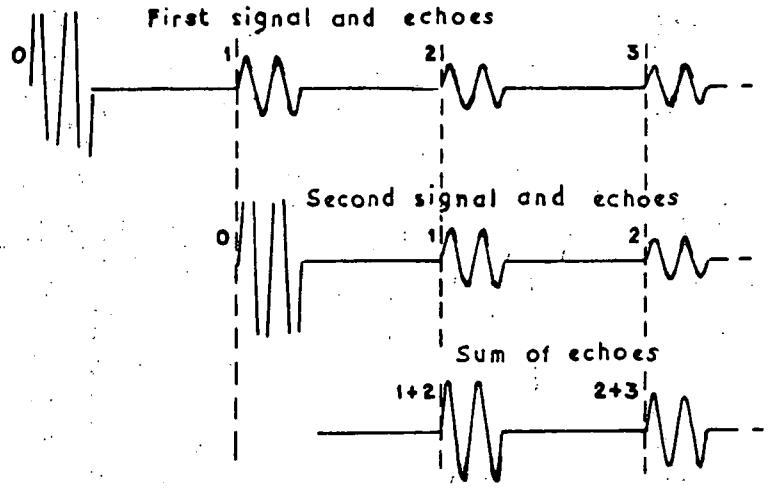

(a) p = 1; pulse repetition period equal to transit time

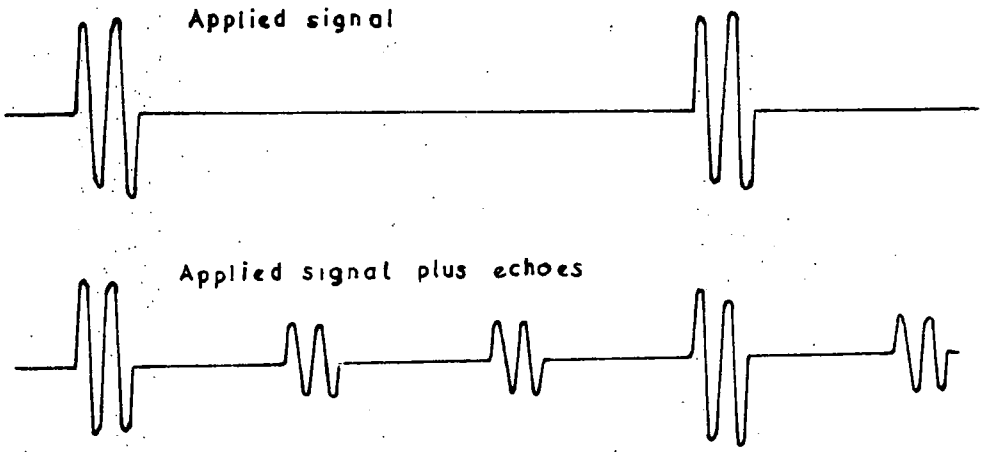

(b) p = 3; pulse repetition period equal to three times transit time

FIGURE 4.1: Superposition of echoes

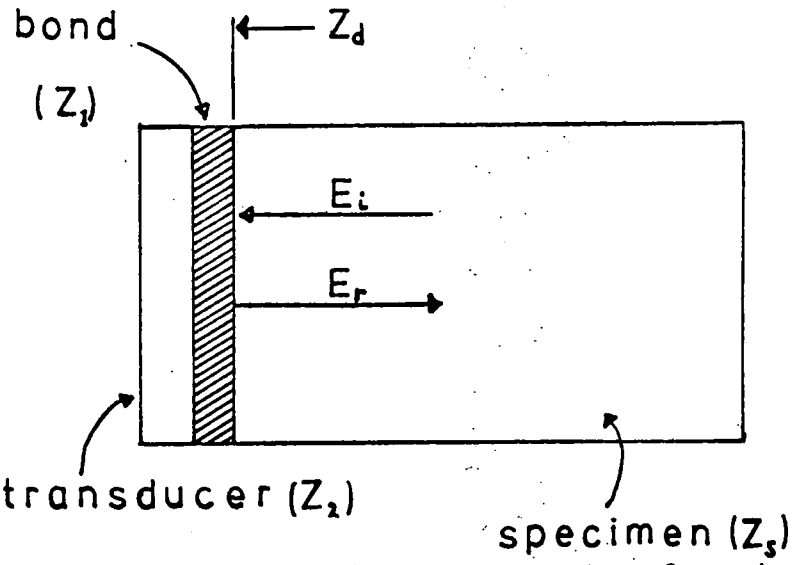

FIGURE 4.2: Acoustic transmission line representation of specimen bond and transducer.

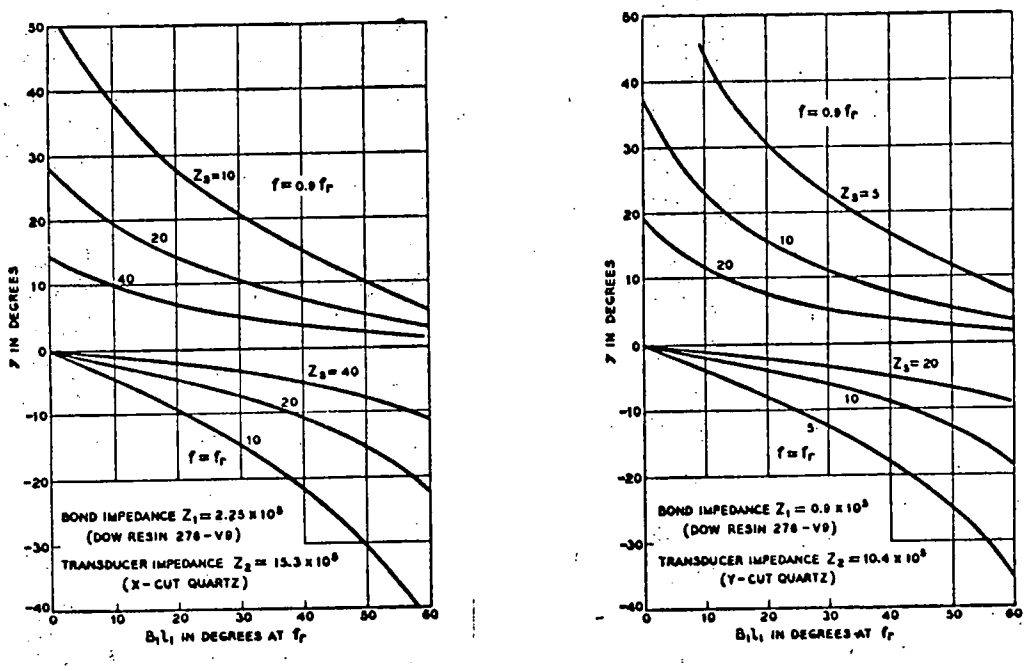

FIGURE 4.3: Variation of the phase angle γ with bond thickness and ultrasound frequency for specimens of various specific acoustic impedances (after McSkimin and Andreatch 1962)

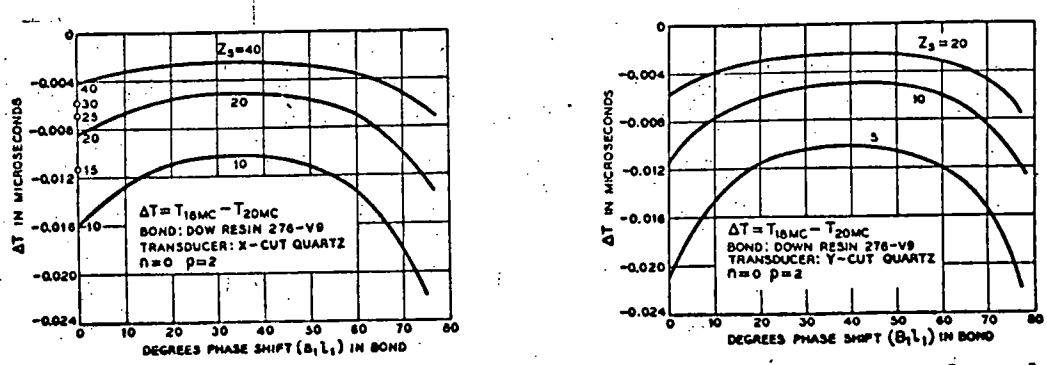

FIGURE 4.4: Variation of ΔT with bond thickness for n=0, p=2, and several specimen impedances (after McSkimin and Andreatch 1962)

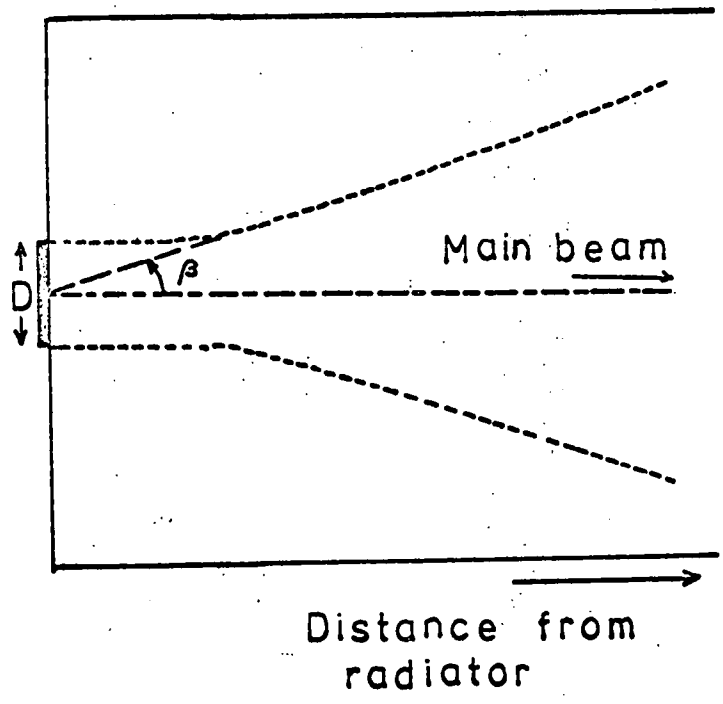

FIGURE 4.5: Beam divergence due to diffraction (after Mason 1958)

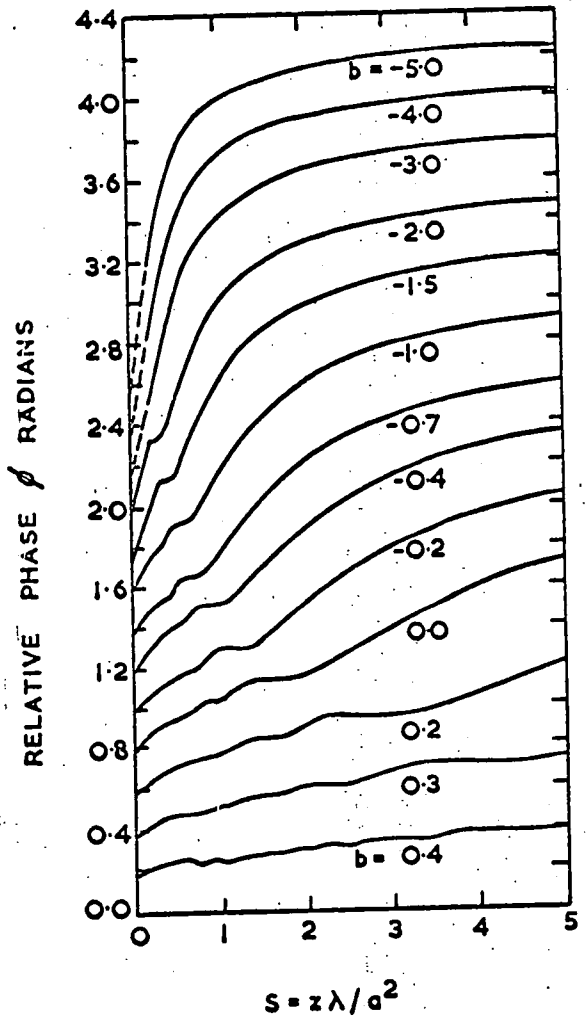

FIGURE 4.6: Relative phase advance of pure longitudinal waves due to diffraction as a function of normalised distance into specimen and the anisotropy factor b (after Papadakis 1966)

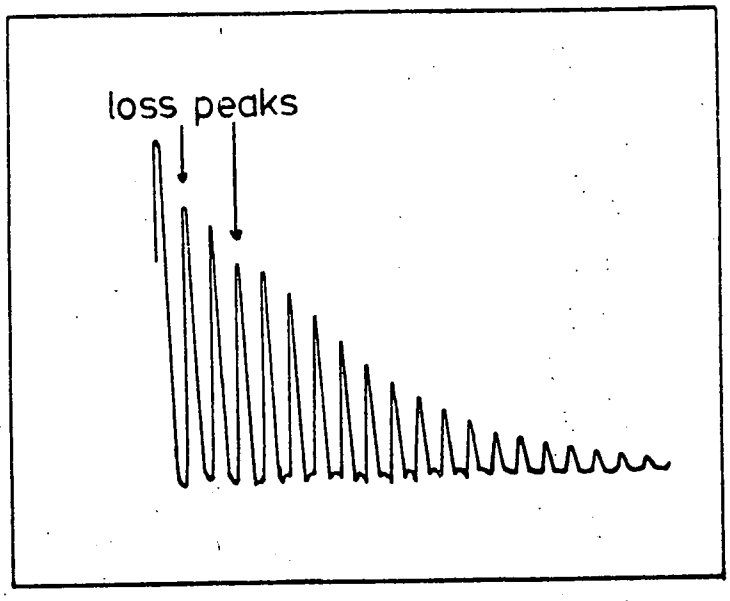

FIGURE 4.7: Tracing of echo train showing loss peaks due to diffraction field of transducer

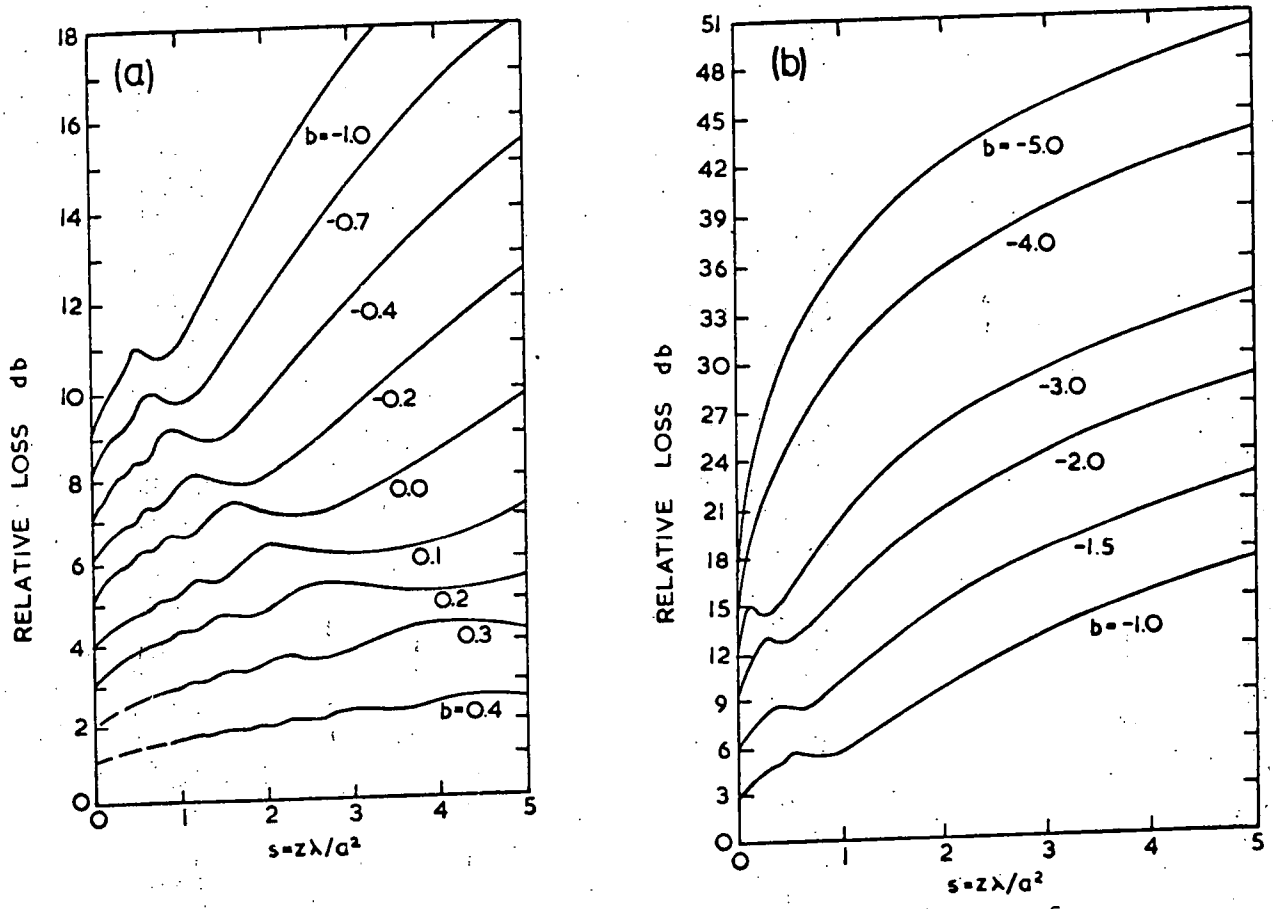

FIGURE 4.8: Relative loss as function of normalised distance from source for longitudinal waves propagating in directions with anisotropy factor b between +0.4 and -5.0 (after Papadakis 1966)

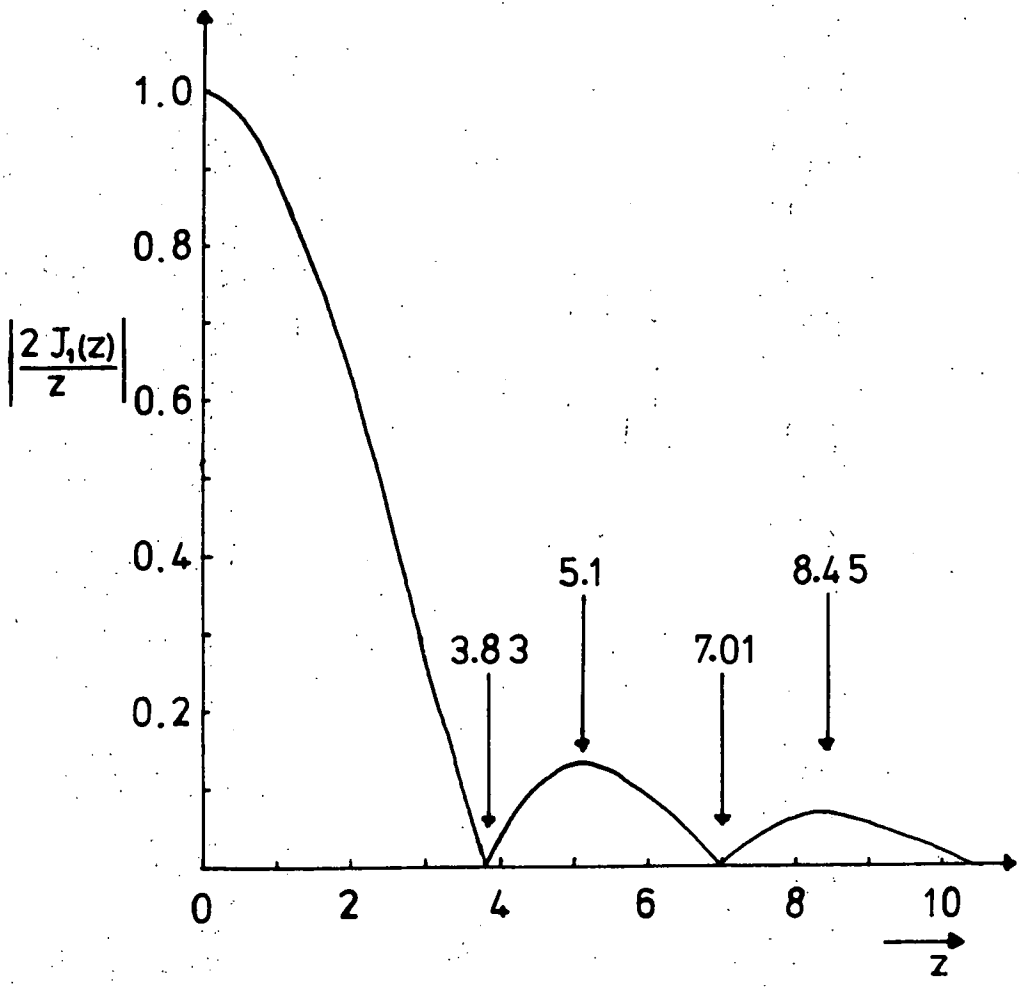

FIGURE 4.9: Theoretical modulation of echo pattern for a non-parallel sample

CHAPTER 5

EXPERIMENTAL DETAILS

In this chapter details of experimental techniques and the measuring system are given. Their application to the characterisation, preparation and ultrasonic study of single crystal specimens of $CaWO_4$ is described.

5.1 CHARACTERISATION OF CRYSTALS

5.1.1 Preliminary examination

The $CaWO_4$ single crystals used in this work were grown at International Research and Development Co. Ltd., Newcastle upon Tyne, by the Czochralski technique of pulling from the melt. Details of the growth procedure were given in the IRD Research Report 66-76 (Buchanan and Casselton 1966). Single crystal boules of length about 5 cm and diameter about 1.2 cm were produced. Each was annealed for 72 hours at a temperature of 1550°C in an oxygen atmosphere. Two of the boules cleaved parallel to the (001) plane during annealing, but usually annealed crystals were less susceptible to fracture during subsequent cutting and polishing. All the boules supplied had growth axes approximately parallel to the fourfold axis and the characteristic cross-section of c-axis grown crystals (Nassau and Broyer 1962), illustrated in Figure 5.1.

Visual observation showed the crystals were free from obvious flaws, cavities or granular structure except at the neck where growth had commenced. Pure crystals were colourless — as was a 0.05 at.% gadolinium doped boule — while neodymium doped crystals varied from pale blue (0.01 at.% Nd) to violet (1.0 at.% Nd). X-ray back reflection photographs showed that each boule was monocrystalline. The c axis misorientation along the length of a boule, measured by taking a series of Laue photographs, was found to be less than the resolution limit of the technique, estimated to be 15' of arc. $CaWO_4$ is soft enough to be appreciably susceptible to surface damage; the texture of the spots

on Laue back reflection photographs was found to be an indication of the extent of this damage rather than of mosaic structure. When the x-ray beam was incident on an undamaged area, the spots were sharp and not split.

To further investigate crystal defects, specimens with faces cut normal to the fourfold axis were chemically polished (by boiling for five minutes in 85% orthophosphoric acid at 270°C) and etched for 5 to 10 minutes in aqua regia at 55°C. Square pits with a density of 10^4 to 10^5 cm^{-2} were observed. Several tests indicated that the pits marked the points of emergence of dislocation lines:

(i) the number of pits remained constant on further etching

(ii) extensive low angle grain boundary arrays were observed

(iii) matching grain boundary arrays were found on the front and rear faces of a very thin (∿200 micron) specimen.

5.1.2 X-ray orientation

The crystallographic axes in the boules were found by means of Laue back reflection x-ray photographs. The Z axis was readily identified by the fourfold symmetry of the Laue pattern obtained with the incident beam parallel to this axis (Figure 5.2). Directions normal to the Z axis could be recognised by the reflection symmetry of the mirror plane of the point group.

Laue photographs taken with the x-ray beam parallel to <100> or <110> directions seemed to exhibit additional symmetry with an apparent mirror symmetry about planes

parallel to {010} and {110} directions respectively (see Figures 5.3 and 5.4). This pseudo-ditetragonal symmetry was first observed by Haga and Jaeger (1916). These workers, knowing that mineral scheelite had a form corresponding to the bipyramidal class concluded that the additional symmetry, which they observed in "a number of scheelite crystals of the best quality and from all kinds of places" was due to a "polysynthetic" twin structure. In fact the pseudo-symmetry arises because, as described in Section 2.1, the calcium and tungsten atoms lie on a framework which has 4/mmm (ditetragonal) symmetry; only the relatively low atomic number oxygen atoms are sited in such positions as to reduce the overall symmetry to 4/m. The <100> and <110> axes can readily be identified but not distinguished by the pseudo-symmetry. The distinction must initially be made by the stereographic projection method, but subsequently for $CaWO_4$ the directions are easily distinguished in c-axis grown crystals by examination of the boule cross-section: the <100> and <110> are respectively parallel to the longest and shortest diameters of the boule section (Fig. 5.1).

The complete orientation of a boule of a TII Laue group tetragonal crystal also requires the determination of the sense of the conventional +Z direction in the boule. Such a determination has been described by Farabaugh et al (1966), who used an x-ray method which depended on a visual comparison of the intensities of pairs ({hkℓ}, {khℓ}) of spots. The differences in intensity between spots of such pairs depend only on the positions of the oxygen atoms relative to the incident x-ray beam. Metal atoms in general positions

in the cell contribute equally to each reflection. Comparison of the observed intensity differences with those predicted from the oxygen coordinates allows the sense of the +Z axis to be determined. The method was described with particular reference to $CaMoO_4$ and used to orient specimens used in the determination of the elastic moduli of that material (Wachtmann et al 1968). Farabaugh et al (1966) found that the technique could not be applied so readily to the orientation of $PbMoO_4$; in this scheelite the differences in the intensities of the {hkℓ} and {khℓ} reflections are not so easily recognised because of the large contribution of the heavy Pb ion (atomic number = 82). Similar problems were encountered in the present work when attempting to orient $CaWO_4$ crystals. The reflections due to the heavy tungsten atoms (atomic number = 74) dominate the intensities of the spots. Indeed the difference in intensity between spots of a pair was often less than was observed between symmetry related spots, and the sense of the +Z axis in a boule could not be determined with certainty. An alternative method has been developed and is described in the next section. For $SrMoO_4$ the x-ray method has been found to be satisfactory: details are given in Chapter 7.

5.1.3 Determination of Z axis sense in pure $CaWO_4$

A novel combination of electron spin resonance and ultrasonic orientation techniques has been developed to find the Z axis sense in pure scheelite structure crystals.

(a) Basis of the method.

An experimental technique to find the sense of

the Z axis must examine a physical property which is sensitive in a predictable way to the positions of the oxygen atoms. The intensities of x-ray reflections are one such property, the crystal field due to the oxygen atoms is another. By doping a scheelite with a rare earth such as Gd or Nd the crystal field can be probed by observation of the e.s.r. spectra (see Section 2.2). Location of the positions of the magnetic axes in the XY plane with respect to the crystallographic axes provides a means of finding the sense of the Z axis in a doped specimen.

The directional dependence of ultrasound wave velocities is another property of scheelite crystals which depends on the positions of the oxygen atoms, though not in a way which can easily be predicted until the elastic constants are known. If ultrasound velocities are not appreciably affected by low levels of doping (an assumption confirmed in the course of this work) then the Z axis sense in a pure specimen can be identified by comparison of ultrasound velocities with those measured in a previously oriented, doped specimen.

(b) Experimental details.

The sense of +Z axis was found in a boule of 0.05 at.% Gd doped $CaWO_4$, (preferred to Nd doped $CaWO_4$ because the Gd^{3+} Q-band resonance spectrum is readily observable at room temperature whereas that of Nd^{3+} is not). An e.s.r. sample was cut in the form of a rectangular parallelopiped with ends normal to the fourfold axis. It was carefully mounted on a short circuiting plunger which terminated the sample arm of a conventional Q-band spectrometer and

located such that the magnetic field direction could be rotated in the XY plane of the sample. The microwave spectrometer is shown in block diagram form in Figure 5.5. It utilises a 34 to 35.5 GHz reflex klystron as the signal source and a magic-tee bridge element with an E-H tuner and short circuit in the balancing arm. Field modulation at 160 kHz and phase sensitive detection are employed. Use of a magnetic field sweep and xy recorder gives a display of the derivative of the resonance line at the frequency of the reflex klystron. By rotating the magnet and plotting the position of a particular resonance line every 5^{o} and where necessary every 1^{o}, the extremes of position of the lines were found. As required by the four-fold site symmetry at the impurity ions, the field maxima repeated every 90^{o} and were separated from field minima by 45^{o}. The extremes of position of the different lines of the spectrum were found to coincide well within the accuracy of setting the magnetic field direction. This is apparent in Figure 5.6 where the positions of lines corresponding to the $\frac{7}{2} \leftrightarrow \frac{5}{2}$ and $\frac{3}{2} \leftrightarrow \frac{1}{2}$ transitions, ~~and some satellites of these~~, are shown for magnetic field directions between the +X and -X axes. The magnetic axes in the XY plane of the specimen were thus located; they were found to be 9^{o} from the <100> axes with the sense of rotation shown in Figure 5.7. By reference to Figure 2.6 the sense of the conventional +Z axis in the specimen, in the boule from which the specimen had been cut, and in the ultrasonics sample was determined.

The velocities of ultrasonic waves propagated in

the direction defined by cosines 1/2, $3^{\frac{1}{2}}/2$, 0 in a sample cut from the doped boule were found to be

$$\begin{aligned} v_{\text{quasi-longitudinal}} &= 5.12\text{x}10^5 \text{ cm s}^{-1} \\ v_{\text{quasi-shear}} &= 2.00\text{x}10^5 \text{ cm s}^{-1} \\ v_{\text{pure shear}} &= 2.33\text{x}10^5 \text{ cm s}^{-1} \end{aligned} \qquad (5.1)$$

Two samples of pure $CaWO_4$ were cut from a single crystal boule to yield ultrasonic samples for propagation in directions ($\underline{n_p}$ and $\underline{n_q}$) in the XY plane, 60^o on either side of a chosen <100> axis as shown in Figure 5.8(a). Without knowledge of the sense of Z axis in the boule it was not known which of the samples (p or q) had direction cosines 1/2, $-3^{\frac{1}{2}}/2$,0 and which had 1/2, $3^{\frac{1}{2}}/2$, 0. The ultrasound velocities in the two samples were measured to be:

Sample p

$$\begin{aligned} v_{\text{quasi-longitudinal}} &= 4.53\text{x}10^5 \text{ cm s}^{-1} \\ v_{\text{quasi-shear}} &= 3.05\text{x}10^5 \text{ cm s}^{-1} \\ v_{\text{pure shear}} &= 2.33\text{x}10^5 \text{ cm s}^{-1} \end{aligned} \qquad (5.2)$$

Sample q

$$\begin{aligned} v_{\text{quasi-longitudinal}} &= 5.17\text{x}10^5 \text{ cm s}^{-1} \\ v_{\text{quasi-shear}} &= 1.98\text{x}10^5 \text{ cm s}^{-1} \\ v_{\text{pure shear}} &= 2.37\text{x}10^5 \text{ cm s}^{-1} \end{aligned} \qquad (5.3)$$

For the pure shear mode, the velocity is the same in all three samples because it must equal $(C_{44}/\rho)^{\frac{1}{2}}$ for all propagation directions in the (001) plane. The velocities (5.3) of the quasi-longitudinal and quasi-shear modes in the pure sample q agree well within experimental error with those (5.1) measured in the Gd doped sample, while the

velocities (5.2) measured in the pure sample p are quite different. Sample q was thus identified as having direction cosines of the normal to its parallel end-faces equal to 1/2, $3^{\frac{1}{2}}/2$, 0 like the Gd doped sample. The position of the +Y axis relative to a +X axis chosen parallel to the $\langle 100 \rangle_1$ axis of Figure 5.8a was thus determined, and the Z axis sense in the pure boule of $CaWO_4$ was that required to complete a right handed set. Thus in Figure 5.8a the $\langle 100 \rangle_2$ axis is in fact the [010] direction (the +Y axis) and the [001] direction (the +Z axis) emerges from the plane of the figure, as shown in Figure 5.8b. Furthermore it can be deduced that the sample p has a propagation direction (cosines) 1/2, $-3^{\frac{1}{2}}/2$, 0 which is equivalent by fourfold symmetry to $3^{\frac{1}{2}}/2$, 1/2, 0 and a direction of propagation at 30° to the +X axis when measured towards the +Y. The agreement between the velocities (5.3 and 5.1) measured in the pure and the doped samples respectively justifies the assumption that low levels of doping do not affect ultrasound velocities appreciably. Sample q was subsequently used in the determination of the elastic constants of $CaWO_4$ (Chapter 6).

This combination of spin resonance and ultrasonic orientation techniques is applicable to all the scheelite structure tungstates and molybdates listed in Table 1. Very accurate knowledge of the oxygen coordinates is not required. The Z axis sense in the doped crystal can be found by the spin resonance method and then found in the pure material by the ultrasonic technique. Once the elastic moduli (including the sign of C_{16}) of a material are known then the Z axis sense in a boule can be found by ultrasonic orientation techniques alone. This will be discussed later in the

light of the elastic moduli of scheelite crystals measured in the course of this work.

5.1.4 Relationship of etch-pit orientation to the sense of +Z axis

Etch pits on the {100} and {1$\bar{1}$0} faces of $CaWO_4$ have a unique orientation with respect to the sense of Z axis in the crystal (see Section 2.3). From boules in which the +Z axis had been located in the manner described above, specimens were cut to have faces normal to the <100> and <110> directions. Each was carefully marked with a flat normal to the emerging +Z axis. They were chemically polished to remove surface damage by boiling in 85% orthophosphoric acid at 270°C. After five minutes the {100} surfaces were almost featureless under a magnification of x200 while the {110} surfaces showed some characteristic markings.

Specimens of each orientation were then etched in either

(i) aqua-regia (4 conc. HCl : 1 conc. HNO_3) for 5 min. at 55°C (Cockayne et al 1964), or

(ii) 1 part saturated NH_4Cl, 1 part 85% orthophosphoric acid and 2 parts distilled water for 15 min. at 100°C (Arbel and Stokes (1965)).

Both etchants gave etch-pits on the two surfaces. In each case the pits had mirror symmetry about long axes parallel to the (001) plane but no symmetry about lines parallel to the [001] axis. On the {100} faces the several types of pit which were evident included many which had a distinct orientation, whereas on the {110} surfaces distinct orientations were not so clear. Attention was therefore concentrated on the {100} faces.

Examples of the pits obtained with the two etchants are shown in Figures 5.9 and 5.10. The +Z axis is marked on these figures so that the orientation of the pits can be compared with the sense of that axis in the specimen. The pits have a characteristic "lozenge" shape and are similar to those observed by Arbel and Stokes (1965) and Levinstein et al (1963), with tails which all point in the same direction on a particular face. A background of "vees" was also observed on the {100} faces etched in aqua-regia. These can be seen as a terracing effect in Figure 5.11. Pits on other {100} faces have tails which point in the directions shown in Figure 5.12; the fourfold symmetry property of the Z axis is obeyed. Viewed along the positive direction of the Z axis the pit tails point in an anti-clockwise direction about the axis.

Checks using samples misoriented from the {100} plane by up to 2^{o} and etches of slightly different composition showed that the orientation of the pits on these planes was not very sensitive to misorientation or etch concentration. Observation of the etch pits produced by either of the aqua-regia or NH_4Cl/orthophosphoric acid etches on a {100} face of $CaWO_4$ thus provides an easy and reliable means of finding the sense of +Z axis in a specimen.

It must be stressed that the orientation of etch pits found here is for two particular etchants on a particular material, $CaWO_4$. Extreme caution must be exercised in extending the method to other scheelites, or to the use of other etches. In the case of the semimetals arsenic, antimony and bismuth a particular etch can give

differently oriented pits on different materials even though these are closely related, and different etchants give different orientations of pit on a particular material (Akgöz, Farley and Saunders 1972).

5.2 SAMPLE PREPARATION

5.2.1 Cutting

Samples for ultrasonic study must have parallel opposite faces cut perpendicular to a specified crystallographic direction. Cutting techniques have been developed to yield parallel faces within $1/4^{\circ}$ of the requisite planes.

A boule is mounted, by gluing with Durofix cement, on a Philips Type PW1031 goniometer and accurately aligned by Laue back reflection x-ray photography to have a crystallographic axis parallel to the x-ray beam. The boule is then rotated on the goniometer through the required angle and cut with a diamond wheel on a Meyer and Burger Type TS 3 slicing machine. By obeying certain precautions, and in particular by

(i) ensuring the sample arms of the x-ray machine are accurately parallel to the beam

(ii) restricting adjustments of the goniometer to rotations about its vertical axis

(iii) covering the head of the goniometer in Durofix to prevent "wobble" during cutting

it is possible to obtain the accuracy of cutting given above and a parallelism of opposite faces somewhat better than this.

5.2.2 Lapping and polishing

Samples for ultrasonics study must be polished to high standards of surface finish, flatness and parallelism. In practice these three may be conflicting requirements, and specific techniques must be developed for materials of different hardnesses. Here the methods which have been found satisfactory for $CaWO_4$ are described.

The $CaWO_4$ samples were prepared by use of a Logitech PM2 precision polishing machine with a PP6 precision polishing jig. Figure 5.13 gives a vertical cross-section of the jig in position on the lapping plate of the polishing machine. The sample is held in place by a vacuum chuck which consists of a small sintered brass area at the centre of a brass reference face. A rotary pump is used to evacuate the sintered region and the sample is then held in place by atmospheric pressure. The attitude of the reference face with respect to the "polishing-plane" is controlled by three adjustment screws. The polishing plane itself is defined by the face of the conditioning ring which rests on the lapping plate. A spring holds the sample against the lapping plate, with the close fit of the piston within the cylinder maintaining the relative attitudes of the reference and polishing planes. The load on the sample is adjusted by a screw tensioner. The jig rotates as it is moved backwards and forwards across the rotating lapping plate by a reciprocating arm. This motion is illustrated in plan view by Figure 5.14.

In principle the faces of a sample may be polished flat and parallel by setting one face against a reference face, polishing the opposite face on a lapping plate which

is maintained parallel to the reference plane, and then turning the sample over and polishing the other side in the same way. In practice many precautions are necessary if accurately parallel faces normal to the required direction are to be obtained:

(i) Initial alignment of the chuck face

To ensure that the reference plane and polishing plane are parallel, the chuck face must be aligned parallel to the conditioning ring. A 15cm. diameter optical flat is placed on the chuck and held in position by the vacuum. The screws are adjusted until the interference fringes between the conditioning ring and the optical flat indicate their mutual parallelism. This parallelism should be re-checked each time the specimen is reversed.

(ii) Mounting of sample

Use of a vacuum chuck avoids the need for glues or cements between the specimen and the reference face; such seals almost inevitably reduce the parallelism attainable. Prior to assembly the chuck face and specimen are carefully cleaned in an ultrasonic bath, and then the contact between the two is observed by means of the interference bands between them. These bands should open out to a single colour when the chuck is evacuated. The faces of the $CaWO_4$ specimens were usually sufficiently flat and smooth to maintain an adequate vacuum seal against the chuck face, but during polishing under high applied loads sideways motion of a small area specimen ($<1cm^2$) occasionally caused leakage and release of the specimen. Such breakaway results in extensive damage to the lapping plates. It is prevented by applying a little

glue around the edge of a specimen held firmly against the chuck-face by the vacuum.

(iii) Lapping and polishing

The polishing action depends on the relative motion between the specimen and particles (harder than the specimen) which are embedded in the lapping plate. The plates themselves must be somewhat softer than the specimen and each must be used for one grade of polishing grit only, as contamination by larger particles causes scratching. Transfer of grit from one plate to another is avoided by cleaning the jig in an ultrasonic bath before changing plates. Scratching can also be caused by tiny pieces breaking away from the edges of the specimen and becoming embedded in the plate. If the edges are slightly chamfered before polishing this problem is avoided.

For $CaWO_4$, successive lapping with 6 micron and 1 micron diamond grits (or alternatively 600 and 320 grade Aloxite) on solder plates gave a fine matt surface. Use of 1/4 micron diamond powder and progressively lighter jig loads gave a fine optical finish. By ensuring that the mating surfaces between the specimen and the chuck face were clean, that the chuck face was maintained parallel to the conditioning ring, and that the lapping plates themselves were flat, specimens of $CaWO_4$ were prepared which were flat to within one wavelength of light across 1 cm and which had opposite faces parallel to better than 3×10^{-5} radians. The flatness was determined by examination of interference fringes between the specimen face and an optical flat, and

the parallelism measured by using a high precision dial gauge. Sample thicknesses were measured at room temperature to an accuracy of 0.0001 cm by use of a vernier micrometer.

5.3 SYSTEM FOR ULTRASONIC MEASUREMENTS BETWEEN 1.5 K AND 300 K

The ultrasonic measuring system developed (see Figure 5.15) has facilities for the following types of measurement:

(i) Simple pulse echo measurement of transit time to an accuracy of ±1% by use of a calibrated delay, at ultrasound frequencies between 10 and 800 MHz.

(ii) Attenuation measurements, by the exponential comparator method, of decays between 0.01 and 4 dB μs^{-1} at frequencies in the 10 to 800 MHz region.

(iii) Attenuation measurements on small signals by use of a Box-car detector in conjunction with the attenuation comparator.

(iv) Pulse superposition measurement of transit time, with a sensitivity often better than 1 part in 10^4, at ultrasound frequencies in the range 10 to 90 MHz.

The simple pulse echo technique was used for the preliminary measurements of ultrasound velocities in $CaWO_4$ and for the room temperature measurements in other scheelites (detailed in Chapter 7). The measurements of attenuation in $CaWO_4$ (reported in Chapter 6) were made using the attenuation comparator.

The measurements of the temperature dependence of ultrasound wave velocities in $CaWO_4$ from 1.5 K to 300 K were made by the pulse super-position method. In the next two sections the ultrasonic equipment and its operation will be described. In Section 5.3.3 experimental details regarding ultrasonic transducers and their bonding to specimens of $CaWO_4$ will be given. In Section 5.3.4 the system for control and measurement of sample temperatures will be described.

5.3.1 Attenuation comparator

Measurements of types (i), (ii) and (iii) were made using a Matec Model 9000 Attenuation Comparator with plug-ins of Types 460 and 470 for the frequency ranges 10 to 300 MHz and 300 to 800 MHz respectively. This apparatus (Figure 5.16) consists of a pulsed rf oscillator and a receiver which can each be tuned to the resonant frequency of an ultrasonic transducer. A repetition rate generator (0 to 1 KHz) triggers a display oscilloscope and also, on alternate cycles, either the rf oscillator or a calibrated delay. The rf pulses (width between 0.5 and 5 μs) and amplitude up to 250 volts (peak to peak) drive the ultrasonic transducer and generate ultrasound pulses in the specimen. Echoes detected by the transducer are amplified by a superheterodyne receiver with an intermediate frequency of 60 MHz, detected and displayed on the oscilloscope.

Measurements of both transit time and attenuation make use of the calibrated delay. After the delay time

(0 to 1000 μs) set by a helipot control, an exponential generator is triggered and its output displayed. A pulse of fast rise time but long exponential decay thus appears superimposed on the echo pattern. By means of the calibrated delay the leading edge of the pulse may be set to coincide in turn with two chosen echoes and the time between them measured. Certain precautions are necessary. The pulsed oscillator must be tuned to the resonant frequency of the transducer (to give minimum attenuation) and the receiver tuned to the same frequency (to give maximum signal). It is important to check that the echoes are equispaced; an uneven spacing is indicative of interference between echoes, due to mixed mode propagation or sidewall reflections. Backlash error in the helipot control of the calibrated delay must be avoided. In this way transit times can be measured with a precision of about ±1%. Many factors govern the accuracy of the ultrasound velocities derived from the transit time measurements. These have been considered in Section 4.3.

The attenuation of the ultrasound is found by adjusting the exponential decay of the comparator pulse by a calibrated helipot control until the exponential curve fits the decay of the echo pattern. Five ranges of the exponential generator permit measurement of decay rates between 0.01 and 4 dB μs^{-1}. To obtain accurate measurements of attenuation it is important to follow certain procedures:

(i) the pulsed oscillator and receiver are both tuned to give minimum attenuation

(ii) the receiver gain is adjusted to maintain a constant amplitude for the first echo in case there is any non-linearity in the display

(iii) echoes near the front of the train which do not fit the overall decay pattern are disregarded.

Measurements of attenuation obtained from echo trains which are not exponential must be treated with great caution. Specimens of $CaWO_4$ polished flat and parallel as described above gave echo trains which were exponential even at 750 MHz (see Chapter 6).

In situations where the received echo signal is barely distinguishable from noise so that the attenuation comparator alone cannot be used, a box-car detector can be employed to eliminate noise from the video output of the comparator and give an xy recorder plot of the echo pattern. In the present system a box-car detector made up of a Type 415 Linear Gate and a Type 425A Scan Delay Generator (Brookdeal Electronics Ltd.) is employed with a Type 7035A xy pen recorder (Hewlett-Packard). To recover the waveform of an echo train from noise the scan mode is employed; in turn each point on the waveform is sampled many times and averaged. Scanning is achieved by slowly increasing the delay time between the trigger and gate pulses; at the output a voltage proportional to the averaged input voltage is recorded.

5.3.2 Pulse superposition apparatus

The pulse superposition equipment used in the study of the temperature dependence of the elastic constants of

$CaWO_4$ is shown in block diagram form in Figure 5.17. A high power 93Ω load is permanently connected at the output of the pulsed oscillator, series attenuators (0 to 300 kΩ) are included between the pulsed oscillator and the simple TR junction. This junction is just an arrangement of diodes as shown in Figure 5.18 which isolates the oscillator circuit from the echo pulses and protects the preamplifier from the high voltage transmitted pulses. The arrangement of equipment is thus essentially that described by McSkimin (1961) with one important difference : in the system used here the pulse repetition frequency is defined by a frequency synthesiser (Adret Codasyn CS201S) which has a stability of 1 part in 10^6 (and a long term stability of 1 part in 10^8).

The pulsed oscillator is operated in the "externally modulated" mode with its repetition rate and output pulse width controlled by the unit pulse generator. In this mode, the large duty cycles necessary for pulse superposition measurements are permitted. With a pulse width of 1 μs it is possible to use repetition rates up to 300 kHz (which gives the maximum allowed duty cycle of 30%). The unit pulse generator is itself triggered by the 6 V sine wave output of the frequency synthesiser. By an appropriate setting of the trigger level of the pulse generator the -80 V output pulses are triggered by the negative-going zero crossing of the sine wave, as shown in Figure 5.19a,b. The rf pulses produced by the external modulation of the PG 650 oscillator have peak to peak voltage of 0 to 500 V and may be tuned to frequencies in the range 0 to 90 MHz.

The ultrasound pulses generated in the sample by the piezoelectric transducer reflect back and forth from the parallel end-faces of the sample and are detected by the same transducer. The echo signals are amplified by the preamplifier, further amplified and detected by the wideband amplifier and displayed on the oscilloscope which itself is triggered by the frequency synthesiser.

In the initial stages of operation the repetition frequency of the input pulses is kept low ($\sim$1kHz). Then, with the pulsed oscillator and the preamplifier each carefully tuned to the resonant frequency of the transducer, echoes are visible for moderate settings of gain. This mode of operation is just that used for simple pulse echo measurements; the disturbance due to each input pulse dies away before the next pulse excites the transducer (Figure 5.19c,d,e).

To obtain pulse superposition the repetition rate must be increased until successive echo trains overlap. When the repetition period (T) of the rf pulses is very close to the transit time in the sample (i.e. $p \approx 1$), no echoes can be seen in the display; they are all masked by the rf pulses themselves (Figure 5.20). It is necessary to interrupt the sequence of input pulses so that the summation of echoes from earlier pulses can be observed. This is accomplished by using a facility of the Tektronic 585A oscilloscope. The pulses which are to be removed from the input sequence are selected and intensified on the display by use of the "B intensified by A" mode of the oscilloscope (Figure 5.21a). The output from the "Gate A"

terminal of the 585A oscilloscope consists of a 50V pulse which coincides in timing and duration with the running of the intensifying A timebase (Figure 5.21a,b). When this pulse is applied to the trigger input of the unit pulse generator, it raises the sine wave input to a level 50V above ground, so that the input does not cross zero for the duration of the pulse, and does not trigger the generator. Consequently for the duration of the intensified region rf pulses are omitted from the input sequence (Figure 5.21b,c,d), and the summation of echoes from the previous rf pulses can be seen (Figure 5.21e,f). By switching to the "A delayed by B" mode the intensified part of the trace can be seen on its own.

The repetition rate (prf) is then critically adjusted — one digit at a time — to maximise the amplitude of the pattern of superposed echoes. It was shown in Figure 4.1a how the superposition pattern is made up by summation of echoes of successive orders from the input pulses. At superposition the repetition period of the input pulses is related directly to the transit time of ultrasound in the sample (see Section 4.2).

In cases when the transit time of ultrasound in a sample is short (e.g. longitudinal waves in samples of $CaWO_4$ less than about 8 mm thick), setting the prf to give a repetition period equal to the transit time would cause the permitted duty cycle to be exceeded. In these cases the prf is adjusted to equal the inverse of an integer multiple ($p>1$) of the transit time. Superposition can then be observed by finding the maximum height of the echoes which

appear between the input pulses, but it is still helpful to follow the procedure of cutting out a number of input pulses as described above, so that a whole "train" of superposed echoes can be seen.

For the $CaWO_4$ measurements reported in Chapter 6, the superposition maxima could always be found unambiguously to 1 part in 10^4 and often to 1 part in 10^5; Figures 5.22a,b and c indicate the sensitivity of the method. Figure 5.22a shows the train of superposed echoes with the prf set to give maximum amplitude, while Figures 5.22b and c show the same train with the frequency changed by 1 part in 10^4 and 1 part in 10^2 respectively.

Such sensitivities were not easily attained. In the early stages of the work before the sample polishing methods had been developed, it was often found that maxima were less well defined, or that spurious maxima, equivalent to the "inhomogeneous responses" found in sampled CW measurements (Cottam and Saunders 1973), appeared on changing the temperature. A cause of particular difficulty for measurements on $CaWO_4$ was the need to measure velocities of impure modes in directions for which the energy flux was not parallel to the propagation vector. Many times as the temperature decreased, a maximum became ill-defined due to deterioration of the echo train. This would be observed first as a gradual deterioration of the pattern of overlapping echoes; these would get wider and less sharp. On switching back to a repetition rate of 1 kHz to observe the actual echo train it would be clear that more than one mode was being excited, or that sidewall reflections were occurring.

To measure the variation of transit times with temperature, these problems had to be avoided by careful positioning and alignment of transducers. Measurements were taken at small intervals (2 K) of temperature to avoid the possibility of swapping from the maximum corresponding to the correct in-phase condition (n=0) to an adjacent (n=±1) maximum. For each measurement care was taken to sweep the pulse repetition frequency above and below the expected value; this was found helpful in avoiding the spurious maxima mentioned above.

5.3.3 Transducers and bonds

(a) Transducers

Quartz piezoelectric transducers have been used to generate and detect ultrasound in the specimens of $CaWO_4$ and other scheelites. Quartz crystal plate transducers have some valuable advantages over evaporated film transducers; plate transducers can be moved to different places on a sample face and the polarisation direction can be rotated as required, whereas evaporated film transducers cannot be moved without being destroyed and take several hours to fabricate. The present work has necessarily involved propagation of impure modes of unknown polarisation and energy flux direction. Many adjustments of transducer position (and of the polarisation direction of shear transducers) have had to be made to excite the modes separately and to ensure that the energy flux deviation was accommodated.

Since the polarisations of the modes were not initially known standard "X-cut" and "Y-cut" transducers were used. These transducers are cut as discs with faces normal to the X and Y axes respectively. An alternating electric field parallel to the axis produces vibration in the direction parallel to the X-axis in the first case (longitudinal transducer) and normal to the Y-axis in the second case (shear transducer). The shear transducers used were marked with a flat parallel to the vibration direction. The resonant frequency of a transducer is determined by its thickness and the appropriate velocity of sound in the quartz; for megahertz operation, transducers need to be thin and are fragile.

Two sizes of transducer (1cm or 6mm in diameter) were used. They had coaxial gold plating as shown in Figure 5.23. This form of plating allows contact to be made to both electrodes from one side, and gives an active area approximately equal to that of the centre electrode. In the course of this work transducers with resonant frequencies 15 MHz, 18 MHz (Brooke's Crystal Co. Ltd.), 20 MHz and 50 MHz (Roditi Corporation) have been employed.

(b) Bonds

Crystal plate transducers must be attached to the specimens under test by use of a suitable bonding agent. The bond formed must be thin, parallel and must provide good acoustic coupling for longitudinal and shear waves. Many different bonding agents are in use. Permanent bonds can be obtained by applying pressure to a Au-In-Au

sandwich (Sittig and Cook 1968), or by use of epoxy resin; solid bonds can be obtained by use of low melting point organic solids including salol, phenyl benzoate, benzoic acid (see Pace (1970) for details); or liquid bonds may be made by use of viscoelastic liquids, oils and greases (e.g. Dow Resin 276-V9, silicone oil 250,000 c.s., Nonaq stopcock grease). The specific mechanical impedances of some of these bonding materials are given in Table 5.1. Here the most suitable bonding materials have been found to be Dow resin 276-V9 (Dow Chemical Co., U.K. agents: R.W. Greef Co. Ltd.) and Nonaq stopcock grease (Fisher Scientific Co., U.K. agents:Kodak Ltd., Research Chemical Sales).

Dow resin is very useful at room temperature; it is a highly viscous liquid which will form satisfactory bonds with almost any solid. To form a bond a little resin is spread over the face of a sample with a razor blade to give a uniform thin layer, and the transducer is pressed into position with light pressure. The extremely viscous nature of the resin permits the transducer to be moved about the face of the sample as required (an important advantage of liquid bonds over solid ones). On cooling below ice temperature Dow resin freezes, the bond crumbles and fails.

Nonaq stopcock grease is less viscous. Bonds are formed by placing a blob of grease on the sample face, putting the transducer in position on top of the grease and then moving it with a circular motion to expel excess bonding material. The circular movement is continued

until a sudden increase in the resistance to motion indicates that a good bond has been formed. Excess Nonaq is removed by cleaning with cotton wool. The quality of a Nonaq bond will usually improve on cooling to about ice temperature, a 'cleaning-up' of the echo pattern usually occurs. Below $0^{o}C$ and down to 1.2 K, Nonaq bonds have been found to be quite satisfactory and were employed for the studies of the temperature dependence of ultrasound velocities and attenuation in $CaWO_4$ (Chapter 6). The technique for making Nonaq bonds has been found to give reproducible transit-time results. It can therefore be assumed that each bond made on $CaWO_4$ has about the same thickness. An estimate of this thickness was obtained by bonding a transducer to a very thin slice of $CaWO_4$ which had been polished in the same way as the ultrasonics samples. From the rear of the slice a microscope was focussed first on the back of the transducer and then on the adjacent face of the $CaWO_4$; the bond thickness was estimated to be 3±2 μm.

To provide good earthing contact to the back face of the transducers via their outer coaxial electrodes the specimen faces were heavily painted with high conductivity paint (Dag 915, Acheson Colloids Ltd.).

5.3.4 System for control and measurement of sample temperature

The system used in this work allowed measurements of ultrasound velocity and attenuation to be made at either stable or slowly changing temperatures in the range

1.2 K to 300 K. In this section the cryostat assembly, the sample holder and the methods of temperature control and measurement are each described.

(a) The cryostat assembly

A conventional glass dewar system employing liquid helium and liquid nitrogen refrigerants has been used (see Figure 5.24). The system has an inner dewar which is supported by a spring harness, and vacuum sealed to the cryostat by a rubber sleeve. With the sample holder in position the inner space can be evacuated by a rotary pump, or the vapour pressure of a refrigerant liquid reduced to produce cooling. The pressure in the inner space is then monitored by a Pirani gauge (Edwards Type M6A head), and mercury and oil manostats. Careful alignment of the non-silvered strips down the inner and outer dewars makes it possible to see the level of the refrigerant liquid in the inner space. An outlet from the cryostat head can be used for connection to the helium collection system. A mercury protection valve is included to ensure the release of any excess pressure which could develop in the inner dewar. Before cooling is begun, the jacket around the inner dewar (known as the "interspace") must first be evacuated to 0.05 torr and sealed off by a ground glass tap.

(b) Sample holder

A sample holder (Figure 5.25) has been designed and built such that over the temperature range 1.5 K to 300 K it allows the specimen to be rigidly located, provides electrical contact to the two electrodes of a quartz

piezoelectric transducer bonded to the specimen (see Section 5.3.3), but avoids any excess pressure on the quartz. The sample is located between a sprung platform and a brass disc — the brass disc making an earthing contact to the outer ring electrode of the transducer via silver dag paint on the sample face. Inside the brass disc, a PTFE bush (recessed slightly to avoid pressure on the transducer) locates a sprung brass plunger which sits lightly on the centre transducer electrode. This assembly (screwed to a brass cylinder of large thermal capacity) is suspended from the sample holder head by copper-nickel tubes so that it is held near the bottom of the inner dewar. A coaxial line carries the radio-frequency signals through the centre tube to the sprung transducer contact. A small resistance heater (200Ω non-inductively wound constantan) fits closely around the sample and is held in position by three nylon grub screws. Current supply leads for the heater pass through the sample holder head via a Stupakoff seal.

(c) Thermometry

Copper-constantan and gold (+0.01% iron)-chromel thermocouples with reference junctions in dewars of liquid nitrogen and liquid helium respectively are used for the measurement of temperatures in the range 4.2 K to 300 K. Both types are made by spark welding in a nitrogen atmosphere. To avoid spurious thermal voltages, joinings other than the sample and reference junctions have been avoided. At the sample holder head a neoprene

vacuum seal is used. In such a seal (Fig. 5.26) the thermocouple leads are trapped between a ring and a disc of neoprene, each lightly coated with vacuum grease and held in place by a brass plate and three screws. A low temperature varnish (G.E.7031) has been found useful for anchoring thermocouples to the sample; it effects good thermal contact and prevents shorting to the sample holder. Elsewhere the thermocouple leads are insulated with PTFE protective sleeving.

It is necessary to calibrate the thermocouples before each temperature run. A cubic approximation, recommended by White (1959), with the form

$$E = AT + BT^2 + CT^3 + D \qquad (5.4)$$

has been assumed for the variation of thermocouple voltage (E) with temperature (T). The procedure requires the determination of thermocouple voltages corresponding to three calibration temperatures and the measurement of the residual voltage (D) with both junctions at the reference temperature. Calibration points must be reasonably well distributed over the temperature range for which the thermocouples are employed. For the copper-constantan thermocouples, the boiling point of liquid helium at the prevailing atmospheric pressure, the triple point of liquid nitrogen (63.15 K) and the appropriate melting point of pure ice are suitable. For the gold (+0.01% iron) - chromel thermocouple (normally only used below 77 K) suitable calibration points are the temperature of liquid helium at a known reduced pressure, the triple point of liquid nitrogen and the boiling point of liquid nitrogen

at atmospheric pressure.

For the measurement of temperatures below 4.2 K vapour pressure thermometry is employed. A mercury manostat is satisfactory for measuring pressures down to 10 torr, below which a silicone oil (density equal to 1/12.44 that of mercury) manostat is to be preferred.

(d) Temperature control

Sample temperatures down to 77 K can be obtained by filling the outer dewar with liquid nitrogen. The sample is then separated from the refrigerant liquid by both the inner space and the evacuated interspace of the inner dewar. By adjustment of the pressure of helium or nitrogen gas in the inner space the cooling rate of the sample can be varied. Steady cooling rates of ∿40 deg K per hour down to 77 K can be achieved in this manner.

By transfer of liquid helium to the inner dewar a sample temperature of 4.2 K is attained. Pumping on the liquid helium can be used to produce lower sample temperatures. Careful control of the vapour pressure above the liquid helium by use of a Cartesian manostat gives stable temperatures in the range 1.2 K to 4.2 K.

After evaporation of the liquid helium the sample temperature rises slowly back to 77 K at a rate which averages 25 deg K per hour, but which can be retarded by evacuation of the inner dewar. Slower warming rates can be maintained by surrounding the sample with activated charcoal (which gradually evolves cold adsorbed helium gas). By these methods slowly changing temperatures between 1.2 K and 300 K were readily achieved for measurements of velocity and attenuation in $CaWO_4$ samples.

Stable temperatures between the above limits can be obtained with the present system by use of an Oxford Instruments Harwell temperature controller. This controller is designed for cryogenic operations where a sample to be studied is attached to the liquid coolant container via a suitable thermal resistance. The controller is a source of current for the resistance heater which is fixed round the sample(Figure 5.25). The amount of power supplied to the heater is determined by an error voltage which is the difference in microvolts between the output of a sensing thermocouple attached to the sample and the control voltage set on a helipot dial. This dial reads directly in microvolts so that with the aid of a thermocouple calibration chart a particular temperature (which must be greater than that of the liquid coolant heat sink) can be "dialled" and the controller then supplies the heat required to maintain the sample at the chosen temperature within ±0.05 K. For operation between room temperature and 77 K, liquid nitrogen in the outer dewar provides the heat sink and the evacuated interspace a suitable thermal resistance; steady temperatures can be readily obtained. Below 77 K, liquid helium in the inner dewar is used as the heat sink and the sample must be enclosed in an evacuated can to provide the necessary thermal resistance.

TABLE 5.1

Mechanical properties of bonds and transducers

	Longitudinal	Shear	Ref.
Nonaq stopcock grease 25°C, 20MHz	$Z_L=2.7\times10^5$	-	[1]
Dow resin 276-V9	$Z_L=2.25\times10^5$	$Z_S=0.9\times10^5$	[1]
	$v_L=2.4\times10^5$	$v_S=1.1\times10^5$	[2]
Silicone oil DC703	$Z_L=1.37\times10^5$	-	[3]
Silicone oil DC200	$Z_L=1.20\times10^5$	-	[3]
Quartz	$Z_L=15.3\times10^5$	$Z_S=10.4\times10^5$	[1]

Z_L, Z_S specific acoustic impedances in mechanical ohms cm^{-2}

v_L, v_S sound velocities in cm s^{-1}

[1] McSkimin and Andreatch (1962)

[2] McSkimin (1950)

[3] McSkimin (1957)

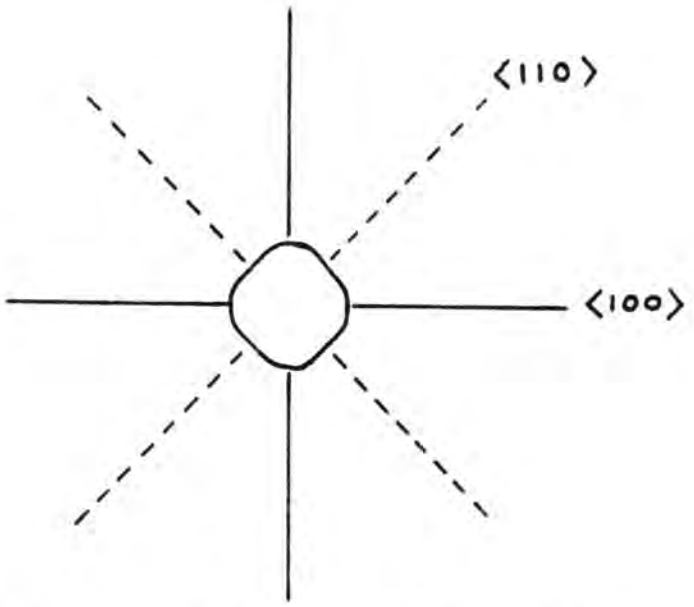

FIGURE 5.1: Cross-section of c-axis grown boule of $CaWO_4$ (after Nassau and Broyer 1962).

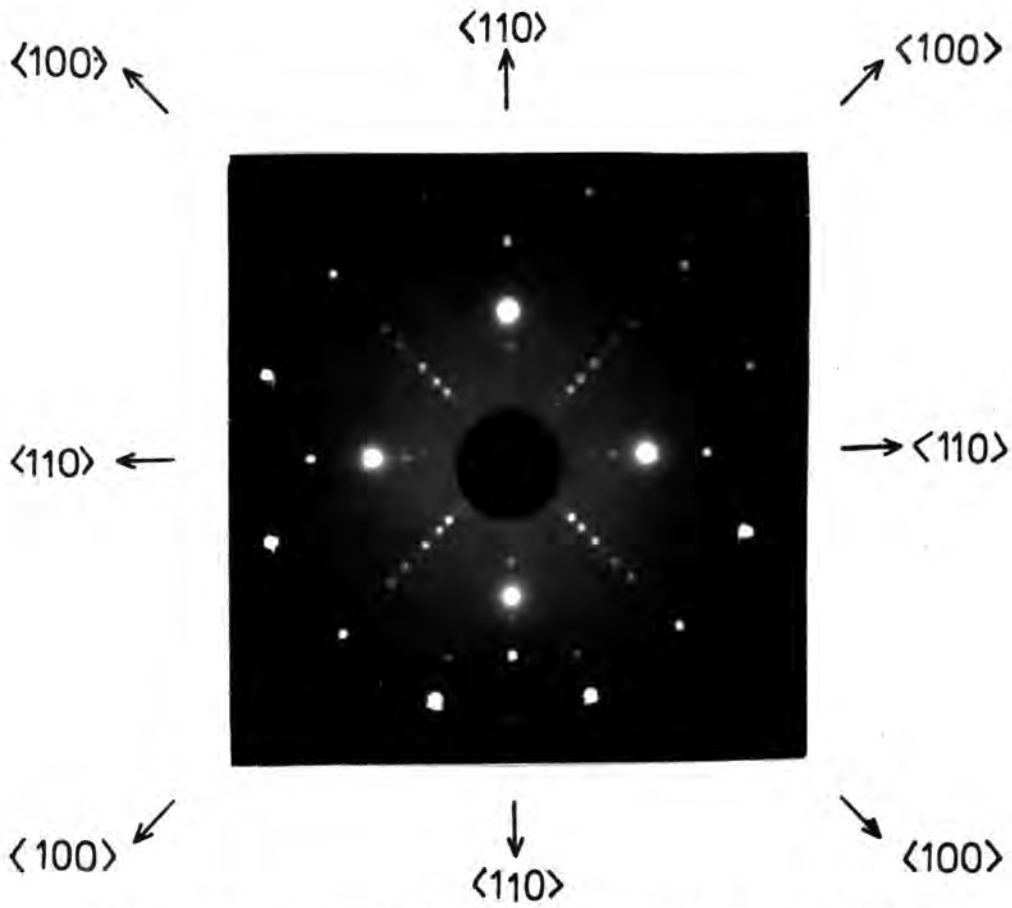

FIGURE 5.2: Laue back reflection photograph taken with X-ray beam incident in Z direction. The photograph shows fourfold symmetry, and pseudo-mirror symmetry about planes normal to the <100> and <110> directions.

FIG 5.3

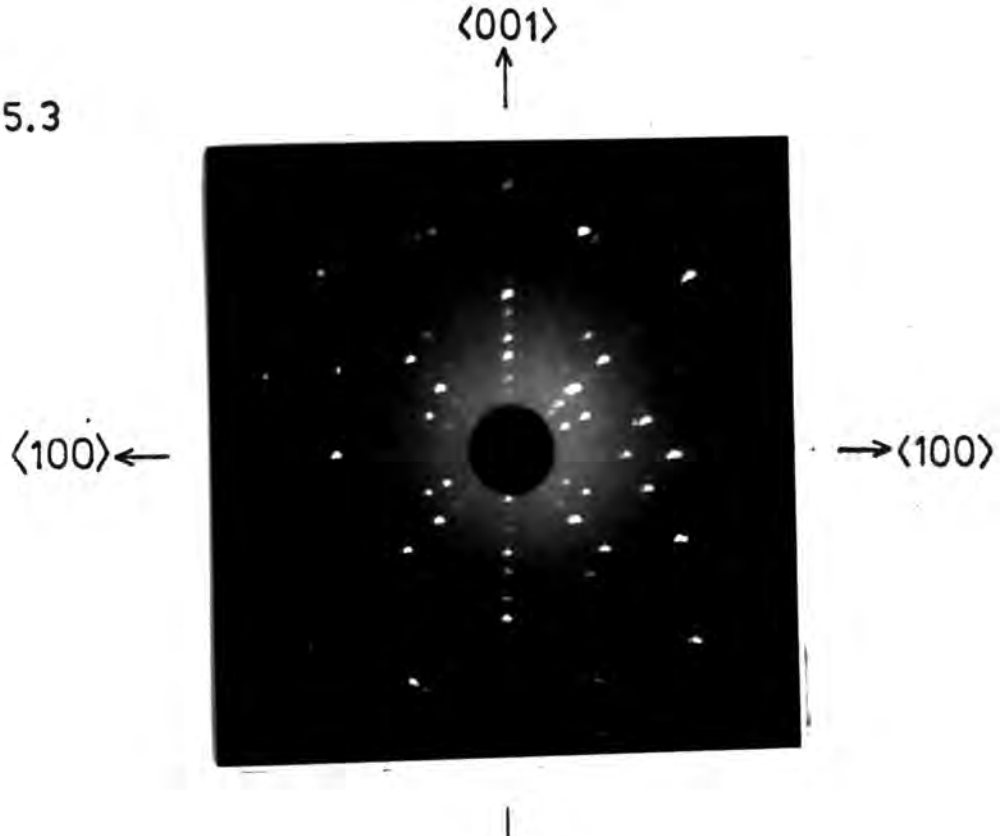

FIG 5.4

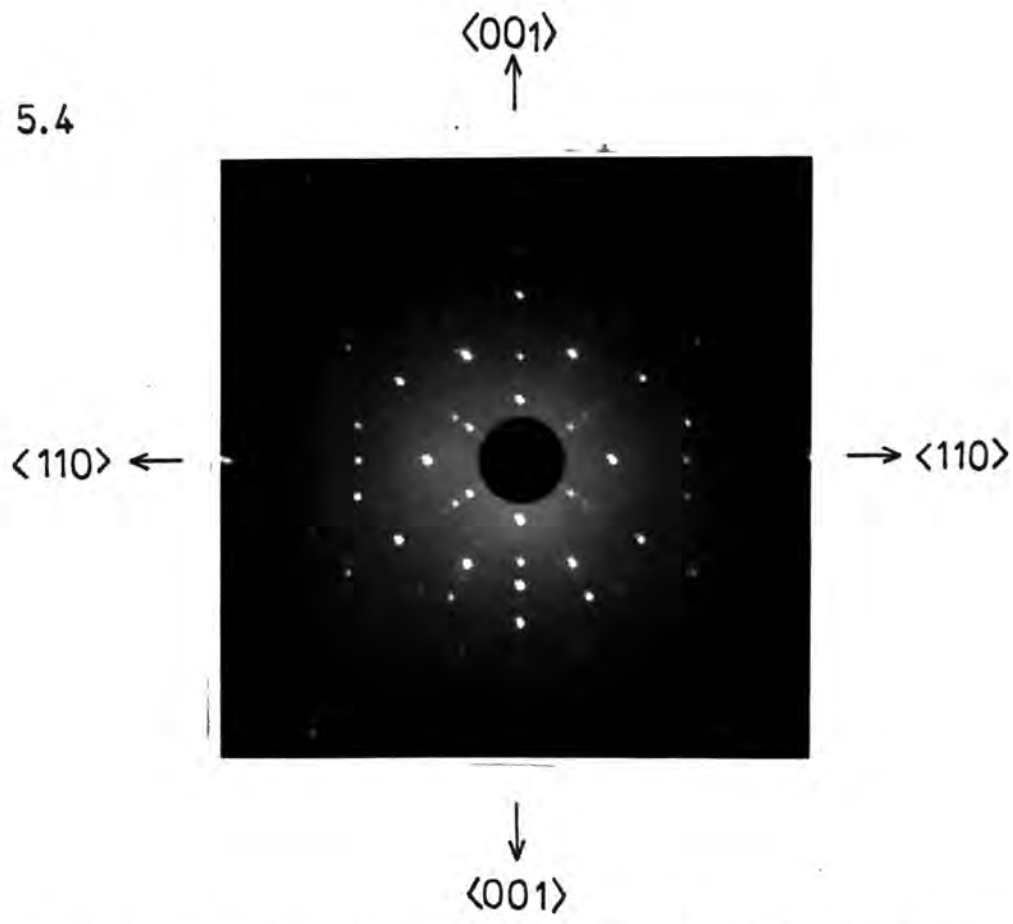

FIGURES 5.3, 5.4: Back reflection x-ray photographs of $CaWO_4$ taken with incident beam parallel to the <100> and <110> directions respectively. Horizontal is the mirror plane of the 4/m point group. Vertical are pseudo-mirror planes.

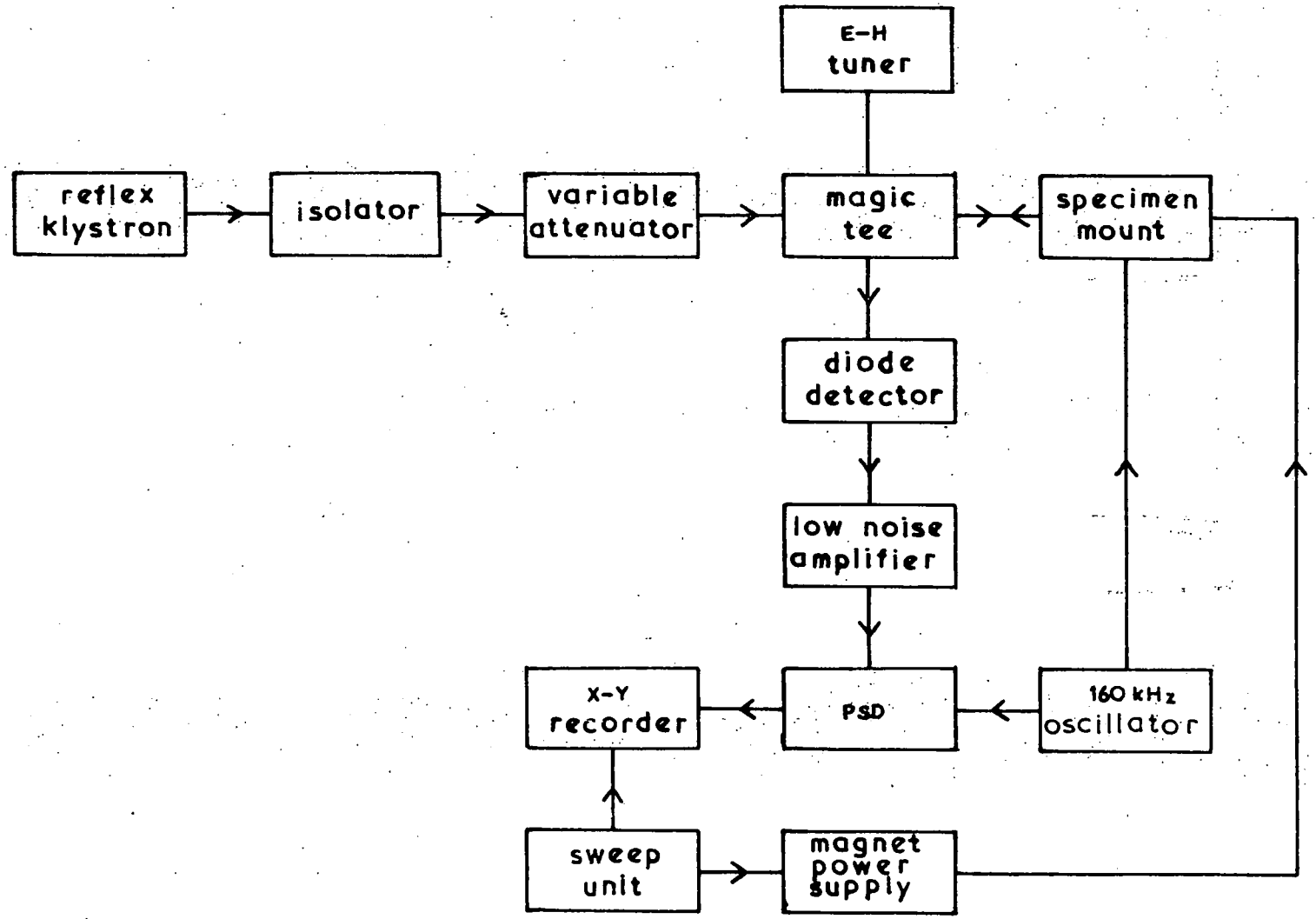

FIGURE 5.5: Block diagram of the Q-band spectrometer.

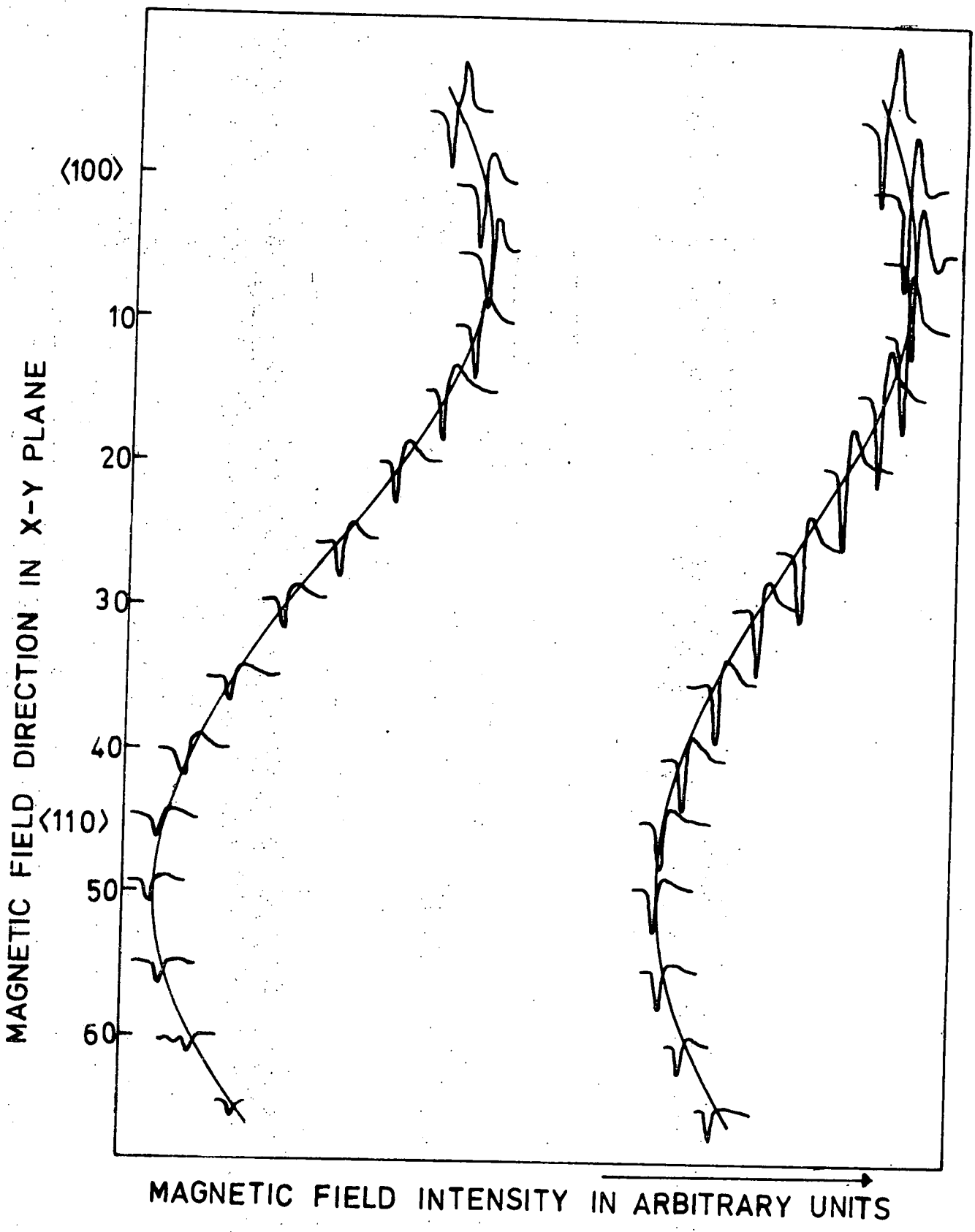

FIGURE 5.6: Location of the extremes of the room temperature Gd^{3+}:$CaWO_4$ resonance spectrum.

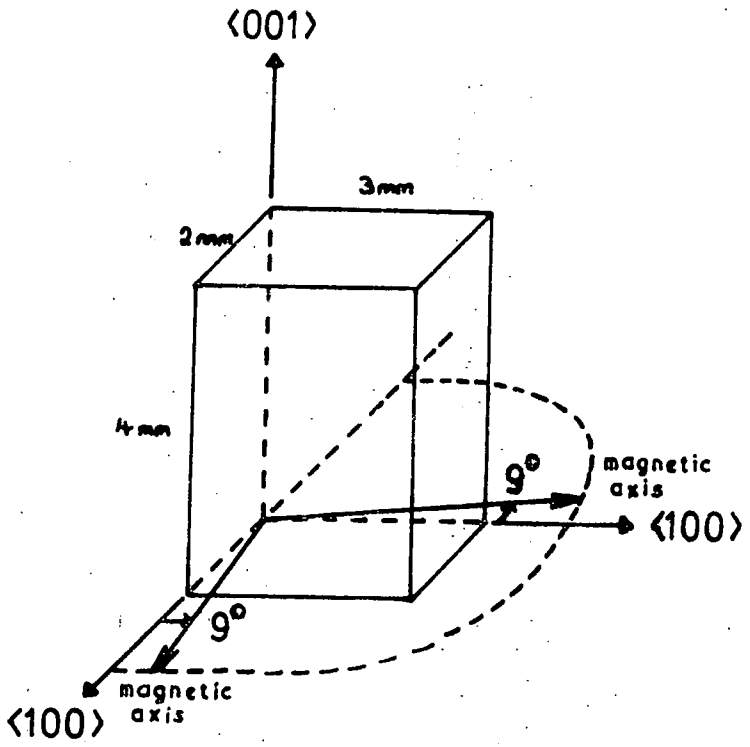

Figure 5.7: Positions of magnetic axes found in the Gd^{3+} doped $CaWO_4$ sample.

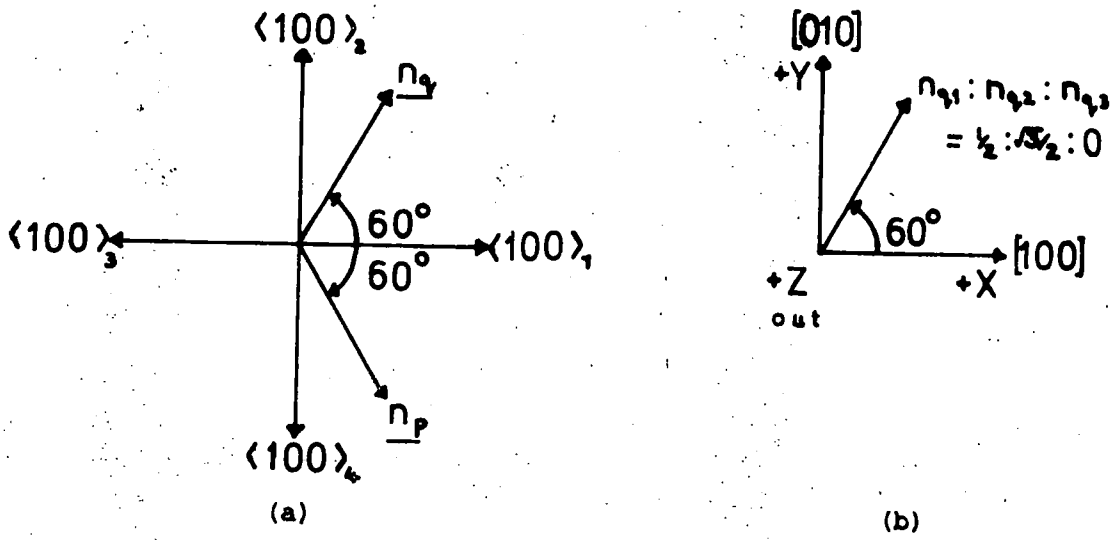

Figure 5.8: Determination of propagation directions in pure $CaWO_4$ samples p and q.

FIGURE 5.9: Etch pits on $CaWO_4$, {100}face, aqua-regia etch

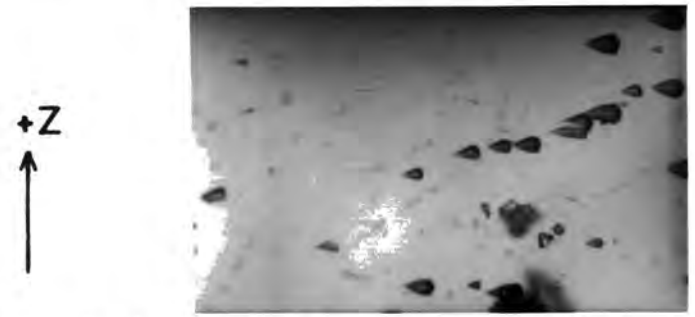

FIGURE 5.10: Etch pits on $CaWO_4$,{100} face, NH_4Cl etch

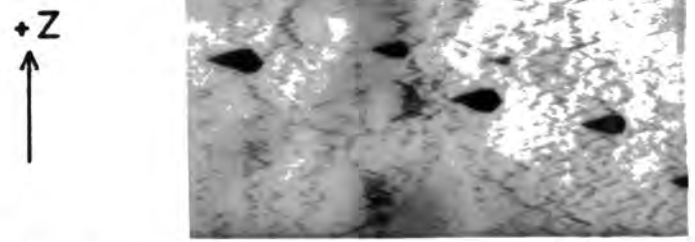

FIGURE 5.11: Etch pits on $CaWO_4$,{100} face, "terracing" background obtained with aqua-regia etch.

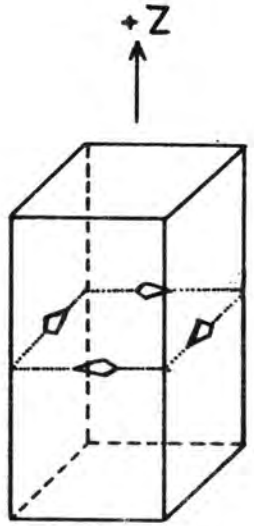

FIGURE 5.12: The orientation of the pits is the same on each {100} type face: the 'tails' of the pits point anticlockwise around the fourfold axis when viewed in the +Z direction.

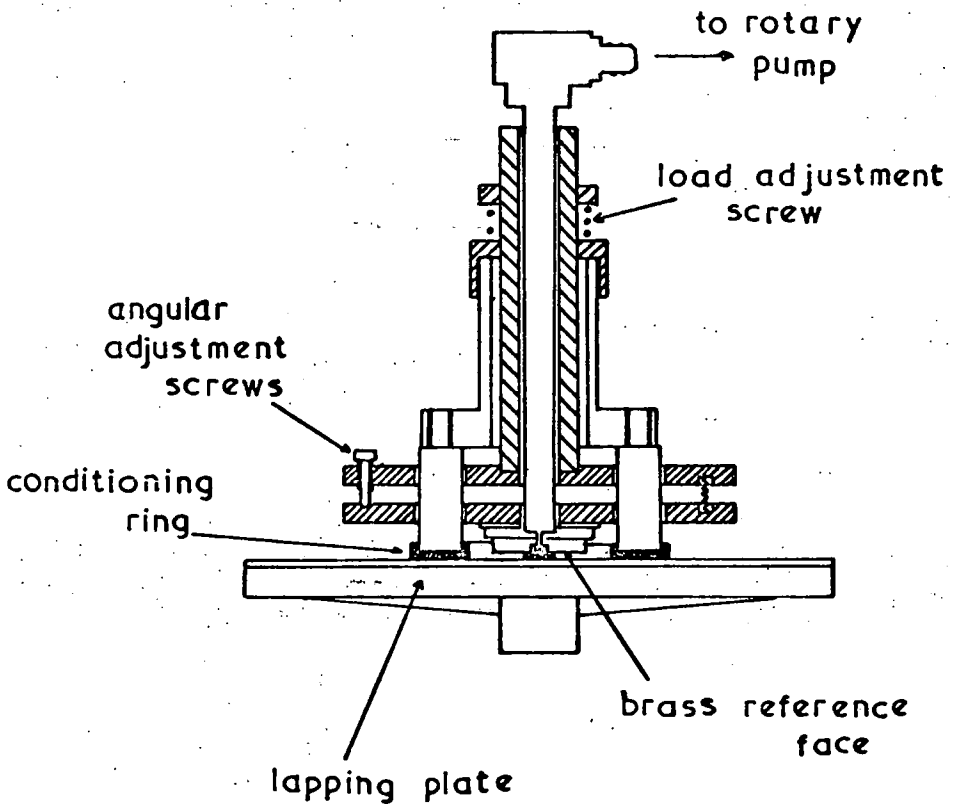

FIGURE 5.13: Vertical plane cross-section of the Logitech pp5 Precision Polishing jig with vacuum chuck.

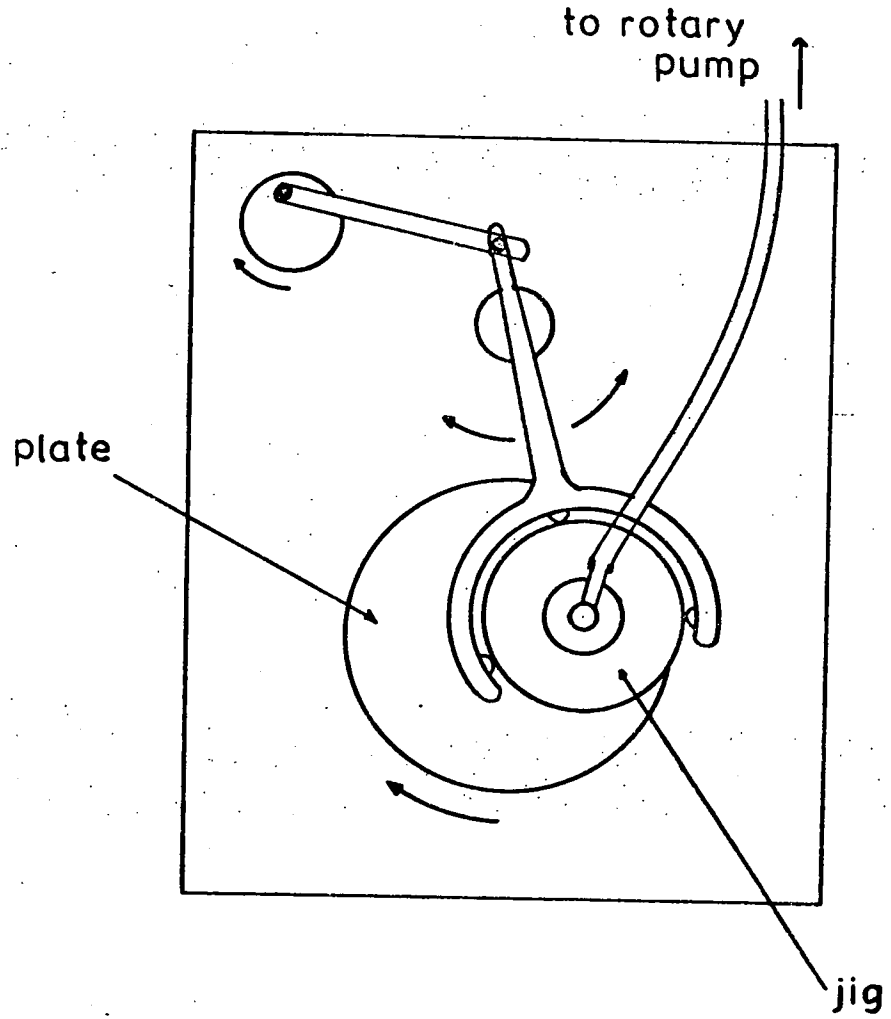

FIGURE 5.14: Plan view of the Logitech PM2 polishing machine.

FIGURE 5.15

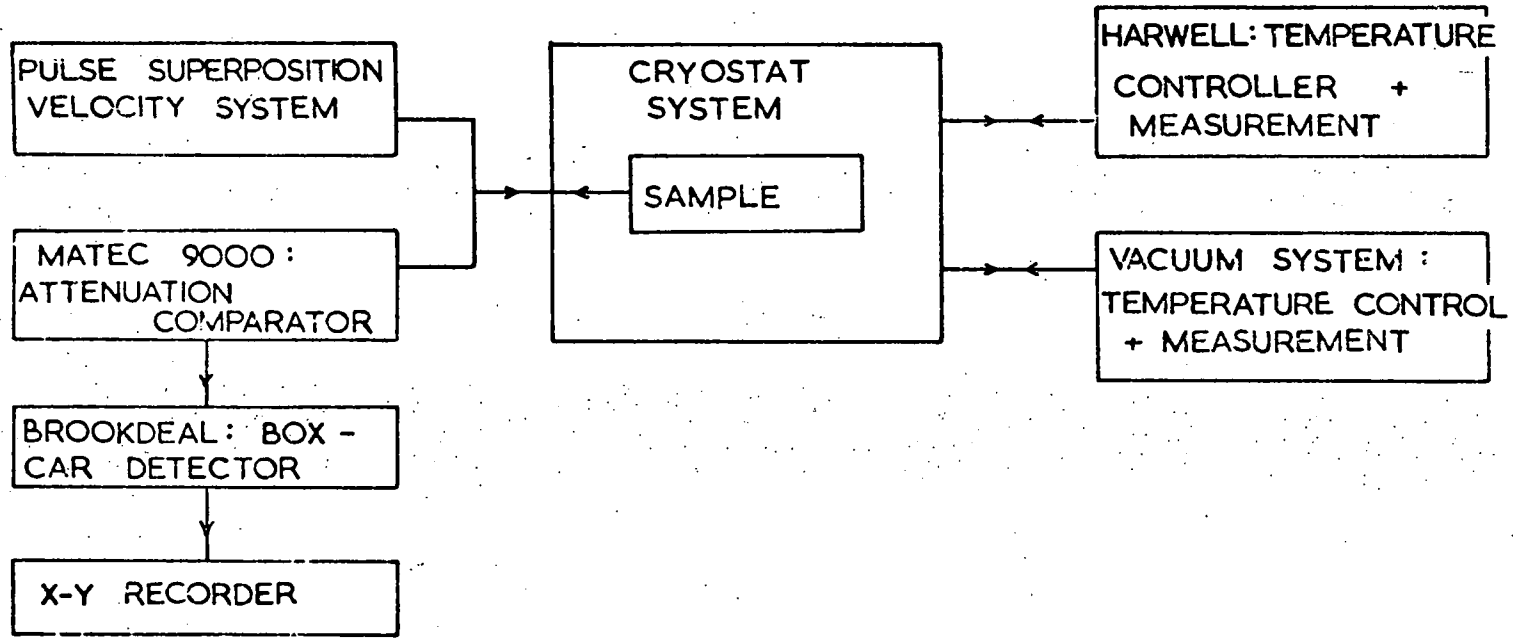

SYSTEM FOR MEASUREMENT OF VELOCITY AND ATTENUATION AS A FUNCTION OF TEMPERATURE FROM $1^{\circ}K - 300^{\circ}K$

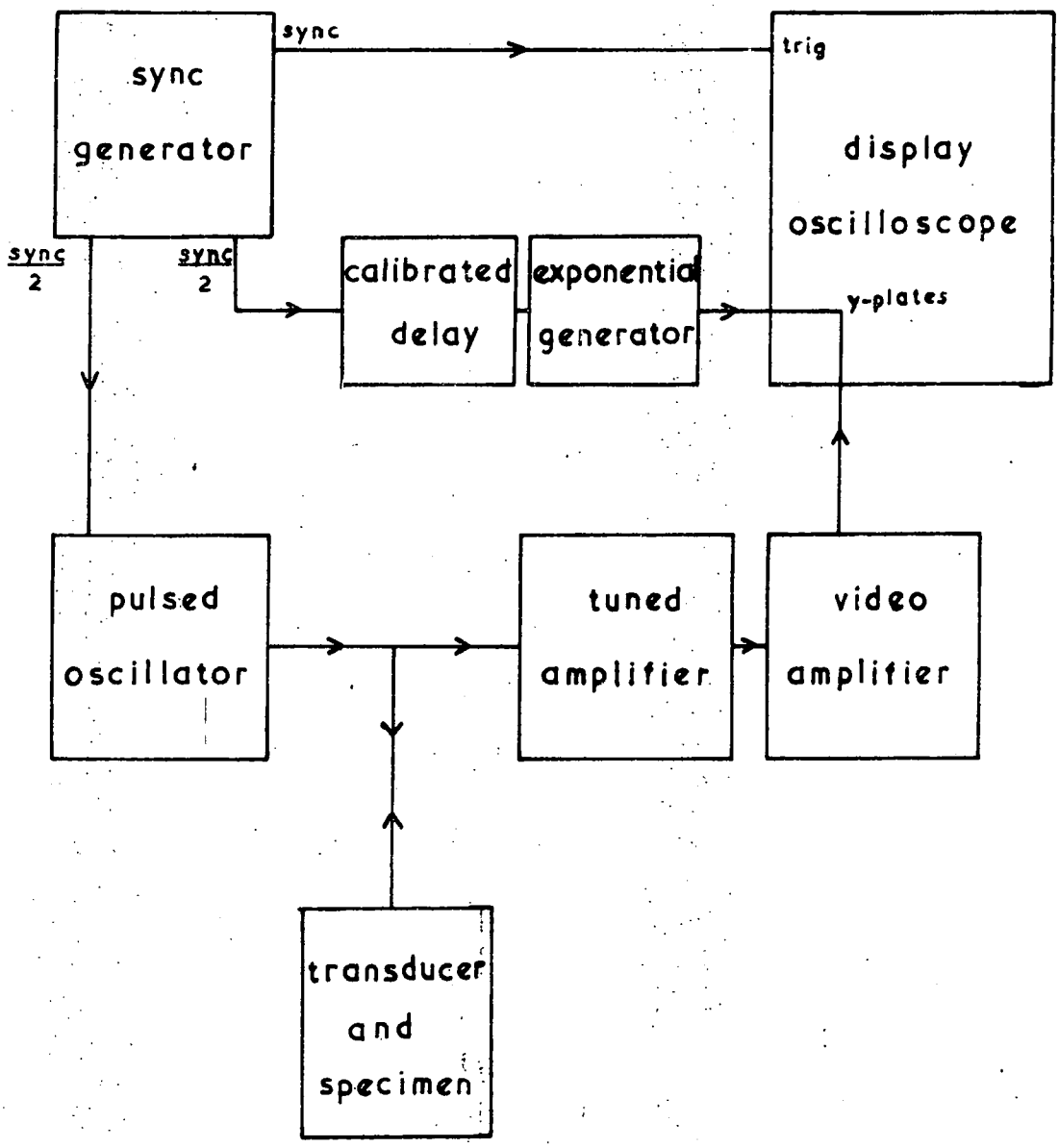

FIGURE 5.16: Block diagram of the Matec Inc Model 9000 Attenuation Comparator used for simple single ended pulse echo experiments.

FIGURE 5.17

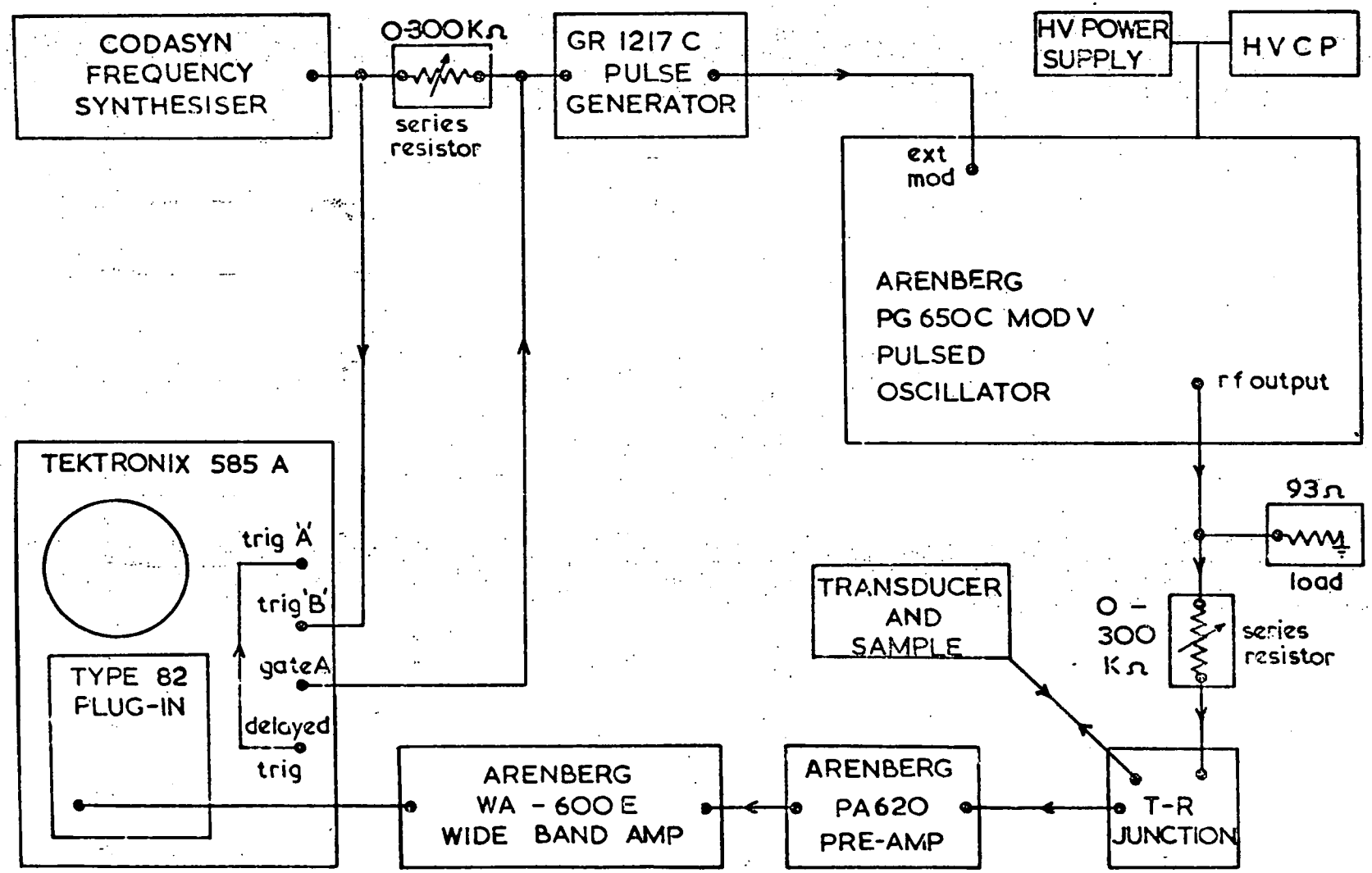

BLOCK DIAGRAM OF PULSE SUPERPOSITION EQUIPMENT

FIGURE 5.18

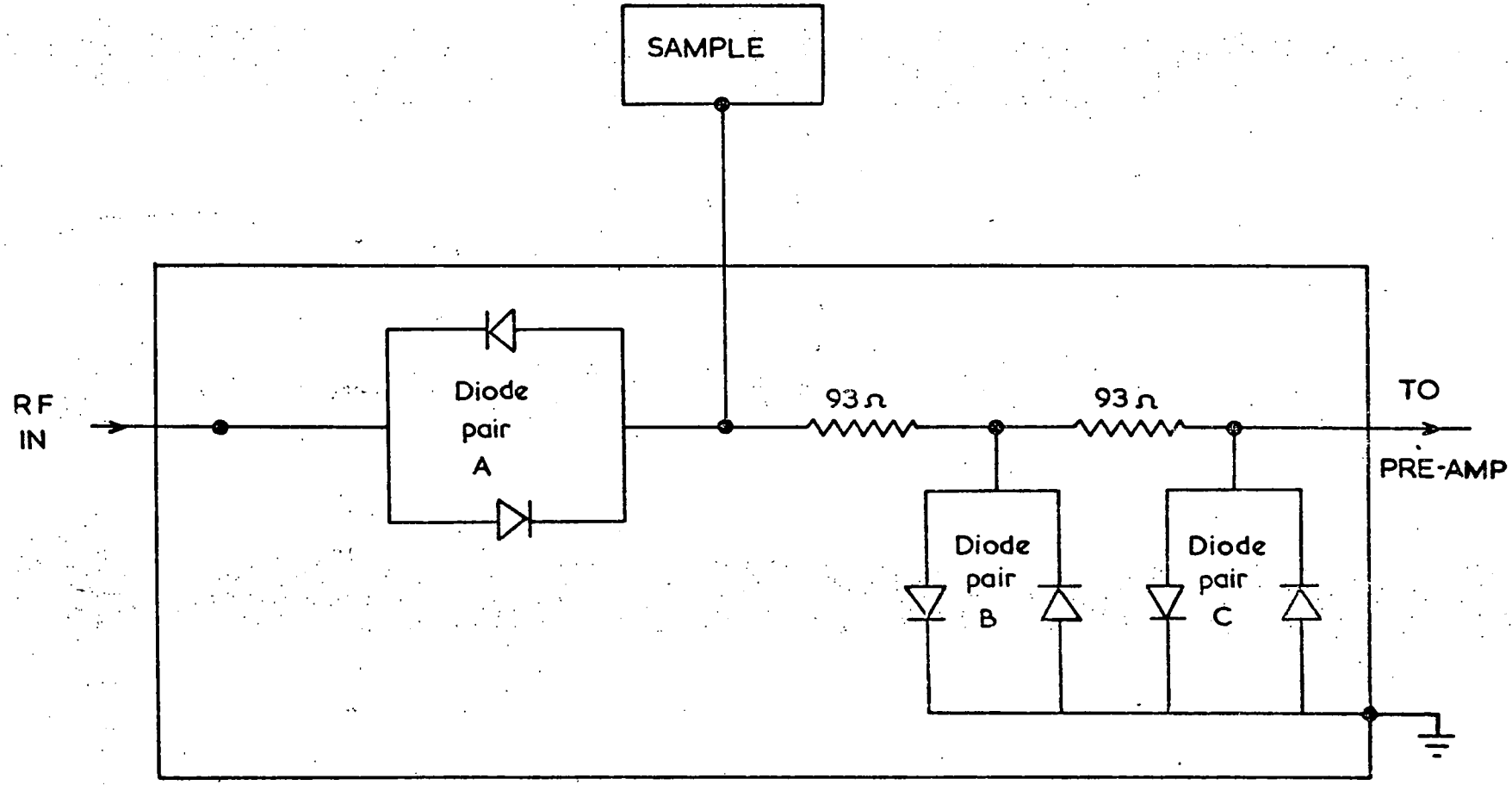

CIRCUIT OF T-R JUNCTION USED IN THE PULSE SUPERPOSITION EQUIPMENT

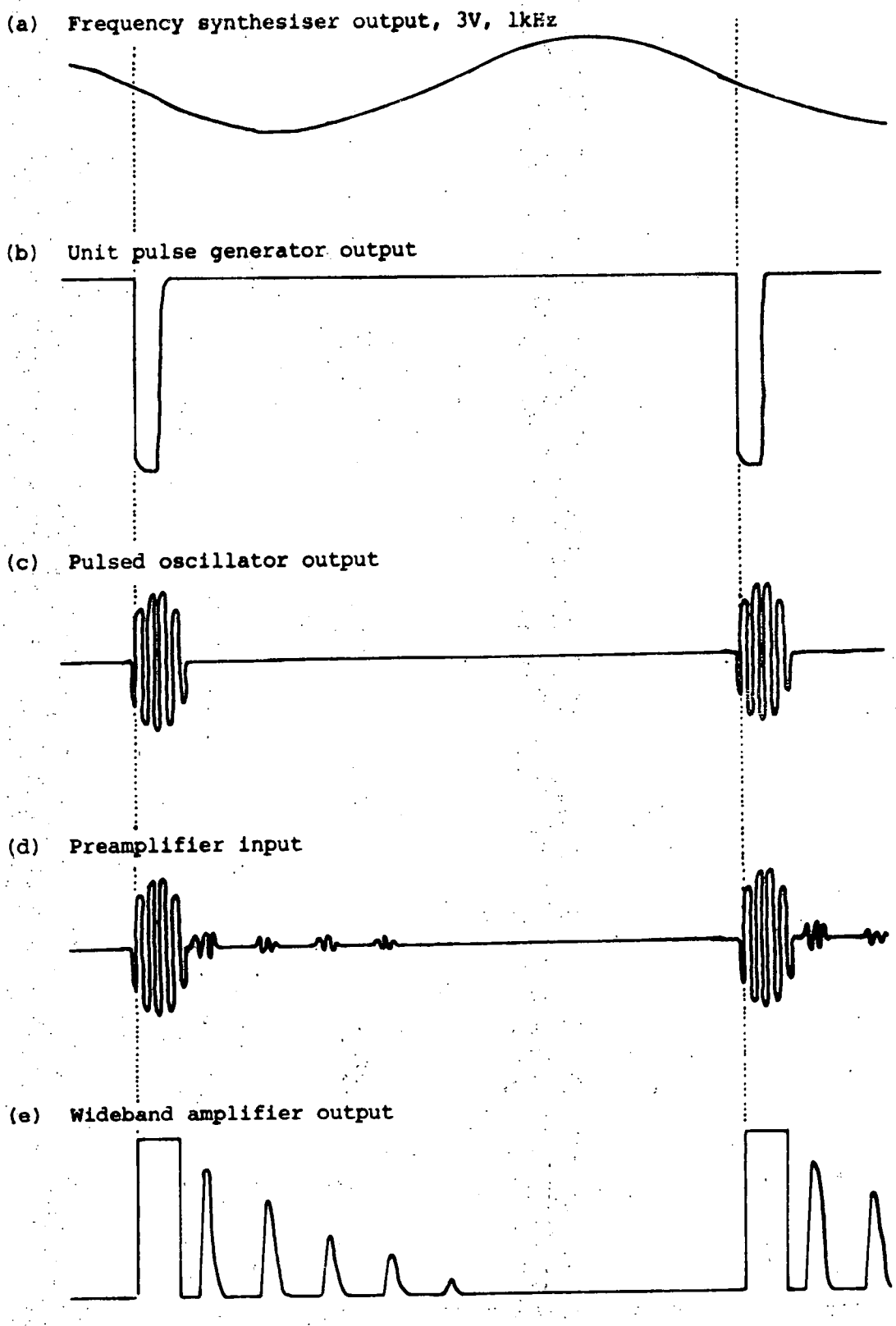

FIGURE 5.19: Pulse superposition; initial setting up with a low repetition rate.

(a) Frequency synthesiser output

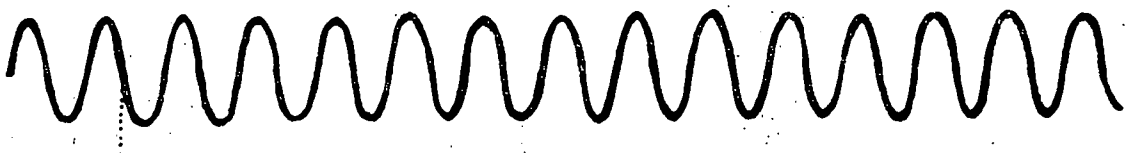

(b) GR1217 output

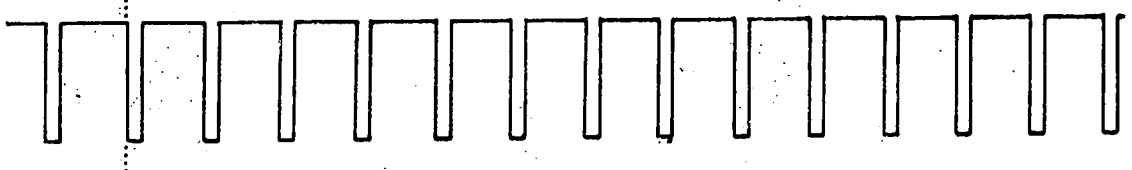

(c) RF pulsed oscillator output

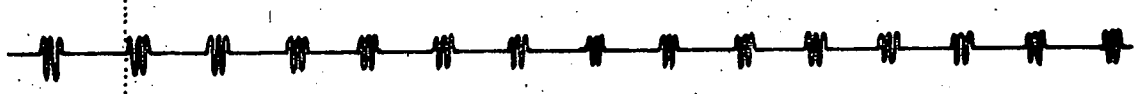

(d) Wideband amplifier output observed on B time-base of Tektronic 585A osilloscope

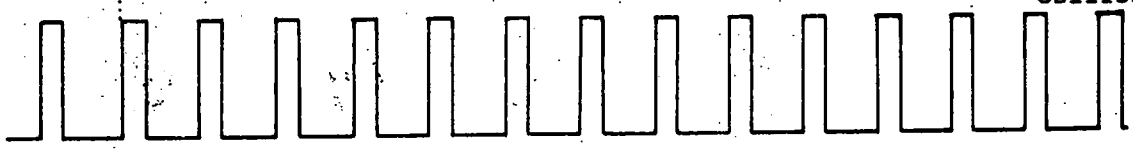

FIGURE 5.20: Pulse superposition : operation with pulse repetition rate approximately equal to reciprocal of transit time.

(a) Wideband amplifier output with 'B intensified by A' display to select pulses to be omitted.

(b) Gate 'A' output of Tektronic oscilloscope

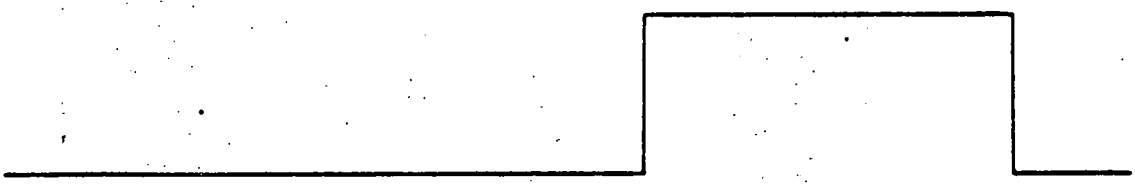

(c) Gate 'A' pulse applied to external trigger terminal of GR1217 pulse generator

(d) Selected RF pulses omitted from pulsed oscillator output

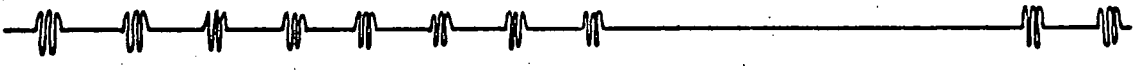

(e) Wideband amplifier output with pulse repetition period approximately equal to the transit time

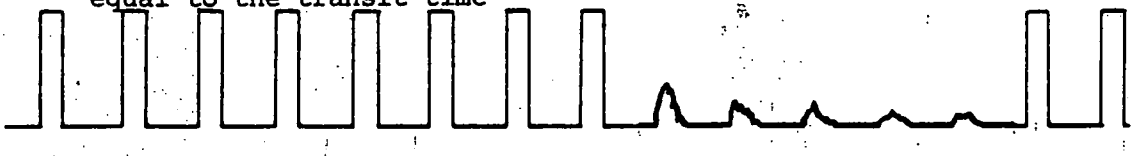

(f) Pulse superposition with pulse repetition period critically adjusted to equal transit time

FIGURE 5.21: Pulse superposition : omission of RF pulses from input train to allow observation of maximum.

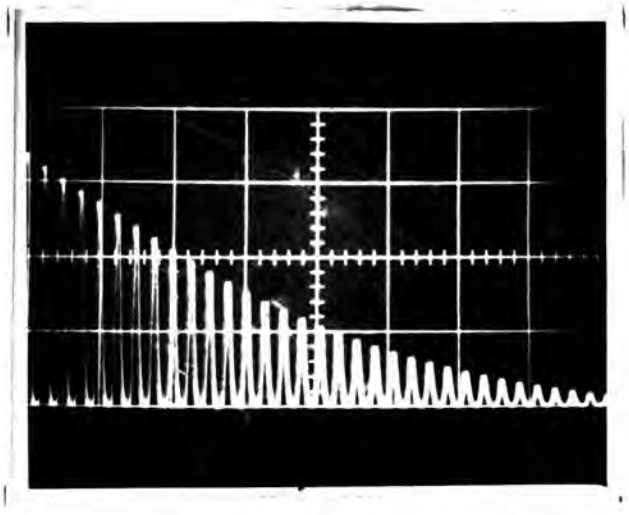

(a) prf set to give maximum amplitude of superposed echoes

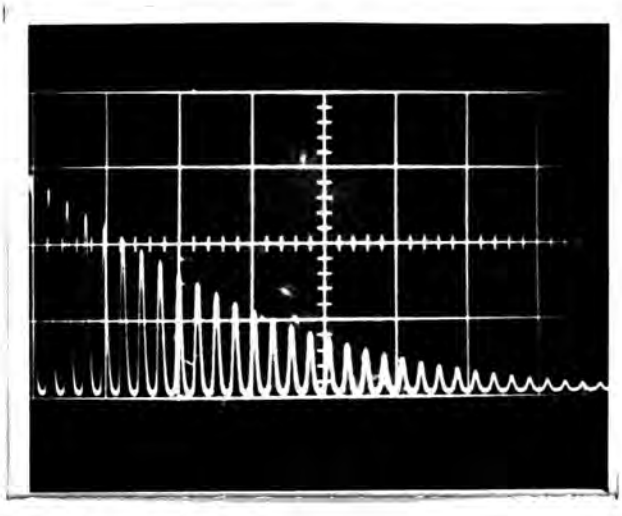

(b) prf changed by 1 part in 10^4

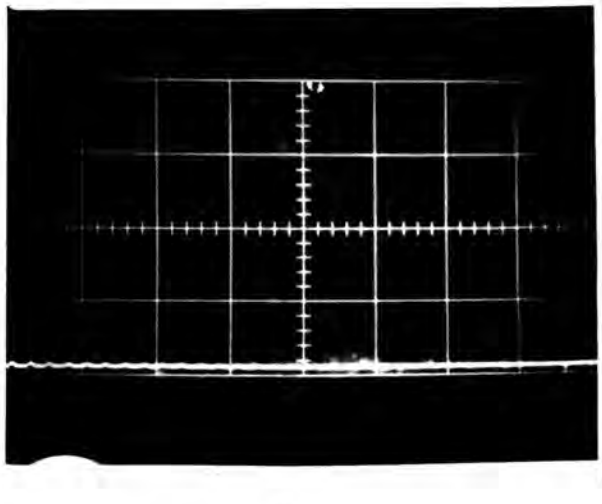

(c) prf changed by 1 part in 10^2

FIGURE 22: To show the sensitivity of the pulse superposition method.

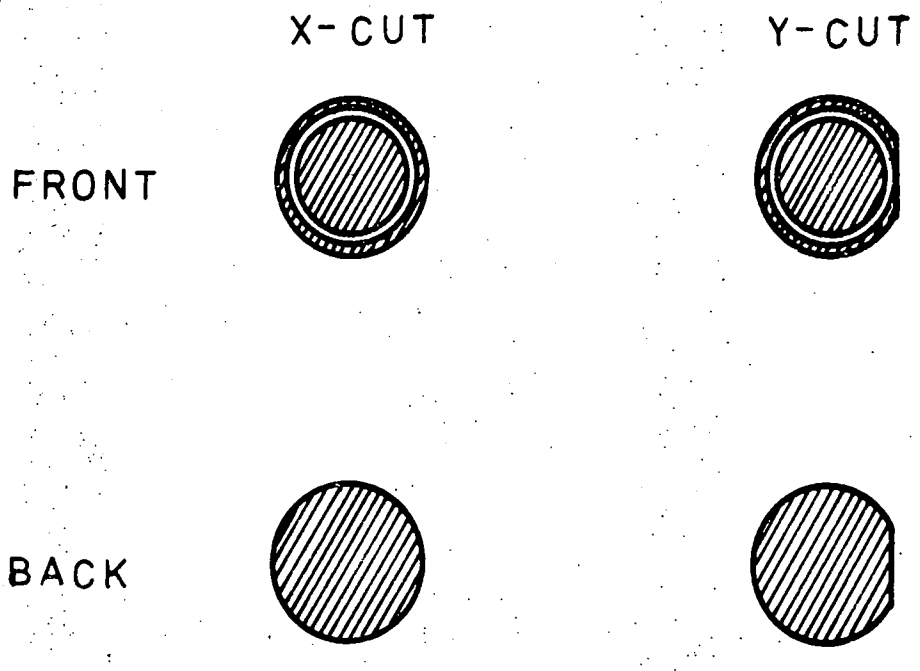

FIGURE 5.23: Quartz crystal transducers showing the coaxial gold plating.

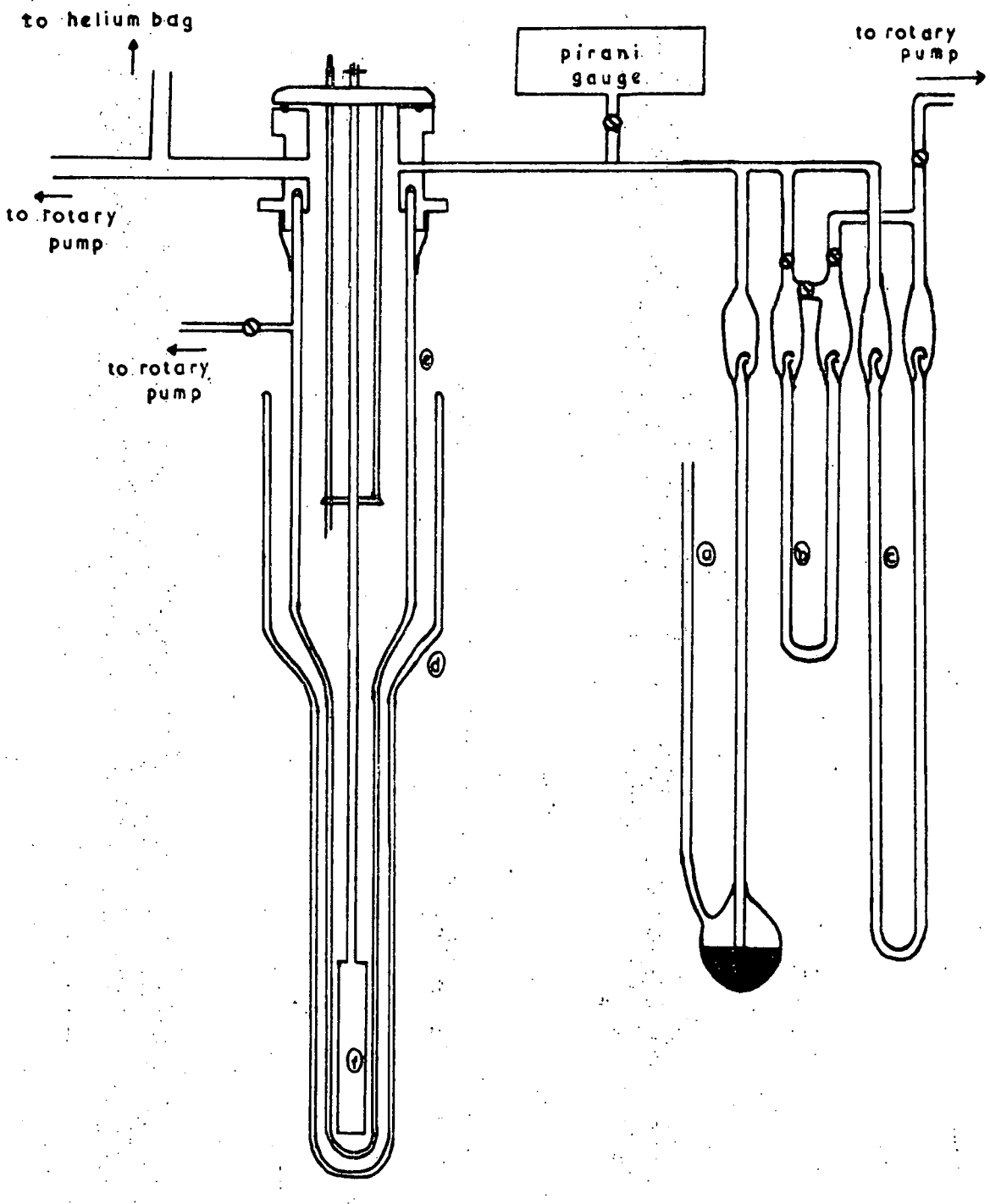

FIGURE 5.24: Cryostat system, showing (a) the mercury protection valve, (b) the oil manometer, (c) the mercury manometer, (d) the outer dewar, (e) the inner dewar, (f) the sample holder.

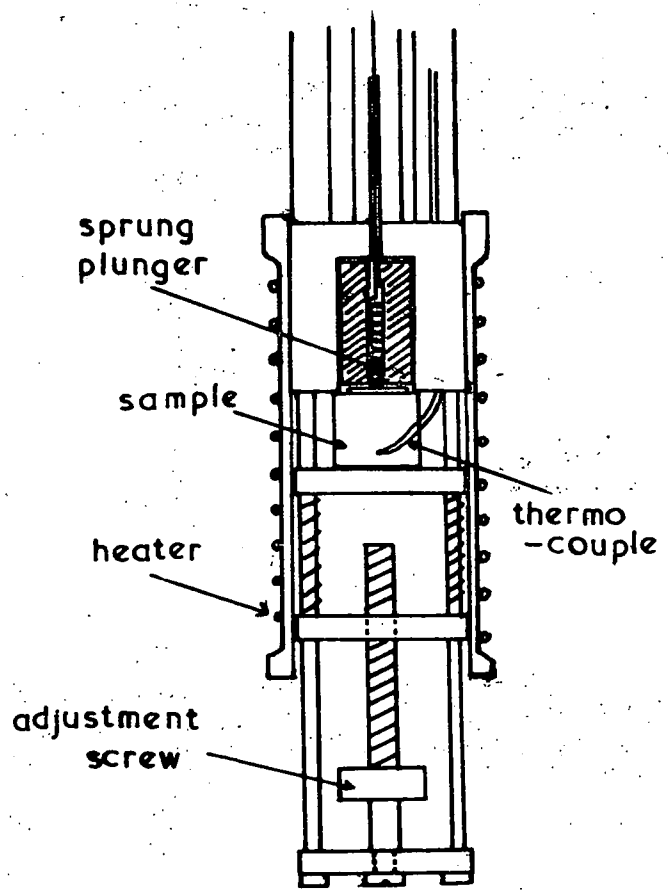

FIGURE 5.25: Sample holder

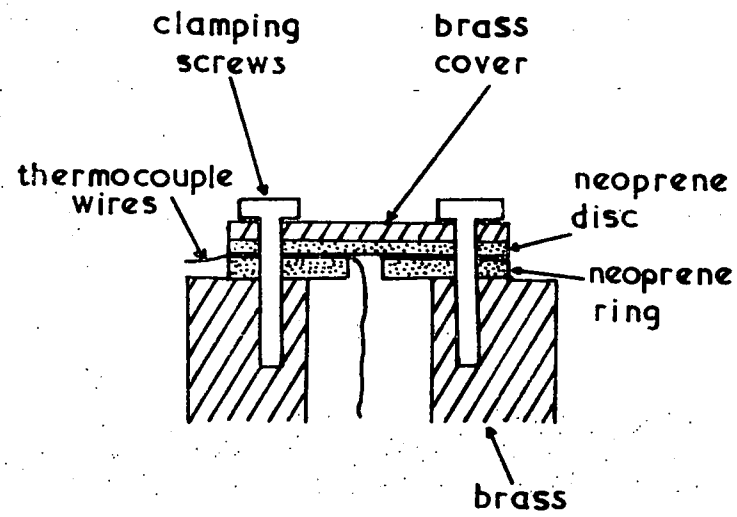

FIGURE 5.26: Neoprene vacuum seal

CHAPTER 6

ULTRASONIC STUDIES OF $CaWO_4$ SINGLE CRYSTALS

In this chapter the results of the ultrasound experiments on $CaWO_4$ single crystals are detailed. Preliminary measurements made at room temperature by the simple pulse echo technique are reported in Section 6.1.1. The set of elastic constants obtained from this preliminary work was used to provide details of the wave propagation characteristics and allowed selection of directions for more accurate measurements and temperature dependence studies. These further measurements were made between 1.5 K and 295 K by the pulse superposition method. They form the main experimental results reported in this thesis and are described in detail in Section 6.1.2. The accuracy and validity of the results are discussed (Section 6.1.3); details of wave propagation characteristics are given. Ultrasound attenuation measurements made in the course of the work are reported and discussed (Section 6.1.4).

The data obtained furnish details of the elastic behaviour of $CaWO_4$. The elastic properties and their orientation dependence are described (Section 6.2.1). The application of the Debye model to $CaWO_4$ is considered (Section 6.2.2) and the results of the present work are taken with those of previous studies of the thermal properties (see Chapter 2) to provide some description of the non-linear elastic properties of the material.

6.1 ULTRASONIC MEASUREMENTS FROM 1.5 K to 295 K

6.1.1 Preliminary measurements of elastic constants at room temperature

Five $CaWO_4$ specimens were oriented, cut and polished as described in Section 5.2 to have end-faces normal to the propagation directions listed in Table 6.1 and the dimensions given there. Each sample was between 7 and 11 mm thick with a cross-sectional area of about 1 cm^2. Ultrasound transit times were measured at room temperature using the Matec 9000 Attenuation Comparator at a frequency of 15 MHz. Quartz transducers (X-cut and Y-cut), bonded to the specimens with Nonaq stopcock grease, were used to generate the ultrasound. For propagation in each of the directions 0,0,1 (pure mode direction), $1/2,3^{\frac{1}{2}}/2,0$ (semi-pure mode direction) and $0,2^{-\frac{1}{2}},2^{-\frac{1}{2}}$ (impure mode direction) the modes were readily excited and distinguished. Good echo trains could be obtained for the quasi-longitudinal and pure shear modes propagated in the directions 1,0,0 and $2^{-\frac{1}{2}},2^{-\frac{1}{2}},0$ but studies of the quasi-shear modes presented difficulties. In neither case could the quasi-shear echoes be observed with certainty, despite many attempts using a wide variety of bonding materials. Great care was taken to ensure that the Y-cut transducers had their vibration direction accurately parallel to the (001) plane, but clean echo trains could not be obtained (see Figure 6.1). Often it seemed that the pure shear and the quasi-longitudinal modes were being excited in addition to the required wave. Similar difficulties were encountered by Gerlich (1964) who was not able to excite these quasi-

shear modes.

The set of ultrasound velocities which could be measured satisfactorily are given in Table 6.1, and compared with the six velocities reported earlier (Gerlich 1964). The two sets agree well. Internal consistency of the present measurements was checked by comparing the values of $C_{11} + C_{66}$ obtained (i) by summing the squares of the velocities of the quasi-longitudinal and quasi-shear modes with propagation vector $1/2, 3^{\frac{1}{2}}/2, 0$ and (ii) from the sum of the squares of the velocities of the three modes with propagation vector $0, 2^{-\frac{1}{2}}, 2^{-\frac{1}{2}}$ (see equation 9 of Table 3.2). The values ($C_{11} + C_{66}$ equal to 19.2×10^{11} dyn cm^{-2} and 18.7×10^{11} dyn cm^{-2} respectively) agreed within experimental error. Values of the elastic constant C_{44} obtained from measurements in different directions were also found to be in good agreement with each other.

The room temperature elastic stiffness constants were then found by a computer least-squares fit (described in Section 3.3.2) to the twelve measured velocities. Data obtained (using the x-ray density of 6.120 gm cm^{-3} at 293 K) are listed in Table 6.2. This elastic constant set was one of four equivalent solution sets (each with SUMSQ equal to 0.00037), and was selected because the values were the most similar to those found for $CaMoO_4$ by Alton and Barlow (1967). A rigorous justification for this choice of solution set will be discussed in the next section.

Knowledge of the elastic constants allows calculation of the positions of the accidental pure mode axes, either by use of the expressions given by Brugger (1965)

or by computation of the eigenvectors of the Christoffel equations (as in Section 6.1.3). It was found that the accidental pure mode axes in the (001) plane — κ and γ — should make angles of $+21.5^{\circ}$ and $+66.5^{\circ}$ with the [100] direction, when measured from this direction towards the [010]. Thus it appeared that in specimen 5, cut at $+60^{\circ}$ to the [100], the propagation direction was within 10° of a pure mode axis, while in both specimens 2 and 3 the propagation directions (1,0,0 and $2^{-\frac{1}{2}},2^{-\frac{1}{2}},0$ respectively) were more than 20° away from such an axis.

6.1.2 Temperature dependence of the elastic constants

(a) Measurements

To measure the temperature dependence of the elastic constants six propagation directions were selected. These directions were the five used in the preliminary measurements plus one making an angle of $+21.5^{\circ}$ with the [100] axis cut for propagation close to the κ accidental pure mode axis (specimen 6). Initial experiments using the pulse superposition equipment established that "clean" echo trains were essential for high precision, and that these were most nearly achieved with very carefully polished, parallel and roughly cylindrical (thickness less than diameter) specimens. Accordingly the specimens used in the previous work were re-cut, and all six specimens polished using the vacuum chuck technique. Thicknesses, measured with a precision micrometer to an accuracy of ± 0.001 mm, are given in Table 6.3.

The ultrasound modes were excited by use of X-cut and Y-cut quartz transducers bonded to the specimens with

Nonaq stopcock grease, and the temperature variation of transit times was measured using the pulse superposition system. Nonaq proved to be a satisfactory bonding material over the whole temperature range. There was a small decrease in apparent attenuation——probably associated with the hardening of the bond——on cooling from room to ice temperature. First the room temperature velocities of the modes labelled v_1, v_2, v_4, v_7, v_9, v_{10}, v_{11}, v_{12}, v_{14}, v_{15}, v_{16}, v_{17} in Table 3.2 were measured, and their internal consistency tested by means of the cross-checks on $C_{11}+C_{66}$ and C_{44}. Then the transit times of the modes labelled v_1, v_2, v_4, v_7, v_9, v_{10}, v_{11}, v_{13}, v_{14}, v_{17} were measured in the range 1.5 K to 295 K at intervals of about 2 K. Measurements were repeated until satisfactory and continuous temperature runs over the whole range were obtained. This was necessary because, particularly in the case of impure modes, there was a tendency for the echo train to deteriorate on cooling, leading to spurious superposition maxima. Many trials were then needed to establish the most suitable transducer size and position (and orientation in the case of Y-cuts) required to give the cleanest echo trains over a complete temperature run. The difficulties in using the McSkimin criterion of cyclic matching when Nonaq bonds are employed were also apparent, though it was not always possible to conclude whether failure of the criterion was due to the lossy bond material or to the difficulty in obtaining perfectly clean echo trains. Measurements were made at 15 MHz or 18 MHz; it was therefore possible to use the second of the alternative methods of cyclic matching discussed in Section 4.2.2. Despite the above difficulties the

final measurements were of high precision; a sensitivity of about 1 part in 10^5 was achieved. The lack of scatter on the experimental points in Figure 6.2 to 6.11 attests to this. These figures show the temperature variations of the pulse repetition frequencies required to achieve superposition for each of the modes listed above.

The corresponding ultrasound velocities were calculated at 5^o intervals using the measured pulse repetition frequencies, the known values of p and the specimen lengths. The lengths were corrected for change due to thermal expansion by use of the linear thermal expansion coefficients $\alpha_\perp$ and $\alpha_\parallel$ reported by Yates and Bailey (1971). Velocities at 1.5 K and 295 K are given in Table 6.3 and the temperature dependences are presented as velocity ratios $v_i(T)/v_i(0\ K)$ in Figure 6.12.

(b) Computation of elastic constants at 295K

The elastic constants were obtained from the velocity data by use of the computer least-squares fitting procedure. The method was first used to determine the room temperature elastic constants from the velocities v_1, v_2, v_4, v_7, v_9, v_{10}, v_{11}, v_{13}, v_{14} and v_{17} listed in Table 6.2 and the x-ray density (6.120 g cm^{-3} at 295 K). A series of widely different starting points produced four equivalent solutions P, Q, R and S to the measured data, each with SUMSQ equal to 0.00013 after 501 cycles (see Table 6.4).

In some cases, when equivalent solution sets are obtained, the correct set can be chosen by reference to the Born stability criteria. For a TII tetragonal the conditions

$$C_{11},\quad C_{33},\quad C_{44},\quad C_{66} > 0\ ;$$
$$C_{11} > |C_{12}|\ ;\ (C_{11}-C_{12})C_{66} > 2C_{16}^2\ ; \qquad (6.1)$$
and $$C_{11}C_{33} > C_{13}^2\ ;\ (C_{11}+C_{12})C_{33} > 2C_{13}^2$$

must be obeyed for a crystal to be stable. However only the set S can be eliminated in this way.

The four solutions each yield values of the quantities Z_i equal to those which were measured. However numerical solution of the cubic determinantal equation for the $0, 2^{-\frac{1}{2}}, 2^{-\frac{1}{2}}$ propagation direction gives the individual velocities, v_9, v_{10} and v_{11}. These are

Set P	$v_9 = 4.48$	$v_{10} = 2.32$	$v_{11} = 2.89$
Set Q	$v_9 = 4.48$	$v_{10} = 2.32$	$v_{11} = 2.89$
Set R	$v_9 = 4.41$	$v_{10} = 0.99$	$v_{11} = 3.02$
Set S	$v_9 = 4.41$	$v_{10} = 0.99$	$v_{11} = 3.02$

(6.2)

in units of 10^5 cm s^{-1}. Only sets P and Q yield velocities which agree with those measured ($v_9 = 4.49$, $v_{10} = 2.32$, $v_{11} = 2.83$ in units of 10^5 cm s^{-1}), and the sets R and S must be eliminated.

The remaining solution sets P and Q differ only in the value of the constant C_{13}. In fact the correct value of C_{13} cannot be found from just the values of the velocities. This was indicated by calculation of the eigenvalues of the Christoffel equations for each of the solution sets P and Q. For propagation directions at 1^o intervals throughout one quadrant of a sphere both sets yield the same eigenvalues and velocities. The reason for this is fundamental; in tetragonal crystals the elastic wave velocities do not depend

on C_{13} itself but on $(C_{13} + C_{44})^2$. This can be shown by solving the cubic determinantal equation for a general direction. The velocities of the three modes which can be propagated in such a direction are given by functional relationships of the form:

$$\rho v_i^2 = f_i \{(C_{13}+C_{44})^2, C_{11}, C_{12}, C_{16}, C_{33}, C_{44}, C_{66}\} \quad (6.3)$$

Such a relationship can be satisfied by two possible values of C_{13} given by

$$C_{13} = \pm M - C_{44} \quad (6.4)$$

where M is known once the other elastic constants and velocities v_i have been found. Here it can be deduced for $CaWO_4$ that M has the value 7.27×10^{11} dyn cm^{-2} since C_{13} could be either 3.92 or -10.62×10^{11} dyn cm^{-2}. Consideration of the expression 6.4 shows that it is not necessarily possible to distinguish between the equivalent roots by means of the Born stability criteria for tetragonals.

The correct solution can be identified by calculation of the eigenvectors of the modes propagated in a chosen direction outside the (001) plane, and comparison with the transducer polarisations used to excite these modes in practice. For the propagation direction (cosines) $0, 2^{-\frac{1}{2}}, 2^{-\frac{1}{2}}$ the eigenvectors were calculated by means of the IBM Scientific Subroutine EIGEN. The components for solution sets P and Q are given in Figure 6.13 and the particle displacement vector for the mode with the highest velocity ($v_9 = 4.48 \times 10^5$ cm s^{-1}) is compared with the propagation vector of the mode. For $C_{13} = 3.92 \times 10^{11}$ dyn cm^{-2} (set P) the fastest mode is quasi-longitudinal with the

deviation of the particle displacement vector from the propagation vector somewhat less than 5^{o}, whereas if $C_{13} = -10.62 \times 10^{11}$ dyn cm^{-2} (Set Q) the mode would be quasi-transverse. In practice the fastest mode in the $0, 2^{-\frac{1}{2}}, 2^{-\frac{1}{2}}$ direction was excited by an X-cut transducer. Clearly this mode is quasi-longitudinal and the correct value of C_{13} is 3.92×10^{11} dyn cm^{-2}.

(c) Temperature dependence

The temperature dependence of the elastic stiffness constants was obtained from the velocity data by using the least squares fitting procedure at a series of temperatures down to 1.5 K. Solution set P was used as a starting point for the search, and the density was corrected for change with temperature by use of the volume expansion coefficient calculated from the data of Yates and Bailey (1971). Values of the C_{ij} at temperatures between 1.5 K and 295 K are given in Table 6.5 and the temperature dependences shown in Figures 6.14 and 6.15. The constant C_{16} is negative in sign.

6.1.3 Accuracy and validity of results

Ultrasound experiments on low symmetry materials involve propagating and studying impure modes. It is therefore, particularly important to estimate the accuracy, and to check the validity of the results—erroneous answers can be obtained if impure modes have not been correctly assigned or if energy flux deviation has resulted in the ultrasound beam impinging on the sample walls.

The internal consistency of the measurements of $CaWO_4$ reported here was checked by comparing the values of

$C_{11}+C_{66}$ and C_{44} obtained from different directions. Agreement in each case was found to be within experimental error.

From the room temperature elastic stiffnesses (Table 6.5) the three wave velocities were calculated for propagation directions at 1^{o} intervals around the (001), (100) and (110) planes by computation of the eigenvalues of the Christoffel equations. The program EIGEN was used (see Appendix 1). The three cross-sections of the velocity surfaces (Figures 6.16 a,b, and c) exhibit the Laue symmetry of the material. Figure 6.16a shows clearly the existence of acoustic axes (directions in which the pure shear and quasi-shear velocities are equal). These axes lie in the (001) plane making angles of $+49^{o}$ and $+89^{o}$ with the [100] direction (measured towards the [010]), and do not coincide with the accidental pure mode axes. The cross-sections allow an estimation of the possible errors in each velocity owing to specimen misorientation. The uncertainty arising from a misorientation of $\pm 1/2^{o}$ is $\pm 1/2\%$ in velocity v_{14} (the quasi-shear mode propagated in the direction $1/2, 3^{\frac{1}{2}}/2, 0$) and is less than this for other modes.

Particle displacement vectors can also be computed from the elastic constants. The modes propagated in the [001] direction are pure: particle displacement is parallel and perpendicular to the propagation direction for the longitudinal and shear modes respectively. For the quasi-longitudinal wave propagated in the $0, 2^{-\frac{1}{2}}, 2^{-\frac{1}{2}}$ direction the deviation of particle displacement vector from the wave normal has already been shown to be small ($<5^{o}$). The modes propagated in the (001) plane are particularly interesting. In this plane there is a pure

shear mode which has a particle displacement in the [001] direction for all directions of the wave normal, and two impure modes with particle displacement vectors which lie at right angles to each other in the (001) plane. The deviation of the particle displacement vector of the mode with greatest velocity has been computed at 1° intervals around the plane (see Figure 6.17). Always the magnitude of the deviation is less than 11° and thus the mode is quasi-longitudinal. For directions making angles of $+23.6^{\circ}$ and $+68.6^{\circ}$ with the X axis the deviation is zero. These directions are the accidental pure mode axes and lie within 3° of the positions predicted from the preliminary measurements (described in Section 6.1.1). Thus specimen 6 had been cut for propagation very close to the κ accidental pure mode axis.

Knowledge of the elastic constants and the particle displacement vectors allows calculation of the energy flux direction of any mode (by use of equations 3.64, 3.65 and 3.66). For modes propagated in the XY plane the energy flux direction lies in that plane. Angular deviations from the propagation direction are given in Figure 6.17. The energy flux vector of the quasi-longitudinal mode is never far from the propagation direction: the maximum deviation is 16°, and for the modes labelled v_4, v_7, v_{13} and v_{16} it is 12°, -14°, -6° and $+4^{\circ}$ respectively. Such deviations were readily accommodated in the specimens used. The quasi-shear mode is much less suited to ultrasonic pulse echo studies; the energy flux deviation varies from $+45.5^{\circ}$ to -45.5° and is close to these maxima for the two propagation

directions, [100] and [110], for which the quasi-shear velocities could not be measured in the preliminary measurements reported here (Section 6.1.1) or in earlier work (Gerlich (1964)). Clearly the difficulties associated with propagating these modes arose from this considerable energy flux deviation. The difficulties may have been compounded by the occurrence of internal conical refraction since both propagation directions are within a few degrees of the acoustic axes in the (001) plane. For propagation of the quasi-shear mode along an acoustic axis the energy flux vector will only lie in the (001) plane if the Y-cut transducer polarisation is accurately normal to the [001] direction. A measurement of v_5 has now been made using a thin sample specially cut so as to avoid wall reflections and a velocity consistent with that predicted from the elastic stiffness constants of Table 6.5 has been measured (2.48×10^5 cm s^{-1} at 295 K). For propagation along the accidental pure mode axes the energy flux deviation of all three modes is zero, but on each side of these axes the energy flux deviation changes very rapidly with changing propagation vector ($\sim$5 degrees per degree).

In the absence of gross errors, which would affect the validity of the results, an assessment can be made of the uncertainty in each elastic constant arising from small errors in each measurement of velocity. These small errors in velocity will be made up of contributions due to misorientation ($<\frac{1}{2}\%$), diffraction effects (0.1%), measurement of sample length (0.03%) and the uncertainty in transit time which arises from the phase change on reflection at the specimen-bond-transducer interface (0.2%). This last

error was estimated by means of equations 4.7 and 4.8 for a quartz transducer bonded to a $CaWO_4$ sample with a 3 μm thick Nonaq bond and operated at its 15 MHz resonant frequency. An additional error of about 1% would arise in any velocity for which the recorded pulse superposition maximum corresponded to n = ±1 cyclic matching rather than to the required n = 0 condition. The internal consistency of the velocity data and the excellent fit of the derived elastic constant set to the measurements (see below) demonstrated that such errors did not arise. An estimate of ±0.8%, made up by addition of the above contributions can therefore be taken as the worst-case error in each velocity. In comparison, the uncertainty in the x-ray density (ρ) is negligible (<0.05%).

The resulting error limits on the stiffnesses C_{33} and C_{44} can be estimated directly but for the other constants extensive computation has been necessary. The least-squares procedure was employed to find the elastic constants corresponding to many different velocity sets in which different combinations of measured velocities were adjusted to the limits allowed by their experimental errors. Initially each of the velocities in turn was adjusted up and then down while keeping the others at their measured values. Next all the quasi-longitudinal velocities and then all the quasi-shear velocities were adjusted together to their respective limits. Finally all the quasi-longitudinal velocities were increased while all the quasi-shear were decreased, and then vice-versa. From the thirty sets of elastic constants so obtained the maximum

deviation of each constant from its initial value was taken as the experimental uncertainty, giving errors of

C_{11} ± 2% C_{12} ± 7% C_{13} ± 20% C_{16} ± 3%

C_{33} ± 2% C_{44} ± 2% C_{66} ± 4%

Uncertainties in the compliance constants and the technical moduli were calculated by the same method (these will be quoted where appropriate).

The degree of scatter of the points in Figures 6.14 and 6.15 indicates that the errors in the temperature dependences of each elastic constant are somewhat less than the uncertainties in their absolute values. This reflects the relative accuracy of the measurements of temperature dependence of the velocities (see Section 4.2.3). It was found that the quality of the overall fit improved slightly at lower temperatures (see Table 6.6). Over the whole range (1.5 to 295 K) the measured quantities Z_i were each predicted to be better than 1% by the elastic constants obtained from the fitting procedure. The velocities calculated from the elastic constants agreed with each of those measured to better than 1%.

6.1.4 Measurements of ultrasound attenuation

In the course of the velocity measurements it was found that at low megahertz frequencies (15 to 20 MHz) the attenuation of each of the modes appeared to be almost independent of temperature. Measurements at higher frequencies were made for the pure longitudinal and pure shear modes propagated in the [001] direction (using

specimen number 1). The end-faces of the specimen were accurately parallel, there was no tendency for mixed mode propagation, and the echo trains obtained were near-exponential at frequencies up to 750 MHz. Measurements of longitudinal wave attenuation were made at this frequency, while shear wave attenuation was measured at 740 MHz. In both cases the Matec Attenuation comparator was used and the attenuation recorded between 1.5 K and 295 K. From 1.5 K up to ice temperature no change in the attenuation of either mode was observed. Above ice temperature there was a small increase in attenuation — believed to be due to deterioration of the bond. Figures 6.18 and 6.19 are photographs of the longitudinal and shear echo trains at 4.2 K and 77 K. The exponential curve was fitted to the echo trains at 77 K and clearly in both cases it fits equally well at 4.2 K. The measured attenuations of the two modes were 0.380 and 0.205 dB μs^{-1}, equivalent to 0.825 and 0.870 dB cm^{-1} respectively. By consideration of the uncertainty in fitting the calibrated exponential curve to the echo pattern it was estimated that the maximum change in attenuation between 4.2 K and 77 K was less than 0.03 dB cm^{-1} (longitudinal) or 0.06 dB cm^{-1} (shear).

The absorption of sound is often a factor which limits the high frequency performance of practical ultrasonic devices (bulk or surface wave filters and delay lines, acousto-optic devices). In good quality dielectric materials the absorption has in many cases been shown to arise from an interaction of the ultrasound wave with the thermal phonon population. Recent attenuation measurements

at 1 GHz in $CaWO_4$ have been reported to be in agreement with the theory of such phonon-phonon interactions (Lewis 1972). The precise nature of the interaction depends on the relationship between the angular frequency of the ultrasound beam (ω) and the relaxation time (τ) of the thermal phonons. If $\omega\tau>1$ (which is true at low temperatures when τ is long) the interaction can be considered to be a microscopic process (Landau and Rumer (1937), Maris (1971)). In this regime the attenuation is proportional to T^4. When $\omega\tau<<1$ (this holds at high temperatures when phonon scattering is increased) the attenuation occurs by a process known as Akhieser damping and can be calculated by an expression (Maris 1971) which in simplified form is

$$\alpha = \frac{\langle\gamma\rangle^2 C T}{2\rho v^3} \quad \frac{\omega^2\tau}{1+\omega^2\tau^2} \quad \text{nepers cm}^{-1} \qquad (6.5)$$

where $\langle\gamma\rangle$ is an averaged Gruneisen constant, C is the specific heat per unit volume and T the absolute temperature. The phonon relaxation time is the mean free time between collisions and can be related to the lattice thermal conductivity (K_T) by the kinetic theory expression

$$K_T = \frac{1}{3} C \bar{v}^2 \tau \qquad (6.6)$$

where $\bar{v}$ is the Debye mean sound velocity. For the condition $\omega\tau<<1$ these equations give

$$\alpha = \frac{3 K_T T \langle\gamma\rangle^2 \omega^2}{2\rho v^3 \bar{v}^2} \times 8.686 \text{ dB cm}^{-1} \qquad (6.7)$$

Over the range of temperature for which the thermal conductivity is proportional to T^{-1} (see Section 2.4.4) the attenuation will be roughly temperature independent. Thus

by means of equation 6.7 an estimate can be made of the increase in attenuation from that at low temperatures (when phonon interaction effects are frozen out) to the temperature independent value.

For $CaWO_4$ at room temperature the density is 6.120 g cm^{-3}, the thermal conductivity K_T is 0.04 watts cm^{-1} K^{-1}. The Debye mean sound velocity has been found to be 2.75×10^5 cm s^{-1} and the value of γ can be taken as 1.1 by averaging the components $\gamma_\perp$ and $\gamma_\parallel$ of the Grüneisen tensor (see Section 6.2). For longitudinal waves (with velocity $v = 4.56 \times 10^5$ cm s^{-1}, frequency = 750 MHz) the expression predicts an attenuation increase of $\sim$0.8 dB cm^{-1}, and for shear waves (velocity = 2.34×10^5 cm s^{-1}, frequency = 740 MHz) and increase of $\sim$5 dB cm^{-1}. Such changes have not been observed here. At 1 GHz the reported changes of ultrasound attenuation (Lewis 1972) are somewhat larger (2.1 dB cm^{-1} for longitudinal waves and about three times this for the shear), and for the longitudinal wave are in excess of the value predicted by the theory. Thus there is a conflict between the experimental results reported here, those given by Lewis (1972) and the simplified theory. Further experiments are needed—at frequencies in the microwave region and higher than those possible with the present system. The calculations could be improved if a more detailed assessment of the value of $\langle\gamma\rangle^2$ were possible. This requires knowledge of the third order elastic constants.

6.2 ELASTIC PROPERTIES OF $CaWO_4$

6.2.1 Elastic moduli

The temperature dependences of the seven independent

components of the elastic stiffness tensor are shown in Figures 6.14 and 6.15, and values at 25 K intervals are listed in Table 6.5. Below room temperature each of the constants increases in magnitude, indicating the increase of stiffness with falling temperature that is found in most crystalline materials. The elastic constants have their maximum values at 0 K and approach these values with zero slope. The temperature dependence is free from evidence of phase transitions, in agreement with specific heat (Lyon and Westrum 1968) and thermal expansion (Yates and Bailey 1971) data.

Knowledge of the elastic constants allows the determination of the response of a single crystal to any applied stress system. The response to particular static loads can be calculated directly by using the elastic compliances (S_{ij}). Values for $CaWO_4$, computed from the stiffnesses by means of equation 3.33, are listed in Table 6.7 for temperatures between 5 K and 295 K. The signs are significant. S_{11}, S_{33}, S_{44} and S_{66} are all positive; this is required by the Born stability criteria. S_{12} and S_{13} are both negative. These compliances describe how a tensile stress applied in the X-direction leads to tensile strains in the Y and Z directions respectively. If the material were isotropic, a compressive stress in the X direction would be expected to lead to expansion in the Y and Z directions. This expansion does occur in $CaWO_4$, but the responses in the two directions are not equal: the expansion in the Y-direction is more than twice that in the Z-direction. This may be deemed a consequence of the

layered nature of the structure. S_{16} is positive (it must have the opposite sign to C_{16}). Thus an applied tensile stress in the X direction (σ_{11} positive) induces a decrease in the angle between the +X and +Y axes (see Figure 6.20).

Relationships between certain simple stresses and strains are given by the technical moduli (see Section 3.1.13). The Young's modulus of a crystal can be represented by a surface; here cross sections of the $CaWO_4$ surface have been computed for applied tensile stresses in three major crystallographic planes — the (001), (100) and (110) — using equation 3.44 and a computer program listed in Appendix 1. The cross-sections at 295 K are given in Figure 6.21. Computation at a series of temperatures showed no significant change of orientation dependence, though the average Young's modulus does increase slightly on cooling (see below). In the planes containing the Z axis Young's modulus is comparatively isotropic with a maximum value in the Z direction. However in the XY plane there are pronounced maxima and minima along directions which coincide with the accidental pure mode directions. The ratio of the maximum Young's modulus in the XY plane to the minimum value in this plane is about 2.1 at 295 K. This anisotropy will be discussed further in Chapter 8 in comparison with other scheelites.

Particularly important in assessing the interatomic binding in a crystal are the bulk modulus (K_V), the volume compressibility (β_V) and the linear compressibilities (β_Z and β_{XY}). Values calculated at a series of temperatures

between 1.5 K and 295 K by means of expressions 3.37, 3.39 and 3.40 are given in Table 6.8. Over the whole range of temperature $\beta_Z \approx 1.5\ \beta_{XY}$; under an applied hydrostatic pressure the crystal has an anisotropic response. It contracts about 1½ times as much in the Z direction as in directions in the XY plane. This anisotropy is similar to that observed in the thermal expansion ($\alpha_{\parallel} > \alpha_{\perp}$) and confirms the suggestion (Deshpande and Suryanarayana 1969) that the binding between the layers of the structure is somewhat weaker than that within the layers. However it needs to be emphasised that the layer structure of $CaWO_4$ is not excessively pronounced; much larger anisotropies of linear compressibility occur in, for example, indium bismuth, arsenic and graphite (Akgöz, Farley and Saunders 1973).

The temperature dependence of the bulk modulus is plotted in Figure 6.22. It has the characteristic shape usually found in crystalline solids: a maximum value at 0 K approached with zero slope and approximately a T^{-1} dependence at higher temperatures (see Section 6.2.3).

Once the single crystal elastic constants of a material are known it is possible to predict, with reasonable accuracy, the elastic constants of a polycrystalline aggregate of the material (Anderson 1965). The polycrystalline aggregate must have zero porosity and randomly oriented grains. Then it can be assumed that either the strain (Voigt approximation) or the stress (Reuss approximation) is uniform throughout each grain. The two approaches yield upper and lower limits for the isotropic Young's, bulk and shear moduli, given by

$$E_R = 5C_{44}(C_{11}-C_{12})(C_{11}+2C_{44})/$$
$$C_{44}(3C_{11}+C_{12})+(C_{11}-C_{12})(C_{11}+2C_{12}) \quad (6.8)$$

$$K_R = \{(2S_{11}+S_{33})+2(S_{12}+2S_{13})\}^{-1} \quad (6.9)$$

$$G_R = 15/\{4(2S_{11}+S_{33})-4(S_{12}+2S_{13})+3(2S_{44}+S_{66})\} \quad (6.10)$$

$$E_V = (C_{11}-C_{12}+3C_{44})(C_{11}+2C_{12})/(2C_{11}+3C_{12}+C_{44}) \quad (6.11)$$

$$K_V = \{(2C_{11}+C_{33})+2(C_{12}+2C_{13})\}/9 \quad (6.12)$$

$$G_V = \{(2C_{11}+C_{33})-(C_{12}-2C_{13})+3(2C_{44}+C_{66})\} \quad (6.13)$$

The averages of these Voigt and Reuss limits can usually be taken as the values of the isotropic elastic constants (Anderson 1965). For $CaWO_4$ the temperature dependence of these parameters is shown in Figure 6.23.

6.2.2 The Debye temperature

The Debye theory assumes a solid to be a non-dispersive, isotropic continuum. Phonons, the quanta of lattice vibrations, are considered to travel with the same velocity whatever their wavelength and propagation vector. This velocity is taken equal to the mean velocity of sound in the material and can be computed by integration over the whole velocity surface, or alternatively can be calculated to a good approximation (Anderson 1963) from the isotropic elastic constants which themselves are averages over all possible crystallographic directions. The mean sound velocity is related to the isotropic bulk (K) and shear (G) moduli by the expressions

$$v_\ell = \{(K + 4G/3)/\rho\}^{\frac{1}{2}} \quad (6.14)$$

$$v_s = \{G/\rho\}^{\frac{1}{2}} \quad (6.15)$$

$$v_m = \left\{\frac{1}{3}\left(\frac{1}{v_\ell^3} + \frac{2}{v_s^3}\right)\right\}^{-1/3} \quad (6.16)$$

where ρ is the crystal density. From the elastic constants and density extrapolated to absolute zero, this gives a Debye mean sound velocity in $CaWO_4$ equal to 2.798×10^5 cm s^{-1}. The value falls with increasing temperature to 2.747×10^5 cm s^{-1} at 295 K, and is estimated to be accurate to ±1%.

From the mean sound velocity and density, the Debye temperature (θ_D) can then be calculated by the expression:

$$\theta_D = \frac{h}{k} \left[\frac{np}{4\pi} \frac{N\rho}{M} \right]^{1/3} v_m \qquad (6.17)$$

where h and k are Planck's and Boltzmann's constants respectively, N is Avogadro's number, and M is the gram formula mass. The theory treats the solid as being composed of a number of "vibrating cells." The number of these cells per formula unit is p and the number of degrees of freedom of each is n. In a monatomic lattice the values of m and n are unambiguous (each atom is counted as a vibrating cell) but in a polyatomic lattice or in a glass (Anderson 1959) there may be more than one choice of vibrating cell.

If the Debye distribution is taken to represent the entire phonon density of states, then each atom must be considered to be a vibrating unit. For $CaWO_4$ with M = 287.9, p = 6 and n = 3, this gives a Debye temperature value of 354 K at absolute zero. However as seen in Figure 2 the experimental heat capacity curve deviates considerably from the normal sigmate shape and as is often the case in polyatomic crystals it may be better to model only part of the phonon density of states by a Debye distribution, and to treat the excluded modes separately.

Optical modes usually have only a small variation of frequency (ω) with wave vector (k) and often are better represented by single frequency Einstein oscillators, since the Debye dispersion relation ($\omega = vk$) does not apply. The $CaWO_4$ specific heat data has been treated in this way (Lyon and Westrum 1968). Group theoretical analysis by Barker (1964) showed that for a $CaWO_4$ primitive cell (containing two formula units and thus 12 atoms) the 36 vibrational degrees of freedom were distributed as follows:

Number of degrees of freedom	Type
3	Acoustical lattice
9	Optical lattice
6	Torsional oscillations of WO_4 groups
18	'Internal' vibrations of WO_4 groups

Initially Lyon and Westrum used Einstein functions with the characteristic frequencies obtained from the work of Scott (1968) to represent just the 24 degrees of freedom associated with the torsional and internal vibrations of the WO_4 groups. The contributions of these modes were subtracted from the total measured heat capacity to leave a "lattice-only" heat capacity, whose variation with temperature was found to be typical of a diatomic ionic solid. The corresponding Debye temperature was calculated by allowing (3+9)/2 = 6 degrees of freedom and two vibrating units per formula unit, and reported to be $\sim$235 K ± 10 K at 0 K. Recently Yates and Bailey (1971), have analysed the specific heat data more rigorously. They converted the measured C_p values to the C_v values needed in the Debye

theory by use of the expression

$$C_P - C_V = \frac{B_V^2 T}{\beta_V} \qquad (6.18)$$

in which C_P and C_V are specific heats per unit volume, T is absolute temperature, β_V is the volume compressibility and B_V is the volume coefficient of thermal expansion. The bulk modulus of $CaMoO_4$ (7.95×10^{11} dyn cm^{-2}) was used since the value for $CaWO_4$ (found here to be 8.0×10^{11} dyn cm^{-2} and very similar to that for $CaMoO_4$) was not then known. From the resulting C_V values the variation of the effective $\theta_{D(\text{diatomic lattice only})}$ with temperature was calculated (see Figure 6.24). This effective Debye temperature can be calculated directly from the mean sound velocity obtained in this work. The value obtained is 246 K ± 2 K at absolute zero and decreases with increasing temperature to 241 K at 295 K. Thus the velocity of sound $\theta_{D(\text{diatomic lattice only})}$ agrees with the less accurate specific heat result of 264 K ± 20 K (from Figure 6.24) only in the limit of very low temperature. This is usually found to be the case (Alers 1965). The $\theta_{D(\text{diatomic lattice only})}$ obtained from sound velocity measurements will therefore predict the contribution of the acoustical and optical lattice modes to the total heat capacity only at very low temperatures ($\lesssim$ 20 K).

It may be preferable to represent just the acoustical mode lattice vibrations by a Debye distribution. To do this Lyon and Westrum (1968) subtracted appropriate Einstein contributions (frequencies obtained from the work of Barker (1964) and Porto and Scott (1967)) for the six optical lattice modes from the "lattice-only" specific

heat to give the "acoustical mode only" heat capacity, and calculated the corresponding effective Debye temperature ($\theta_{D(\text{acoustical mode only})}$ by allowing 3 degrees of freedom per primitive cell. The value so obtained was 155 K ± 10 K at absolute zero. From the Debye mean sound velocity obtained here, taking 3 degrees of freedom per primitive cell gives a $\theta_{D(\text{acoustical mode only})}$ equal to 155 K ± 2 K at zero kelvin and in good agreement with the specific heat value. This result is also consistent with one obtained from spin-lattice relaxation time measurements. The temperature dependence of the spin-lattice relaxation time in Nd doped $CaWO_4$ has been found to agree well with the theory of a Raman process (Kiel and Mims 1967) in the temperature range 4 K to 8 K. To fit the theory to the experimental data the Debye temperature was used as an adjustable parameter. From values of 60, 80, 100, 120, 140, 180 K much the best fit was obtained with a Debye temperature of 140 K. The similarity of this result to the acoustical-mode only θ_D found here (155 K) may be expected: at very low temperatures acoustical phonons dominate the phonon population.

6.2.3 Nonlinear elastic properties

The discussion in Chapter 3 was restricted to linear elasticity by the adoption of a linear relationship — Hooke's law — between stress and strain in a medium. In real crystals Hooke's law does not hold exactly and deviations which may be represented by third and higher order elastic constants are observed for large strains.

The non-linearity is a consequence of anharmonic terms (i.e. terms of order higher than quadratic) in the crystal potential energy and is the origin of many properties of solids including thermal expansion, the volume dependence of the lattice vibration frequencies, phonon interactions and the temperature dependence of the elastic constants.

The volume dependence of the i^{th} lattice vibration frequency (ν_i) can be expressed in terms of a parameter γ_i ($= d(\ell n(\nu_i))/d(\ell n(V))$ which is known as the Grüneisen mode parameter and assumed to be constant (the quasi-harmonic approximation). An average of these parameters is defined by the expression

$$\gamma = \frac{\sum \gamma_i C_i}{C_V} \tag{6.19}$$

in which the weighting factors (C_i) are the relative contributions of each mode to the total specific heat capacity C_V. The weighting factors depend on temperature and hence γ does too. By consideration of the equation of state of a quasi-harmonic solid it can be shown that the Grüneisen parameter γ is important in relating the elastic properties and the thermal expansion. If the solid is anisotropic γ is direction dependent (Key 1967) and in a uniaxial solid is represented by a tensor with two components given by

$$\gamma_{\perp} = \{(C_{11}+C_{12})\ \alpha_{\perp} + C_{13}\ \alpha_{\parallel}\}\ /\rho C_P \tag{6.20}$$

$$\gamma_{\parallel} = \{2C_{13}\ \alpha_{\perp} + C_{33}\ \alpha_{\parallel}\}\ /\rho C_P \tag{6.21}$$

where C_P is the specific heat per unit mass at constant stress, the C_{ij} are adiabatic elastic constants and $\alpha_{\perp}(= \alpha_a)$ and $\alpha_{\parallel}(= \alpha_c)$ are the linear thermal expansion

coefficients. The temperature dependence of $\gamma_\perp$ and $\gamma_\parallel$ for $CaWO_4$ has been calculated for the temperature range 30 to 295 K using the elastic constant data of Table 6.5, the specific heat data of Lyon and Westrum (1968), and thermal expansion data of Yates and Bailey (1971). Figure 6.25 indicates that down to 100 K the Grüneisen parameters are similar in value and remain almost constant. Below 100 K both $\gamma_\perp$ and $\gamma_\parallel$ decrease, but $\gamma_\perp$ does so rather more rapidly and the anisotropy $\gamma_\parallel/\gamma_\perp$ increases. Without thermal expansion data at low temperatures it is not possible to predict the limiting values at absolute zero.

The dependence of elastic constants on temperature is also a consequence of the anharmonicity of the crystal potential energy. Lakkad (1971) has recently derived an expression for the temperature dependence of elastic constants by assuming a linear chain, anharmonic oscillator model of a Debye solid. The expression he obtained is

$$E = E_o (1 - L F (T/\theta_D)) \qquad (6.22)$$

where E_o is the value of an elastic constant E at zero kelvin, θ_D is the Debye temperature, L is a constant and $F (T/\theta_D)$ is the function

$$F(T/\theta_D) = 3(T/\theta_D)^4 \int_0^{\theta_D/T} \{x^3[\exp(x) - 1]\}dx \qquad (6.23)$$

Good fits to the temperature dependences of the elastic constants of certain metals (Lakkad 1971), and semiconductors (Cottam and Saunders 1973) have been obtained. Figure 6.22 indicates that the expression is also suitable for representing the temperature dependence of the bulk

modulus of $CaWO_4$. In the figure the solid, dotted and dashed lines are the fits obtained (using points at 0 K and 295 K to find the constant L) for Debye temperature values 155 K, 246 K and 354 K (see Section 6.2.2) respectively. Clearly the fit obtained using the "acoustical mode only" Debye temperature (155 K) is much the best. This would seem to indicate that the acoustic mode vibrations dominate the mean displacements of the atoms and thus the temperature variation of the bulk modulus.

Table 6.1

Preliminary measurement of ultrasonic velocities in $CaWO_4$ at room temperature

Boule reference number*	Specimen number	Thickness (mm)	Direction cosines of normal to end-faces	v_i †	Measured velocities (10^5 cm s^{-1}) Present work	Gerlich (1964)
142/C	1	7.06	0,0,1	v_1	4.56	4.60
				v_2	2.34	2.34
U1/100	2	10.10	1,0,0	v_3	2.36	2.35
				v_4	4.90	4.90
				v_5	-	-
U1/110	3	8.755	$2^{-\frac{1}{2}},2^{-\frac{1}{2}},0$	v_6	2.36	-
				v_7	4.92	4.89
				v_8	-	-
143/X	4	9.10	$0,2^{-\frac{1}{2}},2^{-\frac{1}{2}}$	v_9	4.55	4.48
				v_{10}	2.36	-
				v_{11}	2.83	-
143/Y	5	10.00	$1/2,3^{\frac{1}{2}}/2,0$	v_{12}	2.37	-
				v_{13}	5.17	-
				v_{14}	1.98	-

* The first part of the reference number is that used by IRD Co. Ltd. to refer to the as-grown boule. The letters or numbers after the oblique line refer to the portion of the boule after initial cutting.

† The suffices (i) refer to the modes listed in Table 3.2

Table 6.2

Preliminary determination of the elastic constants of $CaWO_4$ at room temperature

C_{11}	14.3	C_{33}	12.8
C_{12}	5.54	C_{44}	3.40
C_{13}	5.04	C_{66}	4.49
C_{16}	-2.21	Units: 10^{11} dyn cm^{-2}	

Table 6.3

Ultrasound velocities in $CaWO_4$ at 1.5 K and 295 K

Boule reference number*	Specimen number	Thickness (mm)	Direction cosines of normal to end-faces	v_i †	Measured velocities (10^5 cm s^{-1}) 1.5 K	295 K
142/C	1	7.065	0,0,1	v_1	4.64	4.56
			0,0,1	v_2	2.39	2.34
144/D	2	7.095	1,0,0	v_4	5.04	4.93
U1/110	3	8.733	$2^{-\frac{1}{2}},2^{-\frac{1}{2}},0$	v_7	4.99	4.89
143/X	4	8.688	$0,2^{-\frac{1}{2}},2^{-\frac{1}{2}}$	v_9	4.57	4.49
			$0,2^{-\frac{1}{2}},2^{-\frac{1}{2}}$	v_{10}	2.37	2.32
			$0,2^{-\frac{1}{2}},2^{-\frac{1}{2}}$	v_{11}	2.87	2.83
143/Y	5	7.081	$1/2,3^{\frac{1}{2}}/2,0$	v_{13}	5.23	5.15
			$1/2,3^{\frac{1}{2}}/2,0$	v_{14}	1.98	1.96
143/C	6	5.050	$\cos(21.5^{\circ})$,	v_{17}	3.17	3.11
			$\sin(21.5^{\circ}),0$			

* The first part of the reference number is that used by IRD Co. Ltd. to refer to the as-grown boule. The letters or numbers after the oblique line refer to the portion of the boule after initial cutting.

† The suffices (i) refer to the modes listed in Table 3.2.

Table 6.4

Equivalent solutions found by computer least-mean squares fit to the $CaWO_4$ ultrasound velocity data at room temperature.

	C_{11}	C_{12}	C_{13}	C_{16}	C_{33}	C_{44}	C_{66}	SUMSQ
P	14.6	6.26	3.92	-1.92	12.74	3.35	3.87	0.00013
Q	14.6	6.26	-10.62	-1.92	12.74	3.35	3.87	0.00013
R	11.54	-3.86	3.92	-5.20	12.74	3.35	6.92	0.00013
S	11.54	-3.86	-10.62	-5.20	12.74	3.35	6.92	0.00013

Units : 10^{11} dyn cm^{-2}

Table 6.5

Temperature dependence of C_{ij} of $CaWO_4$

	1.5 K	25 K	50 K	75 K	100 K
C_{11}	15.23	15.23	15.21	15.16	15.10
C_{12}	6.52	6.52	6.51	6.50	6.48
C_{13}	4.08	4.07	4.06	4.04	4.02
C_{16}	-2.04	-2.04	-2.04	-2.04	-2.03
C_{33}	13.24	13.24	13.22	13.20	13.16
C_{44}	3.52	3.52	3.52	3.51	3.49
C_{66}	4.03	4.03	4.02	4.01	4.00

	125 K	150 K	175 K	200 K	225 K
C_{11}	15.03	14.96	14.88	14.81	14.74
C_{12}	6.46	6.43	6.34	6.36	6.32
C_{13}	4.00	3.99	3.98	3.97	3.95
C_{16}	-2.02	-2.00	-1.99	-1.97	-1.96
C_{33}	13.11	13.07	13.01	12.96	12.90
C_{44}	3.48	3.46	3.44	3.42	3.40
C_{66}	3.98	3.97	3.95	3.93	3.91

	250 K	275 K	295 K
C_{11}	14.67	14.61	14.59
C_{12}	6.28	6.24	6.26
C_{13}	3.94	3.95	3.92
C_{16}	-1.94	-1.93	-1.92
C_{33}	12.85	12.79	12.74
C_{44}	3.38	3.36	3.35
C_{66}	3.89	3.87	3.87

UNITS :
10^{11} dyn cm^{-2}
or 10^{10} N m^{-2}

Table 6.6

	T = 295 K		T = 200 K	
	Measured	Calculated	Measured	Calculated
Z_1	2.08×10^{11}	2.08×10^{11}	2.11×10^{11}	2.11×10^{11}
Z_2	5.48×10^{10}	5.48×10^{10}	5.57×10^{10}	5.57×10^{10}
Z_4	2.44×10^{11}	2.44×10^{11}	2.47×10^{11}	2.47×10^{11}
Z_7	2.39×10^{11}	2.39×10^{11}	2.43×10^{11}	2.43×10^{11}
Z_9	3.34×10^{11}	3.37×10^{11}	3.39×10^{11}	3.42×10^{11}
Z_{10}	4.98×10^{22}	4.98×10^{22}	5.12×10^{22}	5.12×10^{22}
Z_{13}	2.65×10^{11}	2.63×10^{11}	2.67×10^{11}	2.67×10^{11}
Z_{15}	3.83×10^{10}	3.83×10^{10}	3.84×10^{10}	3.84×10^{10}
Z_{16}	9.64×10^{10}	9.65×10^{10}	9.82×10^{10}	9.81×10^{10}
	SUMSQ = 0.00013		SUMSQ = 0.00007	

	T = 100 K		T = 200 K	
	Measured	Calculated	Measured	Calculated
Z_1	2.14×10^{11}	2.14×10^{11}	2.15×10^{11}	2.15×10^{11}
Z_2	5.68×10^{10}	5.68×10^{10}	5.73×10^{10}	5.72×10^{10}
Z_4	2.52×10^{11}	2.51×10^{11}	2.54×10^{11}	2.53×10^{11}
Z_7	2.47×10^{11}	2.47×10^{11}	2.49×10^{11}	2.48×10^{11}
Z_9	3.45×10^{11}	3.47×10^{11}	3.48×10^{11}	3.50×10^{11}
Z_{10}	5.28×10^{22}	5.28×10^{22}	5.37×10^{22}	5.37×10^{22}
Z_{13}	2.71×10^{11}	2.72×10^{11}	2.73×10^{11}	2.74×10^{11}
Z_{15}	3.87×10^{10}	3.87×10^{10}	3.92×10^{10}	3.92×10^{10}
Z_{16}	1.00×10^{11}	1.00×10^{11}	1.01×10^{11}	1.01×10^{11}
	SUMSQ = 0.00007		SUMSQ = 0.00005	

Units of Z_i (i = 1,2,4,7,9,13,15,16) are $cm^2\ s^{-2}$

Units of Z_i (i = 10) are $cm^4\ s^{-4}$

Table 6.7

Temperature dependence of S_{ij} of $CaWO_4$

	1.5 K	25 K	50 K	75 K	100 K
S_{11}	+10.12	+10.13	+10.15	+10.19	+10.23
S_{12}	- 4.93	- 4.93	- 4.95	- 4.99	- 5.00
S_{13}	- 1.60	- 1.60	- 1.60	- 1.59	- 1.60
S_{16}	+ 7.62	+ 7.63	+ 7.66	+ 7.70	+ 7.73
S_{33}	+ 8.54	+ 8.54	+ 8.54	+ 8.55	+ 8.57
S_{44}	+28.4	+.28.4	+28.4	+28.5	+28.6
S_{66}	+32.5	+32.5	+.32.6	+32.7	+32.8

	125 K	150 K	175 K	200 K	225 K
S_{11}	+10.28	+10.32	+10.36	+10.39	+10.42
S_{12}	- 5.03	- 5.05	- 5.05	- 5.06	- 5.06
S_{13}	- 1.60	- 1.61	- 1.63	- 1.63	- 1.64
S_{16}	+ 7.75	+ 7.76	+ 7.76	+ 7.75	+ 7.75
S_{33}	+ 8.60	+ 8.64	+ 8.68	+ 8.72	+ 8.76
S_{44}	+28.8	+28.9	+29.1	+29.3	+29.4
S_{66}	+32.9	+33.0	+33.1	+33.2	+33.3

	250 K	275 K	295 K	ERROR	UNITS
S_{11}	+10.45	+10.48	+10.49	± 2%	10^{-13}
S_{12}	- 5.05	- 5.04	- 5.07	± 4%	$cm^2\ dyn^{-1}$
S_{13}	- 1.66	- 1.67	- 1.66	±20%	or
S_{16}	+ 7.74	+ 7.74	+ 7.71	± 4%	10^{-12}
S_{33}	+ 8.80	+ 8.85	+ 8.87	± 5%	$m^2\ N^{-1}$
S_{44}	+29.6	+29.7	+29.8	± 2%	
S_{66}	+33.4	+33.6	+33.5	± 6%	

Table 6.8

Temperature dependence of bulk modulus, volume and linear compressibilities from 1.5 K to 295 K for $CaWO_4$ single crystals.

	Bulk Modulus	Compressibilities		
		Volume	Linear	
Temp.	K_V	β_V	β_Z	β_{XY}
1.5	7.981	12.53	5.34	3.60
25	7.977	12.54	5.34	3.60
50	7.963	12.56	5.35	3.60
75	7.939	12.60	5.36	3.62
100	7.909	12.64	5.38	3.63
125	7.875	12.70	5.40	3.65
150	7.843	12.75	5.42	3.67
175	7.813	12.80	5.43	3.69
200	7.781	12.85	5.45	3.70
225	7.743	12.92	5.47	3.72
250	7.711	12.97	5.49	3.74
275	7.687	13.01	5.50	3.75
295	7.664	13.05	5.54	3.75
Error(%)	±4	±4	±6	±4
Units	10^{11} dyn cm^{-2}		10^{-13} cm^2 dyn^{-1}	

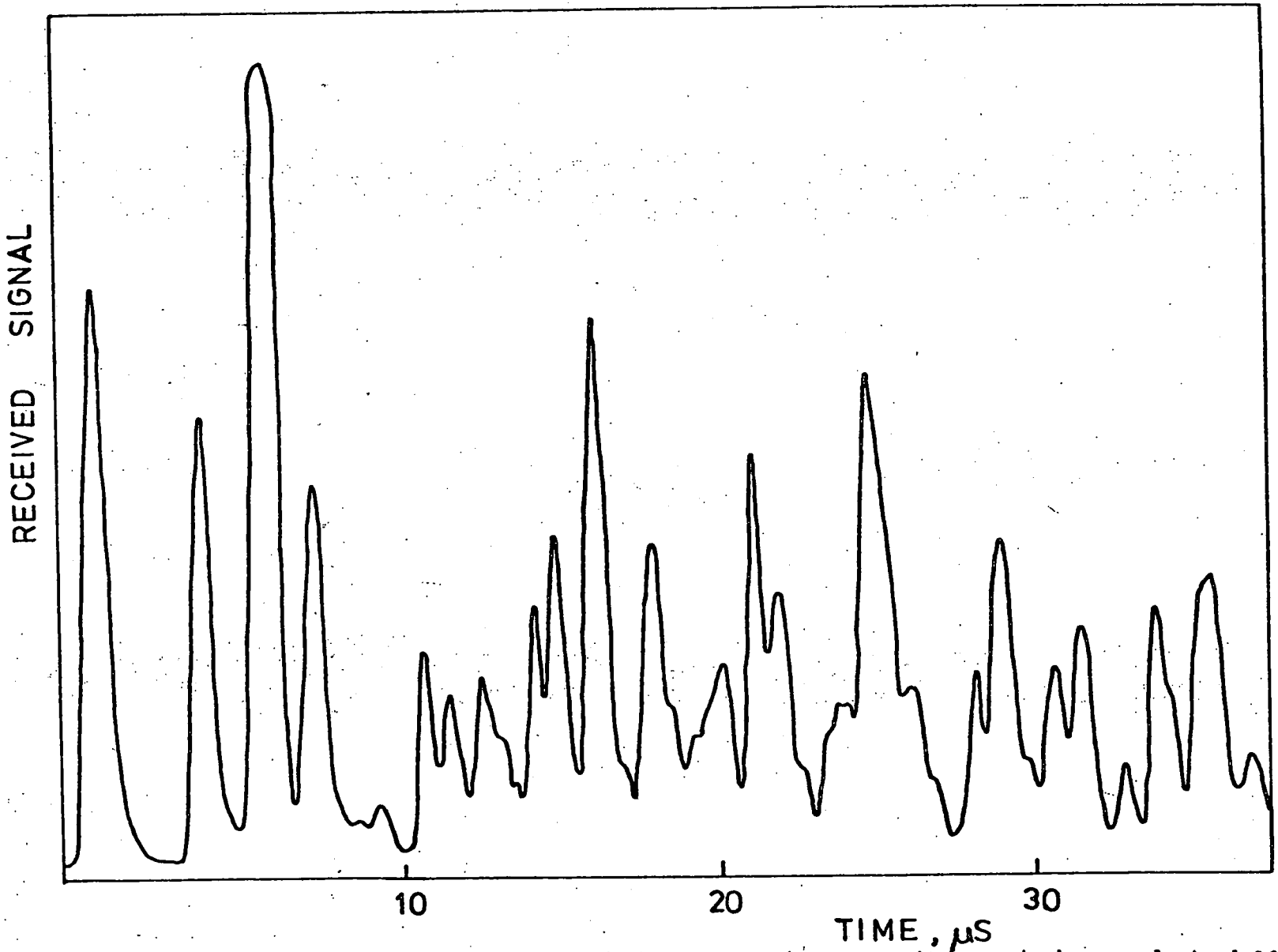

FIGURE 6.1: Typical echo pattern obtained when attempting to excite quasi-shear mode in [100] direction for $CaWO_4$.

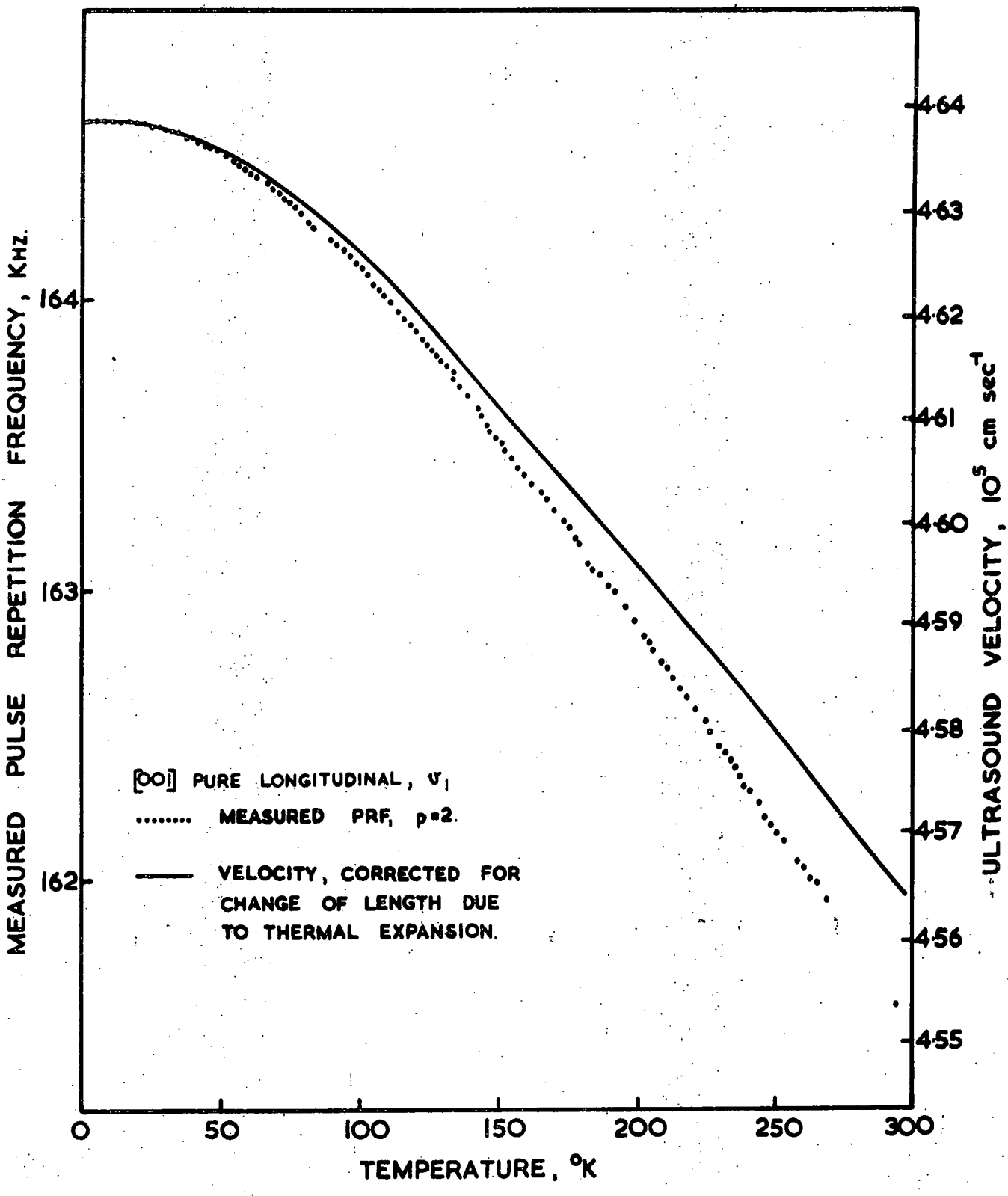
MEASURED PULSE REPETITION FREQUENCY, KHz.
ULTRASOUND VELOCITY, 10^5 cm sec^{-1}
TEMPERATURE, °K
164
163
162
4·64
4·63
4·62
4·61
4·60
4·59
4·58
4·57
4·56
4·55
0
50
100
150
200
250
300
[001] PURE LONGITUDINAL, v_l
..... MEASURED PRF, p=2.
VELOCITY, CORRECTED FOR CHANGE OF LENGTH DUE TO THERMAL EXPANSION.

FIGURE 6·2

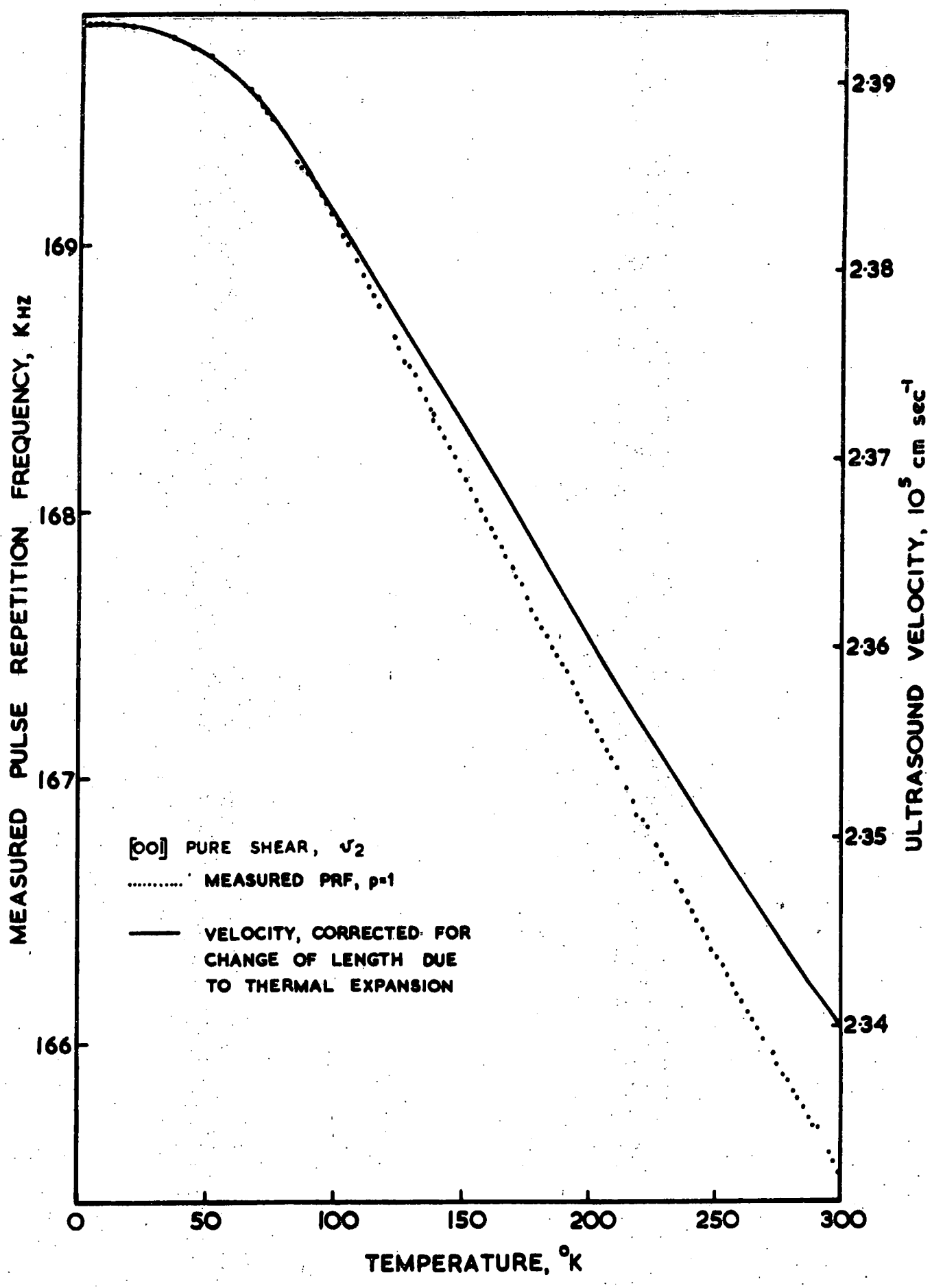
MEASURED PULSE REPETITION FREQUENCY, KHz
ULTRASOUND VELOCITY, 10^5 cm sec^{-1}
TEMPERATURE, °K
169
168
167
166
2·39
2·38
2·37
2·36
2·35
2·34
0
50
100
150
200
250
300
[001] PURE SHEAR, $\sqrt{2}$
MEASURED PRF, p=1
VELOCITY, CORRECTED FOR CHANGE OF LENGTH DUE TO THERMAL EXPANSION

FIGURE 6·3

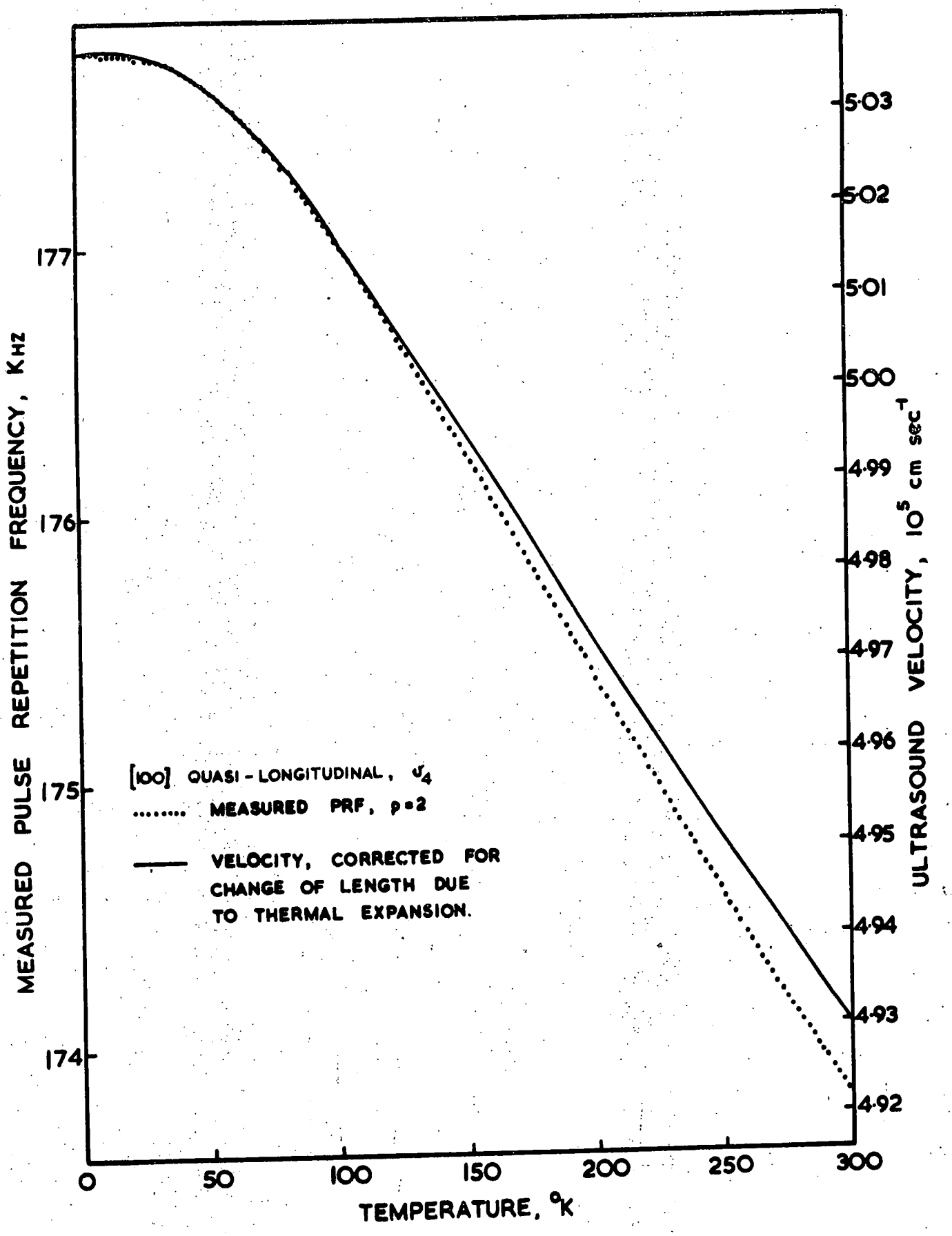

Temperature dependence of the measured pulse repetition frequency and of the ultrasound velocity after taking account of thermal expansion. Direction of propagation : 1, 0, 0. Mode : quasi - longitudinal.

FIGURE 6.4

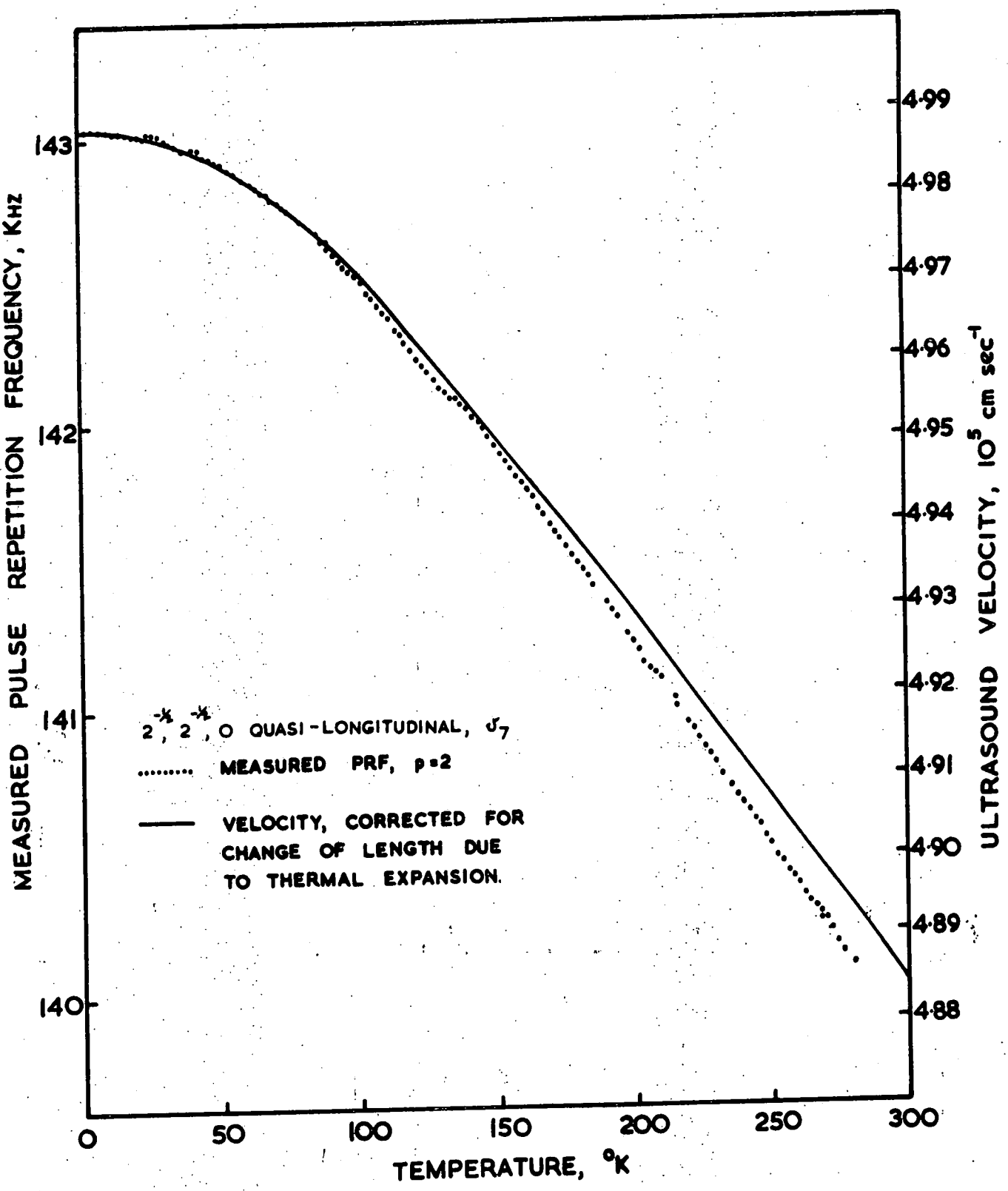
MEASURED PULSE REPETITION FREQUENCY, KHZ
ULTRASOUND VELOCITY, 10^5 cm sec^{-1}
TEMPERATURE, °K
143
142
141
140
4·99
4·98
4·97
4·96
4·95
4·94
4·93
4·92
4·91
4·90
4·89
4·88
0
50
100
150
200
250
300
$2^{-\frac{1}{2}}, 2^{-\frac{1}{2}}, 0$ QUASI-LONGITUDINAL, σ_7
MEASURED PRF, p=2
VELOCITY, CORRECTED FOR CHANGE OF LENGTH DUE TO THERMAL EXPANSION.

FIGURE 6·5

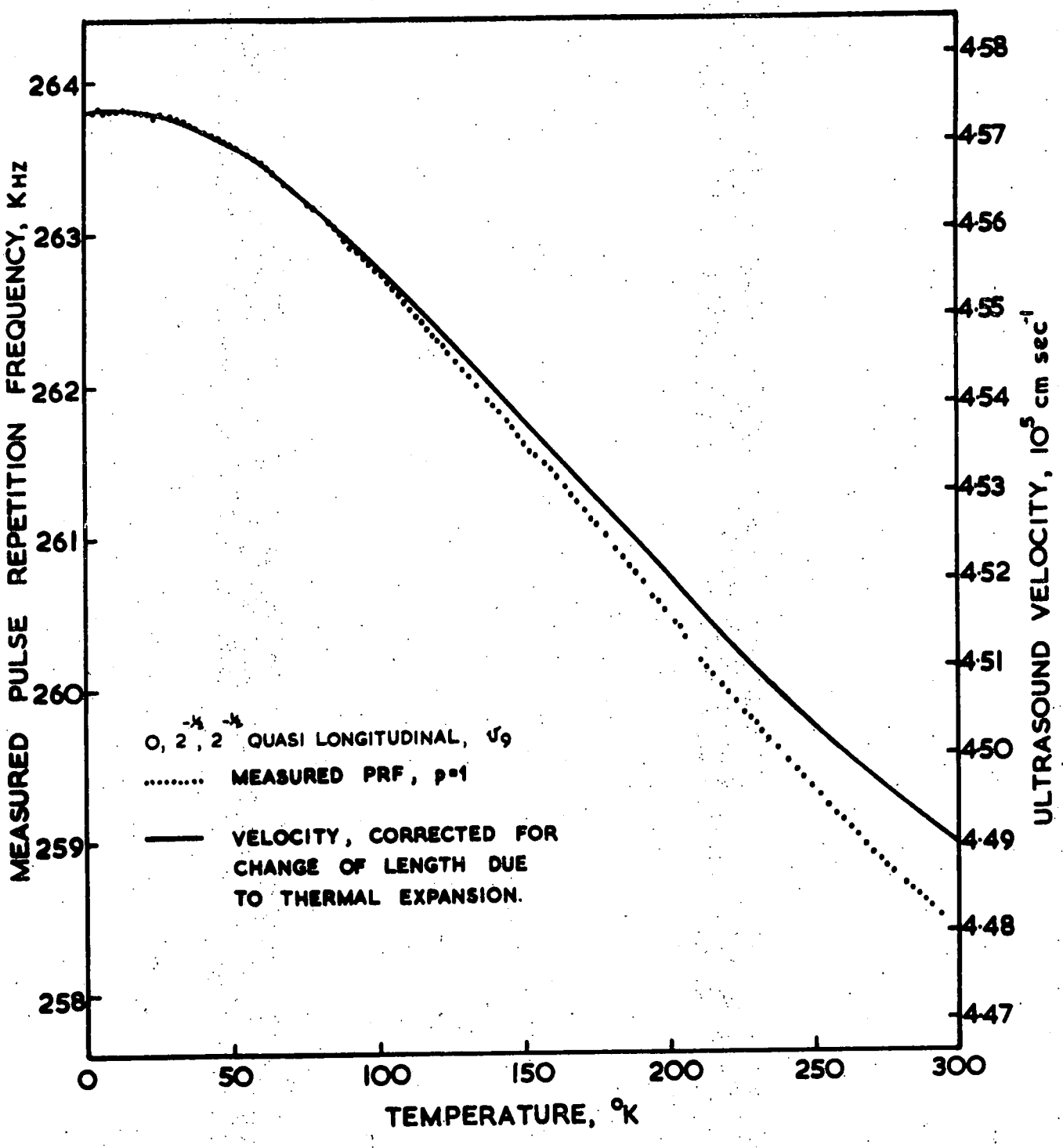
MEASURED PULSE REPETITION FREQUENCY, KHz
ULTRASOUND VELOCITY, 10^5 cm sec^{-1}
TEMPERATURE, °K
264
263
262
261
260
259
258
4·58
4·57
4·56
4·55
4·54
4·53
4·52
4·51
4·50
4·49
4·48
4·47
0
50
100
150
200
250
300
0, $2^{-\frac{1}{2}}$, $2^{-\frac{1}{2}}$ QUASI LONGITUDINAL, ν_9
..... MEASURED PRF, p=1
VELOCITY, CORRECTED FOR CHANGE OF LENGTH DUE TO THERMAL EXPANSION.

FIGURE 6·6

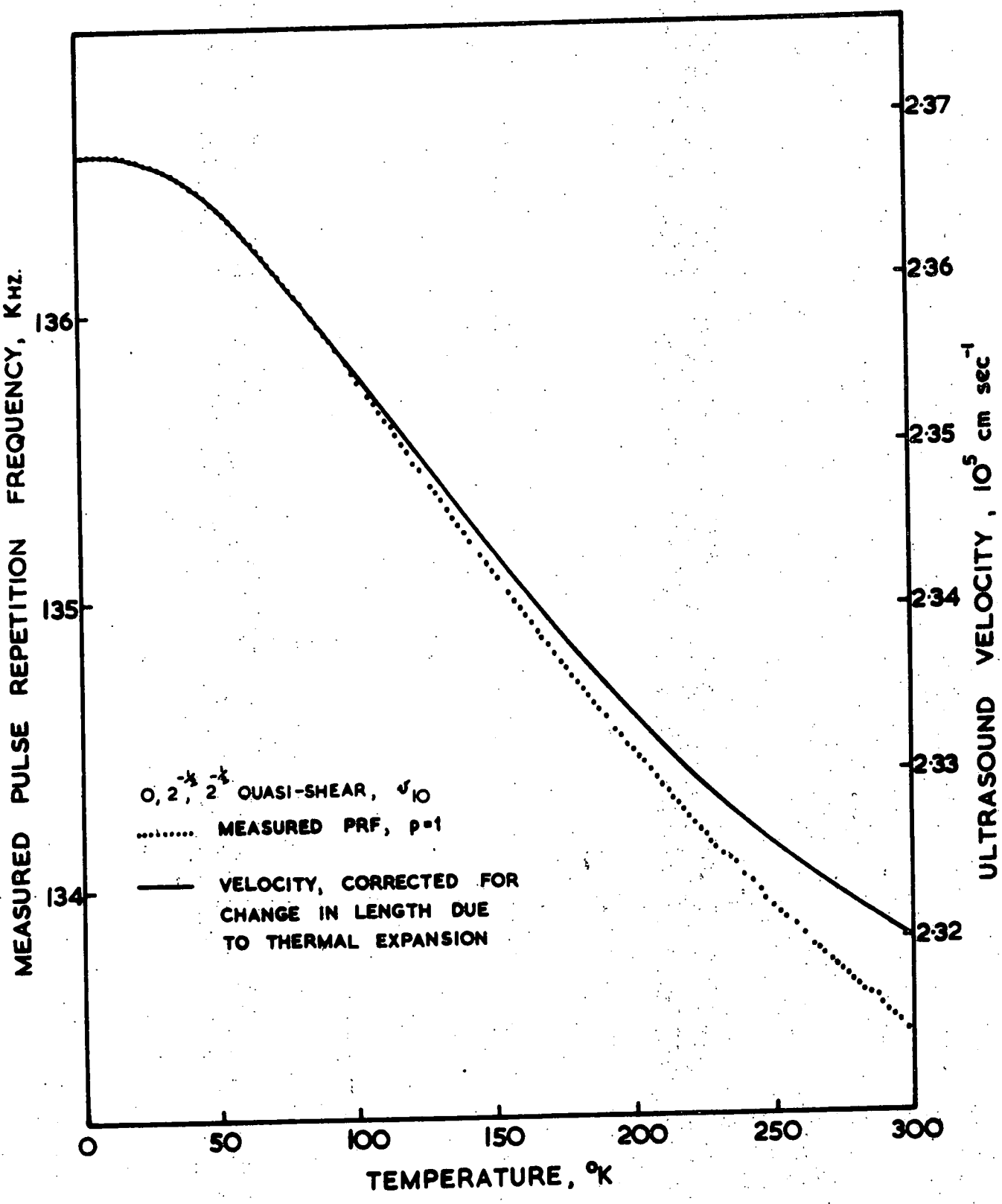
MEASURED PULSE REPETITION FREQUENCY, KHz.
136
135
134
ULTRASOUND VELOCITY, 10^5 cm sec^{-1}
2·37
2·36
2·35
2·34
2·33
2·32
0, 2$^{-\frac{1}{2}}$, 2$^{-\frac{1}{2}}$ QUASI-SHEAR, $\sqrt{10}$
MEASURED PRF, p=1
VELOCITY, CORRECTED FOR CHANGE IN LENGTH DUE TO THERMAL EXPANSION
0
50
100
150
200
250
300
TEMPERATURE, °K

FIGURE 6·7

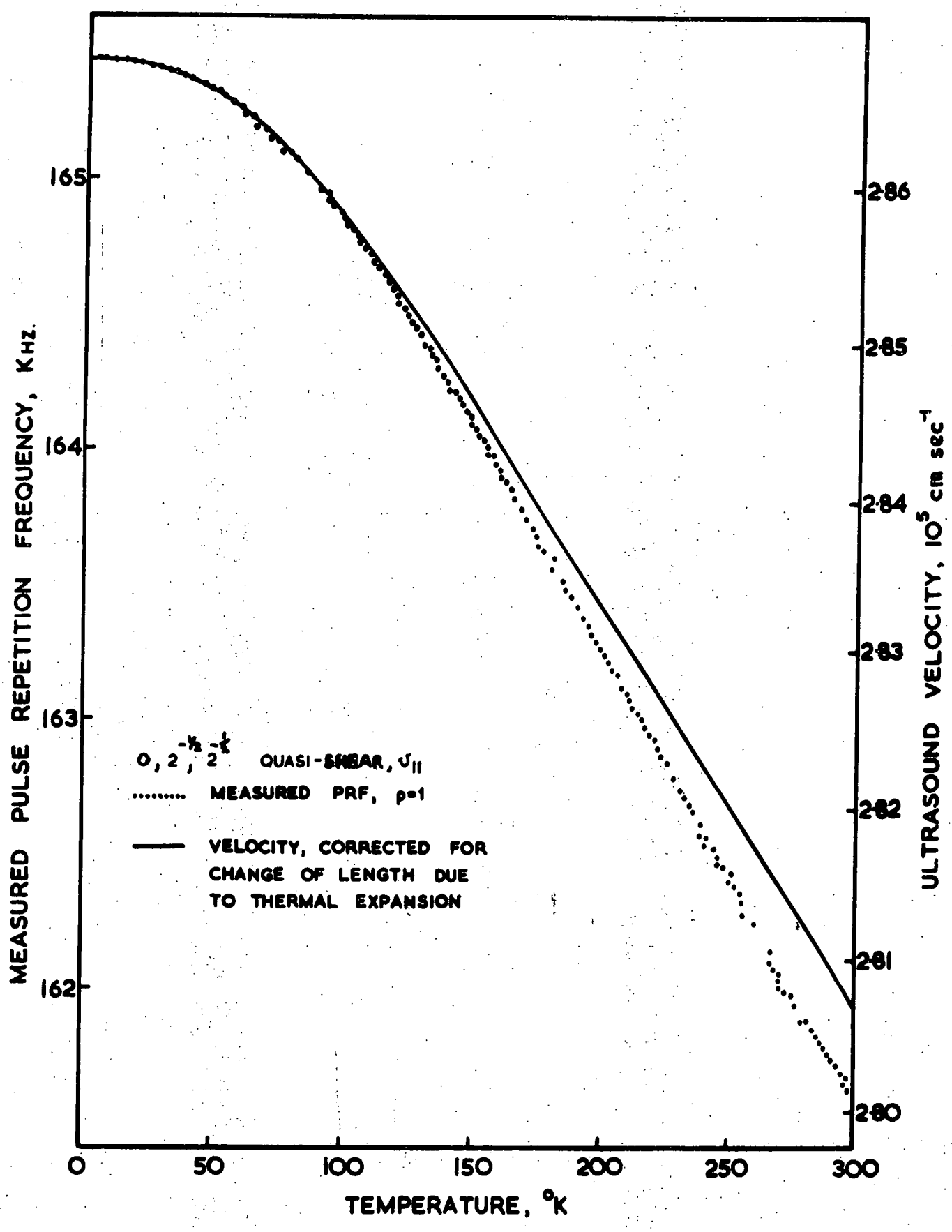
MEASURED PULSE REPETITION FREQUENCY, KHz.
ULTRASOUND VELOCITY, 10^5 cm sec^{-1}
TEMPERATURE, °K
165
164
163
162
2·86
2·85
2·84
2·83
2·82
2·81
2·80
0
50
100
150
200
250
300
0, $2^{-\frac{1}{2}}$, $2^{-\frac{1}{4}}$ QUASI-SHEAR, v_{11}
MEASURED PRF, p=1
VELOCITY, CORRECTED FOR CHANGE OF LENGTH DUE TO THERMAL EXPANSION

FIGURE 6·8

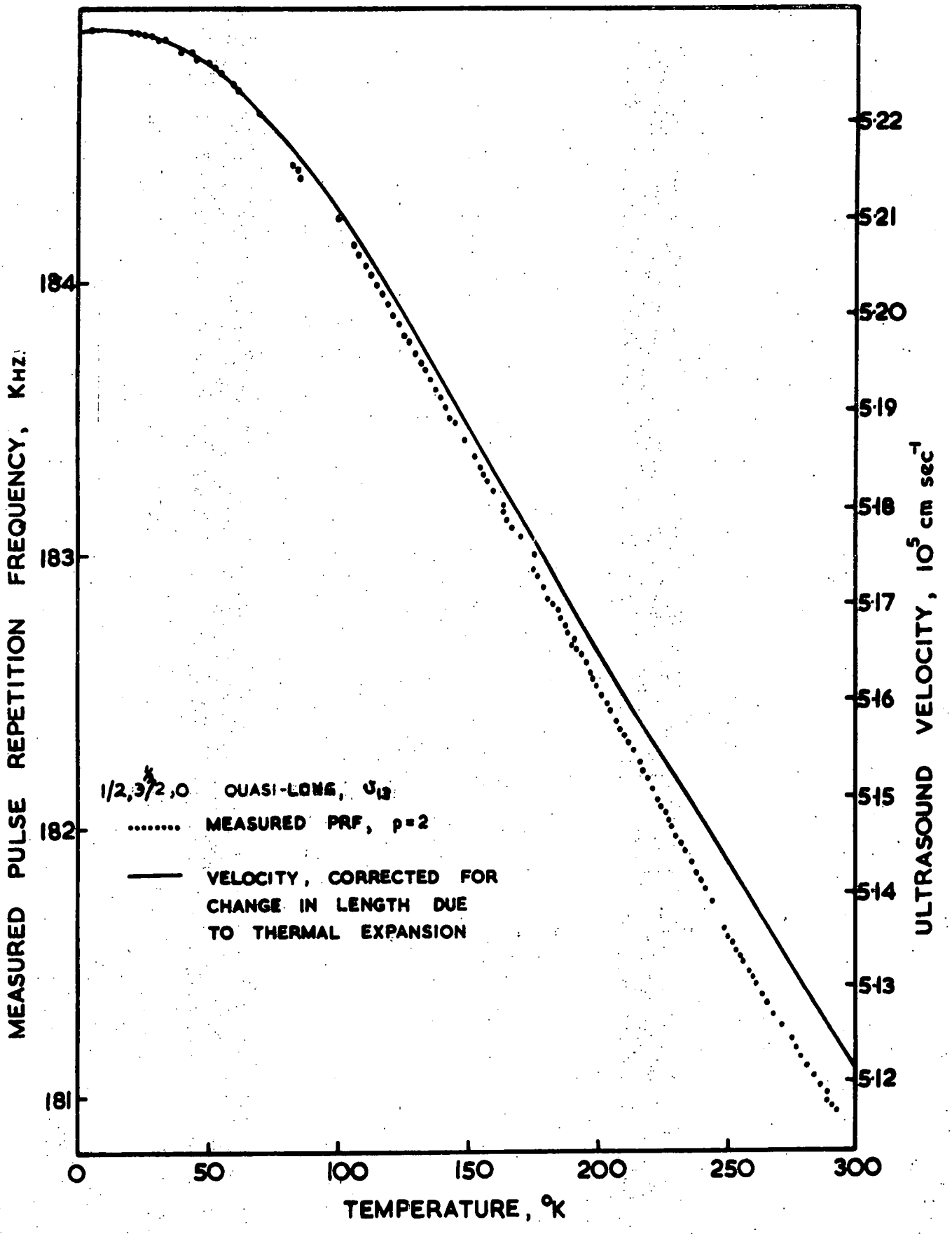
MEASURED PULSE REPETITION FREQUENCY, KHz.
ULTRASOUND VELOCITY, 10^5 cm sec^{-1}
TEMPERATURE, °K
184
183
182
181
5·22
5·21
5·20
5·19
5·18
5·17
5·16
5·15
5·14
5·13
5·12
0
50
100
150
200
250
300
1/2,3/2,0 QUASI-LONG, v_{13}
MEASURED PRF, p=2
VELOCITY, CORRECTED FOR CHANGE IN LENGTH DUE TO THERMAL EXPANSION

FIGURE 6·9

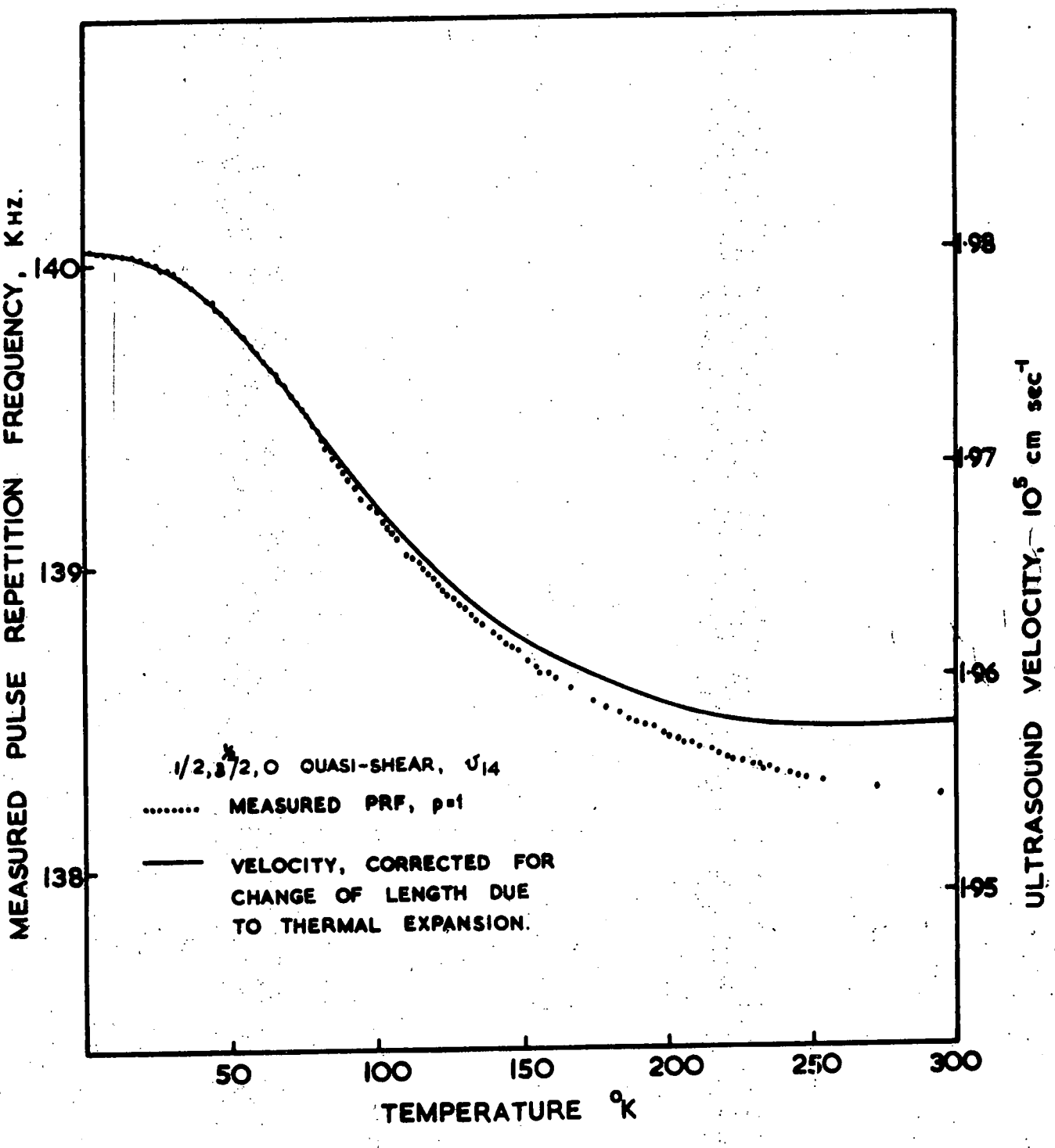
MEASURED PULSE REPETITION FREQUENCY, KHz.
140
139
138
ULTRASOUND VELOCITY, 10^5 cm sec^{-1}
1·98
1·97
1·96
1·95
1/2,3/2,0 QUASI-SHEAR, v_{14}
..... MEASURED PRF, p=1
VELOCITY, CORRECTED FOR CHANGE OF LENGTH DUE TO THERMAL EXPANSION.
50
100
150
200
250
300
TEMPERATURE °K

FIGURE 6·10

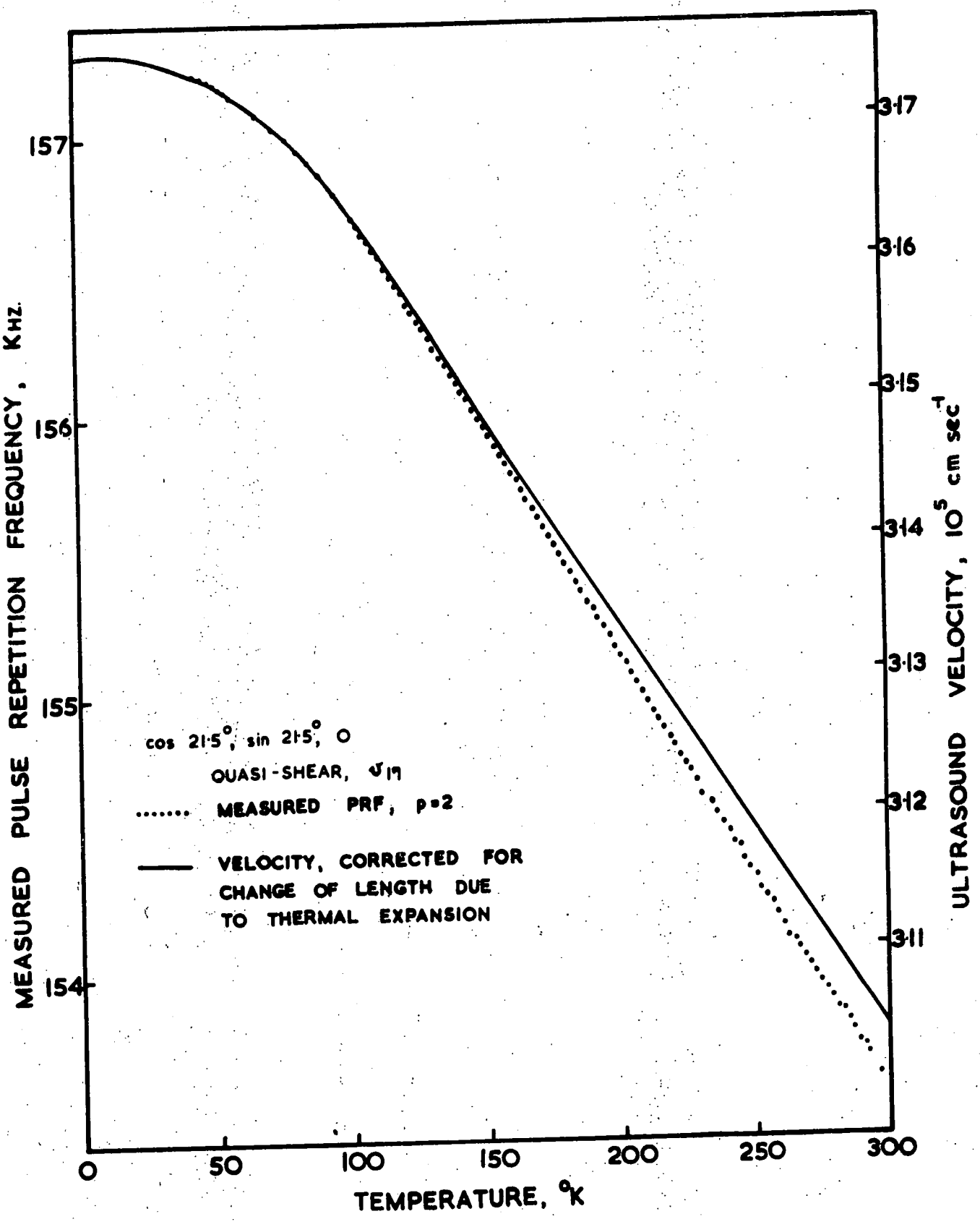
MEASURED PULSE REPETITION FREQUENCY, KHZ.
ULTRASOUND VELOCITY, 10^5 cm sec^{-1}
TEMPERATURE, °K
157
156
155
154
3·17
3·16
3·15
3·14
3·13
3·12
3·11
0
50
100
150
200
250
300
cos 21·5°, sin 21·5°, 0
QUASI-SHEAR, v_{19}
..... MEASURED PRF, p=2
—— VELOCITY, CORRECTED FOR CHANGE OF LENGTH DUE TO THERMAL EXPANSION

FIGURE 6·11

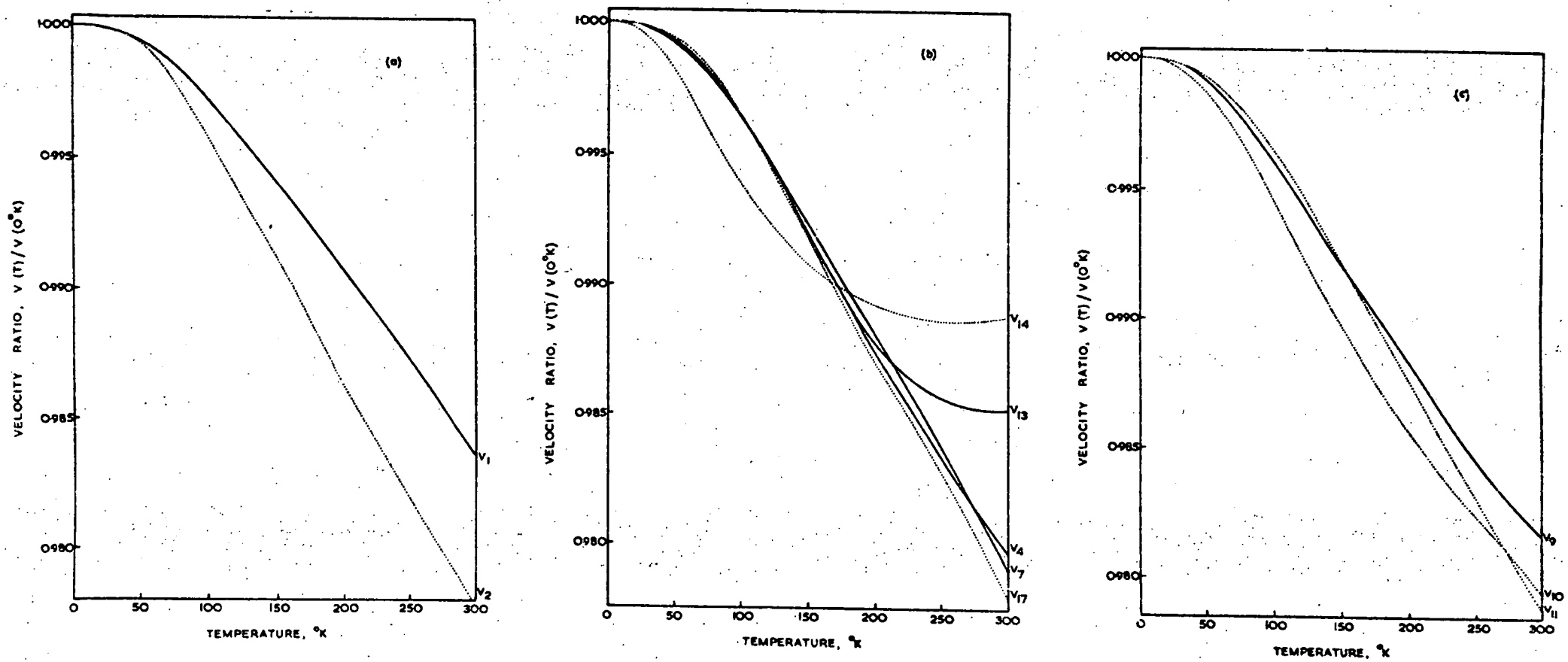

FIGURE 6.12: Temperature dependence of the velocities of modes with propagation vectors (a) in the [001] direction (b) in the (001) plane (c) with direction cosines $0, 2^{-\frac{1}{2}}, 2^{-\frac{1}{2}}$. The labels v_i refer to the modes listed in Table 3.2.

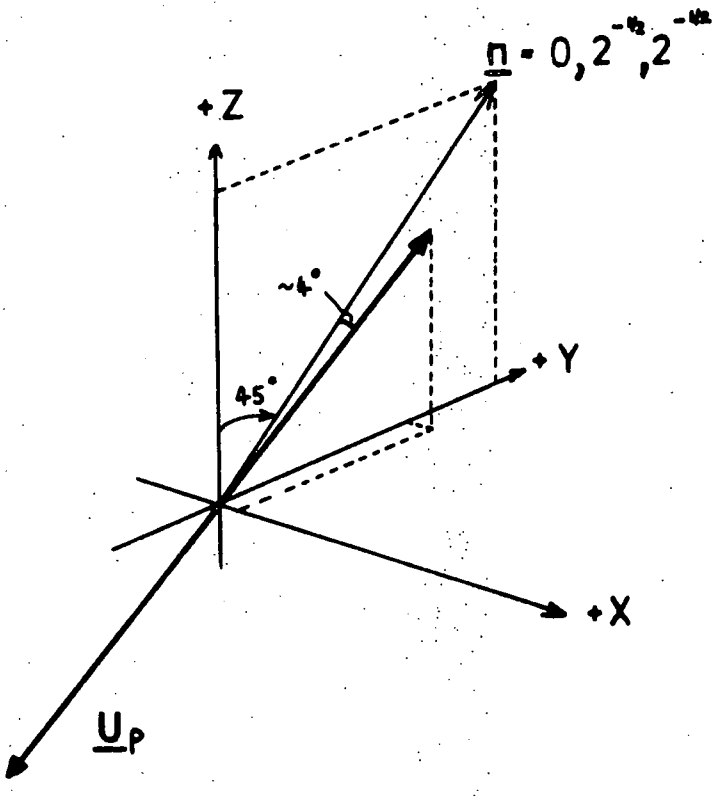

Components of particle displacement for propagation direction $\underline{n}$ (cosines) 0, $2^{-\frac{1}{2}}$, $2^{-\frac{1}{2}}$:

Set P (C_{13} = 3.92x10^{11} dyn cm^{-2})	Set Q (C_{13} = -10.62x10^{11} dyn cm^{-2})
u_1 = 0.084	u_1 = 0.084
u_2 = 0.752	u_2 = 0.752
u_3 = 0.653	u_3 = -0.653
i.e. Set P predicts mode is quasi-longitudinal (as shown in the figure)	i.e. Set Q predicts mode is quasi-shear

FIGURE 6.13: Distinction between solution sets P and Q by computation of the eigenvectors of the fastest mode (propagation in the direction 0, $2^{-\frac{1}{2}}$, $2^{-\frac{1}{2}}$).

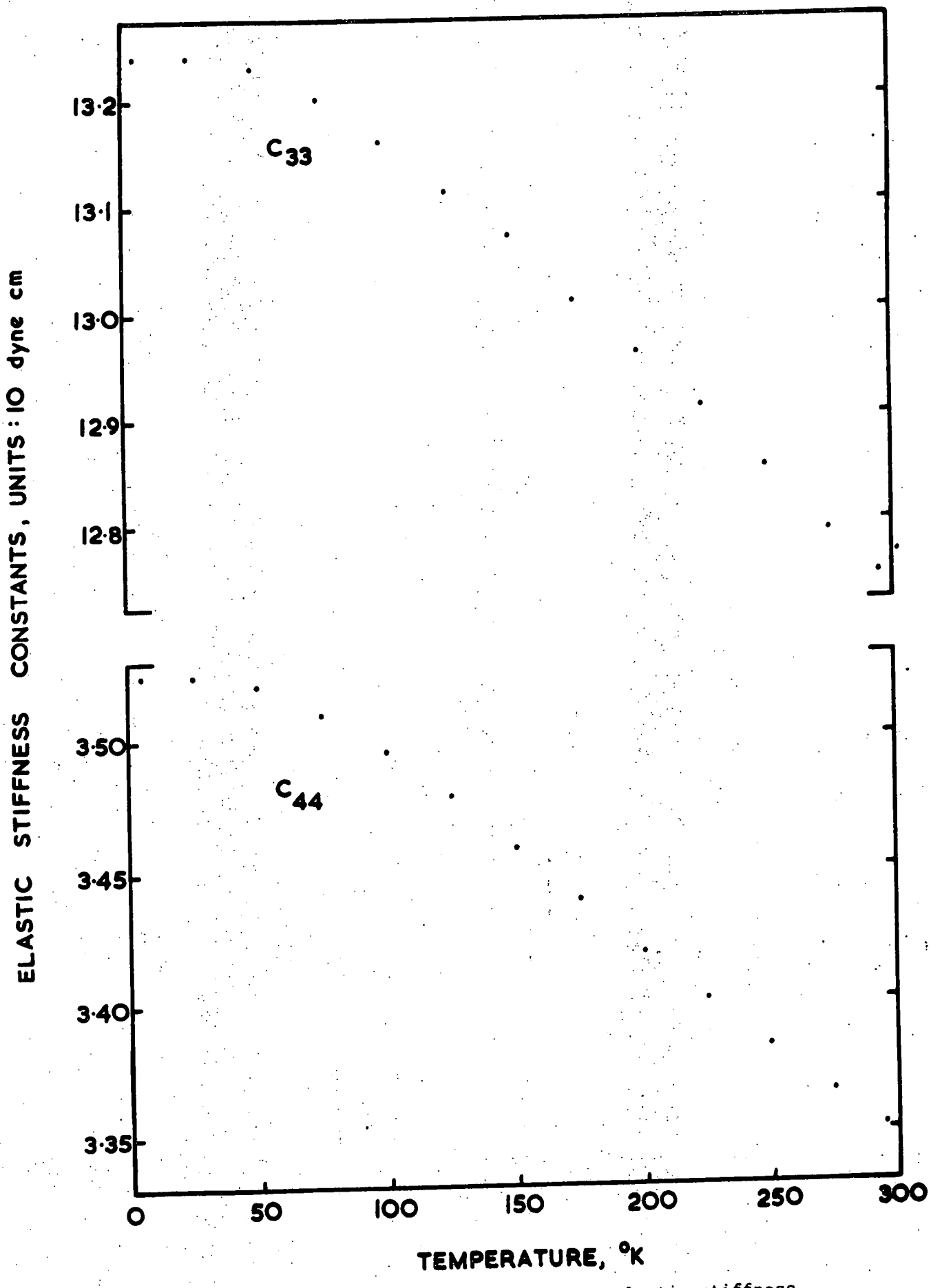

FIGURE 6.14: Temperature dependence of the elastic stiffness constants C_{33} and C_{44} of $CaWO_4$ single crystals.

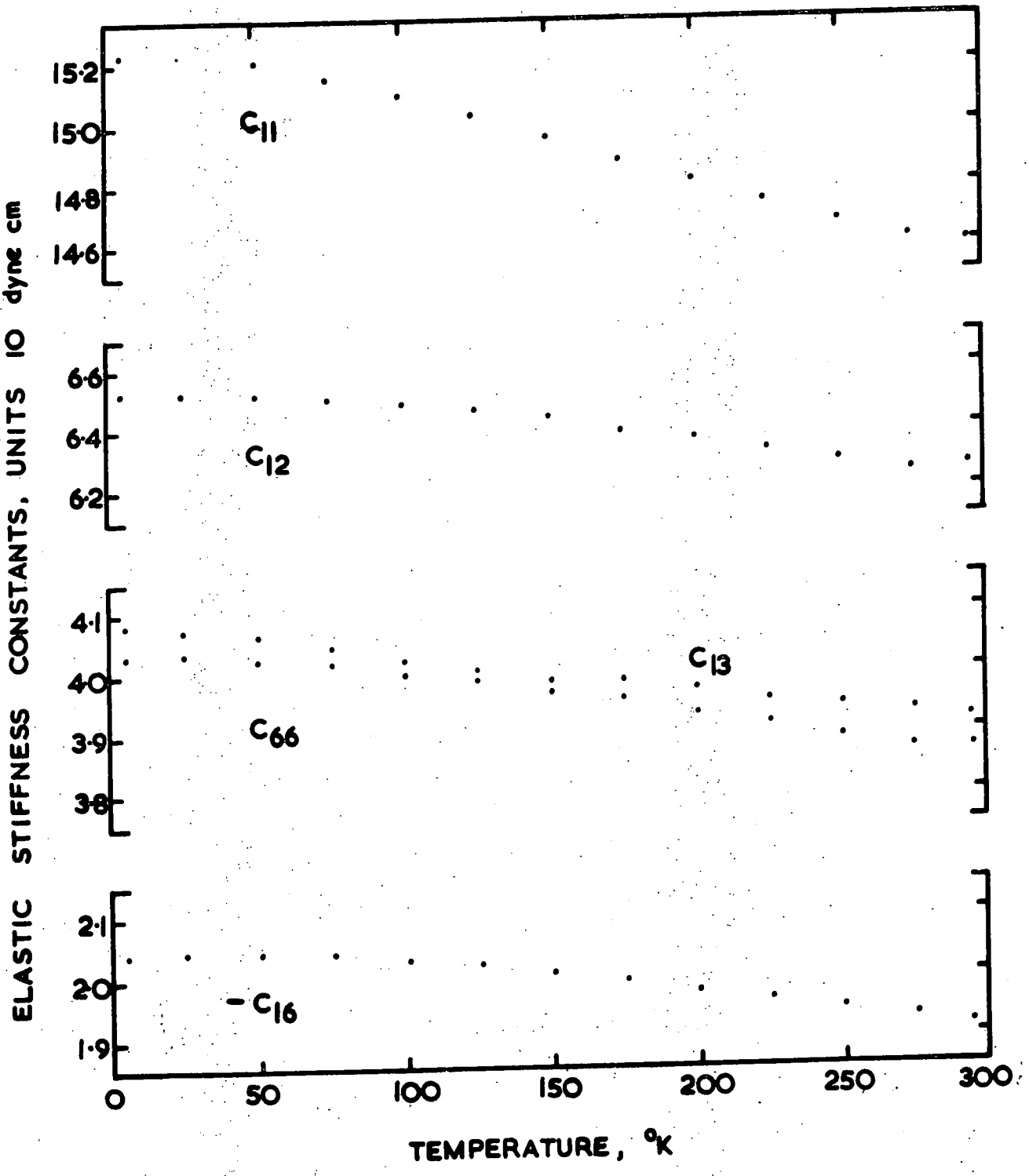

FIGURE 6.15: Temperature dependence of the elastic stiffness constants C_{11}, C_{12}, C_{13}, C_{66} and $-C_{16}$ of $CaWO_4$ single crystals.

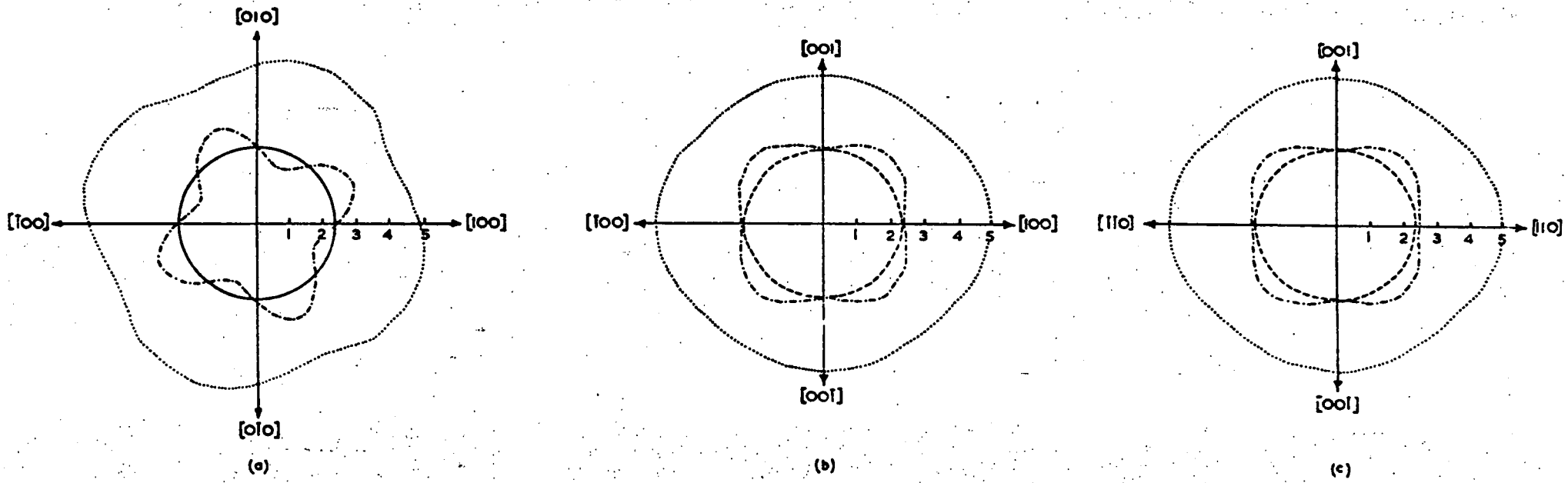

FIGURE 6.16: (a) (001), (b) {100} and {110} cross-sections of the velocity surfaces of $CaWO_4$ at 295 K. Units are 10^5 cm s^{-1}. ..... denotes quasi-longitudinal mode; ---- and -·-·- quasi-shear modes; and —— the pure shear mode.

FIGURE 6.17

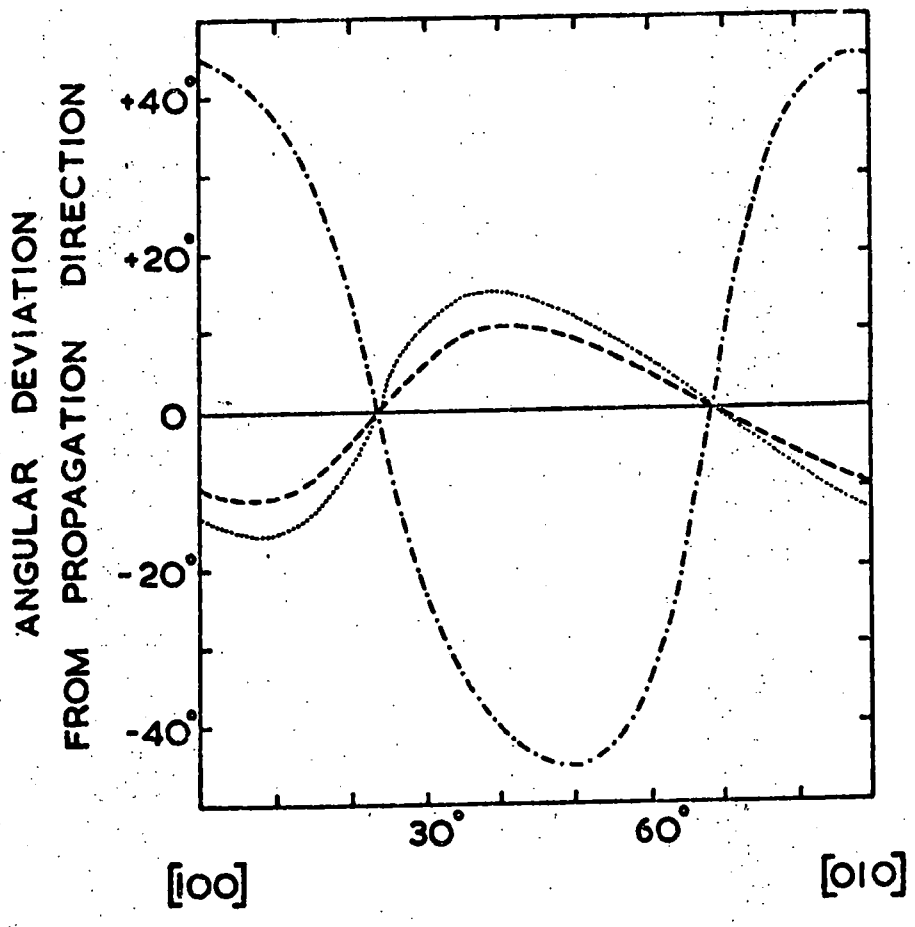

The deviations of energy flux vectors of the quasi longitudinal (·····), and quasi-shear (-·-·-) modes, and of the particle displacement vector of the quasi-longitudinal wave (----), for propagation directions in the (001) plane of $CaWO_4$.

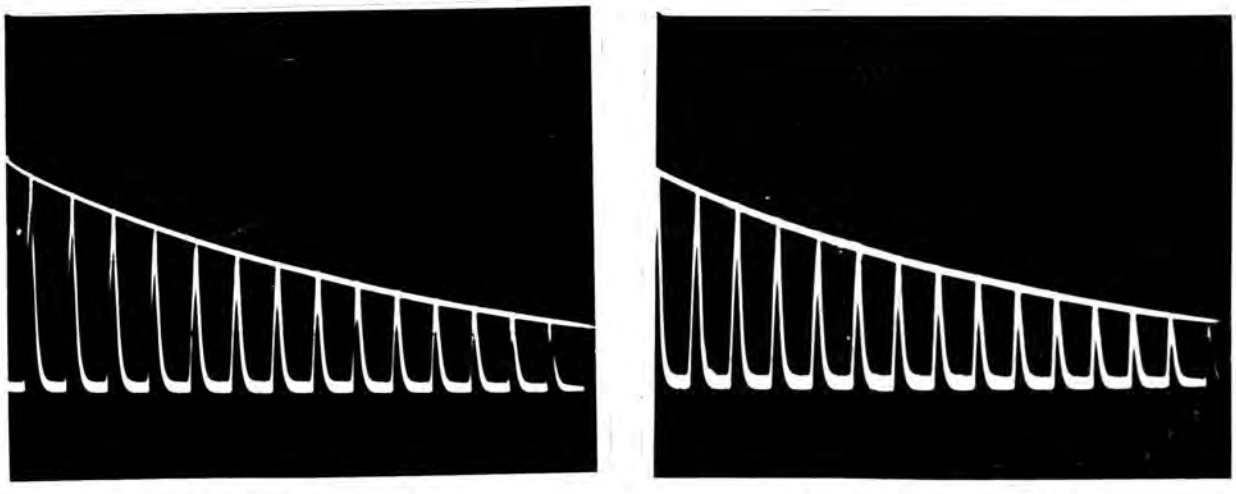

Temperature = 4.2 K

Temperature = 77 K

FIGURE 6.18: Longitudinal echo train, 750 MHz, decay set to 0.308 dB μs^{-1}

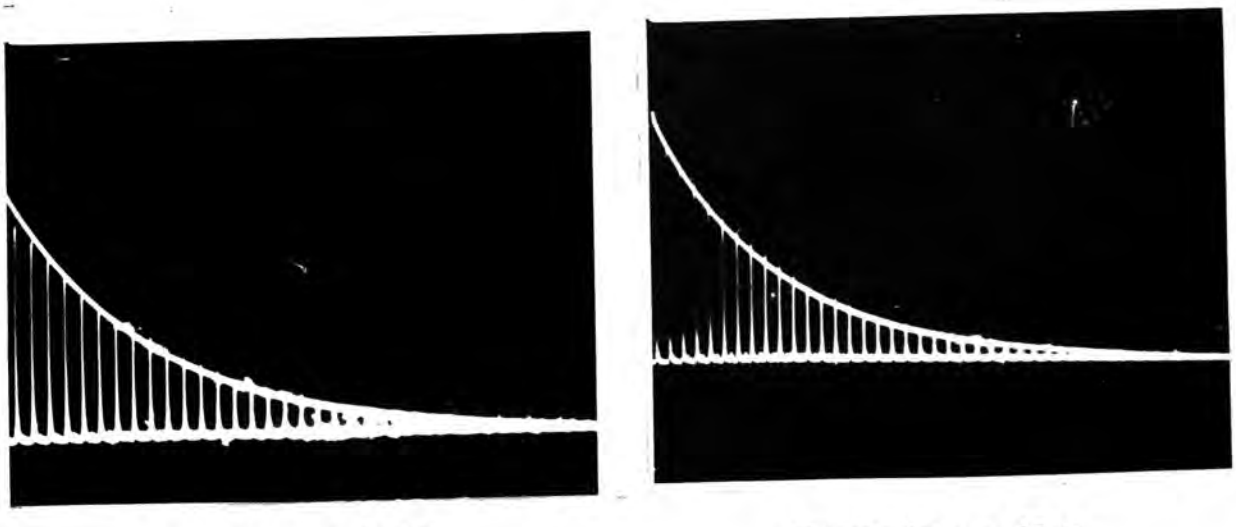

Temperature = 4.2 K

Temperature = 77 K

FIGURE 6.19: Shear echo train, 740 MHz, decay set to 0.205 dB μs^{-1}

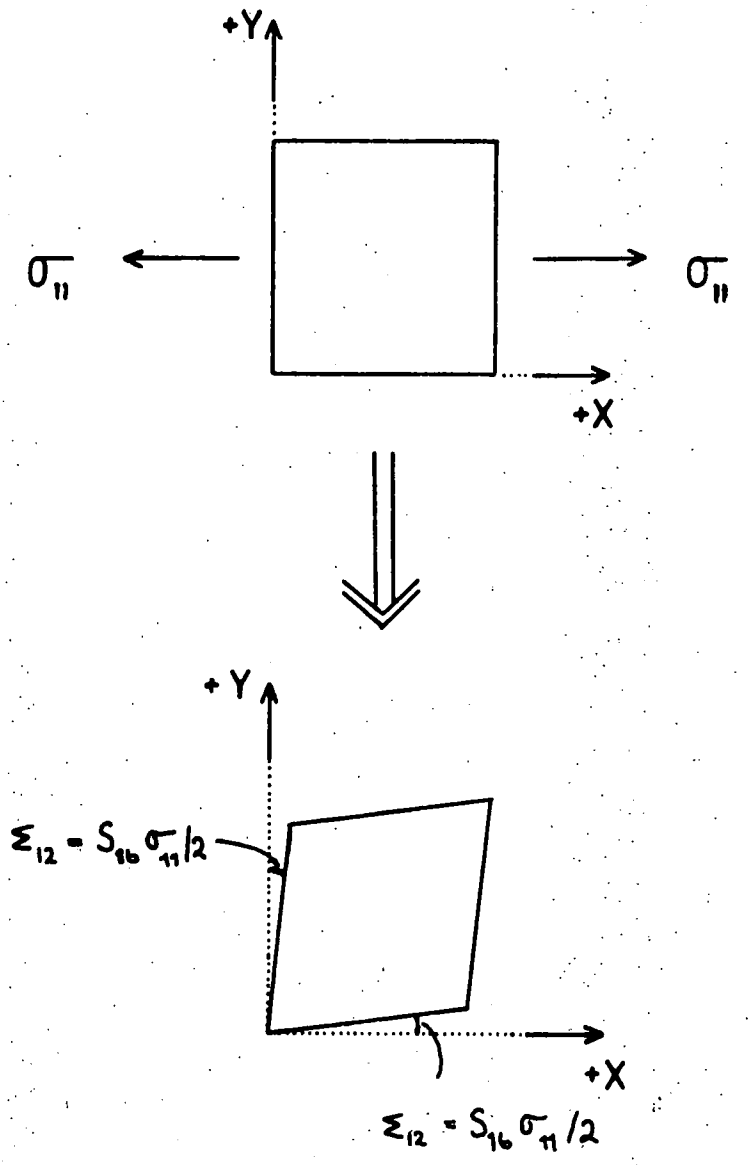

FIGURE 6.20: To show the sense of the response of a single crystal of $CaWO_4$ to a tensile stress (σ_{11}, + ve) applied in the X-direction. S_{16} (= $2S_{1112}$) is positive, and the angle between the +X and +Y axes decreases (ε_{12}, + ve).

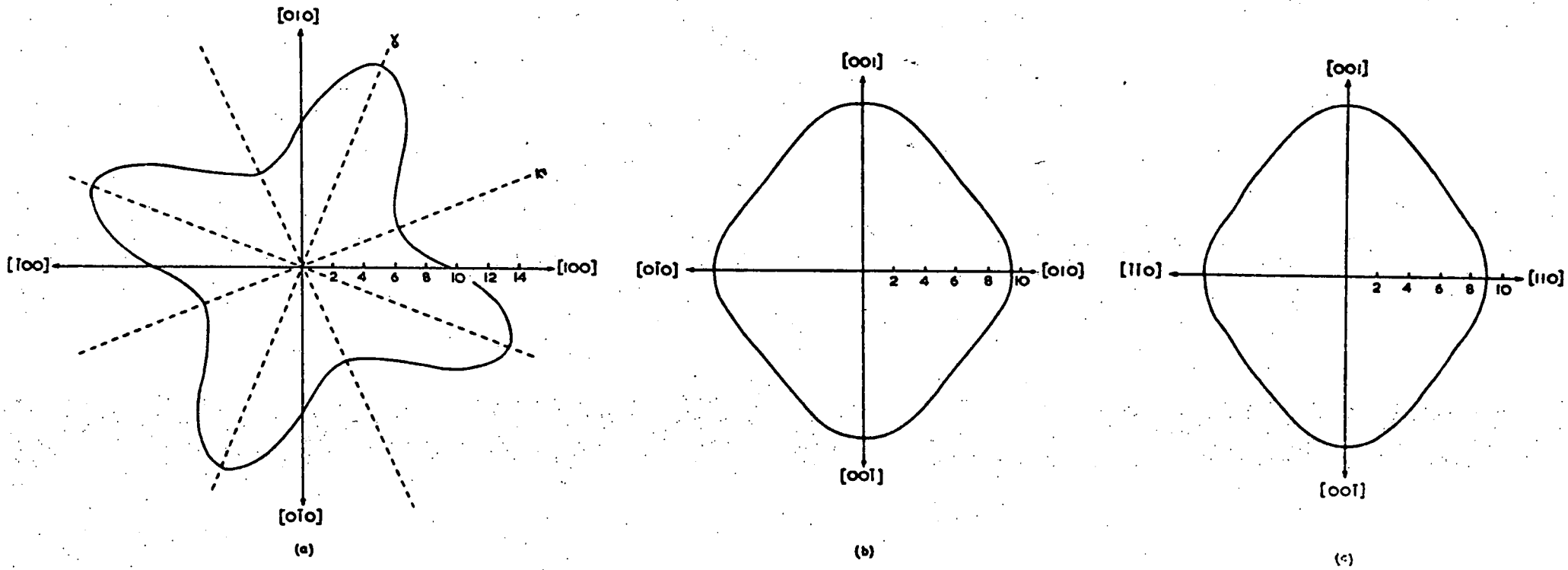

FIGURE 6.21: (a) {001}, (b) {100} and (c) {110} cross-sections of the Young's modulus surface of $CaWO_4$ at 295 K. Units are 10^{11} dyn cm^{-2}.

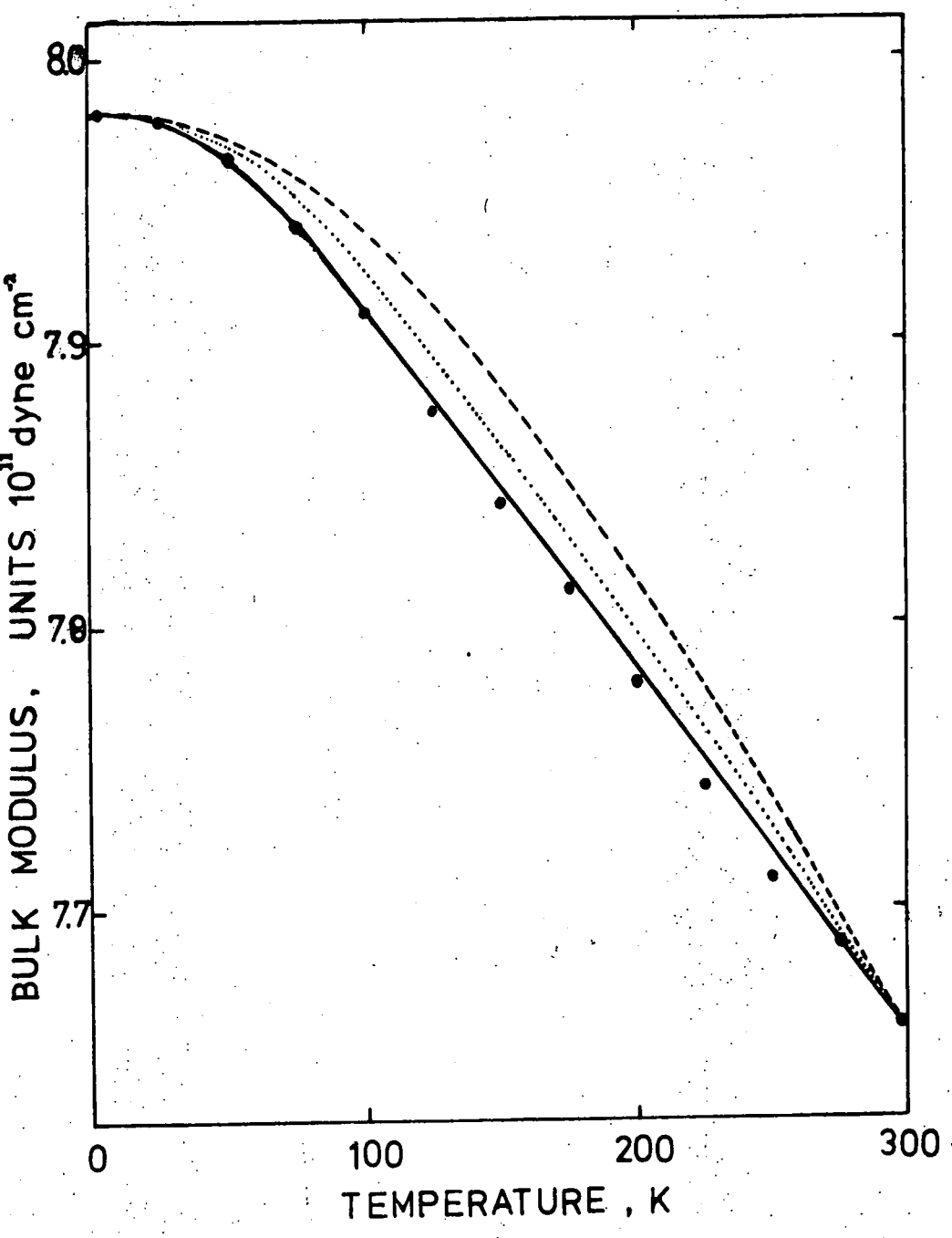

FIGURE 6.22: Temperature dependence of bulk modulus of $CaWO_4$. Solid points (●) are experimental data. The lines ----, ····· and —— are Lakkad fits using effective Debye temperature values of 354 K, 246 K, and 155 K respectively. The fit obtained using the "acoustical-mode only" Debye temperature (155 K) is clearly the best of the three.

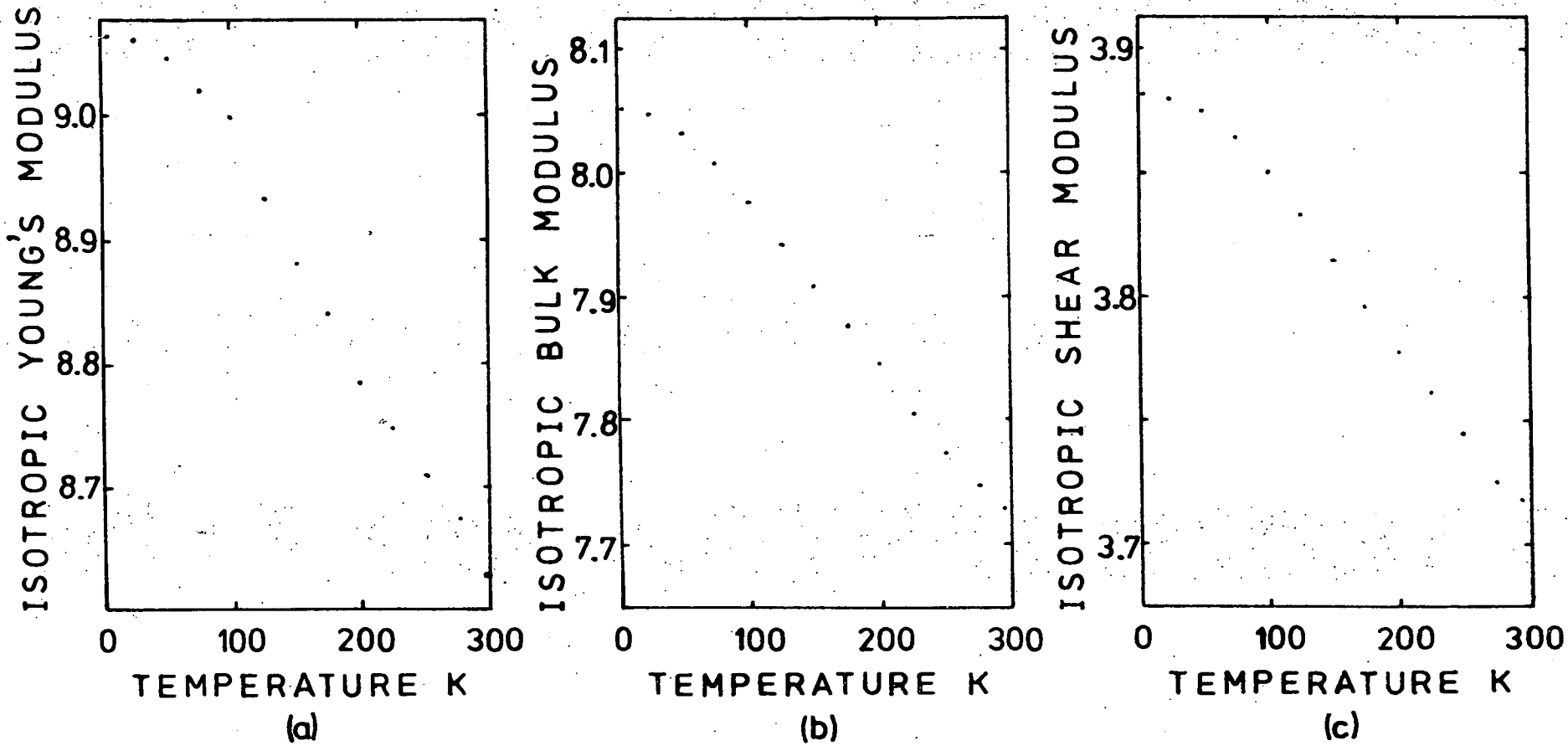

FIGURE 6.23: Temperature dependence of the isotropic Young's, bulk and shear moduli. Units are 10^{11} dyn cm^{-2}.

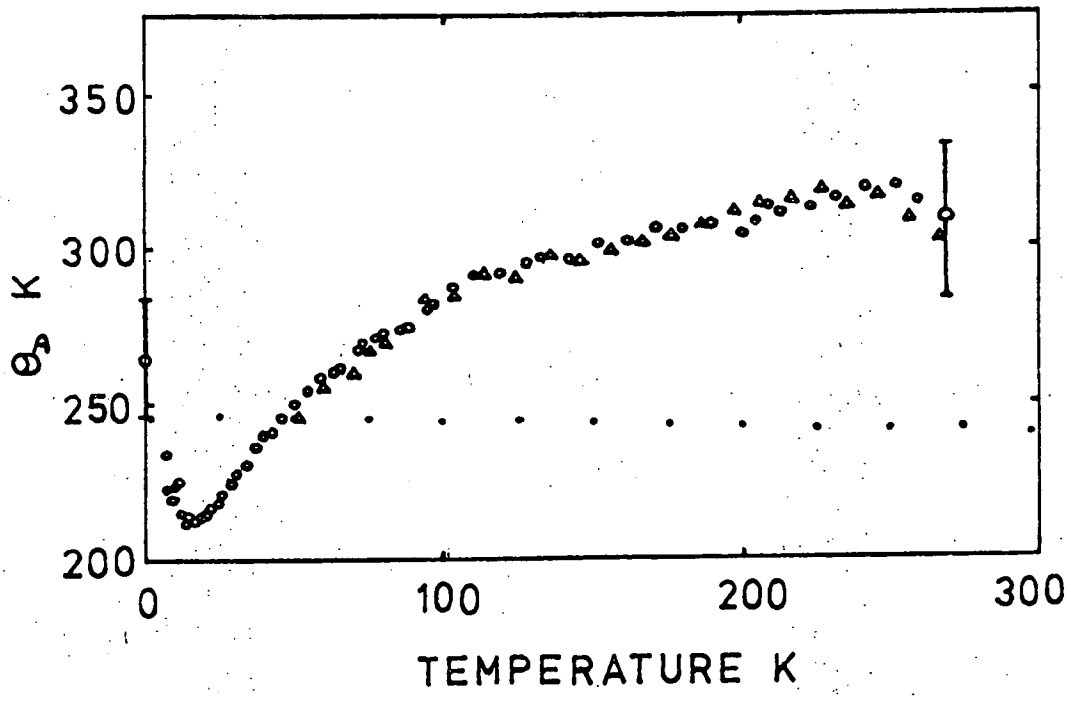

FIGURE 6.24: Variation of $\theta_{D(\text{diatomic lattice only})}$ of $CaWO_4$ with temperature, circles (O) and triangles (Δ) calculated by Yates and Bailey (1971) from specific heat data. Dots (.) calculated from the present elastic constant measurements.

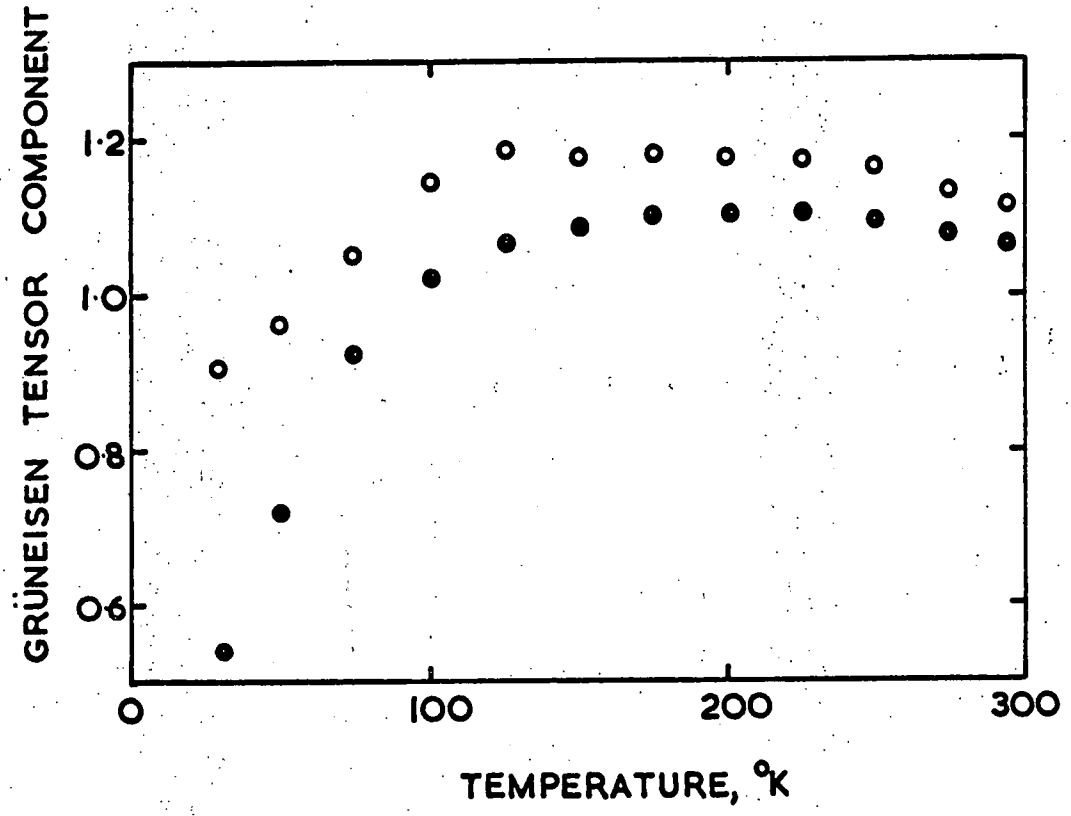

FIGURE 6.25: Temperature variation of the components $\gamma_{\perp}$ (●) and $\gamma_{\parallel}$ (O) of the Grüneisen tensor of $CaWO_4$.

CHAPTER 7

RELATED EXPERIMENTS ON OTHER SCHEELITE STRUCTURE CRYSTALS

Room temperature values of the elastic constants of several scheelite structure crystals have now been measured (Alton and Barlow (1967), Wachtmann et al (1968), Coquin et al (1971), Chung and Li (1971 a,b). To provide a basis for comparison of the elastic properties of the different scheelites with those of $CaWO_4$ the reported data have been carefully examined and reassessed. Some further experimental work on $SrMoO_4$ and $PbMoO_4$ has been undertaken.

7.1 CALCIUM MOLYBDATE

The elastic constants of $CaMoO_4$ were first determined by Alton and Barlow (1967) by an ultrasonic phase comparison technique at 230 MHz. These workers measured the room temperature velocities of the modes numbered v_1 to v_{14} in Table 3.2 and obtained the data reproduced here in Table 7.1. The fourteen equations relating these velocities to the elastic constants do not have a purely analytical solution, but combine (see Table 1† of Alton and Barlow (1967)) to form a quartic which must be solved numerically. Corresponding to the four roots of the quartic there are four equivalent solution sets to the velocity data. For $CaMoO_4$ one solution set could be eliminated because it did not obey the Born criteria for crystal stability, and from the other three Alton and Barlow chose the set which predicted the polarisation vectors of the modes v_4 and v_5 to be most nearly pure and concluded that the elastic constants had the values given here in Table 7.2a.

The minimisation technique employed in Chapter 6 to find elastic constants from ultrasound velocity measurements gives the set of constants which yield the best overall fit to an overdetermined velocity set. Using this technique the $CaMoO_4$ elastic constants have been reassessed, giving the values listed in Table 7.2b. It was found that the parameter SUMSQ — a measure of the quality of the overall fit of the elastic constant solution set to the measured velocity set — was reduced from 0.00047 (the value found

† This table contains some typographical errors. The last two lines of the right hand column should read "$C_{33}^2/4 + 5C_{44}^2/4 + A/2 + B'/4$" and "$C_{44}^2 + B' + 3D'/8 + 3^{\frac{1}{2}}F/2$" respectively.

using the data of Table 7.2a as a starting point for the search) to 0.00009 after 501 cycles of the minimisation procedure. This small value of SUMSQ is an indication of the very good internal consistency in Alton and Barlow's measurements, a consistency which is also apparent from the excellent agreement in the values of $C_{11} + C_{66}$ obtained by summing the squares of the velocities of the quasi-longitudinal and quasi-shear modes for the different propagation directions in the (001) plane that were employed (see Table 7.3). Values of the compliances, the bulk modulus and the linear compressibilities calculated from the elastic constants are given in Table 7.2b. Cross-sections of the velocity surfaces and of the Young's modulus surface have been computed; these are presented in Figures 7.1 and 7.2. Computed values of the deviation of energy flux vector, and quasi-longitudinal particle displacement vector from the propagation direction for modes propagated in the XY plane are given in Figure 7.3.

More recently the elastic constants of $CaMoO_4$ have been measured by Wachtmannet al (1968) using resonance methods. These workers measured the Young's and torsional moduli of 21 rod specimens of different orientations, and found the elastic compliances (S_{ij}) by a least squares fit. In the crystals studied the sense of the Z axis — defined in accordance with the convention outlined here in Section 2.1 — had been found by the x-ray method of Farabaugh et al (1966) and therefore the signs of the elastic constants C_{16} and S_{16} could be determined. S_{16} was found to be positive, and C_{16} to be negative. The basic agreement between the elastic constant data from the two

sources indicates that the choice of solution set made by Alton and Barlow was indeed correct. Both methods of measurement are capable of giving very accurate values for the directly determined stiffnesses or compliances, but in each case the constants obtained only from combinations of many measurements are subject to relatively large uncertainties. The difference in the signs of C_{16} and S_{16} found by Wachtmann et al and Alton and Barlow indicates that the arbitrary choice of Z axis made by the latter workers was opposite to that defined here as the conventional.

7.2 STRONTIUM MOLYBDATE

The first determination of the room temperature elastic constants of $SrMoO_4$ was reported by Chung and Li (1971a, 1971b). These workers used pulse superposition at 45 MHz to measure the velocities of the seventeen modes listed in Table 7.4 and obtained the values given there. From this measured data set the elastic constants were obtained by an analytical solution method. Details of the method of solution are given by Chung and Li (1971b); expressions are obtained for each constant in terms of the measured velocities. The elastic constants which were thus determined are listed in Table 7.5.

In the course of the present work it became apparent that there were inconsistencies in the velocity data reported in the above study. It was stated earlier (Section 3.2.3 of this thesis) that there is a useful cross-check on the measured velocities of modes propagated in the XY plane of tetragonal crystals: for all such

propagation directions the sum of the squares of the wave velocities of the quasi-longitudinal and quasi-shear modes, multiplied by the crystal density must equal $C_{11} + C_{66}$. This rule is not obeyed by the published velocities (see Table 7.6) — the equality does not hold within the bounds permitted by the possible experimental error (± 4%).

7.2.1 Experimental study of $SrMoO_4$

To discover the origin of the inconsistencies and to provide a corrected set of elastic constants further measurements of ultrasonic velocities in $SrMoO_4$ were required. Dr. Chung very kindly offered the loan of his specimens, and thus made it possible for the measurements reported here to be made. A systematic experimental study has been conducted to find the cause of the errors, to find the correct values of the elastic constants and to determine the signs of the constants C_{16} and S_{16}.

The specimens were those used in Chung and Li's original work. They had been cut from boules grown at the National Bureau of Standards to yield rectangular parallelopipeds with end-faces normal to the required propagation directions. They were nominally pure, colourless and had the dimensions given in Table 7.7. Laue back reflection photographs were obtained using 40 kV radiation from a Cu target; spots were sharp and no splitting was apparent. The photographs showed the pseudo-ditetragonal symmetry also observed in $CaWO_4$. It was confirmed that each specimen was monocrystalline. The orientations were checked by back reflection techniques and found to be within $\pm 1^{o}$ of

the directions specified by Chung and Li and listed here in Table 7.4. One possible cause of the inconsistencies in the published velocity data — gross misorientation of some of the specimens — was thus excluded.

The original work had not taken account of the sense of the Z axis in the crystal specimens, and therefore could not have given the signs of the constants C_{16} and S_{16}. Only in samples E and F (each cut to yield propagation directions in the XY plane, 60° apart and 30° on either side of the X axis) do the sound velocities depend on the signs of these constants, and thus on the sense of the Z axis. It was possible to orient these $SrMoO_4$ samples uniquely by the x-ray method of Farabaugh et al (1966); clear intensity differences were observed between pairs of spots $(hk\ell)$ and $(kh\ell)$ and were compared with intensity differences predicted by using the known atomic coordinates for $SrMoO_4$ (see Table 2.1) and the structure factor equations for the $I4_1/a$ space group of the scheelite structure.

The structure factor (F) is given by (International Tables of x-ray Crystallography 1952):

$$F(hkl) = \left\{ \left[\sum_r f_r A_r \right]^2 + \left[\sum_r f_r B_r \right]^2 \right\}^{\frac{1}{2}} \qquad (7.1)$$

where f_r are the atomic scattering factors ,

$$A_r = G_r \cos\left(\frac{2k+\ell}{8}\right) ,$$

$$B_r = G_r \sin\left(\frac{2k+\ell}{8}\right) ,$$

and

$$G_r = 8\left[\cos^2 2\pi\left(\frac{h+k+\ell}{4}\right)\right]\left[\cos 2\pi(hx+ky)\cos 2\pi\left(\ell z-\frac{2k+\ell}{8}\right) + \cos 2\pi(hy-kx)\cos 2\pi\left(\ell z+\frac{2k+\ell}{8}\right)\right]$$

For $SrMoO_4$ the summations are taken over the three types of atom present. Coordinates x_r, y_r, z_r are the atomic coordinates of any one of the equivalent positions at which a particular atom is sited. The expressions for A_r and B_r are obtained by summing over all the equivalent positions in a unit cell. In the experimental situation where an x-ray beam directed parallel to the Z axis is normally incident on a flat crystal face, the relative intensities of a pair of spots (hkℓ; khℓ) are predicted directly by the ratio of the squares of the structure factors for the two reflections. In such a case the absorption, Lorentz and polarisation corrections are the same for the pair of reflections.

Farabaugh et al (1966) found for $CaMoO_4$ that the biggest differences of intensity were observed in the pairs (1,3,18), (3,1,18); (1,2,11), (2,1,11); (1,2,13), (2,1,13); (2,1,15), (3,2,15). The relative intensities of these pairs were therefore calculated for $SrMoO_4$. Since the atomic scattering factors (f_r) are themselves functions of the Bragg angle (θ) and the x-ray wavelength (λ), it was first necessary to calculate the interplanar spacing (d) corresponding to the reflections listed above. The scattering factors are tabulated (International Tables for X-ray Crystallography 1952) for different atoms as functions of $\frac{\sin\theta}{\lambda}$ (equal to 1/2d by the Bragg law). Appropriate values of f_r can therefore be obtained by interpolation, and the relative values of $|F|^2$ can be computed from equation (7.1). A programme written for this purpose is included in Appendix I.

The computer programme was first checked by repeating the calculations of Farabaugh et al (1966) for $CaMoO_4$, using in turn three different sets of atomic coordinates for the oxygen atoms, namely (i) those for $CaMoO_4$ determined by Sillén and Nylander (1943), (ii) those for $CaWO_4$ found by Zalkin and Templeton (1964) and (iii) those found by Gürmen et al (1971) in their recent neutron diffraction study of $CaMoO_4$ (see Table 2.1). It was found that the intensity differences predicted by set (i) did not completely agree with those which were observed by Farabaugh et al (1966) whereas those predicted by sets (ii) and (iii) did.

For $SrMoO_4$, using the oxygen atomic coordinates determined for this material by neutron diffraction (Gürmen et al 1971) it was calculated that the intensity differences ($I(3,1,18) < I(1,3,18)$, $I(2,1,13) > I(1,2,13)$, $I(2,1,11) > I(1,2,11)$, $I(3,2,15 < I(2,3,15)$) should be similar to those which are seen for $CaMoO_4$. The sense of the Z axis which emerged from an {001} face on which an x-ray beam was normally incident could therefore be identified by comparison of the observed intensity differences with those predicted by the calculation. In this way, sample E was found to have an orientation $3^{\frac{1}{2}}/2$, 1/2, 0 while sample F was 1/2, $3^{\frac{1}{2}}/2$, 0.

Ultrasound velocities were then remeasured by the single-ended pulse echo technique at 15 MHz using 5 mm diameter quartz transducers. Dow resin 276-V9 proved to be a satisfactory bond at room temperature for both X-cut and Y-cut transducers. With this bonding material it was possible to slide the transducer to different positions on

the "end-faces" of the specimen; transit times were measured for different transducer positions. The velocities of the modes numbered v_1, v_2, v_3, v_4, v_6, v_7, v_9, v_{10}, v_{11}, v_{12}, v_{13}, v_{15}, v_{16} and v_{17} were found to agree within the combined experimental errors with those reported previously (see Table 7.4), but for the quasi-shear modes numbered v_5, v_8 and v_{14} it was found that reproducible measurements of transit times could not at first be obtained. The samples B, C and E used for measuring these velocities had each been cut as shown in Figure 7.4 so that the shortest edge of the parallelopiped was parallel to the [001] direction, the longest edge was parallel to the propagation direction n_1, n_2, 0 used in the initial measurements and the third edge was parallel to the direction $-n_2$, n_1, 0 (equivalent by the fourfold symmetry to n_1, n_2, 0). For each of the samples B, C and E it was found that for different positions of Y-cut transducers on the smallest end-faces, different sets of echo patterns with different transit times could be observed. The magnitude of the energy flux deviation which had been encountered in $CaWO_4$ (see Figure 6.17) for propagation of quasi-shear modes in the XY plane suggested that these different echo patterns might have arisen due to the ultrasound beam impinging on the sample walls, suffering mode conversion and finding its way back to the transducer by various different routes. Indeed the geometry of the samples was such that an energy flux deviation greater than about 20° was bound to give rise to wall reflections if 5 mm diameter transducers were used.

Transducer/sample configurations were then devised so as to allow for such large energy flux deviations. This was possible without re-cutting the specimens. Quasi-shear waves were excited by bonding transducers to the long and narrow faces of the three specimens. By positioning the transducers towards the appropriate ends of such faces the energy flux deviations could be accommodated, as shown in Figure 7.5. Indeed experiments using separate transmitting and receiving transducers showed that only for a position of the transmitter which accommodated the relevant deviation of energy flux was it not possible to detect the ultrasound beam with transducers sited on the side-walls (the ends of the parallelopiped) of the sample. Reproducible values of the velocities v_5, v_8 and v_{14} were thus obtained. These values (see Table 7.4) were quite different, and in fact somewhat larger than those reported by Chung and Li (1971). The reassessed velocities were found to give good agreement for the cross-check on the value of $C_{11} + C_{66}$ (Table 7.6).

7.2.2 Corrected set of elastic constants

Elastic constants were then obtained from the velocities of all seventeen modes by use of the least-squares minimisation procedure. The velocities used were v_1, v_2, v_3, v_4, v_6, v_7, v_9, v_{10}, v_{11}, v_{12}, v_{13}, v_{15}, v_{16}, v_{17} as measured previously by pulse superposition (Chung and Li 1971b) and the velocities v_5, v_8 and v_{14} reassessed here by the simple pulse echo method. The density value $\rho = 4.54$ g cm^{-3} was used. A good fit was obtained; after

501 cycles SUMSQ had the value 0.0036. Velocities calculated from the elastic constants which were obtained agreed with the measured velocities to within ± 2%. By using different starting values of C_{ij} for the search procedure it was possible to obtain four different, equivalent solutions. In the same way as was used for $CaWO_4$ (see Section 6.1.2) all but one of these were eliminated. The values of the elastic constants obtained, with the corresponding compliances and compressibilities are given in Table 7.5. The large discrepancies between the values reported by Chung and Li (1971a, b) for C_{16}, C_{66} and some of the derived constants and the values found here are immediately apparent. This present work has allowed the signs of the constants C_{16} and S_{16} to be determined for the conventional sense of the Z axis. C_{16} is negative and S_{16} is positive. The signs of these constants are therefore the same as those found for $CaWO_4$ here and for $CaMoO_4$ (Wachtmann et al 1968).

Cross sections of the velocity surfaces and of the Young's modulus surface — each computed as described in Section 6.6 from the new set of elastic constants — are presented in Figures 7.6 and 7.7. From the elastic constants the energy flux direction of any mode can be found. Knowledge of the energy flux directions affords an immediate check on the validity of the present experiments and on the conclusions drawn as to the cause of the inconsistencies in the original work. For the modes of interest here — the quasi-longitudinal and quasi-shear waves propagated in the (001) plane — the energy flux vector lies in that

plane but may deviate from the propagation direction. Computed values of this deviation, along with the deviation of the particle displacement vector, are shown in Figure 7.8. The energy flux vector for the quasi-longitudinal mode is never far from the propagation direction, the maximum deviation being $\pm 13^{\circ}$. However for the quasi-shear mode the deviation can be much greater: indeed for the propagation directions 1,0,0; $2^{-\frac{1}{2}},2^{-\frac{1}{2}},0$; $3^{\frac{1}{2}}/2,1/2,0$ (modes v_5, v_8 and v_{14}) it is $+34^{\circ}$, -37°, and -34° respectively. These deviations, though not so large as those found in $CaWO_4$ (Figure 6.17) were bound to cause wall reflections in the original transducer/sample configurations employed to find v_5, v_8 and v_{14}, but they do not cause the ultrasound beam to impinge on the sample walls in the new configurations used here. It is also clear now why measurements on sample F presented much less difficulty; the propagation direction — $1/2,3^{\frac{1}{2}}/2,0$ — coincides almost exactly with the accidental pure mode direction at 60.15° to the +X axis.

7.2.3 James' analysis of Chung and Li's original velocity data

During the later stages of the experimental work on $SrMoO_4$ described in Section 7.2.1, a new analysis of Chung and Li's (1971b) velocity data was published (James 1972). James noticed the inconsistencies (see Table 7.6) in the velocity data reported by Chung and Li (1971b) and observed that they are associated with measurement of the velocities of impure modes propagated in the XY plane. In view of the difficulties reported by

Gerlich (1964) and ourselves (Farley and Saunders 1971), in exciting the quasi-shear modes for the [100] and $2^{-\frac{1}{2}}, 2^{-\frac{1}{2}}, 0$ directions of propagation, James suggested that it was plausible that Chung and Li's measurements of the quasi-shear mode velocities v_5, v_8, v_{14} and v_{17} were in error.

The analytical solution method devised by Chung and Li to calculate the elastic constants cannot be used unless all seventeen velocities are known. However, James obtained the elastic constants by using our SUMSQ minimisation technique to fit the constants to the thirteen velocities v_1, v_2, v_3, v_4, v_6, v_7, v_9, v_{10}, v_{11}, v_{12}, v_{13}, v_{15} and v_{16} — the quasi-shear velocities v_5, v_8, v_{14} and v_{17} being completely omitted from the fitting procedure. As must be expected in the light of our experimental results above (Section 7.2.2) a good fit was obtained, with a small value of SUMSQ (equal to 0.00196) indicating the internal consistency of the thirteen velocities. The elastic stiffness constants found are listed in Table 7.5; they are in good agreement with the values found here.

In conclusion it should be remarked that our experimental work of Section 7.2.1 provides the only complete justification for James' decision to choose to omit the velocities of quasi-shear modes propagated in the XY plane from the least squares fitting procedure. In fact the measurement of the velocity v_{17} (the velocity of the quasi-shear mode propagated in the $1/2, 3^{\frac{1}{2}}/2, 0$ direction and equal to 2.17×10^5 cm s^{-1}) was correct and need not have been omitted.

7.3 LEAD MOLYBDATE

The elastic constants of single crystal $PbMoO_4$ have been measured by Coquin et al (1971) during a study of physical properties relevant to the use of the material in acousto-optic device applications. Eight velocities, listed in Table 7.8 were measured by the ultrasonic pulse echo technique. The constants C_{33} and C_{44} were calculated directly, and the others found by an iterative method. The values obtained are given in Table 7.9. Although Coquin et al were fully aware that signs of the constants C_{16} and S_{16} depended on the choice of the sense of the Z axis with respect to the crystal structure — the choice also affected the signs of certain photoelastic constants which they measured — they do not appear to have known of the work of Wachtmann et al (1968) on $CaMoO_4$. They state that "In the absence of a convention for selecting the positive sense of axes for non-piezoelectric crystals they will somewhat arbitratily chose +Z such that the elastic constant C_{16} is positive." The crystals were then oriented with respect to this "convention" by sound velocity measurements. The sign quoted for C_{16} was thus referred to a completely arbitrary sense of Z axis whose relationship to the crystal structure was not determined. On the basis of this data alone comparison of the orientation dependence of the elastic behaviour of $PbMoO_4$ with that of other scheelite materials is not possible, and further experiments have been necessary. Details are given in Section 5.3.1.

Following Coquin et al (1971) there have been studies —referred to in Section 2.2 —of the optical and

crystalline perfection of $PbMoO_4$ and of the anisotropy of the acoustic wave velocities in the material (Namikata and Esashi (1972), Esashi and Namikata (1972)). It was reported that etch-pits, produced on (001) plane surfaces by immersion in a 5% aqueous solution of caustic soda at room temperature for 4 to 5 minutes, were square but had sides which were oriented at angles of about 30° and 60° to the <100> crystallographic axes. By relating the orientation of the etch-pits on a particular specimen to the anisotropy of ultrasound velocities, Namikata and Esashi were able to relate the etch-pit orientation to the arbitrary sense of Z axis chosen to make C_{16} positive. It appears that the edges of the etch-pits were very nearly parallel to the directions in the XY plane for which the quasi-shear mode velocity was a minimum. In the second paper (Esashi and Namikata 1972) it is suggested that the orientation of the etch-pits "may be related with the tetragonal structure of MoO_4 in $PbMoO_4$ and especially with the Mo-O-Mo chain." This suggestion cannot be substantiated unless the relationship of the Z axis to the crystal structure is known. Etching experiments carried out here are reported in the next section.

7.3.1 Experimental studies of $PbMoO_4$ single crystals

Experiments have been carried out to find the sense of the Z axis in a single crystal of $PbMoO_4$ and then to determine the signs of the elastic constants C_{16} and S_{16}. The etch pit orientation on faces normal to the Z axis, and its relationship to the atomic arrangement have been studied.

A boule of Czochralski grown $PbMoO_4$ doped with 0.05 at% gadolinium was purchased from IRD Co. Ltd., Newcastle. Doped $PbMoO_4$ was required because the spin resonance method of locating the Z axis — devised in the present work on $CaWO_4$ — was preferred to the x-ray intensities method in view of the difficulties noted by Farabaugh et al (1966). The boule had been air-annealed for ten hours and was slightly yellow in colour on the outside, but colourless within. Laue photographs, which exhibited the pseudo-ditetragonal symmetry observed in other scheelites, were used to locate the [001], <100> and <110> directions, the latter two being distinguished by comparison with similar photographs of $CaWO_4$. The magnetic axes in the XY plane were located using the method described in Section 5.1.3 by finding the extremes of the 33.8 GHz resonance spectrum which was readily observable at room temperature with a specimen 4 mm by 3.5 mm by 2.5 mm. The magnetic axes were found to lie at an angle of $8.5^{\circ} \pm 0.5^{\circ}$ to the crystallographic <100> axes†. The agreement of this measurement with the value of $8^{\circ}55'$ calculated (Section 2.2) from the oxygen coordinates determined by Leciejeiwicz (1965) attests to the validity of the method. By reference to Figure 2.6 the sense of the conventional Z axis in the specimen and in the boule from which it had been cut could readily be determined.

† The experiment has been repeated by observation of the X-band resonance spectrum at room temperature (J. Hodgson, private communication). Using a simple microwave bridge spectrometer with crystal-video detection and 50 Hz field modulation the magnetic axes were found to make angles of $10^{\circ} \pm 2^{\circ}$ with the <100> axes.

(a) Ultrasonics experiments

An ultrasonic sample was cut from the boule to yield end-faces which were normal to a direction defined by the cosines $1/2, 3^{\frac{1}{2}}/2, 0$. This particular direction was chosen because it was one of two directions at 30° on either side of the <100> axes in the XY plane for which velocity measurements were made by Coquin et al (1971), and a direction in which the velocities of the impure modes are dependent on the sign of C_{16} (equations relating elastic constants and velocities for these directions can be obtained from equations 14, 15 and 16 of Table 3.2 by replacing the angle 21.5° with 30° and 60° in turn). The velocities of the pure shear, quasi-longitudinal and quasi-shear modes in the $1/2, 3^{\frac{1}{2}}/2, 0$ sample were measured by the single-ended pulse echo method and found to be

$$v_{\text{pure shear}} = 1.960 \times 10^5 \text{ cm s}^{-1}$$

$$v_{\text{quasi longitudinal}} = 4.300 \times 10^5 \text{ cm s}^{-1}$$

$$v_{\text{quasi shear}} = 1.300 \times 10^5 \text{ cm s}^{-1}$$

The velocity of the pure shear mode is thus very similar to that measured by Coquin et al (1971) for the pure shear mode propagated in the [100] direction; for directions in the XY plane the pure shear mode with polarisation vector parallel to the Z axis has a velocity given by $(C_{44}/\rho)^{\frac{1}{2}}$. The velocities of the impure modes were then compared with those of Table 7.8 for propagation in the directions described as $1/2, 3^{\frac{1}{2}}/2, 0$ and $3^{\frac{1}{2}}/2, 1/2, 0$. The velocities for the second of these directions are in good agreement with those measured here; clearly the direction denoted

$3^{\frac{1}{2}}/2,1/2,0$ by Coquin et al with respect to their arbitrary definition of the Z axis must be denoted $1/2,3^{\frac{1}{2}}/2,0$ with respect to the conventional sense of Z axis. The sense of Z axis which was chosen to give C_{16} positive is therefore the opposite of that defined here for scheelite materials, and with respect to the conventional axes the stiffness constant C_{16} will be negative and the corresponding compliance S_{16} positive. Thus for the same definition of axes these constants have the same signs in $PbMoO_4$ as in $CaWO_4$, $CaMoO_4$ and $SrMoO_4$. The elastic constants of $PbMoO_4$, with the sign of C_{16} now determined are given in Table 7.10 along with values of the bulk modulus, the compliances and the compressibilities computed directly from them.

Major plane sections ((001), (100) and (110)) of the velocity and Young's modulus surfaces have been computed from the elastic constants and are presented in Figures 7.9 and 7.10. Now that the Z axis direction can be related to the crystal structure the orientation dependence of elastic behaviour can be related to the atomic arrangement. The deviations of the sound energy flux and the quasi-longitudinal polarisation vector from the propagation direction have been computed for propagation directions in the (001) plane (see Figure 7.11). The energy flux deviation is comparable in magnitude with that of $CaWO_4$. It is apparent from the figure that the $1/2,3^{\frac{1}{2}}/2,0$ propagation direction used here is very close to an accidental pure mode direction (γ).

(b) Etching experiments

Thin slices were cut with faces normal to the

fourfold axis. Each slice was marked to indicate the sense of the Z axis, which had previously been found by the magnetic axis technique. After polishing with 1 micron diamond grit on solder metal laps the specimens were etched for 2½ minutes in 5% caustic soda at room temperature and examined under the optical microscope. With a magnification of x400 an array of flat bottomed pits covering the whole slice was observed (Figure 7.12a). Under a higher magnification (x1000) somewhat smaller, well defined square pits with pointed bottoms were seen (Figure 7.12b). The appearance of the etched samples was very similar to that reported by Esashi and Namikata (1972) for $PbMoO_4$ crystals grown from low purity starting materials. Pit densities were large and estimated to be of the order of 10^{+8} cm^{-2}.

Both types of etch-pits (flat and pointed bottoms) had sides which as reported previously (Namikata and Esashi 1972) did not lie parallel to the simple crystallographic directions <100> or <110>. The orientations of pits on the +Z and -Z faces were observed to be related by the mirror plane symmetry of the 4/m point group. As shown in Figure 7.13, on the +Z faces (+Z axis emerging from the face) the pit sides have been found to make angles of $64^{o} \pm 2^{o}$ and $26^{o} \pm 2^{o}$ with the +X and +Y axes respectively while on the -Z faces these angles are reversed. Thus in a sample in which the positions of the <100> axes are known the conventional sense of the Z axis can easily be found by observation of the orientation of the etch-pits. As discussed earlier (Section 5.1.4) it is important to use only the etch specified for a particular material. For

$PbMoO_4$ the etch is alkaline (see above) and the Z axis determination is by observation of the etch-pits on the Z faces. For $CaWO_4$ the etch to be used is acidic (see Section 5.1.4) and the Z axis determination is by observation of pits on the X or Y faces. Further work to attempt to find a general etching method for all scheelites has proved fruitless; pits could not be produced on $CaWO_4$, $PbMoO_4$ and $SrMoO_4$ with the same etch (J. Hodgson, private communication).

By relating the etch-pit orientation on crystals of $PbMoO_4$ to the conventional sense of Z axis in the crystals, the relationship between the etch-pit orientation and the atomic arrangement has been established. A comparison of Figure 7.13a with Figures 2.2, 2.5 and 2.6 indicates that the etch-pit sides lie within $\pm 2^{\circ}$ of the <120> crystallographic directions. It appears that neither the edges nor the diagonals of the pits are parallel to any of the Pb....(MoO_4) periodic bonding chains found to be important (Vesselinov 1971) in determining the growth form of mineral specimens of wulfenite ($PbMoO_4$). The <120> directions in fact make angles of $53^{\circ}\,8'$ with the directions, $\langle\bar{1}20\rangle$, of the projections in the (001) plane of the very nearly straight Mo-O...O-Mo chains (see Figure 7.14); the tentative explanation of the pit orientation given by Esashi and Namikata (1972) is not substantiated.

TABLE 7.1

Ultrasound velocities in $CaMoO_4$ (after Alton and Barlow 1967)

Specimen	Mode v_i †	Velocity (Units : 10^5 cm s^{-1})
1	v_1	5.4531
	v_2	2.9448
2	v_3	2.9433
	v_4	5.8629
	v_5	3.2195
3	v_6	2.9455
	v_7	5.9771
	v_8	2.9834
4	v_9	5.4910
	v_{10}	2.9953
	v_{11}	3.2830
5*	v_{12}	2.9483
	v_{13}	6.1473
	v_{14}	2.6000

*for the arbitrary sense of +Z axis chosen by Alton and Barlow the propagation direction in this specimen was described as having direction cosines $3^{\frac{1}{2}}/2, 1/2, 0$.

† the subscripts (i) refer to the modes listed in Table 3.2

TABLE 7.2

Elastic constants of $CaMoO_4$

	(a) Alton & Barlow (1967)	(b) Alton & Barlow (reassessed here)	(c) Wachtmann et al (1968)
C_{11}	+14.47 ± 0.28	+14.4	+14.50
C_{12}	+ 6.64 ± 3.32	+ 6.48	+ 6.18
C_{13}	+ 4.46 ± 0.09	+ 4.48	+ 4.96
C_{16}	1.34 ± 0.67	1.42	- 1.46
C_{33}	+12.65 ± 0.28	+12.6	+12.82
C_{44}	+ 3.69 ± 0.006	+ 3.69	+ 3.674
C_{66}	+ 4.51 ± 0.22	+ 4.61	+ 4.558
S_{11}	+ 9.89	+ 9.92	+ 9.74 ± 0.05
S_{12}	- 4.32	- 4.3	- 3.8 ± 0.1
S_{13}	- 1.96	- 2.0	- 2.3 ± 0.09
S_{16}	4.22	4.4	+ 4.33 ± 0.1
S_{33}	+ 9.29	+ 9.4	+ 9.58 ± 0.04
S_{44}	+27.10	+27.1	+27.22 ± 0.09
S_{66}	+24.68	+24.4	+24.71 ± 0.22
Bulk Modulus	7.94	7.92	8.19
Compressibilities:			
Volume β_v	12.59	12.6	12.23
Linear β_z	5.37	5.3	4.98
Linear β_{xy}	3.61	3.6	3.64

Units: stiffness moduli, bulk modulus 10^{11} dyn cm^{-2}

compliance moduli, compressibilities 10^{-13} cm^2 dyn^{-1}

TABLE 7.3

Propagation direction (cosines)	$C_{11} + C_{66}$ (Units : 10^{11} dyn cm^{-2})
1,0,0	19.036
$2^{-\frac{1}{2}}, 2^{-\frac{1}{2}}, 0$	19.090
$1/2, 3^{\frac{1}{2}}/2, 0$	18.956

TABLE 7.4

Ultrasonic velocities in $SrMoO_4$ at 25°C

Sample Code	Propagation direction (cosines)	Mode	Polarisation	v_i †	Measured velocities in units of 10^5cm s^{-1}	
					Chung & Li 1971b	Present work
A	0,0,1	pure longitudinal	[001]	v_1	4.77*	4.68
A	0,0,1	pure shear	[001]	v_2	2.77*	2.80
B	1,0,0	quasi longitudinal	(001)	v_3	5.10*	5.07
B	1,0,0	pure shear	[001]	v_4	2.77*	2.75
B	1,0,0	quasi shear	(001)	v_5	1.64	2.96
C	$2^{-\frac{1}{2}},2^{-\frac{1}{2}},0$	quasi longitudinal	(001)	v_6	5.55*	5.37
C	$2^{-\frac{1}{2}},2^{-\frac{1}{2}},0$	pure shear	[001]	v_7	2.77*	2.77
C	$2^{-\frac{1}{2}},2^{-\frac{1}{2}},0$	quasi shear	(001)	v_8	2.56	2.41
D	$0,2^{-\frac{1}{2}},2^{-\frac{1}{2}}$	quasi longitudinal		v_9	5.00*	4.90
D	$0,2^{-\frac{1}{2}},2^{-\frac{1}{2}}$	quasi shear		v_{10}	2.61*	2.54
D	$0,2^{-\frac{1}{2}},2^{-\frac{1}{2}}$	quasi shear		v_{11}	3.08*	3.09
E#	$3^{\frac{1}{2}}/2,1/2,0$	pure shear	[001]	v_{12}	2.78*	2.76
E	$3^{\frac{1}{2}}/2,1/2,0$	quasi longitudinal	(001)	v_{13}	5.12*	5.08
E	$3^{\frac{1}{2}}/2,1/2,0$	quasi shear	(001)	v_{14}	1.86	3.01
F##	$1/2,3^{\frac{1}{2}}/2,0$	pure shear	[001]	v_{15}	2.77*	2.79
F	$1/2,3^{\frac{1}{2}}/2,0$	quasi longitudinal	(001)	v_{16}	5.52*	5.42
F	$1/2,3^{\frac{1}{2}}/2,0$	quasi shear	(001)	v_{17}	2.17*	2.16

†, *, # see over

Notes relevant to Table 7.4

† The subscripts (i) are those used in Table 1 of Chung and Li (1971b). This table gives the equations which relate the seventeen velocities to the elastic constants but contains several typographical errors: (i) the right-hand sides of equations 3 and 5 must be interchanged, (ii) the right-hand sides of equations 13 and 14 must be interchanged with the right-hand sides of equations 16 and 17. With these changes the equations given by Chung and Li for velocities v_1 to v_{11} and v_{15} to v_{17} are the same as those given here in Table 3.2 . The equations for v_{12}, v_{13} and v_{14} can be obtained from equations 14, 15 and 16 of Table 3.2 by replacing 21.5^{o} with 30^{o}.

* These velocities, measured previously by Chung and Li 1971a,b have been found here to be correct.

Samples E and F are respectively samples 6 and 5 of the original work. By determining the sense of the Z axis in the crystals (see Section 2.3.1) it was found that sample 6 (E) had direction cosines $3^{\frac{1}{2}}/2,1/2,0$ and sample 5 (F) had direction cosines $1/2,3^{\frac{1}{2}}/2,0$.

TABLE 7.5

Elastic constants of $SrMoO_4$ at 25°C. Stiffness moduli and bulk modulus are in units of 10^{11} dyn cm^{-2}, compliance constants and compressibilities in units of 10^{-13} cm^2 dyn^{-1}.

	Chung and Li (1971 b)	Present work	James (1972)
C_{11}	+12.75	+11.9	+11.5
C_{12}	+ 8.87	+ 6.2	+ 6.0
C_{13}	+ 5.01	+ 4.8	+ 4.4
C_{16}	0.40	- 1.2	1.2
C_{33}	+10.3	+10.4	+10.4
C_{44}	+ 3.47	+ 3.49	+ 3.50
C_{66}	+ 2.13	+ 4.2	+ 4.7
S_{11}	+16.4	+13.6	-
S_{12}	-10.4	- 6.3	-
S_{13}	- 2.9	- 3.4	-
S_{16}	5.1	+ 5.7	-
S_{33}	+12.5	+12.7	-
S_{44}	+28.8	+28.7	-
S_{66}	+48.9	+27.1	-
Bulk Modulus	+ 7.8	+ 7.2	-
Compressibilities:			
Volume β_v	+12.8	+13.8	-
Linear β_z	+ 6.7	+ 6.0	-
Linear β_{xy}	+ 3.1	+ 3.9	-

TABLE 7.6

Propagation direction (cosines)	$C_{11} + C_{66}$ (in units of 10^{11} dyn cm^{-2})	
	Previous measurements	Present measurements
	Chung and Li 1971 b	
1,0,0	13.05	15.8
$2^{-\frac{1}{2}}, 2^{-\frac{1}{2}}, 0$	16.95	16.6
$3^{\frac{1}{2}}/2, 1/2, 0$	13.49	16.0
$1/2, 3^{\frac{1}{2}}/2, 0$	16.00	16.0

TABLE 7.7

Dimensions (in mm) of the strontium molybdate specimens

	Length	Width	Thickness
A	3.42	-	-
B	6.18	-	-
C	7.27	6.54	3.42
D	5.97	4.57	4.20
E	7.34	5.10	3.40
F	6.94	5.47	3.10

TABLE 7.8

Ultrasonic velocities in $PbMoO_4$

Direction cosines of propagation vector†	Mode	Polarisation	Measured velocity in units of 10^5cm s^{-1} (Coquin et al 1971)
0,0,1	pure long	[001]	3.632
1,0,0	pure shear	[001]	1.961
1,0,0	quasi long	(001)	4.003
$0,2^{-\frac{1}{2}},2^{-\frac{1}{2}}$	quasi long		3.860
$3^{\frac{1}{2}}/2,1/2,0$	quasi long	(001)	4.339
$3^{\frac{1}{2}}/2,1/2,0$	quasi shear	(001)	1.312
$1/2,3^{\frac{1}{2}}/2,0$	quasi long	(001)	3.970
$1/2,3^{\frac{1}{2}}/2,0$	quasi shear	(001)	2.198

† defined by Coquin et al with respect to an arbitrary sense of Z axis.

TABLE 7.9

Elastic constants of $PbMoO_4$

(Coquin et al, 1971)

$C_{11} = 10.92$	$C_{33} = 9.17$
$C_{12} = 6.83$	$C_{44} = 2.67$
$C_{13} = 5.28$	$C_{66} = 3.37$
$C_{16} = 1.36$	

Units: 10^{11} dyn cm^{-2}

TABLE 7.10

Elastic constants of $PbMoO_4$ at room temperature. Stiffness moduli and bulk modulus are in units of 10^{11} dyn cm^{-2}, compliance constants and compressibilities in units of 10^{-13} cm^2 dyn^{-1}.

C_{11}	+10.92	S_{11}	+21.0
C_{12}	+ 6.83	S_{12}	-12.4
C_{13}	+ 5.28	S_{13}	- 4.9
C_{16}	- 1.36	S_{16}	+13.5
C_{33}	+ 9.17	S_{33}	+16.6
C_{44}	+ 2.67	S_{44}	+37.5
C_{66}	+ 3.37	S_{66}	+40.6

Bulk Modulus	7.15
Volume Compessibility β_v	14.0
Linear Compressibility β_z	6.7
Linear Compressibility β_{xy}	3.6

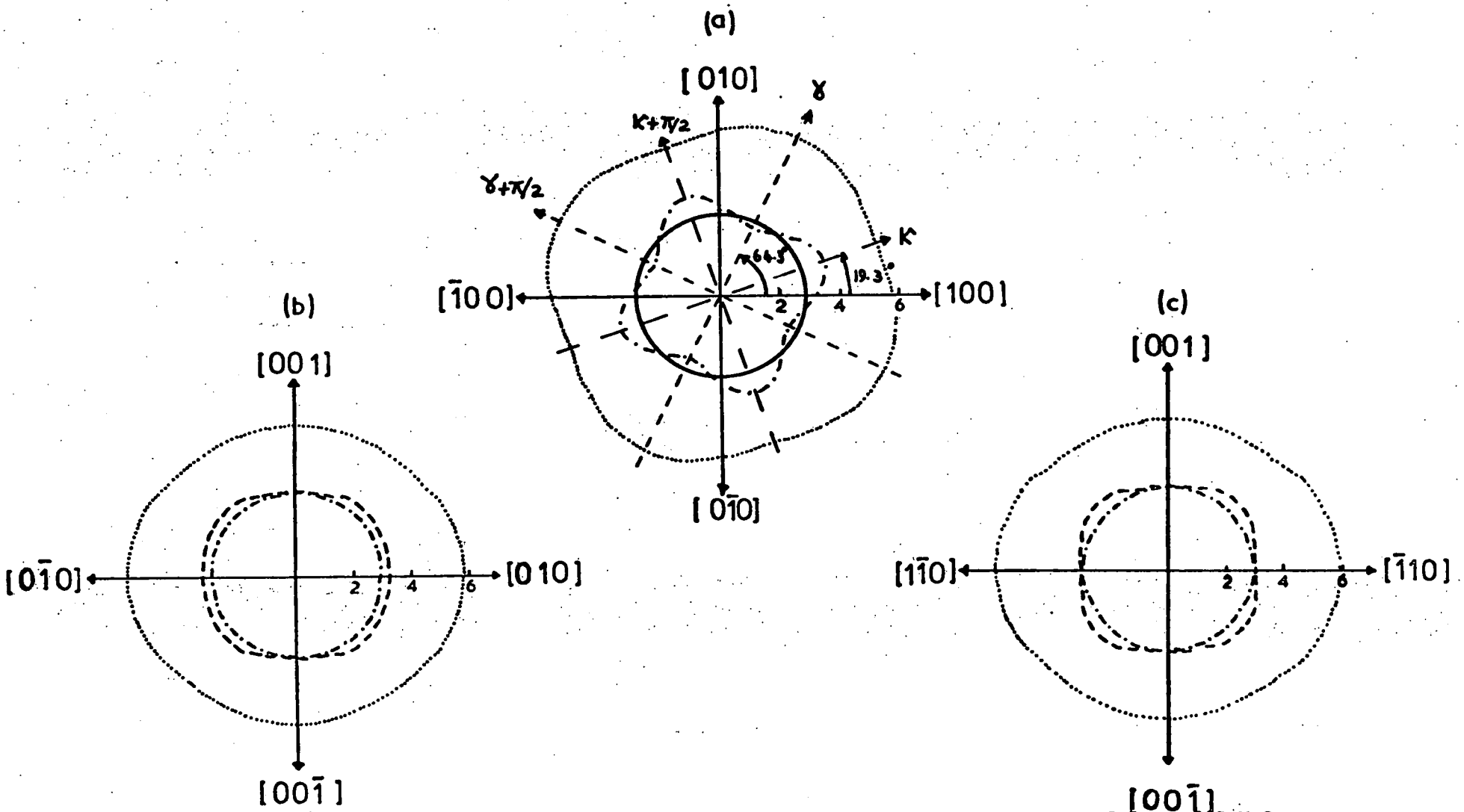

FIGURE 7.1: (a) (0̄01), (b) (100) and (c) (110) cross-sections of the velocity surfaces of $CaMoO_4$ at room temperature. Units are 10^5 cm s^{-1}; ..... denotes quasi-longitudinal mode, ----- and -·-·-· quasi-shear modes; and ——— the pure shear mode.

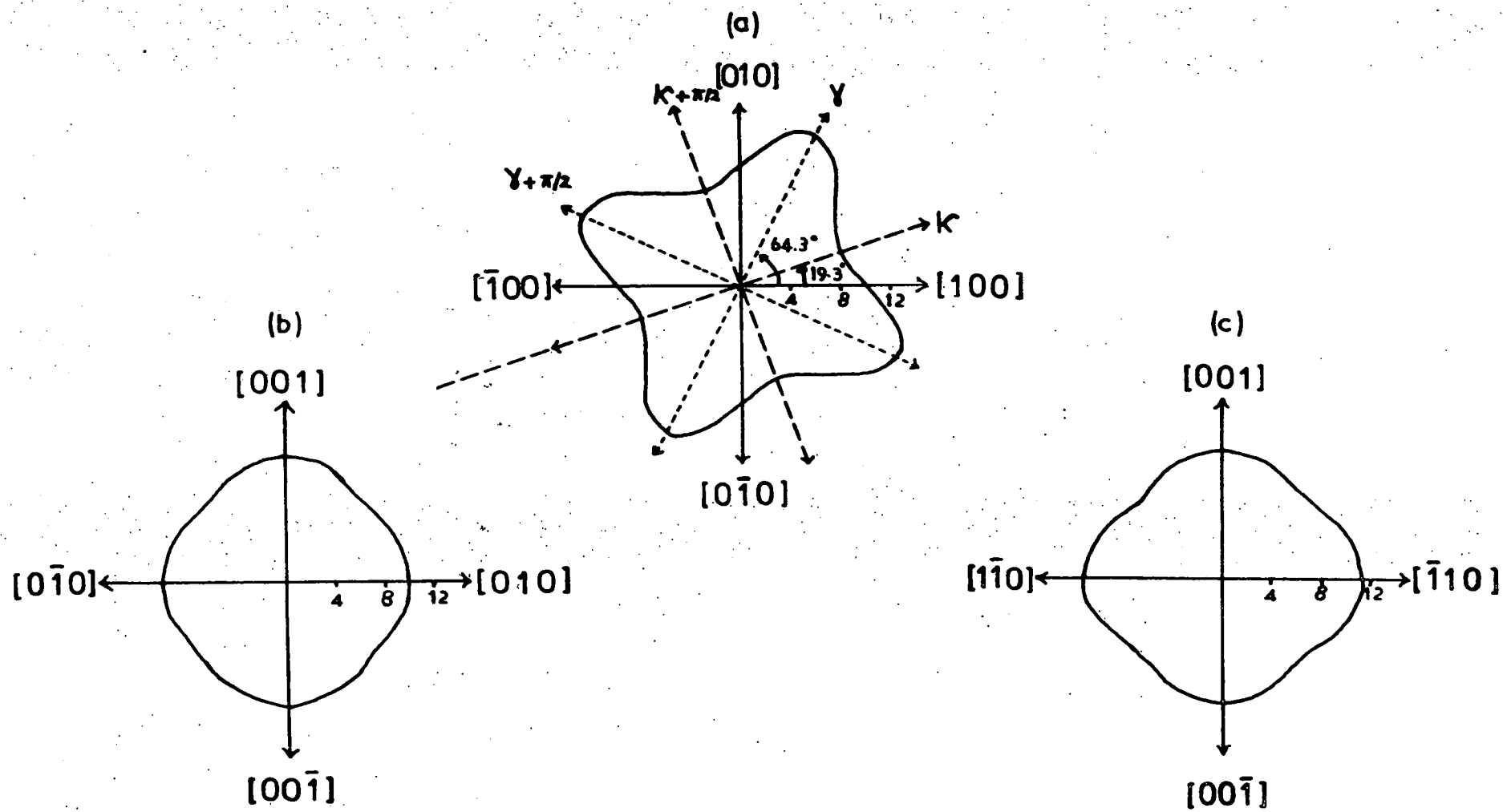

FIGURE 7.2: (a) (001), (b) (100) and (c) (110) plane cross-sections of the Young's modulus surface of $CaMoO_4$ at room temperature. Units are 10^{11} dyne cm^{-2}.

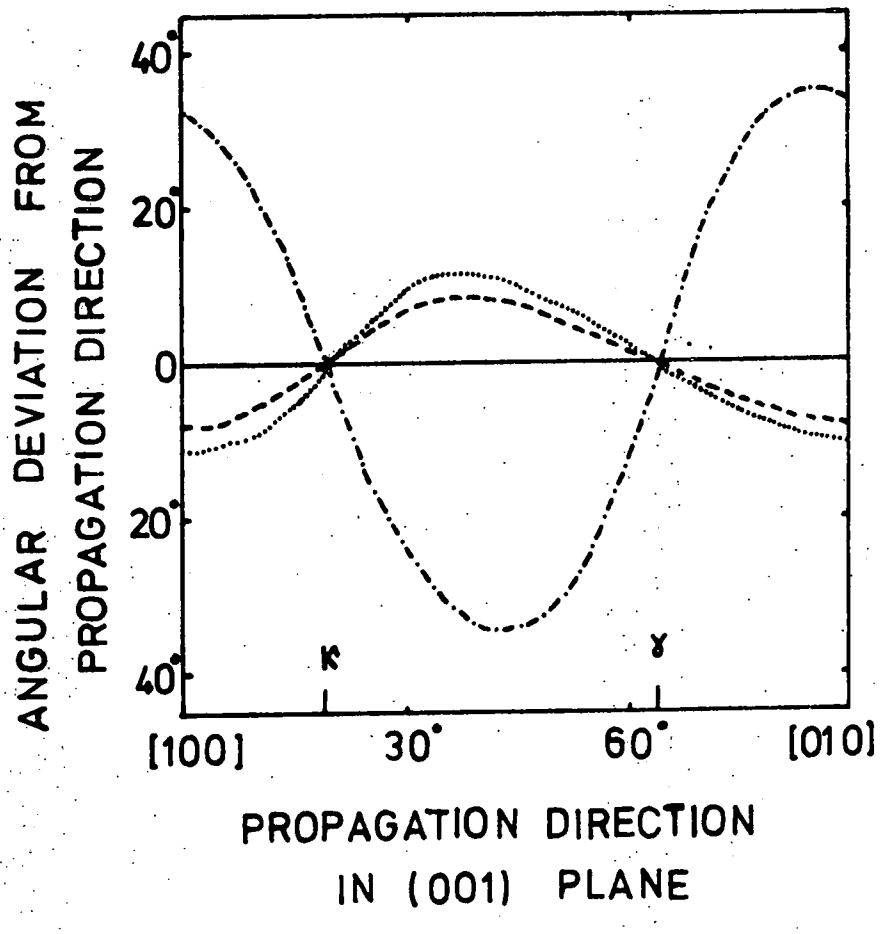

FIGURE 7.3: The deviations from the propagation direction of the energy flux vectors of the quasi-longitudinal (····) and quasi-shear (-·-·-·) modes, and of the particle displacement vector of the quasi-longitudinal wave (----) for propagation in the (001) plane of $CaMoO_4$ at room temperature.

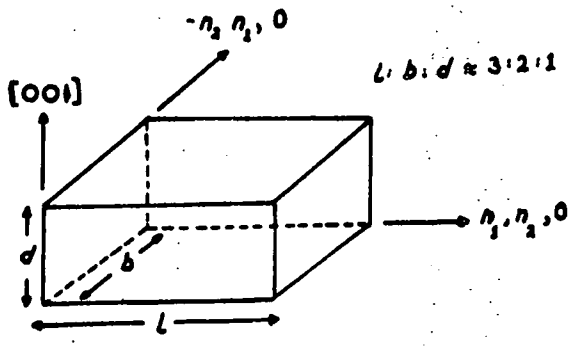

FIGURE 7.4: Form of $SrMoO_4$ samples B, C and E. Directions n_1, n_2, 0 and $-n_2$, n_1, 0 are equivalent by fourfold symmetry.

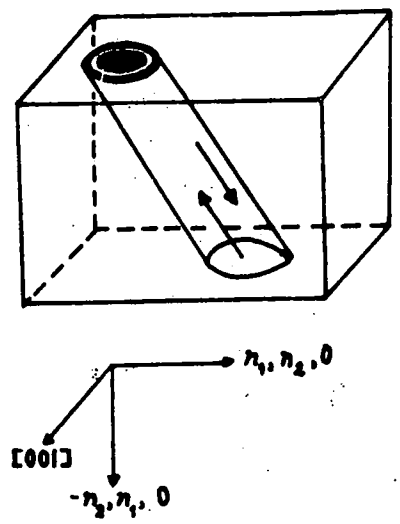

FIGURE 7.5: Transducer/sample configuration used to avoid wall reflections due to energy flux deviation.

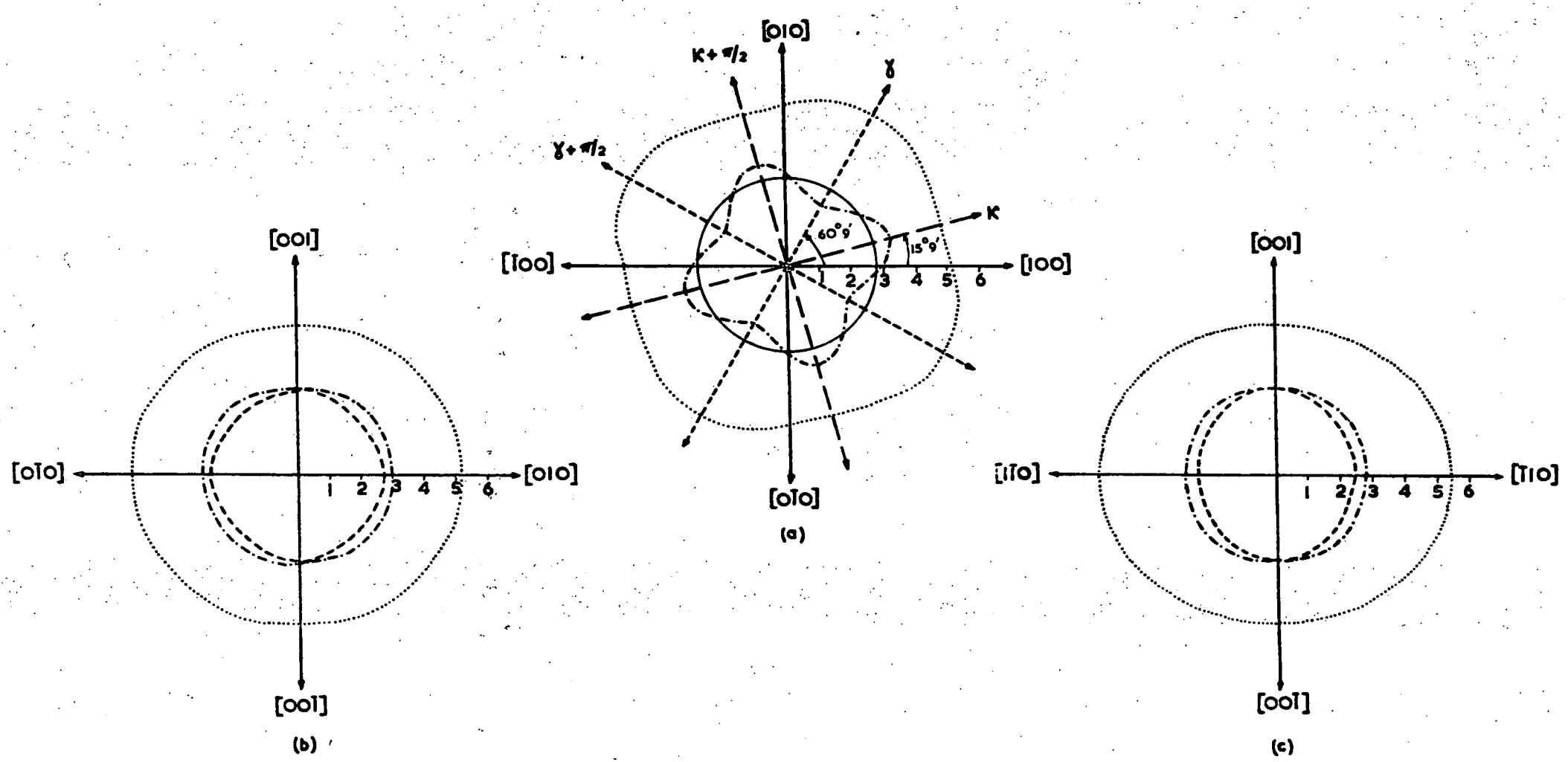

FIGURE 7.6: (a) (001), (b) (100) and (c) (110) cross sections of the velocity surfaces of $SrMoO_4$ at 295 K. Units are 10^5 cm s^{-1}; ..... denotes quasi-longitudinal mode; ---- and -·-·-· quasi-shear modes; and ——— the pure shear mode.

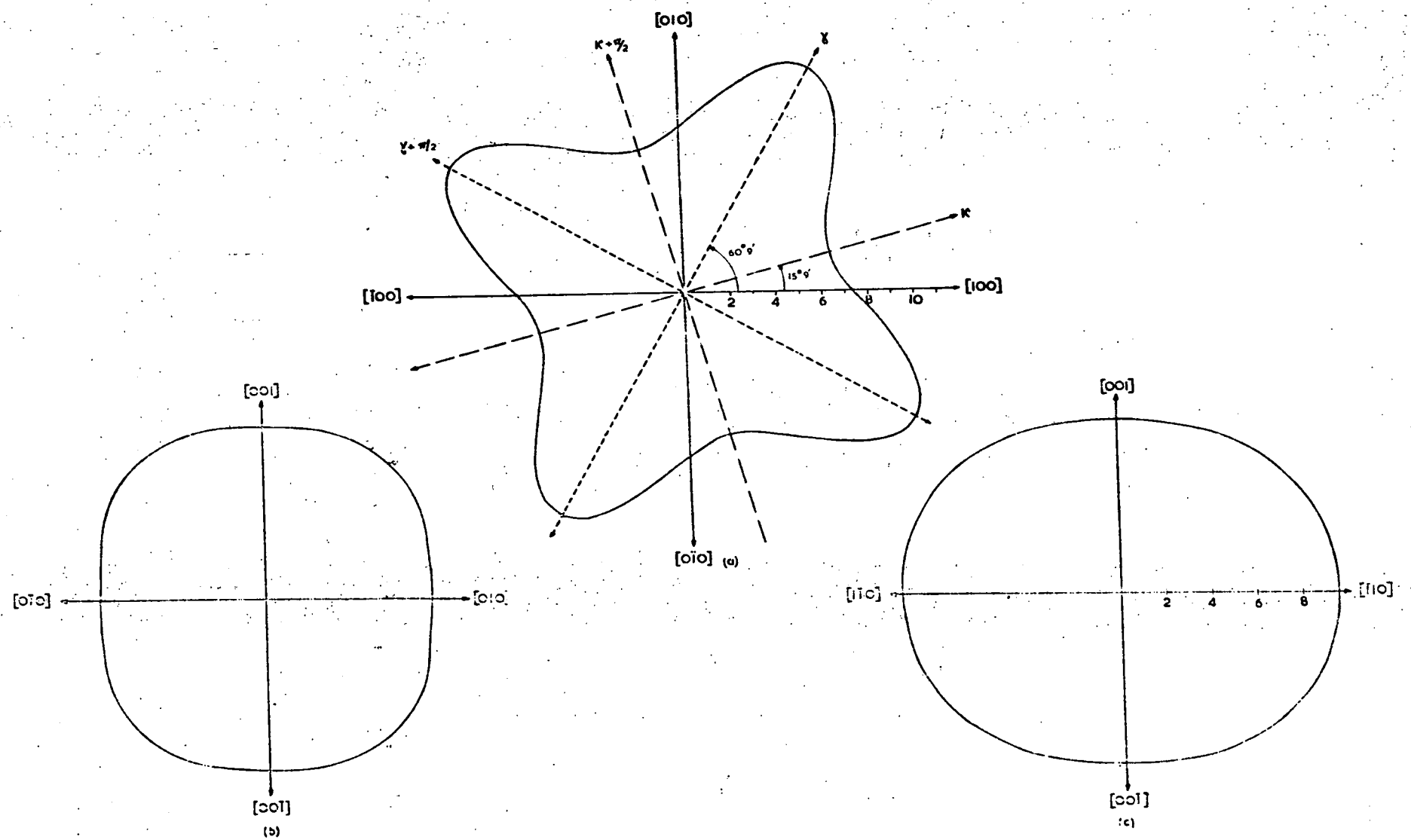

FIGURE 7.7: (a) (001), (b) (100) and (c) (110) plane cross sections of the Young's modulus surface of $SrMoO_4$ at 295 K. Units are 10^{11} dyn cm^{-2}.

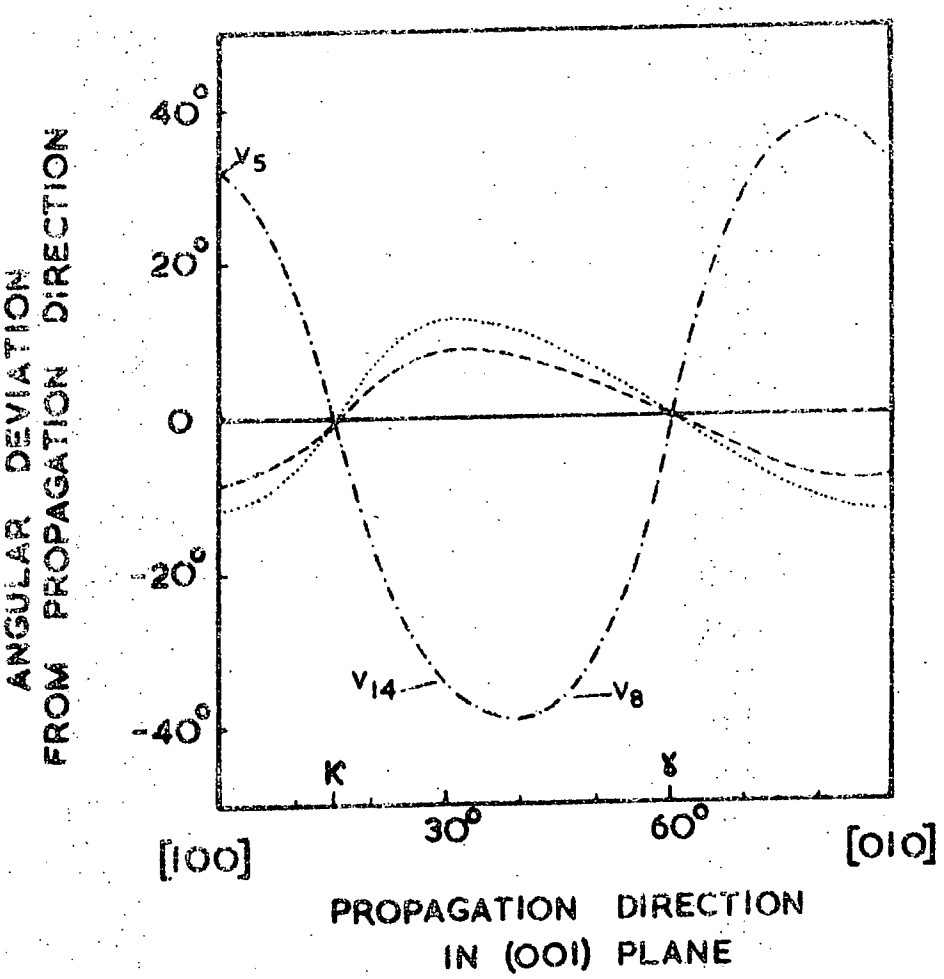

FIGURE 7.8: The deviations from the propagation direction of the energy flux vectors of the quasi-longitudinal (·····) and quasi-shear modes (-·-·-·-), and of the particle displacement vector of the quasi-longitudinal wave (----) for propagation in the (001) plane of $SrMoO_4$ at room temperature.

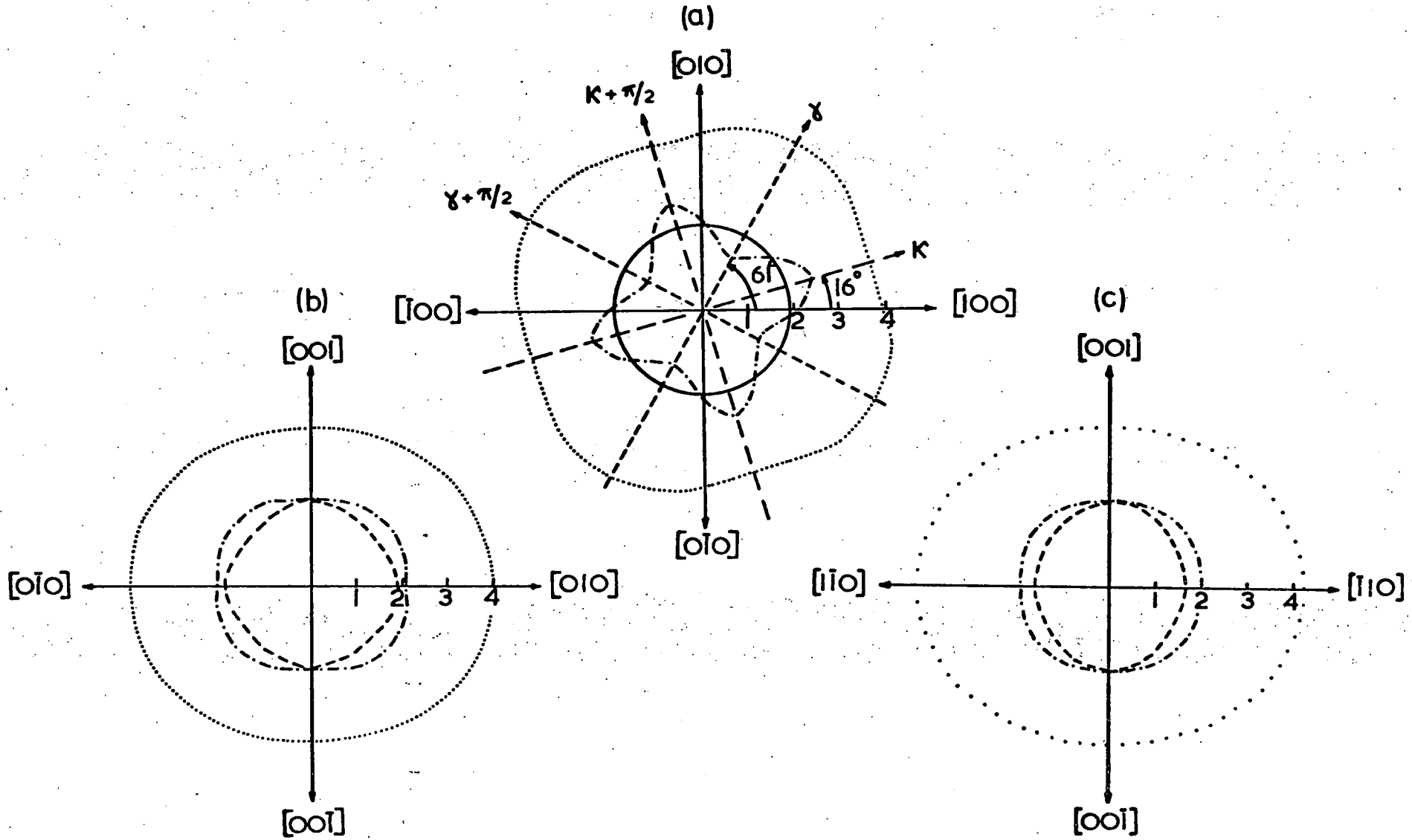

FIGURE 7.9: (a) (001), (b) (100) and (c) (110) cross sections of the velocity surfaces of $PbMoO_4$ at room temperature. Units are 10^5 cm s^{-1}; ..... denotes quasi-longitudinal mode; ----- and -·-·-· quasi-shear modes and ——— the pure shear mode.

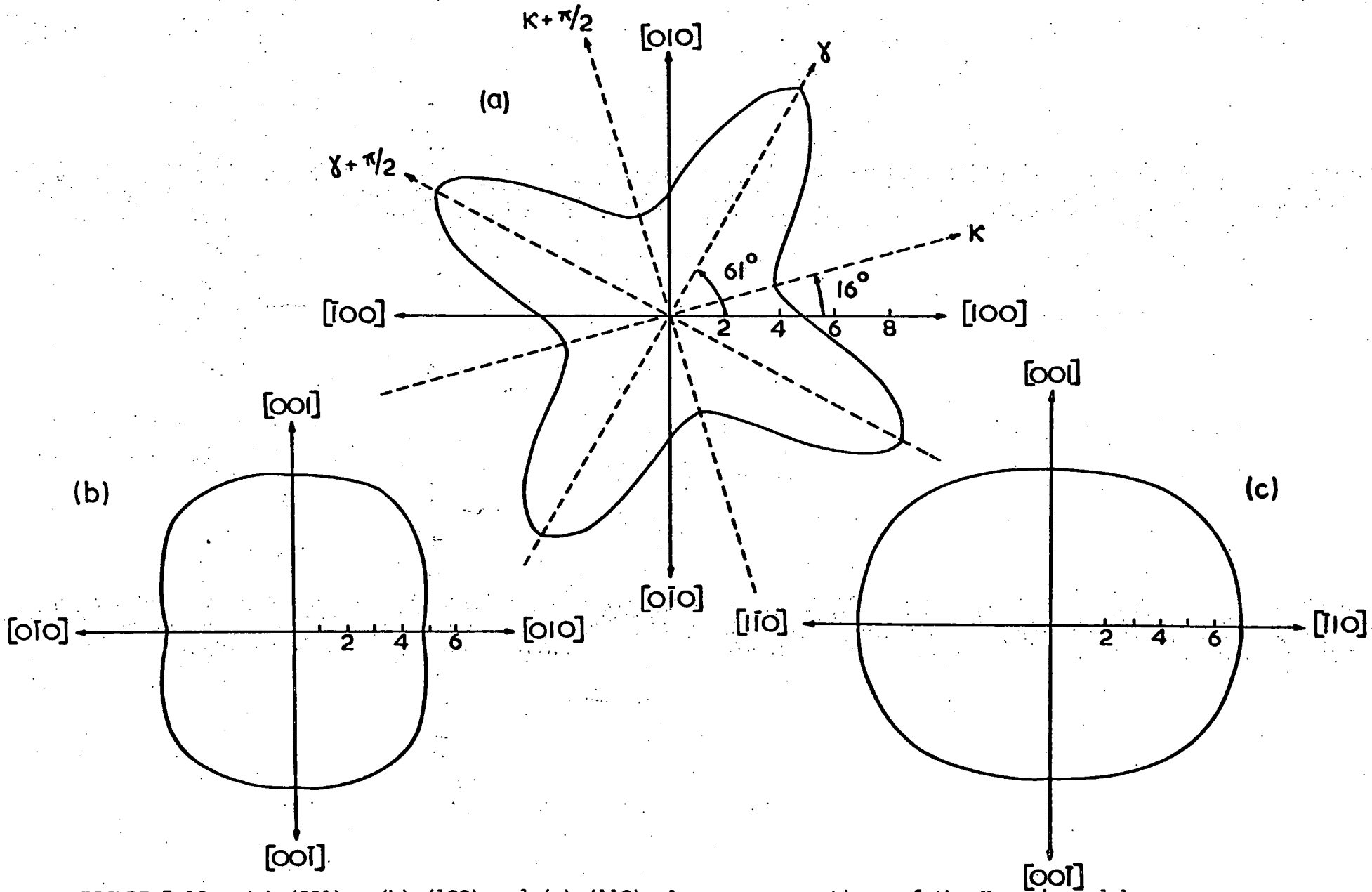

FIGURE 7.10: (a) (001), (b) (100) and (c) (110) plane cross sections of the Young's modulus surface of $PbMoO_4$ at room temperature. Units are 10^{11} dyn cm^{-2}.

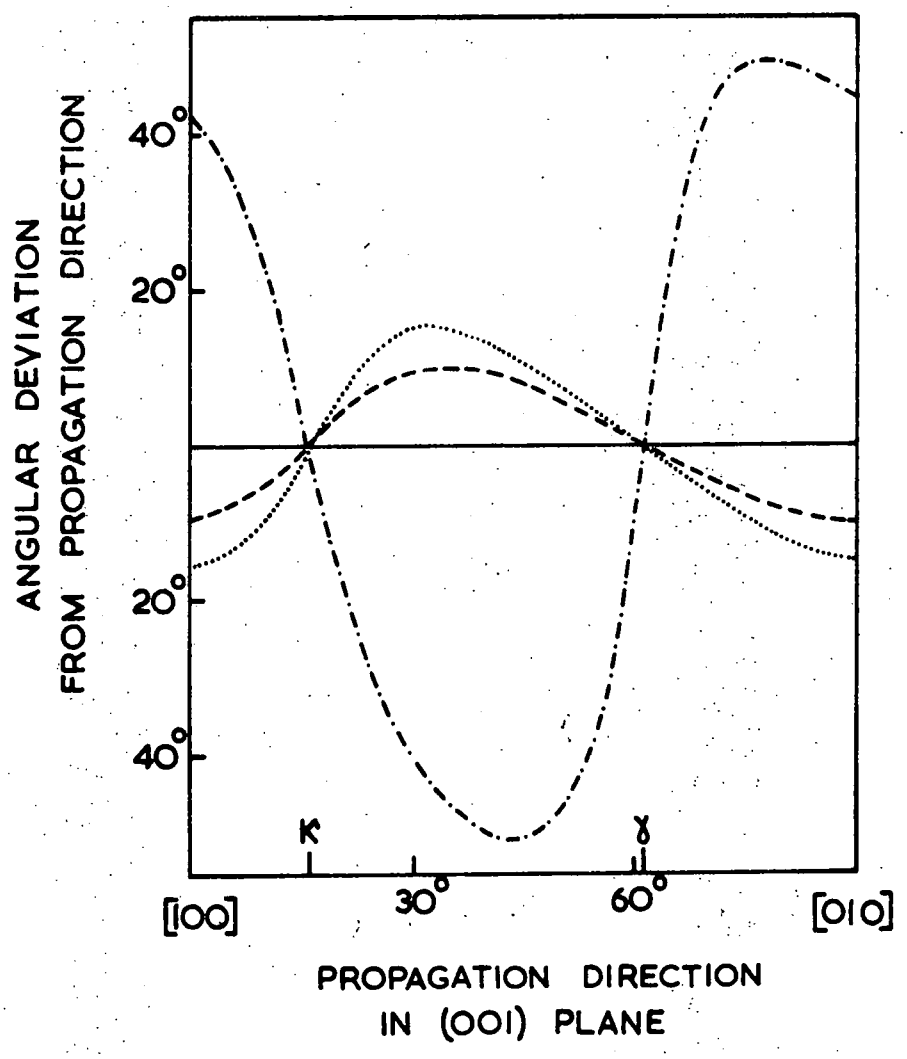

FIGURE 7.11: The deviations from the propagation directions of the energy flux vectors of the quasi-longitudinal (····) and quasi-shear modes (-·-·-·), and of the particle displacement vector of the quasi-longitudinal wave (----) for propagation in the (001) plane of $PbMoO_4$ at room temperature.

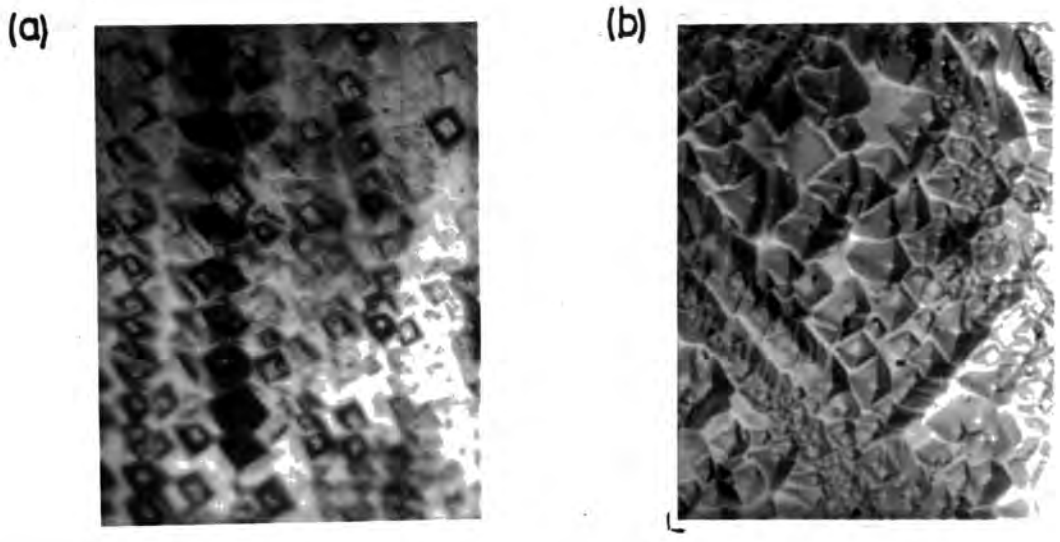

FIGURE 7.12: (a) flat-bottomed pits on +Z face of $PbMoO_4$
(b) pointed-bottom pits on -Z face of $PbMoO_4$
(Micrographs kindly prepared by J. Hodgson)

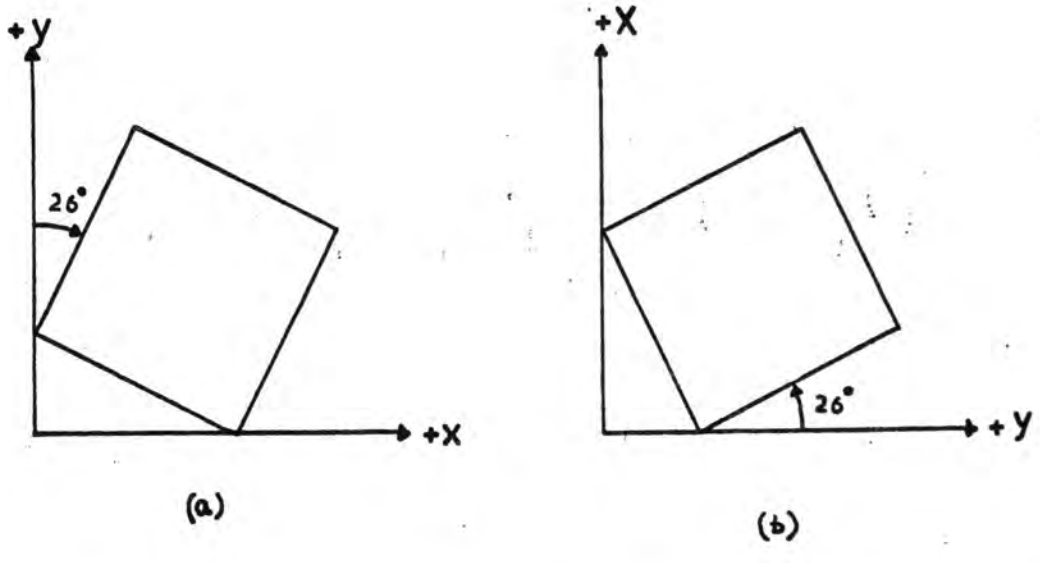

FIGURE 7.13: The orientation of etch-pits on (a) the +Z face and (b) the -Z face of $PbMoO_4$.

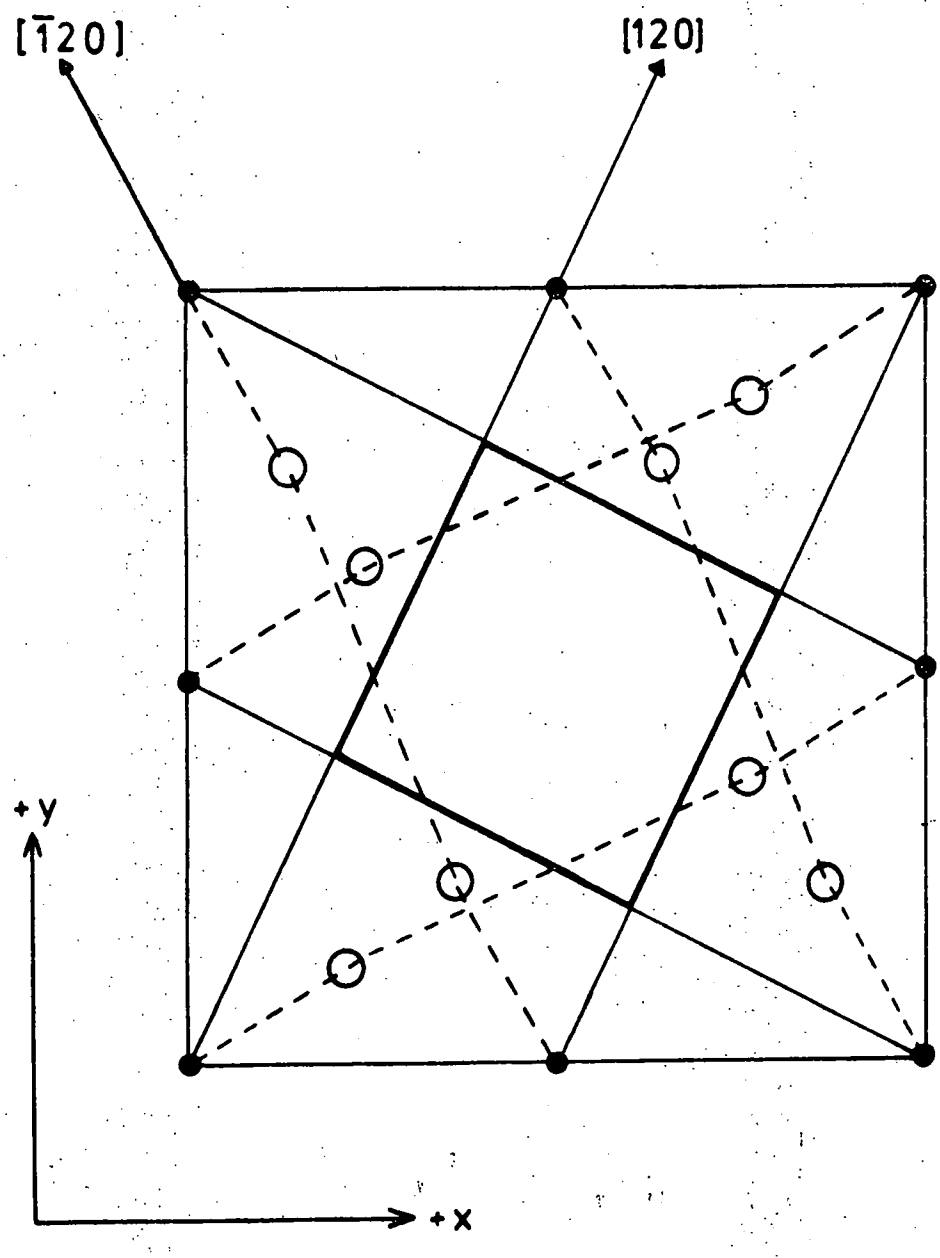

FIGURE 7.14: Etch pit orientation on +Z face relative to the atomic arrangement <u>projected</u> on to an (001) plane. Etch-pit sides are parallel to the <120> directions. The projections of the Mo — O ····· O — Mo chains zig-zag along the <$\bar{1}$20> directions.

CHAPTER 8

CONCLUSION

In this chapter the elastic properties of $CaWO_4$, $CaMoO_4$, $SrMoO_4$ and $PbMoO_4$ are compared and contrasted. Characteristics of wave propagation in the different materials are discussed. It is shown how the apparent differences in elastic and acoustic behaviour between TI and TII symmetry solids can be attributed to the deviation of "axes of acoustic symmetry" from the major crystallographic axes in the later group of solids. Interatomic binding in the scheelite structure tungstates and molybdates is discussed; a simple ionic model is shown to be inadequate.

8.1 COMPARISON OF ELASTIC PROPERTIES OF THE SCHEELITE STRUCTURE CRYSTALS STUDIED

8.1.1 Elastic constants

The room temperature elastic constants of $CaWO_4$, $CaMoO_4$, $SrMoO_4$ and $PbMoO_4$ (collected from the experimental results of Chapters 6 and 7) are listed in Table 8.1. Elastic constants measure the resistance of a medium to elastic deformation. A comparison of the values in the table with published data on a variety of other solids (see for example Musgrave (1970)) indicates that the scheelites are somewhat stiffer than most alkali halides, many metals and water soluble oxides, but do not resist deformation so strongly as diamond, or high melting point oxides and metals.

It is clear from the table that while there are differences in the magnitudes of the constants between the materials, the scheelite structure tungstates and molybdates form a group of solids with similar elastic properties. Both the bulk moduli and the volume compressibilities are equal within the limits of experimental error (see Table 8.2). The anisotropy of linear compressibility is about 1.5 in $CaWO_4$, $CaMoO_4$ and $SrMoO_4$, and about 1.9 in $PbMoO_4$. In each material the elastic stiffnesses and compliances have the same signs as were found for $CaWO_4$ and discussed in Section 6.2.1. This is particularly interesting in the case of C_{16} and S_{16}. The present work allows a comparison of the signs of these constants since the same definition of Z axis sense has been used in each material. In each case C_{16} has been found to be negative and S_{16} positive. Thus an applied tensile stress

in the X direction (σ_{11} positive) induces in each material an identical sense of response with respect to the atomic arrangement, namely a decrease in the angle between the planes normal to the +X and +Y axes. In each material S_{12} is greater in magnitude than S_{13}; this indicates that the cross-linking within the layers of the structure is greater than between them.

More detailed examination of the magnitudes of the compliances listed in Table 8.1 shows that in the molybdates there is a definite trend of increasing resistance to elastic deformation with increasing molecular weight, and that the two calcium compounds ($CaWO_4$ and $CaMoO_4$) have very similar elastic moduli. In units of 10^{-13} cm^2 dyn^{-1} the shear compliances S_{44} and S_{66} have similar values in $CaWO_4$, $CaMoO_4$ and $SrMoO_4$ (29.8 and 33.5, 27.1 and 24.4, 28.7 and 27.1 respectively) but are larger in $PbMoO_4$ (37.5 and 40.6). S_{11} and S_{33} are very similar in $CaWO_4$ and $CaMoO_4$ (10.5 and 8.8, 9.9 and 9.4), larger in $SrMoO_4$ (13.6 and 12.7) but much larger in $PbMoO_4$ (21.0 and 16.6). The constants S_{12} and S_{13} are greater in magnitude in $PbMoO_4$ than in $SrMoO_4$, and greater in $SrMoO_4$ than in either $CaWO_4$ or $CaMoO_4$. S_{16} has values in $CaWO_4$ and $CaMoO_4$ which are somewhat different (7.7 and 4.4), but within the group of molybdates it follows the same trend as the other constants (5.7 in $SrMoO_4$, 13.5 in $PbMoO_4$). The similarities between the two calcium compounds and the trends in the stiffnesses of the molybdates are also apparent in the values of the isotropic Young's and shear moduli listed in Table 8.2.

Empirical relationships

$$E_H = 15.5 \times 10^{11} M^{-0.8} \qquad G_H = 6.9 \times 10^{11} M^{-0.8} \text{ dyn cm}^{-2} \qquad (8.1)$$

have been found between the isotropic Young's (E_H) and shear (G_H) moduli and the molecular weights (M) of the molybdates by means of the logarithmic plots of Figure 8.1. These relationships allow the isotropic moduli of other scheelite structure molybdates to be estimated. They are not applicable to tungstates as shown by the $CaWO_4$ data points in the figures. This was to be expected; the elastic constants of $CaWO_4$ are very similar to those of $CaMoO_4$ but the molecular weights are quite different. An important conclusion of the present work is therefore the finding that the elastic properties of scheelites depend much more on the nature of the cation than on the anion. The elastic constants of $SrWO_4$ can thus be expected to be similar to those of $SrMoO_4$ and the elastic constants of the tetragonal form of $PbWO_4$ should be similar to those of $PbMoO_4$. Some other implications of the finding will be discussed in Section 8.1.5.

The orientation dependences of the Young's moduli of the four materials studied are shown in Figures 6.21, 7.2, 7.7 and 7.10. In the major crystallographic planes ({100} and {110}) containing the Z axis the Young's moduli change only slowly with direction, but for stresses in the XY plane the parameter has pronounced maxima and minima. In each material the maxima lie between the <100> and <110> directions and the minima are 45° away between the <110> and <010> directions. The ratio of the maximum Young's modulus

in the XY plane to the minimum value varies between the materials. It is 2.1 in $CaWO_4$, 1.6 in $CaMoO_4$, 1.7 in $SrMoO_4$ and 2.5 in $PbMoO_4$. The directions of the maxima and minima vary between the materials. This is discussed in Section 8.1.4.

8.1.2 Characteristics of wave propagation

Cross-sections of the wave velocity surfaces of $CaWO_4$, $CaMoO_4$, $SrMoO_4$ and $PbMoO_4$ have been given in Figures 6.16, 7.1, 7.6 and 7.9 respectively. In each material the quasi-longitudinal wave velocity is comparatively isotropic; it is slightly larger for directions in the XY plane than for the Z direction. One of the quasi-shear modes is also nearly isotropic in velocity in all four materials, and is completely independent of direction for propagation in the XY plane. The second quasi-shear mode is more anisotropic, particularly in the XY plane where it has pronounced maxima and minima of velocity. These extrema occur between the <100> and <110> and the <110> and <010> directions respectively. In each material there are acoustic axes (directions in which the shear velocities are equal) in the (001) plane and within a few degrees of the <100> axes.

The (001) cross-sections of the velocity surfaces now provide a ready means for the identification of the sense of the conventional +Z axis in pure or doped boules of any of the scheelites studied here. An ultrasonics sample can be cut for propagation at a measured angle θ to the X axis in the XY plane (the sense of θ will not be known at this stage), and the ultrasound velocities in the sample measured. The direction of propagation and the sense of the angle θ can then be found by comparing the measured velocities with those

predicted by the appropriate (001) plane cross section, and the sense of the +Z axis in the boule identified. The most suitable directions for the velocity measurement can be established by reference to the energy flux diagram of the material (Figures 6.17, 7.3, 7.8 and 7.11). If the sample is small, it is important to check that the velocities measured obey the cross-check on the value of $C_{11} + C_{66}$.

The similar shapes of the velocity surfaces in the four scheelites exemplify similarities in all the details of wave propagation. These are further demonstrated for propagation vectors in the (001) plane by comparison of Figures 6.17, 7.3, 7.8 and 7.11 which show the deviations from the propagation direction of the particle displacement vector of the quasi-longitudinal wave, and of the energy flux vectors of the quasi-longitudinal and quasi-shear modes. In each material the fastest mode is always quasi-longitudinal and has only a small deviation of energy flux from the propagation direction. The large variations of the quasi-shear mode velocity with direction lead to large deviations of energy flux for this mode. The maximum deviations occur for propagation along the acoustic axes. The deviations are largest in $PbMoO_4$ for which the ratio of the maximum quasi-shear mode velocity to the minimum is 1.88 , and smallest in $CaMoO_4$ for which the ratio is 1.42. Only for a few degrees (about $\pm 3^{\circ}$) on each side of the κ and γ accidental pure mode axes are the deviations less than 10° in any of the materials.

The mean velocities of sound in each material at room temperature have been calculated by the method due to Anderson (1965) which has been used earlier for $CaWO_4$ (Section 6.2.2). The values (listed in Table 8.2) show that the

velocities are highest in $CaMoO_4$ (which has the lowest density of this group of materials) and lowest in $PbMoO_4$ (which is the most dense and least stiff). The velocity of the quasi-shear mode propagated along the γ accidental pure mode axis in the (001) plane of $PbMoO_4$ is the lowest in any direction in any of the scheelites studied here; this is the mode which is particularly useful in some acousto-optic device applications (Coquin et al 1971).

An empirical relationship between the mean velocities of sound (v_m) and the molecular weights (M) of the scheelites has been found by means of a suitable logarithmic plot (Figure 8.2). The expression

$$v_m \simeq 6.1 \times 10^5 \, M^{-0.8} \text{ cm s}^{-1} \qquad (8.2)$$

holds sufficiently well to predict the velocities of sound in each of the materials studied to better than ±5%, and should allow the mean velocities of sound in other scheelites to be estimated to the same accuracy. Estimates so obtained are listed in Table 8.3. In the two scheelites so far employed in acousto-optic devices the velocities are respectively the highest ($CaMoO_4$) and among the lowest ($PbMoO_4$) of those likely to be found in any of the scheelite structure tungstates or molybdates. The table shows that the sound velocities in both $BaWO_4$ and $PbWO_4$ are likely to be lower than those found in $PbMoO_4$. The potential of $PbWO_4$ as an acousto-optic device material has already been examined (Pinnow et al 1969) but $PbMoO_4$ was preferred for reasons which have not been reported. If the slightly slower velocities in $BaWO_4$ are accompanied by significant changes in other parameters which contribute to the appropriate acousto-optic figure-of-merit this material

might give improved efficiency in some types of device.

8.1.3 Debye temperatures

Debye temperatures calculated from the mean sound velocities at room temperature are given in Table 8.4. The small differences between the values obtained for $CaWO_4$ from the room temperature and absolute zero elastic constants and densities indicate that the errors involved in using room temperature data for $CaMoO_4$, $SrMoO_4$ and $PbMoO_4$ are for many purposes insignificant (< 2%). The different Debye temperatures which are listed in Table 8.4 correspond to representing

(i) the whole phonon density of states (θ_D)

(ii) the lattice-only vibrational modes ($\theta_{D(\text{diatomic lattice only})}$)

(iii) the acoustical modes ($\theta_{D(\text{acoustical mode only})}$)

by a Debye distribution, in the manner discussed for $CaWO_4$ in Section 6.2.2. The results for $CaWO_4$ showed that a Debye distribution can be a useful representation of the acoustical modes in scheelites, and perhaps of the lattice-only modes, but will not be valid for the whole vibration spectrum. The significant differences in the Debye temperatures between the materials indicate considerable differences in the phonon populations at a particular temperature. The effects of these different phonon populations on spin-lattice relaxation times in some Nd, Gd and Cr doped scheelites are to be the subject of a separate study.

8.1.4 Occurrence of acoustic symmetry

The relationship between the elastic constant tensors of TI and TII symmetry solids was discussed in Section 3.1.8. It was pointed out that, with respect to an axial set (X'Y'Z) rotated about the fourfold axis by an angle ϕ (given by equation 3.30) from the conventional axial set (XYZ), the elasticity tensor (C'_{ij}) of a TII Laue symmetry crystal takes the form of that of a TI Laue symmetry solid: the constant C'_{16} is zero and the tensor C'_{ij} has just six independent non-zero components. For both the tetragonal Laue groups the symmetry properties of the elastic behaviour are the same and are those of the 4/mmm point group (see Figure 2.1b). In a TI material the elastic properties have fourfold symmetry about the Z axis and mirror symmetry about planes whose intersections are parallel to the <001>, <100> and <110> crystallographic directions. In a TII crystal the elastic behaviour has the same symmetry properties but the intersections of the mirror planes which contain the Z axis with the mirror plane normal to the Z axis are parallel to the axes κ, γ and their equivalents. These axes (κ and γ) are rotated from the <100> directions by angles ϕ_κ and ϕ_γ respectively. Values of ϕ_κ and ϕ_γ, given by the roots of equation 3.30 for the scheelites studied here, are listed in Table 8.5. The axes κ and γ can be termed "axes of acoustic symmetry". They have the same acoustic symmetry properties as the <100> and <110> directions of a TI tetragonal, and coincide with the accidental pure mode axes in the (001) plane (hence the designations κ and γ).

The existence of the acoustic symmetry axes is clearly demonstrated by the cross-sections of the velocity

and Young's modulus surfaces (see Figures 6.16, 6.21, 7.1, 7.2, 7.6, 7.7, 7.9 and 7.10). These surfaces have the ditetragonal symmetry of the TI Laue group. The {100} and {110} plane cross-sections exhibit inversion symmetry and the mirror plane normal to the fourfold axis. The (001) plane sections show clearly the fourfold axis of rotation and the mirror symmetry of the planes $Z\kappa$, $Z\gamma$ and their equivalents. Comparison of the different (001) cross-sections shows that in each material studied the κ axis is a direction of minimum Young's modulus, minimum quasi-longitudinal velocity and maximum quasi-shear velocity. In the direction of the γ axis these extrema are reversed. The angles ϕ_κ and ϕ_γ are positive in each of the scheelites studied but their magnitudes vary somewhat. As a result, although in all four materials the Young's modulus surfaces have similar overall shapes, they are rotated by different amounts with respect to the crystallographic axes and present quite different cross-sections in the <100> and <110> directions.

To compare just the anisotropy of the elastic behaviour but not its relationship to the atomic arrangement then the elastic constants transformed to the axial sets $X' = \kappa$, $Y' = \kappa + \pi/2$, $Z' = Z$ or $X' = \gamma$, $Y' = \gamma + \pi/2$, $Z' = Z$ are appropriate. Values are given in Table 8.5. Knowledge of these transformed constants can be useful for computational purposes; programmes and expressions derived for TI solids can be used for TII solids if directions are referred to the new axial set.

The difficulties encountered in the ultrasonic study of the elastic properties of scheelites (referred to in Chapters 6 and 7) are a direct consequence of the deviation

of the acoustic symmetry axes from the {100} and {110} crystallographic directions. The κ and γ axes of acoustic symmetry are pure mode axes of the first kind; furthermore, they are directions normal to mirror planes of acoustic symmetry, and directions in which both longitudinal and shear modes propagate without deviation of energy flux (Waterman's conditions (1959) hold for axes and planes of acoustic symmetry). A ditetragonal TI crystal can be regarded as a special case of tetragonal in which ϕ_κ is zero and the acoustic symmetry axes (and thus the pure mode axes in the (001) plane) coincide with the crystallographic axes; in these materials the acoustic symmetry axes can therefore be found by x-ray orientation techniques alone. For propagation in these directions there are no difficulties caused by energy flux deviation. In TII symmetry solids the acoustic symmetry axes (and thus the pure mode directions in the XY plane) do not coincide with the crystallographic axes and can only be located by studies of elastic properties. The directions [100] and [110] which can be readily found by x-ray methods are well away from the acoustic symmetry axes, and in scheelites are directions for which the energy flux deviation tends to be rather large. The crystallographic axes [100] and [110] are directions in which velocity measurements must be made if the elastic constants are to be found by the methods of Alton and Barlow (1967) or Chung and Li (1971b). The methods developed in the present work for determining elastic constants from velocity measurements in arbitrary directions (see Section 3.3.3) are therefore particularly appropriate for TII symmetry solids.

The need to describe elastic and acoustic properties with respect to a particular sense of Z axis in TII crystals is very obvious when considered in terms of acoustic symmetry. To describe the positions of the κ and γ axes, it is necessary to describe the magnitude and sense of their rotation from the <100> crystallographic axes. In the scheelites studied here this rotation is clockwise about the Z axis when viewed in the +Z direction. The sense of the rotation can only be defined for a particular sense of the Z axis which must be referred to the atomic arrangement. In a TI crystal however there is no rotation of the κ and γ axes from the <100> and <110> axes and no need to define a sense of Z axis to give a full description of the elastic and acoustic behaviour.

From the elastic constants of the scheelites the positions of the pure mode axes in the (001) plane are given by the values of ϕ_κ and ϕ_γ (see Table 8.4). Knowledge of these positions will be useful if a material is to be employed in devices, or to be the subject of further study (e.g. ultrasonic attenuation, measurement of third order elastic constants or photoelastic constants). It would facilitate work on other scheelites if the positions of the axes of acoustic symmetry could be predicted, at least approximately. The possibility of such predictions is discussed below.

The deviations of the κ and γ acoustic symmetry axes from the crystallographic axes (measured by the value of ϕ_κ) vary somewhat between the materials (see Table 8.5) and increase with increasing values of the setting angle

of the anion. This is demonstrated in Figure 8.3. Data points for the materials studied lie on a smooth curve. By reference to this figure it should be possible to predict the positions of the axes of acoustic symmetry in other scheelites whose oxygen atom coordinates are accurately known.

8.1.5 Interatomic binding in scheelite structure tungstates and molybdates

From the work reviewed in Chapter 2 there emerges a general description of the interatomic binding in $CaWO_4$ and the other scheelites. The studies of crystal structure, vibrational spectra, deformation by slip, specific heat and thermal expansion each provide some information about the nature of the interatomic forces. It appears that the tungstate and molybdate groups behave as rigid structural units, and that they are negatively charged and ionicly bound to positive metal cations. The work on slip deformation (Arbel and Stokes 1965) and thermal expansion (Deshpande and Suryanarayana 1969) has suggested that the scheelites may be regarded as having a complex layer structure and that the binding between the layers (parallel to the (001) planes) is weaker than that within the layers.

Some of the findings of the present work are consistent with the above description of the binding, others are not. In particular the layered nature of the structure has been confirmed: in all the scheelites studied the linear compressibility in the Z direction (normal to the layers) is somewhat larger (between 1½ and 2 times) than that parallel to the layers. The cross-linking within

the layers is stronger than that between them ($|S_{12}|>|S_{13}|$). The present results also show that the binding between the layers is not especially weak compared with that found in some other solids which have pronounced layer type structures and which exhibit very much larger anisotropies of linear compressibility (Akgöz, Farley and Saunders 1973).

In the earlier stages of the present work it was intended to test quantitatively the simple ionic model of the binding and with this in mind a Madelung constant for $CaWO_4$ was calculated. It was assumed that under hydrostatic pressure deformation would occur by a relative movement of the cations with respect to the anions, and that the latter (WO_4^{--}) would remain undistorted. The Madelung constant was calculated by the Evjen method (Evjen 1932) for a lattice with doubly-charged spherical ions (assumed to be point charges) at the Ca and W atom sites. After counting over five shells, each the shape of the unit cell, the sum had converged to the value 1.615† sufficiently rapidly to give an accuracy of ±1.2%. During the summation process an unusual feature of the simple ionic model became apparent: according to the model there is no net attractive Coulombic force between adjacent layers of the structure. With respect to a particular reference ion (take for example a cation sited at the Ca site in layer 3 of the unit cell shown in Figure 2.2), the ions in an adjacent layer (e.g. layer 2) are arranged

†The Madelung constant is defined here with respect to the nearest neighbour distance (Ca^{++} to WO_4^{--}). The value agrees well with the estimate of 1.623 made by Hoppe (1956).

as follows:

2 anions at a distance of $\left\{(\frac{a}{2})^2 + (\frac{c}{4})^2\right\}^{\frac{1}{2}}$

2 cations at a distance of $\left\{(\frac{a}{2})^2 + (\frac{c}{4})^2\right\}^{\frac{1}{2}}$

4 anions at a distance of $\left\{\frac{5a^2}{4} + (\frac{c}{4})^2\right\}^{\frac{1}{2}}$

4 cations at a distance of $\left\{\frac{5a^2}{4} + (\frac{c}{4})^2\right\}^{\frac{1}{2}}$

6 anions at a distance of $\left\{\frac{13a^2}{4} + (\frac{c}{4})^2\right\}^{\frac{1}{2}}$

6 cations at a distance of $\left\{\frac{13a^2}{4} + (\frac{c}{4})^2\right\}^{\frac{1}{2}}$

etc.

etc.

There are similar arrangements of ions on successive even numbered layers. Thus according to the model there will be no net Coulombic attraction between parallel layers which are separated by distances $(2n+1)c/4$ where n is a positive or negative integer. This feature of the model may explain why the binding is weaker between the layers than within them, but it also suggests that the model is inadequate.

The validity of an ionic model can be checked by comparing the theoretical cohesive energy (calculated from the Madelung energy, the measured bulk modulus and the unit cell parameters) with an experimental cohesive energy which is determined from electrochemical data by means of a Born-Haber cycle. For alkali halides the good agreement which obtains is taken as confirmation that the binding is ionic. However for $CaWO_4$ (and indeed for any of the other scheelites) there is not sufficient electrochemical data available to allow this test; the electron affinities of the WO_4 and MoO_4 groups are not known.

Some of the present experimental results do provide further evidence that the simple ionic model is not a very good representation of the binding. If the binding were purely ionic with doubly charged spherical ions located at the sites of the metal atoms, then the array of charges in the lattice would have a point group 4/mmm, and the elastic properties of the material would have TI symmetry with acoustic symmetry axes parallel to the <100> and <110> crystallographic directions. The oxygen atoms in the WO_4^{--} and MoO_4^{--} ions would have no preferred positions and there would be no means of defining a sense of Z axis. In fact the anion setting angles appear to be such that each oxygen atom is sited closer to a pair of metal cations than would be the case if the setting angles were zero. This indicates that there may be short range binding directly between the metal (Ca, Sr, Pb etc.) cations and the oxygen atoms. The suggestion is substantiated by the experimental finding (see Section 8.1.1) that the elastic constants of the scheelites depend much more on the cation than on the anion. The relative strength of the additional binding forces is indicated by, firstly, the significant dependence of the isotropic Young's and shear moduli on the cation and, secondly, by the orientation dependence of the elastic properties. The large deviations of the acoustic symmetry axes from the <100> and <110> crystallographic directions which have been found in each of the scheelites studied, and the pronounced extrema of the Young's modulus and quasi-shear velocities which occur in these directions are

a direct consequence of the significant effect of the additional binding forces. These findings provide a clear demonstration that the simple 'diatomic' ionic model is not an adequate description of the binding.

Table 8.1

Comparison of the room temperature elastic constants of $CaWO_4$, $CaMoO_4$, $SrMoO_4$ and $PbMoO_4$

	$CaWO_4$	$CaMoO_4$	$SrMoO_4$	$PbMoO_4$
Stiffness constants (Units: 10^{11} dyn cm^{-2})				
C_{11}	+14.6	+14.4	+11.9	+10.9
C_{12}	+ 6.3	+ 6.5	+ 6.2	+ 6.8
C_{13}	+ 3.9	+ 4.5	+ 4.8	+ 5.3
C_{16}	- 1.9	- 1.4	- 1.2	- 1.4
C_{33}	+12.74	+12.63	+10.4	+ 9.17
C_{44}	+ 3.35	+ 3.69	+ 3.49	+ 2.67
C_{66}	+ 3.87	+ 4.61	+ 4.2	+ 3.37
Compliance constants (Units: 10^{-13} cm^2 dyn^{-1})				
S_{11}	+10.5	+ 9.9	+13.6	+21.0
S_{33}	+ 8.8	+ 9.4	+12.7	+16.6
S_{44}	+29.8	+27.1	+28.7	+37.5
S_{66}	+33.5	+24.4	+ 27.1	+40.6
S_{12}	- 5.1	- 4.3	- 6.3	-12.4
S_{13}	- 1.7	- 2.0	- 3.4	- 4.9
S_{16}	+ 7.7	+ 4.4	+ 5.7	+13.5

TABLE 8.2

Room temperature elastic properties

	$CaWO_4$	$CaMoO_4$	$SrMoO_4$	$PbMoO_4$
Bulk modulus, K_v	7.7	7.9	7.2	7.1
Volume compressibility, β_v	13.0	12.6	13.8	14.0
Linear compressibilities, β_z	5.5	5.3	6.0	6.7
β_{xy}	3.7	3.6	3.9	3.6
Isotropic Young's modulus	8.6	9.0	7.6	5.4
Isotropic Shear modulus	3.7	4.0	3.3	2.4
Debye mean velocity	2.74	3.42	3.02	2.11

Bulk, Young's and shear moduli are in units of 10^{11} dyn cm^{-2}.

Compressibilities are in units of 10^{-13} cm^2 dyn^{-1}.

Velocities are in units of 10^5 cm s^{-1}.

TABLE 8.3

Estimates of mean sound velocities in some scheelite structure tungstates and molybdates, obtained by the empirical relationship (8.2)

$v_m \propto 6.1 \times 10^5 \; M^{-0.8}$ cm s^{-1}

$BaWO_4$	2.0×10^5	cm s^{-1}
$BaMoO_4$	2.5×10^5	cm s^{-1}
$PbWO_4$	1.8×10^5	cm s^{-1}
$CdMoO_4$	2.7×10^5	cm s^{-1}

Table 8.4

Comparison of the effective Debye temperatures of $CaWO_4$, $CaMoO_4$, $SrMoO_4$ and $PbMoO_4$

	(i) θ_D	(ii) θ_D (diatomic lattice only)	(iii) θ_D (acoustical mode only)
$CaWO_4$ [a]	354 K	246 K	155 K
$CaWO_4$ [b]	348 K	241 K	152 K
$CaMoO_4$ [b]	433 K	300 K	191 K
$SrMoO_4$ [b]	363 K	252 K	159 K
$PbMoO_4$ [b]	264 K	183 K	115 K

[a] Calculated from elastic constants and density extrapolated to absolute zero.

[b] Calculated from room temperature elastic constants and density.

Table 8.5

Room temperature elastic constants in units of 10^{11} dyn cm^{-2} transformed to axial sets $X'=\kappa$, $Y'=\kappa+\pi/2$, $Z'=Z$ and $X'=\gamma$, $Y'=\gamma+\pi/2$, $Z'=Z$ by rotation about the Z axis through angles ϕ_κ and ϕ_γ respectively.†

	$CaWO_4$		$CaMoO_4$		$SrMoO_4$		$PbMoO_4$	
	$\phi_\kappa=23.6^o$	$\phi_\gamma=68.6^o$	$\phi_\kappa=19.3^o$	$\phi_\gamma=64.3^o$	$\phi_\kappa=15.1^o$	$\phi_\gamma=60.1^o$	$\phi_\kappa=16.0^o$	$\phi_\gamma=61.0^o$
C'_{11}	12.5	16.4	13.3	16.2	11.2	13.9	8.74	11.8
C'_{12}	8.3	4.5	7.6	4.7	6.9	4.1	7.7	4.6
C'_{13}	3.9	3.9	4.5	4.5	4.8	4.8	5.3	5.3
C'_{16}	0	0	0	0	0	0	0	0
C'_{33}	12.74	12.74	12.6	12.6	10.4	10.4	9.17	9.17
C'_{44}	3.35	3.35	3.69	3.69	3.49	3.49	2.67	2.67
C'_{66}	5.9	2.1	5.7	2.8	4.9	2.1	4.2	1.2

† Equation 3.30 has two roots separated by $\pi/4$ in each quadrant. ϕ_κ is taken as the angle from the [100] direction to the first axis of acoustic symmetry in the +X+Y quadrant and is measured towards the [010] direction. ϕ_γ is equal to $\phi_\kappa + \pi/4$.

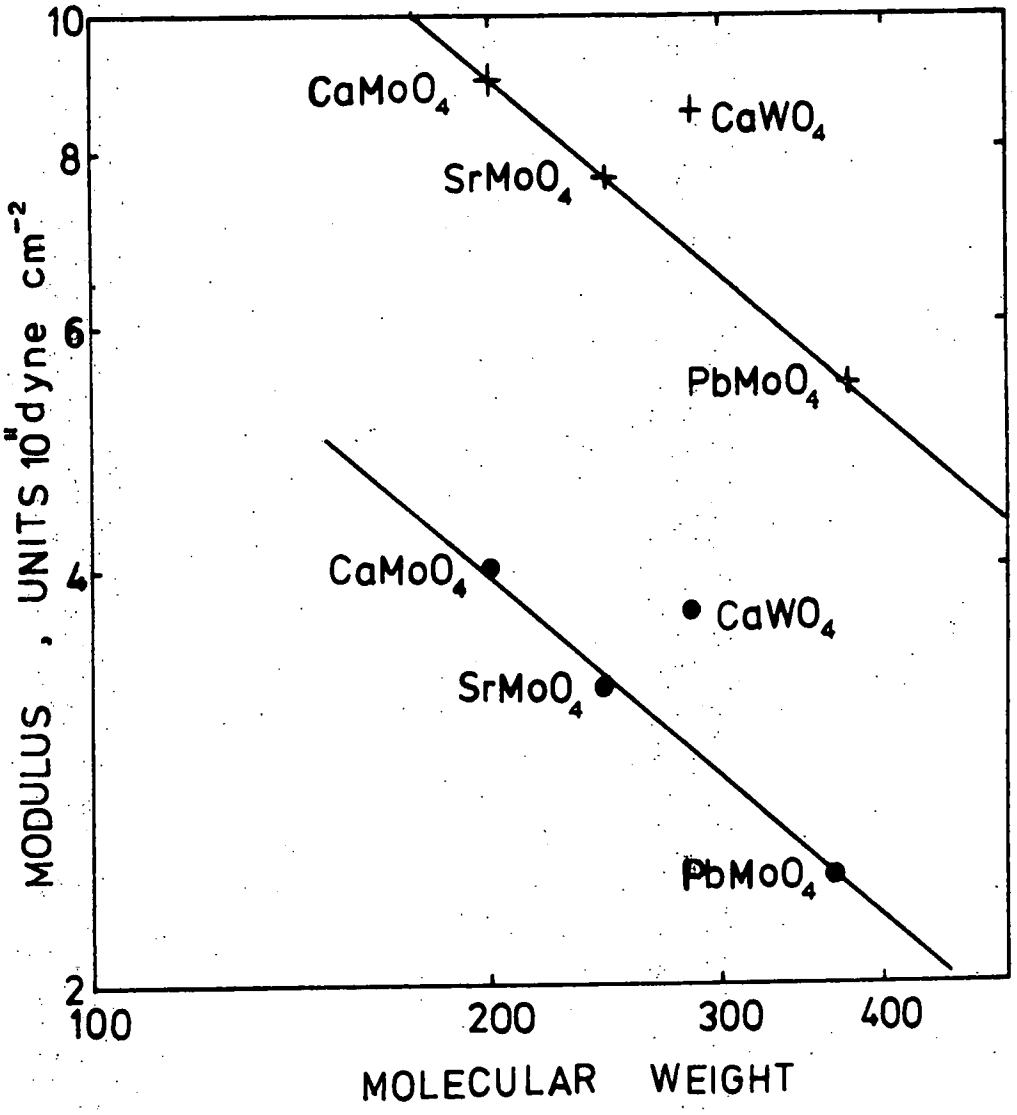

FIGURE 8.1: Plot of isotropic Youngs Modulus E_H (+) and shear modulus G_H (●) against molecular weight for the scheelites studied.

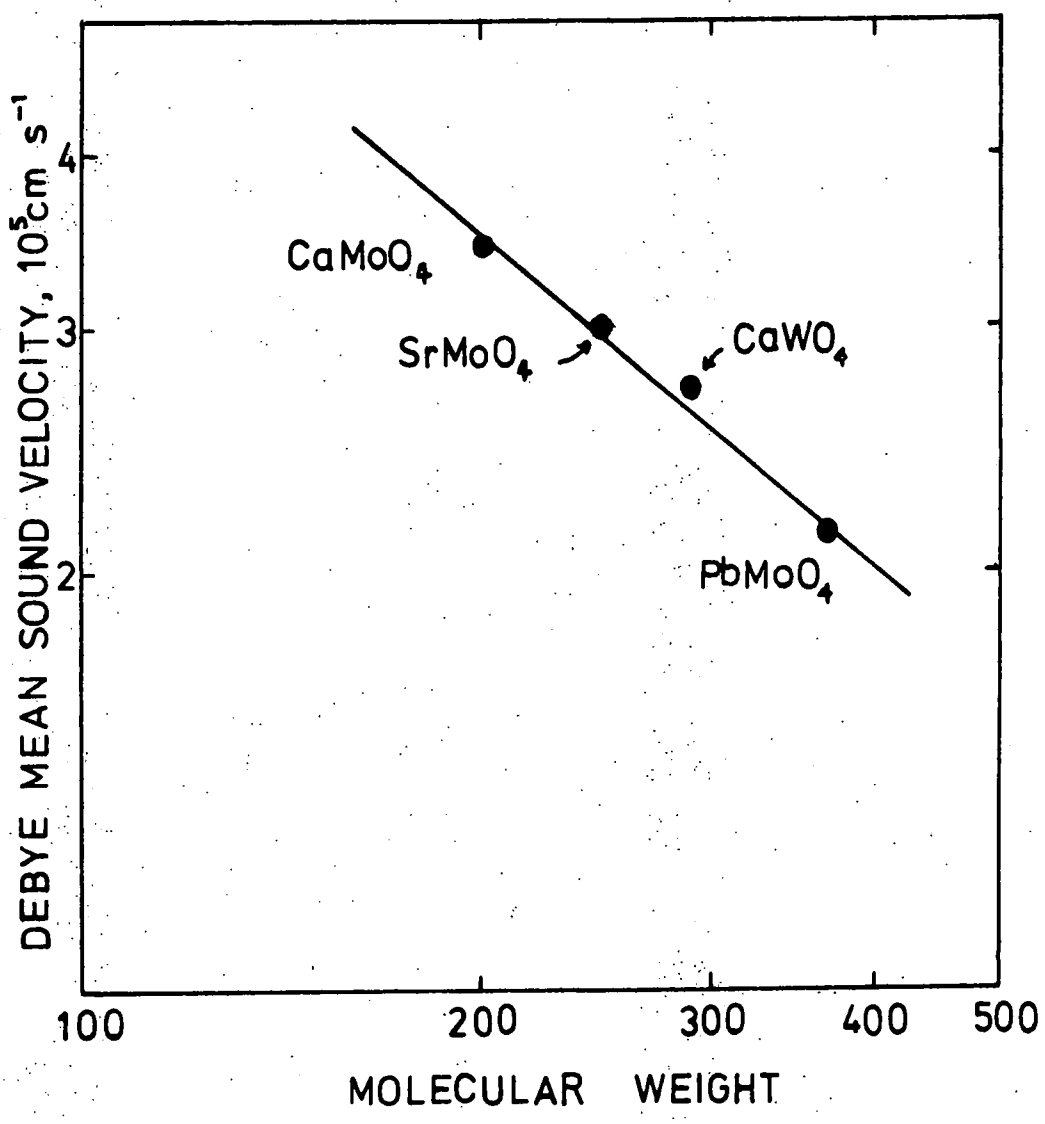

FIGURE 8.2: Plot of Debye mean sound velocity against molecular weight for the scheelites studied.

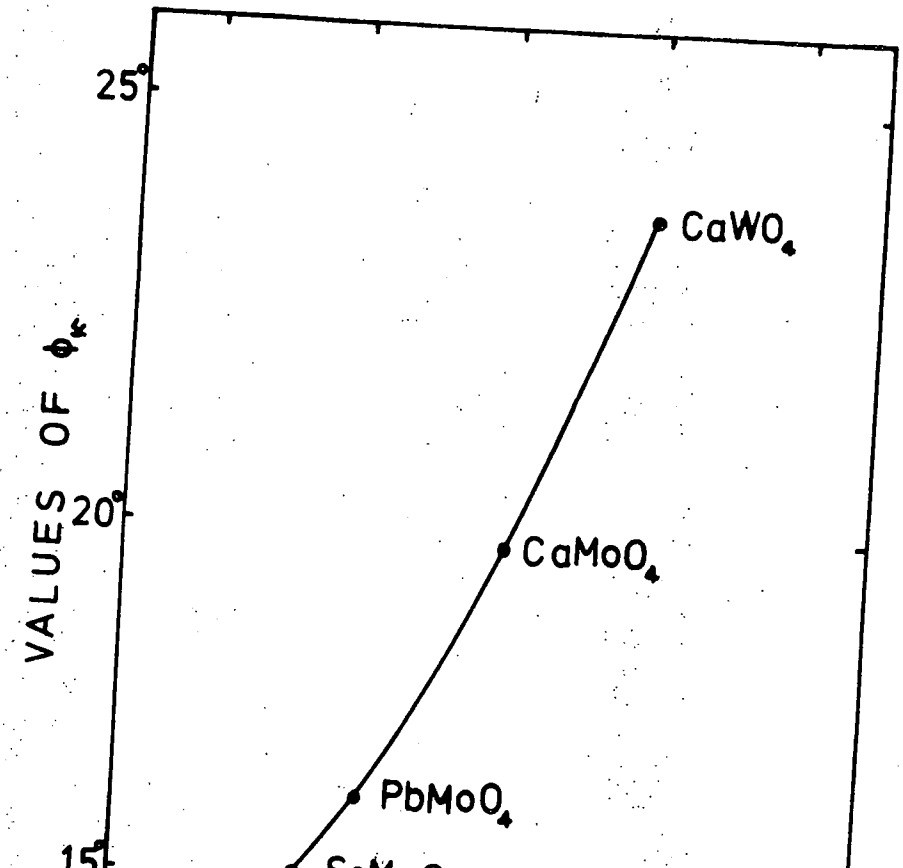

FIGURE 8.3: Plot to show the relationship between the positions of the "acoustic symmetry axes" and the anion orientation in scheelites. ϕ_κ is the angle between the [100] axis and the κ acoustic symmetry axis; the setting angle of the anion is the angle between the [100] axis and the projection of a W-O or Mo-O bond in the (001) plane.

REFERENCES

Akgöz Y C, Farley J M and Saunders G A (1972) J. Mat. Sci. 7, 598-600

Akgöz Y C, Farley J M and Saunders G A (1973) J. Phys. Chem. Solids 34, 141-9

Alers G A (1965) "Physical Acoustics" Vol 3B ed. W P Mason Chap. 1 Pg.1 Academic Press, London

Alton W J and Barlow A J (1967) J. Appl. Phys. 38, 3817-20

Anderson O L (1959) J. Phys. Chem. Solids 12, 41-52

Anderson O L (1963) J. Phys. Chem. Solids 24, 909-17

Anderson O L (1965) "Physical Acoustics," Vol 3B ed. W P Mason Chap.2 Pg.43 Academic Press, London

Arbel A and Stokes R J (1965) J. Appl. Phys. 36, 1460-8

Arenberg D L (1948) J. Acoust. Soc. Am. 20, 1

Barker A S (1964) Phys. Rev. 135, A742

Bolef D I and Miller J G (1971) "Physical Acoustics" eds. W P Mason and R N Thurston, Pg.95, Academic Press, New York

Bonner W A and Zydzik G J (1970) J. Cryst. Growth 7, 65-8

Borgnis F E (1955) Phys. Rev. 98, 1000

Born M and Huang K (1954) "Dynamical theory of crystal lattices" Clarendon Press, Oxford

Brixner L H (1968) Electrochem. Tech. 6, 88

Brugger K (1965) J. Appl. Phys. 36, 759

Buchanan I C and Casselton R E W (1966) I.R.D. Research Report 66-76

Cady W G (1964) "Piezoelectricity" Dover Publications Inc. New York

Chadhuri A R and Phaneuf L E (1963) J. Appl. Phys. 34, 2162

Chang L L Y, Scroger M G and Philips B (1966) J. Amer. Ceram. Soc. 49, 385

Chang Z P (1968) J. Appl. Phys. 39, 5669

Chung D Y and Li Y (1971a) Phys. Lett. 34A, 392-4

Chung D Y and Li Y (1971b) Phys. Status Solidi (a) 5, 669

Christoffel E G (1877) Ann. di. Mat. 8, 193

Cockayne B and Hollox G E (1964) Phil. Mag. 9, 911

Cockayne B and Robertson D S (1964) B. J. Appl. Phys. 15, 643

Cockayne B, Robertson D S and Bardsley W (1964) B. J. Appl. Phys. 15, 1165

Coquin G A, Pinnow D A and Warner A W (1971) J. Appl. Phys. 42, 2162-8

Cottam R I and Saunders G A (1973) J. Phys. C: Solid State Phys. 6, 2105-18

Cottam R I and Saunders G A (1973) J. Phys. D: Applied Physics (in press)

Crocker A G and Singleton G A A M (1971) Phys. Stat. Solidi 6, 635

Deshpande V T and Suryanarayana S V (1969) J. Phys. Chem. Solids 30, 2484-6

Deshpande V T and Suryanarayana S V (1972) J. Mat. Sci. 7, 255

Drabble J R and Brammer A J (1967) Proc. Phys. Soc. (London) 91, 959

Esashi S and Namikata T (1972) Fujitsu Scientific and Technical Journal 8, 211-45

Evjen H M (1932) Phys. Rev. 39, 675

Farabaugh E N, Peiser H S and Wachtmann J P (1966) J. Res. Nat. Bur. Stands. 70A, 379

Farley J M and Saunders G A (1971) Solid Stat. Comm. 9, 965

Flinchbaugh D E (1971) "Acoustic Surface Wave and Acousto-optic Devices" ed. T. Kallard Pg.139 Optosonic Press, New York

Flournoy P A and Brixner L H (1965) J. Electrochem. Soc. 112, 779

Forgacs R L (1960) J. Acoust. Soc. Am. 32, 1697

Gerlich D (1964) Phys. Lett. 12, 314

Gunton D J and Saunders G A (1972) J. Mat. Sci. 7, 1061-8

Gürmen E, Daniels E and King J S (1971) J. Chem. Phys. 55, 1093

Haga H and Jaeger F M (1916) Proc. Acad. Sci. Amsterdam 18, 1350-7

Handbook of Chemistry and Physics (1966-7) 47th edition, The Chemical Rubber Co., U.S.A.

Harris S E, Nieh S T K and Feigelson R S (1970) Appl. Phys. Lett. 17, 223-5

Hemstead C F and Bowers K D (1959) Phys. Rev. 118, 131-4

Hobden M V (1972) "Modern Oxide Materials" eds. B Cockayne and D W Jones, Pg.29, Academic Press, London

Holder J (1970) Rev. Sci. Inst. 41, 1355-6

Holland M G (1962) J. Appl. Phys. 33, 2910

Hoppe R (1956) Z. Anorg. Chem. 283, 196

International Tables for X-ray Crystallography (1952) eds. N F M Henry and K Lonsdale, Vol.1, Kynoch Press, Birmingham

James B W (1972) Phys. Stat. Solidi (a) 13, 89

Jeavons A P and Saunders G A (1969) Proc. Roy. Soc. A310, 415-32

Johnson L F, Boyd G D, Nassau K and Soden R R (1962) Phys. Rev. 126, 1406

Johnson L F (1963) J. Appl. Phys. 34, 897-909

Kay M I, Frazer B C and Almodovar I (1964) J. Chem. Phys. 40, 504

Kelvin, Lord (1904) "Baltimore Lectures" Cambridge University Press

Key S W (1967) J. Appl. Phys. 38, 2923-8

Khanna R K, Brower W S, Guscott B R and Lippincott E R (1968) J. Res. Natl. Bur. Stand. 72A, 81-4

Khanna R K and Lippincott E R (1968) Spectrochim Acta G.B. 24A, 905

Kharusi M S and Farnell G W (1970) J. Acoust. Soc. Am. 48, 665

Khatkevich A G (1962) Sov. Phys. Cryst. 6, 561-3

Khatkevich A G (1963) Sov. Phys. Cryst. 7, 742-5

Kiel A and Mims W B (1967) Phys. Rev. 161, 386

King E G and Weller W W (1961) U.S. Bureau of Mines Rept. Invest. No.5791

Klein P H (1968) Proc. of 7th Conf. on Thermal Conductivity (Gaithersburg, Maryland 13-16 Nov. 1967) Pg.399, Natl. Bur. of Stand. Washington

Klemens P G (1958) "Solid State Physics" Vol.7 eds. F. Seitz and D Turnbull, Pg.1, Academic Press, New York

de Klerk J and Musgrave M J P (1955) Proc. Phys. Soc. B 68, 81

Kopp H (1865) Phil. Trans. Roy. Soc. (London) 155, 71

Lacy L L and Daniel A C (1972) J. Acoust. Soc. Am. 52, 189-95

Lakkad S C (1971) J. Appl. Phys. 42, 4277-81

Landau L and Rumer G (1937) Phys. Z. Sowjetunion 11, 18

Leciejewicz J (1965) Z. Krist 121, 158

Levelut A (1969) Acta. Crystallogr. A25, 553-563

Levinstein H J, Loiacono G M and Nassau K (1963) J. Appl. Phys. 34, 3603

Lewis M F (1972) Phys. Lett. 38A, 465-6

Liu J M and Green R E (1972) J. Appl. Phys. 43, 2010

Love A E H (1944) "A Treatise on the Mathematical Theory of Elasticity" Dover Publ. Inc. New York

Lyon W G and Westrum E F (1968) J. Chem. Phys. 49, 3374

McSkimin H J (1950) J. Acoust. Soc. Am. 22, 413-8

McSkimin H J (1957) IRE Trans on Ultrasonic Engineering PGUE-5, 25-43

McSkimin H J (1960) J. Acoust. Soc. Am. 32, 1401-4

McSkimin H J (1961) J. Acoust. Soc. Am. 33, 12-16

McSkimin H J and Andreatch P (1962) J. Acoust. Soc. Am. 34, 609-15

McSkimin H J (1964) "Physical Acoustics" Vol. 1A, ed. W P Mason, Pg.271, Academic Press, New York

McSkimin H J and Andreatch P (1967) J. Acoust. Soc. Am. 41, 1052-6

Malgrange J-L, Quentin G, Thuillier J-M (1964) Phys. Stat. Solidi 4, 139-41

Maris H J (1971) "Physical Acoustics" Vol.8, eds. W P Mason and R N Thurston Pg.280

Mason W P (1958) "Physical Acoustics and Properties of Solids" Van Nostrand, New Jersey

May J E Jr (1958) IRE Natl. Conv. Rec. 6, 134-42

Miller J G and Bolef D R (1970) J. Appl. Phys. 41, 2282

Musgrave M J P (1954) Proc. Roy. Soc. (Lond.) A226, 339

Musgrave M J P (1957) Acta Crystallogr. 10, 316

Musgrave M J P (1970) "Crystal Acoustics" Holden-Day San Francisco

Namikata T and Esashi S (1972) Japan J. Appl. Phys. 11, 772-3

Nassau K and Van Uitert L G (1960) J. Appl. Phys. 31, 1508

Nassau K and Broyer A M (1962) J. Appl. Phys. 33, 3064

Nassau K and Loiacono G M (1963) J. Phys. Chem. Solids 24, 1503

Nassau K (1963) J. Phys. Chem. Solids 24, 1511

National Bureau of Standards (1962) Monograph 25

Nye J F (1957) "Physical Properties of Crystals" OUP, Clarendon Press

Pace N G (1970) "Ultrasound wave propagation and binding in solids" Ph.D. Thesis, University of Durham

Pace N G, Saunders G A and Sümengen Z (1970) J. Phys. Chem. Solids 31, 1467

Papadakis E P (1966) J. Acoust. Soc. Am. 40, 863

Papadakis E P (1967) J. Acoust. Soc. Am. 42, 1045

Papadakis E P (1969) J. Acoust. Soc. Am. 45, 1547

Pinnow D A, Van Uitert L G, Warner A W and Bonner W A (1969) Appl. Phys. Lett. 15, 83

Porto S P S and Scott J P (1967) Phys. Rev. 157, 716

Preziosi S, Soden R R, Van Uitert L G (1962) J. Appl. Phys. 33, 1893

Russell J P and Loudon R (1965) Proc. Phys. Soc. 85, 1029

Russell J P (1966) "Phonons in perfect lattices and in lattices with point imperfections" ed. R W Stevenson, Pg.235, Oliver and Boyd, Edinburgh and London

Scott J F (1968) J. Chem. Phys. 48, 874

Seki H, Granato A and Truell R (1956) J. Acoust. Soc. Am. 28, 230

Shapovalova R D, Mikhailova N P and Gerasimov YaI (1960) Russian J. Phys. Chem. (English Trans) 34, 978

Sillén L G and Nylander A K (1943) Arkiv. Kemi. Miner. Geol. 17A, 4

Sittig E K and Cook H D (1968) Proc. IEEE 56, 1375-7

Swanson H E, Gilfrich N T and Cook M I (1956) Natl. Bur. Stand. Circular No.539, 6

Standards on Piezoelectric Crystals (1949) Proc. IRE 37, 1378

Thornton J R, Fountain W D, Flint G W and Crow T G (1969) Appl. Optics 8, 1087

Truell R , Elbaum C and Chick B B (1969) "Ultrasonic methods in Solid State Physics" Academic Press, New York

Vesselinov I (1971) J. Cryst. Growth 10, 45-55

Wachtmann J B, Brower W S and Farabaugh E N (1968) J. Am. Ceram. Soc. 51, 341-4

Watermann P C (1959) Phys. Rev. 113, 1240

Weller W W and King E G (1963) U.S. Bureau of Mines Rept. Invest. No.6174

White G K (1959) "Experimental Techniques in Low Temperature Physics" OUP, Clarendon Press

Williams J and Lamb J (1958) J. Acoust. Soc. Am. 30, 308

Wyckoff R W G (1960) "Crystal Structures" Vol.II, Interscience, New York

Yakoleva R A and Rezukhina T N (1960) Russ. J. Phys. Chem. (English trans) 34, 390

Yates B and Bailey A C (1971) J. Low. Temp. Phys. 4, 117

Zalkin A and Templeton D H (1964) J. Chem. Phys. 40, 501

APPENDIX I : COMPUTER PROGRAMS

1. Least squares fitting procedure for determining elastic constants of TII crystals from sound velocity measurements.

```
LASTIC CONSTANTS OF TETRAGONAL CRYSTALS  MK2 */


/*      ELASTIC CONSTANTS OF TETRAGONAL CRYSTALS  MK2 */
 ELASTIC:PROC OPTIONS (MAIN);
/*                                                                  */
       DCL((SOLN,STEP,MAX,MIN,HOLD)(7),(CAL,COEFF,W,P)(13),SMALL,Q,D,
       SUMSQ(2))FLOAT;
       DCL(VELEX(14))FLOAT;
      DCL(STEP1(7))FLOAT;
       ON ENDFILE(SYSIN)STOP;
/*                                                                  */
      GET LIST (MAX,MIN,P,SMALL,J,STEP1,SOLN);
       PUT PAGE LIST ('INITIAL GUESSED SOLUTION=',SOLN);
  TEMP:GET LIST (T,D,VELEX);
       PUT SKIP(3) EDIT ('TEMPERATURE=',T,'DENSITY=',D)(A(12),F(3),
       X(2),A(8),F(6,3));
/*                                                                  */
/*      CALCULATION OF COEFFICIENTS FROM MEASURED VELOCITIES        */
       DO I=1 TO 8;
            COEFF(I)=VELEX(I)**2;
            END;
            COEFF(9)=VELEX(9)**4+VELEX(10)**4+VELEX(11)**4;
            COEFF(10)=VELEX(9)**2+VELEX(10)**2+VELEX(11)**2;
            COEFF(11)=VELEX(12)**2;
            COEFF(12)=VELEX(13)**2;
            COEFF(13)=VELEX(14)**2;
       DO I=1 TO 14;
            PUT SKIP EDIT ('VELEX',I,'=',VELEX(I))(X(3),A(5),F(2),A(1)
            ,E(10,3));
            END;
       PUT SKIP LIST ('DATA CROSS-CHECKS');
       PUT SKIP LIST ('C11+C66:0,0.707,0.707,=',D*(2*COEFF(10)-
       COEFF(1)-3*COEFF(2)));
       PUT SKIP LIST ('C11+C66:0.86,0.5,0,=',D*(COEFF(13)+COEFF(12)))
       ;
/*                                                                  */
/*      CALCULATION OF WEIGHT COEFFICIENTS                          */
       DO I=1 TO 13;
            W(I)=1/P(I);
            END;
/*                                                                  */
/*      SYSTEMATIC ADJUSTMENT OF SOLUTION TO MINIMISE SUMSQ         */
       HOLD=SOLN;
       CALL EQUATE;
       PUT SKIP(2) LIST ('INITIAL VALUES OF CAL,COEFF,RATIO');
       PUT SKIP EDIT ('CAL','COEFF','CAL/COEFF')(X(7),A,X(7),A,X(5),
       A);
       DO N=1 TO 4,6,7,9 TO 13;
            PUT SKIP EDIT (N,CAL(N),COEFF(N),CAL(N)/COEFF(N))
            (F(2,0),2(E(12,2)),F(10,3));
            END;
       PUT SKIP LIST ('INITIAL SUMSQ=',Q);
       PUT SKIP LIST ('SEARCH INITIATED');
       PUT SKIP EDIT ('C11','C12','C13','C16','C33','C44','C66',
       'SUMSQ1','SUMSQ2')(X(1),7(X(7),A(3)),X(11),A(6),X(5),A(6));
      STEP=STEP1;
      CYCLE=0;
       DO WHILE(CYCLE<=J);
```

```
LASTIC CONSTANTS OF TETRAGONAL CRYSTALS  MK2 */


            DO I=1 TO 7;
                SUMSQ(1)=0;
                IF SUMSQ(1)<SMALL THEN GOTO EXIT;
                H=1;
                DO WHILE((SOLN(I)>MIN(I))&(SOLN(I)<MAX(I)));
                    SOLN(I)=SOLN(I)+H*STEP(I);
                    CALL EQUATE;
                    SUMSQ(2)=0;
                    IF SUMSQ(2)>SUMSQ(1) THEN IF H=1 THEN DO;
                                              SOLN(I)=SOLN(I)-STEP(I);
                                              H=-1;
                                              GOTO SEARCH;
                                              END;
                                         ELSE GOTO NEXT;
                     SUMSQ(1)=SUMSQ(2);
                SEARCH:END;
            NEXT:SOLN(I)=SOLN(I)-H*STEP(I);
                CALL EQUATE;
                END;
            DO K=1 TO 7;
                IF (SOLN(K)>(HOLD(K)+STEP(K)*0.1))|(SOLN(K)<(HOLD(K)-
                STEP(K)*0.1))THEN GOTO NO;
                END;
            PUT EDIT ('FINER SEARCH INITIATED,CYCLE',CYCLE)(SKIP,A(28)
            ,F(3));
            PUT EDIT (CYCLE,SOLN,SUMSQ)(SKIP,F(3),X(2),7 F(10,3),X(4),
            F(10,5),X(2),F(10,5));
            STEP=STEP*0.25;
         NO:CYCLE=CYCLE+1;
            HOLD=SOLN;
            END;
/*                                                                    */
/*          FINAL SOLUTION AND QUALITY OF FIT TO MEASUREMENTS         */
     EXIT:PUT SKIP LIST ('FINAL SOLN CYCLE=1',CYCLE);
          PUT EDIT (CYCLE,SOLN,SUMSQ)(SKIP,F(3),X(2),7 F(10,3),X(4),
          F(10,5),X(2),F(10,5));
          PUT SKIP EDIT ('CAL','COEFF','CAL/COEFF')(X(7),A,X(7),A,X(5),A
          );
          DO N=1 TO 4,6,7,9 TO 13;
              PUT SKIP EDIT (N,CAL(N),COEFF(N),CAL(N)/COEFF(N))
              (F(2,0),2(E(12,2)),F(10,3));
              END;
/*                                                                    */
          GO TO TEMP;
/* SUBROUTINE TO CALCULATE SUMSQ FOR EACH GUESSED SOLUTION           */
   EQUATE:PROCEDURE;
          DCL(A(7),Z(13))FLOAT;
          A=SOLN;
          B1=A(1)**2+A(7)**2+2*A(4)**2;
          D1=A(2)**2-A(1)**2+2*A(7)*(A(1)+A(2));
          X1=SQRT((A(1)+A(7))**2-4*(A(1)*A(7)-A(4)**2));
          X2=SQRT((A(2)+A(7))**2+4*(A(4)**2));
          X3=SQRT((A(1)/2-A(7)/2+A(4)*SQRT(3))**2+
          4*((A(4)/2+(SQRT(3)/4)*(A(2)+A(7)))**2));
```

```
LASTIC CONSTANTS OF TETRAGONAL CRYSTALS  MK2 */


        Z(1)=(A(5))/D;
        Z(2)=(A(6))/D;
        Z(3)=(A(6))/D;
        Z(4)=(A(1)+A(7)+X1)/(D**2);
        Z(6)=(A(6))/D;
        Z(7)=(A(1)+A(7)+X2)/(D**2);
        Z(9)=((A(5)**2)/4+(5*A(6)**2)/4+(A(3)**2+A(6)*(A(1)+A(5)+A(7)
             +2*(A(3))))/2+(B1))/4)/D**2;
        Z(10)=(A(1)+A(7)+A(5)+3*A(6))/(2*D);
        Z(11)=A(6)/D;
        Z(12)=(A(1)+A(7)+X3)/(2*D);
        Z(13)=(A(1)+A(7)-X3)/(2*D);
        CAL=Z;
        O=((CAL(1)/COEFF(1)-1.0)*W(1))**2
         +((CAL(2)/COEFF(2)-1.0)*W(2))**2
         +((CAL(3)/COEFF(3)-1.0)*W(3))**2
         +((CAL(4)/COEFF(4)-1.0)*W(4))**2
         +((CAL(6)/COEFF(6)-1.0)*W(6))**2
         +((CAL(7)/COEFF(7)-1.0)*W(7))**2
         +((CAL(9)/COEFF(9)-1.0)*W(9))**2
         +((CAL(10)/COEFF(10)-1.0)*W(10))**2
         +((CAL(11)/COEFF(11)-1.0)*W(11))**2
         +((CAL(12)/COEFF(12)-1.0)*W(12))**2
         +((CAL(13)/COEFF(13)-1.0)*W(13))**2;
        END EQUATE;
/*                                                                    */

        END ELASTIC;
```

2. Calculation of eigenvalues and eigenvectors of Christoffel equations.

```
      $COMPILE
      C    AP7L  J.M.FARLEY
      C       CALCULATED FROM CIJ AND DENSITY
      1       REAL L(6),R(9),L11,L22,L33,L12,L23,L31,N1,N2,N3
      2       INTEGER PHI,THETA
      C READ ELASTIC CONSTANTS,TEMP,AND DENSITY. FOR 4/MMM PUT C16=ZERO
      3     3 READ(5,100) T,C11,C12,C13,C16
      4   100 FORMAT(F10.1,4E10.3)
      5       READ(5,101) C33,C44,C66,P
      6   101 FORMAT(3E10.3,F10.4)
      C PRINT OUT INPUT DATA
      7       WRITE(6,102) T,C11,C12,C13,C16
      8   102 FORMAT('TEMP=',F5.1,/4E10.3)
      9       WRITE(6,103) C33,C44,C66,P
      10  103 FORMAT(3E10.3,/'DENSITY=',F10.4)
      C THETA IS ANGLE OF PROPAGATION DIRECTION MEASUREDAWAY FROM THE+Z-AXIS
      C PHI IS ANGLE IN X-Y PLANE MEASURED AWAY FROM +X AXIS TOWARDS +Y AXIS
      11      DO 1 I=24,69,45
      12      PHI=I-1
      13      WRITE(6,104) PHI
      14  104 FORMAT('PHI=',I4)
      15      WRITE(6,107)
      16  107 FORMAT('   ANGLE        V1         V2         V3         VM         VTOT'
          1)
      17      DO 2 THETA=1,90
      18      A=THETA/57.2956
      19      B=PHI/57.2956
      20      N3=(COS(A))
      21      N2=(SIN(A))*(SIN(B))
      22      N1=(SIN(A))*(COS(B))
      C CALCULATE THE COMPONENTS OF THE CHRISTOFFEL DETERMINANT
      23      L11=(N1**2)*C11+(N2**2)*C66+(N3**2)*C44+2*N1*N2*C16
      24      L22=(N2**2)*C66+(N2**2)*C11+(N3**2)*C44-2*N1*N2*C16
      25      L33=(N1**2)*C44+(N2**2)*C44+(N3**2)*C33
      26      L23=N2*N3*(C13+C44)
      27      L31=N1*N3*(C13+C44)
      28      L12=(N1**2)*C16-(N2**2)*C16+N1*N2*(C12+C66)
      C STORE THE COMPONENTS AS A DIAGONAL MATRIX,STORAGE MODE 1
      29      L(1)=L11
      30      L(2)=L12
      31      L(3)=L22
      32      L(4)=L31
      33      L(5)=L23
      34      L(6)=L33
      35      CALL EIGEN(L,R,3,0)
      C CALCULATE THE VELOCITIES FROM THE EIGENVALUES
      36      V1=SQRT(L(1)/P)
      37      V2=SQRT(L(3)/P)
      38      V3=SQRT(L(6)/P)
      3     2 WRITE(6,99) R
      4    99 FORMAT(1X,3E15.4)
      5     1 CONTINUE
      6       GO TO 3
      7       STOP
```

3. Program to calculate particle displacement directions and energy flux directions in (001) plane of TII crystals.

```
      $COMPILE
      C     CHARACTERISTICS OF ELASTIC WAVE PROPAGATION IN THE (001) PLANE
      C     OF TETRAGONAL LAUE T2 CRYSTALS
      C     IN THE (001) PLANE N3 IS ZERO
      C     P IS THE CRYSTAL DENSITY
      C     WAVE VELOCITIES IN T2 LAUE CRYSTALS
      C     PROGRAMME TO CALCULATE THE TWO VELOCITIES IN THE (001) PLANE
      C     OTHER THAN THAT OF THE PURE SHEAR MODE
  1         REAL N1(360),N2(360),A1(360),L11(360),L12(360),L13(360),L22(360),
     1L23(360),L33(360),B(360),C(360),D(360),E(360),V1(360),V2(360)
  2         REAL C11,C12,C13,C16,C33,C44,C66,P
  3         REAL P211(360),P212(360),P213(360),QP211(360),QP212(360),
     1QP213(360),QPX211(360),QPX212(360),QPX213(360)
  4         REAL DEGA1(360),X1(360),X2(360),AX1(360),AX2(360)
  5         REAL DEV1(360),DEV2(360)
      C     P IS THE DENSITY
  6         READ(5,7) C11,C12,C13,C16,C33,C44,C66,P
  7       7 FORMAT(8E10.3)
  8         WRITE(6,1) C11,C12,C13,C16,C33,C44,C66,P
  9       1 FORMAT(8E12.3)
      C     A1(I) IS THE PROPAGATION DIRECTION IN THE (001) PLANE
      C     A1(I) IS MEASURED FROM THE +X AXIS (AN ANTICLOCKWISE ROTATION
      C     ABOUT THE Z-AXIS FROM THE +X AXIS)
 10         A1(1)=0.001
 11         DO 2 I=2,360
 12       2 A1(I)=A1(I-1)+0.01745
 13         DO 3 I=2,360
      C      DEGA1(I) IS A1(I) IN DEGREES
 14         DEGA1(I)=A1(I)*57.2956
XTENSION*      FN-4
BSCRIPTS ON RIGHT HAND SIDE OF STATEMENT FUNCTION
 15         N1(I)=COS(A1(I))
 16         N2(I)=SIN(A1(I))
 17         L11(I)=(N1(I)**2)*C11+(N2(I)**2)*C66+2.0*N1(I)*N2(I)*C16
 18         L12(I)=(N1(I)**2)*C16-(N2(I)**2)*C16+N1(I)*N2(I)*(C12+C66)
 19         L13(I)=0
 20         L22(I)=(N1(I)**2)*C66+(N2(I)**2)*C11-2.0*N1(I)*N2(I)*C16
 21         L23(I)=0
 22         L33(I)=(N1(I)**2)*C44+(N2(I)**2)*C44
      C     SOLUTION OF THE QUADRATIC STARTS HERE
 23         B(I)=L11(I)+L22(I)
 24         C(I)=-(L12(I)**2)+L11(I)*L22(I)
      C     ONE SOLUTION IS CALLED D(I) AND THE OTHER E(I)
      C     THESE ARE IN PV**2
 25         D(I)=(B(I)+SQRT((B(I)**2)-4.0*C(I)))/2.0
 26         E(I)=(B(I)-SQRT((B(I)**2)-4.0*C(I)))/2.0
      C     THE V$S ARE THE TWO REQUIRED VELOCITIES IN THE (001) PLANE
 27         V1(I)=SQRT(D(I)/P)
 28         V2(I)=SQRT(E(I)/P)
      C     THE X$S ARE THE RATIO U01/U02 FROM THE CHRISTOFFEL EQUATIONS
      C     X1(I) REFERS TO THE WAVE WITH A VELOCITY V1(I)
      C     X2(I) REFERS TO THE WAVE WITH A VELOCITY V2(I)
 29         X1(I)=-(L11(I)-D(I))/L12(I)
 30         X2(I)=-(L11(I)-E(I))/L12(I)
      C     NOW THE X$S MUST BE TRANSFORMED TO AN ANGLE
      C     CALL AX1 THE POLARISATION VECTOR ASSOCIATED WITH THE WAVE WITH
      C     A VELOCITY V1 AND A RATIO X1
      C     SIMILARLY FOR AX2
 31         AX1(I)=ATAN(X1(I))
 32         AX2(I)=ATAN(X2(I))
```

```
3           AX1(I)=AX1(I)*57.2956
4           AX2(I)=AX2(I)*57.2956
      C     DEV1,2 ARE DEVIATIONS OFPARTICLE DISPLACEMENTS FRO
      C      PROPAGATION VECTOR
5           DEV1(I)=AX1(I)-DEGA1(I)
6           DEV2(I)=AX2(I)-DEGA1(I)
      C      ENERGY FLUX VECTORS
      C     P211 IS THE RATIO P2/P1 FOR MODE 1
      C     P212 IS THE RATIO P2/P1 FOR MODE 2
7           P211(I)=(N1(I)*(X1(I)*C66+X1(I)*C12+C16-(X1(I)**2)*C16)
           1+N2(I)*(C66+(X1(I)**2)*C11-2.0*X1(I)*C16))/
           2(N1(I)*(C11+2.0*X1(I)*C16+(X1(I)**2)*C66)
           3+N2(I)*(C16+X1(I)*C66+X1(I)*C12-(X1(I)**2)*C16))
8           P212(I)=(N1(I)*(X2(I)*C66+X2(I)*C12+C16-(X2(I)**2)*C16)
           1+N2(I)*(C66+(X2(I)**2)*C11-2.0*X2(I)*C16))/
           2(N1(I)*(C11+2.0*X2(I)*C16+(X2(I)**2)*C66)
           3+N2(I)*(C16+X2(I)*C66+X2(I)*C12-(X2(I)**2)*C16))
      C     CALL QP211 THE ANGLE BETWEEN THE ENERGY FLUX DIRECTION AND THE
      C     +X AXIS MEASURED TOWARDS THE +Y AXIS
9           QP211(I)=ATAN(P211(I))
0           QP212(I)=ATAN(P212(I))
1           QP211(I)=QP211(I)*57.2956
2        23 QP212(I)=QP212(I)*57.2956
      C     QPX211 IS THE ANGLE BETWEEN THE ENERGY FLUX VECTOR ASSOCIATED
      C     WITH THE MODE 1 AND THE PROPAGATION VECTOR
3           QPX211(I)=QP211(I)-DEGA1(I)
4         3 QPX212(I)=QP212(I)-DEGA1(I)
5           DO 4 I=2,360
6         8 FORMAT(1F12.4,2E15.5)
7         4 WRITE(6,8) DEGA1(I),V1(I),V2(I)
NSION*      IO-C
ID ELEMENT IN AN OUTPUT LIST
8           DO 6 I=2,360
9         9 FORMAT(1F10.4,2E14.5)
0         6 WRITE(6,9) DEGA1(I),DEV1(I),DEV2(I)
NSION*      IO-C
ID ELEMENT IN AN OUTPUT LIST
1           DO 17 I=2,360
2        18 FORMAT(6F10.4)
3        17 WRITE(6,18) DEGA1(I),QPX211(I),QPX212(I)
NSION*      IO-C
ID ELEMENT IN AN OUTPUT LIST
4           STOP
5           END
```

4. Program to calculate Sij from Cij, bulk modulus, volume and linear compressibilities, isotropic moduli and mean sound velocity, and the orientation dependence of the Young's modulus.

```
$COMPILE
      REAL KV,GV,KR,GR,KH,GH,VL,VS,VM,THETAD,PE,M
      REAL ER,EV
      REAL V1,V2,V3,P
      REAL L1,L2,L3,YM,MY,R,A
      REAL LZ,LXY
      REAL T,X
      REAL C
    4 READ(5,105,END=99) X,T
  105 FORMAT(F10.1,F10.1)
      WRITE(6,106)
  106 FORMAT('  MATERIALX     TEMP')
      WRITE(6,105) X,T
      READ(5,7) C11,C12,C13,C16,C33,C44,C66
    7 FORMAT(7E10.3)
      WRITE(6,131)
  131 FORMAT('    C11         C12       C13        C16          C33        C44
     1     C66')
      WRITE(6,102) C11,C12,C13,C16,C33,C44,C66
  102 FORMAT(7E10.3)
      C=C44*C44*((C11-C12)*C66-2*C16*C16)*(C11*C33+C12*C33-2*C13*C13)
      S11=(C11*C33*C66-C13*C13*C66-C16*C16*C33)*C44*C44/C
      S12=-(C12*C33*C66-C13*C13*C66+C16*C16*C33)*C44*C44/C
      S13=(C12*C66-C11*C66+2.0*C16*C16)*C13*C44*C44/C
      S16=-(C12*C33+C11*C33-2.0*C13*C13)*C16*C44*C44/C
      S33=(C66*(C11*C11-C12*C12)-2.0*(C11*C12)*C16*C16)*C44*C44/C
      S44=1/C44
      S66=(C33*(C11+C12)-2*C13*C13)*(C11-C12)*C44*C44/C
      WRITE(6,125)
  125 FORMAT(/'  SIJ IN CMS**2/DYNE')
      WRITE(6,132)
  132 FORMAT('    S11         S12       S13        S16          S33        S44
     1     S66')
      WRITE(6,102) S11,S12,S13,S16,S33,S44,S66
      BM=1/(2*S11+S33+2*S12+4*S13)
      WRITE(6,126) BM
  126 FORMAT(5X,'BULK MODULUS=',E10.3,'DYNE/CM**2')
      LXY=S11+S12+S13
      LZ=S33+2.0*S13
      VCOMP=LZ+2.0*LXY
      WRITE(6,127) LZ,LXY
  127 FORMAT(5X,'LINEAR COMP.LZ=',E10.3,'LXY=',E10.3)
      WRITE(6,128) VCOMP
  128 FORMAT(5X,'VOLUME COMPRESSIBILITY=',E10.3,'CM**2/DYNE')
      EV=((C11-C12+3*C44)*(C11+2*C12))/(2*C11+3*C12+C44)
      ER=(5*C44*(C11-C12)*(C11+2*C44))/(C44*(3*C11+C12)+(C11-C12)*(
     2C11+2*C12))
      WRITE(6,150) ER,EV
  150 FORMAT('ER',E10.3,'  EV'E10.3)
      KV=((2*C11+C33)+2*(C12+2*C13))/9
      GV=((2*C11+C33)-(C12+2*C13)+3*(2*C44+C66))/15
      KR=1/((S11*2+S33)+2*(S12+2*S13))
      GR=15/(4*(2*S11+S33)-4*(S12+2*S13)+3*(2*S44+S66))
      KH=(KR+KV)/2
      GH=(GR+GV)/2
      D=4.255
      VL=SQRT((KH+1.333*GH)/D)
      VS=SQRT(GH/D)
      VM=1/((0.3333*(2/(VS**3)+1/(VL**3)))**0.33333)
```

```
      C      YOUNG'S MODULUS IN 001 PLANE,L3=0
   56         WRITE(6,109)
   57       109 FORMAT('(001)PLANE,X-Y PLANE')
   58         DO 9 I=1,360
   59         A=I
   60         R=A/57.2956
   61         L1=COS(R)
   62         L2=SIN(R)
   63         L3=0
   64         MY=(L1**4+L2**4)*S11+L3**4*S33+(L1**2)*(L2**2)*(2*S12+S66)+
             1(L3**2)*(1-L3**2)*(2*S13+S44)+2*L1*L2*(L1**2-L2**2)*S16
   65         YM=1/MY
   66       8 FORMAT(F9.1,E17.3)
   67       9 WRITE(6,8) A,YM
      C       YM IN 100 PLANE
   68         WRITE(6,110)
   69       110 FORMAT('100 PLANE,Y-Z PLANE')
   70         DO 14 I=1,360
   71         A=I
   72         R=A/57.2956
   73         L1=0
   74         L3=COS(R)
   75         L2=SIN(R)
   76         MY=(L1**4+L2**4)*S11+L3**4*S33+(L1**2)*(L2**2)*(2*S12+S66)+
             1(L3**2)*(1-L3**2)*(2*S13+S44)+2*L1*L2*(L1**2-L2**2)*S16
   77         YM=1/MY
   78        14 WRITE(6,8) A,YM
      C       YM IN 110 PLANE
   79         WRITE(6,112)
   80       112 FORMAT('110 PLANE')
   81         DO 15 I=1,360
   82         A=I
   83          R=A/57.2956
   84         L3=COS(R)
   85         L1=(SIN(R))/1.414
   86         L2=L1
   87         MY=(L1**4+L2**4)*S11+L3**4*S33+(L1**2)*(L2**2)*(2*S12+S66)+
             1(L3**2)*(1-L3**2)*(2*S13+S44)+2*L1*L2*(L1**2-L2**2)*S16
   88         YM=1/MY
   89        15 WRITE(6,8) A,YM
   90         GO TO 4
   91        99 STOP
   92         END
```

5. Program to calculate the intensities of pairs {hkl}, {khl} of spots on a Laue back reflection photograph taken with the x-ray beam parallel to the Z axis.

```
  FACTC:PROC OPTIONS (MAIN);
        DCL((X,Y,Z)(3))FLOAT;
        DCL(H,K,L)FLOAT;
        DCL((A,B,G)(3))FLOAT;
  DCL(F)(3)FLOAT;
    DCL (D,A1,C1)FLOAT;
    GET LIST (C1,A1);
    PUT EDIT ('C=',C1,'A=',A1)(2(A,F(7,4)));
    PUT LIST ('A1          A2          A3          B1          B2          B3');
    DO I=1 TO 3;
    GET LIST (X(I),Y(I),Z(I));
    END;
NEW:GET LIST (H,K,L);
    PUT SKIP EDIT (H,K,L)(3 F(4));
    D=SQRT(1/(((H**2+K**2)/(A1**2)+L**2/C1**2));
    DIN=1.0/(2*D);
   PUT EDIT (' DIN',DIN)(A,F(6,3));
    DO I=1 TO 3;
    G(I)=8*((COS(2*3.142*(H+K+L)*0.25))**2)*(COS(2*3.142*
         (H*(X(I))+K*(Y(I))))*COS(2*3.142*(L*Z(I)-(2*K+L)/8))+COS(2*
         3.142*(H*Y(I)-K*(X(I))))*COS(2*3.142*(L*Z(I)+(2*K+L)/8)));
    A(I)=G(I)*COS((2*K+L)/8);
    B(I)=G(I)*SIN((2*K+L)/8);
    END;
    PUT EDIT (A(1),A(2),A(3),B(1),B(2),B(3))(6 F(10,3));
  DO I=1 TO 3;
    GET LIST (F(I));
   END;
    QZ=((F(1)*A(1)+F(2)*A(2)+F(3)*A(3))**2)+
   ((F(1)*B(1)+F(2)*B(2)+F(3)*B(3))**2);
    PUT SKIP LIST (QZ);
    GO TO NEW;
    END;
```

APPENDIX II

PUBLICATIONS

1. "THE ELASTIC CONSTANTS OF $CaWO_4$"
   J M Farley and G A Saunders (1971) Solid State Comm. 9, 965-9

2. "EFFECT OF CURRENT BLACKENING ON THE ELASTIC CONSTANTS OF YTTRIA STABILISED ZIRCONIA"
   J M Farley, J S Thorp, J S Ross, G A Saunders (1972) J. Mat. Sci. 7, 475-6

3. "CONVERSELY ORIENTED ETCH PITS IN A7 STRUCTURE SEMIMETALS"
   Y C Akgöz, J M Farley and G A Saunders (1972) J. Mat. Sci. 7, 598-600

4. "ULTRASONIC STUDY OF THE ELASTIC BEHAVIOUR OF CALCIUM TUNGSTATE BETWEEN 1.5 K and 300 K"
   J M Farley and G A Saunders (1972) J. Phys. C:Solid State 5, 3021-37

5. "THE ELASTIC BEHAVIOUR OF InBi SINGLE CRYSTALS"
   Y C Akgöz, J M Farley and G A Saunders (1973) J. Phys. Chem. Solids 34, 141-9

6. "ACOUSTIC SYMMETRY OF SCHEELITE STRUCTURE CRYSTALS"
   J M Farley and G A Saunders (1973) Paper read at Institute of Physics Solid State Physics Conference, Manchester

7. "THE ELASTIC CONSTANTS OF STRONTIUM MOLYBDATE"
   J M Farley, G A Saunders and D Y Chung (1973) J. Phys. C:Solid State 6, 2010-9